Surface Modification of Bipolar Plates for Fuel Cells by Plasma Treatment

Der Fakultät für Physik der Universität Duisburg-Essen vorgelegte

Dissertation

zur Erlangung des akademischen Grades eines Doktors der Naturwissenschaften

- Dr. rer. nat. -

von

Tatiana N. Fedosenko-Becker

geboren am 21.09.1988

in Gomel, Weißrussland

Tag der Disputation: 24.01.2019

Vorsitzender: Prof. Dr. Jürgen König
Gutachter: Prof. Dr. Dr. h.c. Volker Buck
Gutachterin: Prof. Dr. Angelika Heinzel
Prüfer: Prof. Dr. Gerhard Wurm


BY NC ND

Contents

Acknowledgements

First and foremost, I want to express my deep gratitude to Prof. Dr. rer. nat. Dr. h.c. Volker Buck, my supervisor, for giving me the opportunity to start and complete this work and to contribute to the research of his group, for helping me with all the occurring issues since the beginning of my work in his research group and especially for his valuable and patient guidance, sound advice, care and useful criticism concerning my work. I am deeply thankful for all his support, help and for believing in me.

I'm grateful to various people from F. Skorina Gomel State University, who supported me, helped me to solve numerous organizational problems and contributed in any way to my doctoral study at the University of Duisburg-Essen in Germany. Especially I would like to thank Prof. Dr. Alexander V. Rogachev, my Belarusian supervisor, for his guidance, support and advice. I am also very thankful to Prof. Dr. Sergei A. Khakhomov for all his help and support.

I am very grateful to Prof. Dr. rer. nat. Dieter Mergel for his valuable advice and for the constructive criticism of my work.

I would like to express my very great appreciation to all my colleagues from the research group of Prof. Buck, whom I consider friends now, for their help and pleasant environment we created in our group. It was a real pleasure to work together with them.

I am particularly grateful for the assistance given by Dr. Nicolas Wöhrl, whose friendly attitude and enthusiastic encouragement motivated me a lot. Thanks a lot for guiding me and believing in me.

I want to offer my special thanks to Reinhard Remfort for guiding and helping me in many ways in the beginning of my work, for helping me very much to cope with a lot of organizational challenges and for his great contribution to assembly of my plasma device. Particularly, I want to thank Reinhard for lending me the best bike I have ever ridden when I had lack of transport to come to work.

I wish to acknowledge all the help provided by Sebastian Schipporeit, particularly for SEM and EDX measurements. Besides his contribution to my work, I am thankful for his contribution to my integration: for his guitar and for many fun moments we shared.

I am deeply thankful to Monika Timpner for her help with Raman measurements and for friendly, kind, sincere and unconditional personal help.

Another person whom I want to thank particularly is Regina Berendakova, who did a lot to introduce me to the work of the group and often helped me in many ways.

I am sincerely thankful to Viktoria Khlopyanova for her generous help and care concerning my integration and the start of my work at the University of Duisburg-Essen. I remember and appreciate it a lot.

I am also very grateful to my colleague Mario Gillmann for all the resistance measurements, which are very important for this research work, and also for being always friendly, responsible and willing to answer all my questions. He invested his time to show and explain me how the ASR was being measured. It was a pleasure to work with him.

I would like to express my very great appreciation to Dr. Martin Schade for the willingness to give his time so generously and for his help with AES, FTIR and wettability measurements. Some important conclusions of this research could be made due to his professionalism and accurate measurements. I also appreciate his friendly attitude and personal qualities very much.

The assistance of Dr. Ulrich Hagemann and his time invested for XPS measurements and for teaching me operating the PHI 710 Scanning Auger Nanoprobe instrument has been very much appreciated. I am very grateful for his patience and help.

I would like to express my very great appreciation to Dr. Nadezhda G. Ariko for the willingness to give her time, professional guidance and immeasurable help with the analysis of FTIR and Raman spectra.

Thanks a lot to Dr. Valentina G. Sholoh for valuable and informative consultations and assistance.

I also deeply appreciate the help of Nina A. Krekoten' and colleagues for her professional assistance and for SEM and EDX measurements.

I would like to express my deep gratitude to Dmitry Gorbachev from F. Skorina Gomel State University for AFM measurements and for his kind help in many challenges.

Thanks a lot to Ana Luiza F. Ferraz for the experiments conducted with Tigres plasma source and for the results provided.

I would like to thank Benedikt Funke and colleagues for the measurements by the confocal microscope μsurf from NanoFocus and for the results provided.

I am very thankful to Stanislav Gorelkov for his friendly assistance with FTIR measurements and for the willingness to give his time and to help. Thanks to Igor Zagoranskiy for his assistance with AFM measurements. I would also like to thank Dr. Tomáš Homola for his valuable and constructive suggestions during the development of this research work, also for his support and sharing his scientific experience.

Prof. Dr. Alexander Čaus from Slovak Technical University provided me with very valuable knowledge and experience, which helped me a lot in my research work and in writing this dissertation, therefore I am deeply thankful to him.

I want to thank AiF-Project "Kontinuierliches Fertigungskonzept zur Herstellung großflächiger Compound-Bipolarplatte" (ZN 09570/12) 2013 – 2015, for making this research possible and for the financial support.

I am immeasurably grateful to my family members, who created the conditions for me to start and to complete this work. Their contribution is priceless. My parents – Dr. Nikolay N. Fedosenko and Elena A. Fedosenko raised my scientific interest and inspired me all my life, supported and motivated me, always assisted my work, solving all the problems occurring, and provided me with the time to write this doctoral thesis. Elke Becker, my mother-in-law, supported me in many ways all this time. I would definitely not manage to complete this work without her generous help.

I am especially and sincerely grateful to Michael Becker, my colleague and my husband, for all his assistance, help and care, for his daily patience, for inspiring, supporting and motivating me, for sharing scientific ideas and teaching me, for being such a great husband and father.

It is not possible to mention all the people I want to thank, but I am very thankful to all my friends and to all the people who believed in me, supported, or motivated, or helped me in any possible way. I do appreciate it and I am deeply grateful to each of them!

Zusammenfassung

Brennstoffzellen werden im Allgemeinen als eine moderne und vielversprechende alternative Energiequelle angesehen, weswegen sie ein großes wissenschaftliches Interesse erhalten haben. Brennstoffzellen auf der Basis von Protonen-Austausch-Membranen, dessen Erforschung und Produktion ein Schwerpunkt im ZBT ist, bestehen typischerweise aus zwei Elektroden - Bipolarplatten, welche durch die Protonen-Austausch-Membranen voneinander getrennt sind. Bei der Herstellung von Bipolarplatten auf der Basis von Grafit/Polypropylen wird die Oberfläche der Bipolarplatten mit Polypropylen angereichert, was wiederum zu einer signifikanten Verringerung der elektrischen Leitfähigkeit und somit des Wirkungsgrades der Brennstoffzelle führt. Es ist möglich, die Oberflächenleitfähigkeit mit der Hilfe einer Plasmabehandlung zu verbessern. In dieser Arbeit wurde eine Plasmaquelle vom Typ CYRANNUS® der Firma IPLAS verwendet, bei welcher die Probe nicht direkt im Plasma, sondern im Remote-Bereich positioniert werden kann. Die Plasmaquelle erlaubt es, eine Vielzahl von Parametern einzustellen und ermöglicht es so die idealen Behandlungsparameter für Bipolarplatten zu finden. Plasmaätzen ist technisch einfacher zu beherrschen als die Beschichtung der Bipolarplatten mit elektrokatalytischen Materialien, da diese Beschichtungen eine Vielzahl von Bedingungen erfüllen müssen, wie zum Beispiel eine gute Adhäsion zwischen Beschichtung und Bipolarplatte und eine große Widerstandsfähigkeit gegen hohe Temperaturen und Wasser.

Es wird gezeigt, wie die Plasmabehandlung das Polymer von der Oberfläche entfernt. Für diesen Zweck werden die besten Parameter bestimmt. Die Entfernung des Polypropylens von der Oberfläche der Bipolarplatten wird durch Messungen mittels FTIR Spektroskopie nachgewiesen. Weiterhin wird mittels Raman Spektroskopie gezeigt, dass der Grafit an der Oberfläche, welches der Plasmabehandlung ausgesetzt ist, seine Struktur von Nanokristallin zu Poly-

kristallin ändert. Weniger Korngrenzen zwischen den Kristallen führen zu einer Verringerung der Elektronenstreuung, was wiederum zu einer Vergrößerung der elektrischen Leitfähigkeit der plasmabehandelten Bipolarplatten im Gegensatz zu den unbehandelten Bipolarplatten führt.

Die Mechanismen des Plasmaätzen der Oberfläche stehen in Verbindung mit der chemischen Zusammensetzung des Plasmas, was mithilfe der optischen emissions-Spektroskopie beobachtet werden kann. Eine Vielzahl von Änderungen der Oberflächenchemie, Morphologie und Topografie nach der Plasmabehandlung werden aufgezeigt und beschrieben.

Die Messung des flächenspezifischen Widerstandes der Bipolarplatten zeigen, dass die elektrischen Eigenschaften der Bipolarplatten für die Anwendung in Brennstoffellen erfolgreich durch das Plasmaätzen verbessert werden konnten. Es wird gezeigt, dass Plasmabehandlung mit Luft unter Atmosphärendruck eine äußerst effiziente Methode darstellt, um die elektrische Leitfähigkeit von Bipolarplatten zu verbessern.

Abstract

Fuel cells are regarded as modern and promising alternative energy sources, therefore they have earned scientific interest. Proton exchange membrane fuel cells, which are of main interest for research and development in ZBT (Duisburg), typically consist of two electrodes – bipolar plates, separated by a proton exchange membrane. During the process of fabrication of graphite/polypropylene composite bipolar plates the surface of bipolar plates is enriched by polypropylene significantly reducing the electrical conductivity and thus the efficiency of the fuel cells. Surface conductivity can be improved by plasma treatment. In this work the plasma source CYRANNUS® by IPLAS was used in a remote mode. This device allows to vary a lot of parameters to find the treatment conditions suitable for carbon bipolar plates. Plasma etching is more technologically advanced than the deposition of a coating of electrocatalytic materials onto the surface of the bipolar plates, since such coating must meet many criteria, including a very good adhesion and the coating should not be degraded by high temperatures and water.

It is shown how plasma treatment removes polymer from the surface. The most suitable experimental parameters for this task are found. The removal of polypropylene from the surface of bipolar plates is corroborated by the measurements using FTIR spectroscopy method. Furthermore, it is shown by Raman spectroscopy that graphite on the surfaces of the samples exposed in plasma changed its structure from nanocrystalline to polycrystalline. Fewer interfaces between the crystals lead to the reduction of electron scattering and hence the conductivity of the plasma treated samples is higher than the conductivity of the untreated ones.

The etching effect on the surface is correlated with the plasma chemistry, what can be observed by optical emission spectroscopy. Various changes of surface

chemistry and also morphology and topography of the surface after the plasma treatment are described and explained.

The measurements of area specific resistance of bipolar plates showed that the electrical properties of bipolar plates for fuel cells were efficiently and successfully improved by the method of plasma treatment. It is demonstrated that plasma treatment by air at atmospheric pressure is an efficient method to improve the electrical conductivity of bipolar plates.

1 Introduction

Fuel cells with proton exchange membrane are energy converters suitable for various applications with different requirements [1]. Their main advantages are ecological compatibility and high efficiency compared to other energy conversion devices. However, there are still issues to work through before the applications of fuel cells can be significantly commercialized [2]. For example, the cost of automotive fuel cells should be competitive with today's internal combustion engines. Stack technology, system optimization and development of new materials are the drivers to achieve the cost target [3]. Therefore, in recent years there are vigorous efforts worldwide to solve the existing problems and especially to find suitable materials for bipolar plates of fuel cells [4]. Unfortunately, some investigations of material combinations remained unpublished, as it is often proprietary company know-how [1].

For bipolar plates of fuel cells two different kinds of materials, graphitic and metallic, are the most commonly used. The requirement of high power densities at very low cost for mobile applications of fuel cells is quite difficult to fulfill though the lifetime is limited to several thousand operational hours. In this case (stainless) steel can be the material of choice, because it is already a mass product and its forming processes are well established in the automotive industry. Thin sheets show sufficient mechanical strength. Two sheets of thin structured metal plates can be combined into a bipolar plate. Metallic bipolar plates have excellent electrical conductivity. Modern fuel cells with metallic bipolar plates are smaller in size than the fuel cells with graphitic bipolar plates. But they are susceptible to corrosion, so a corrosion-protective coating (carbon-based or metal-based) is typically required to improve the lifetime. This is the main disadvantage of metallic bipolar plates compared to the graphitic ones. Moreover, steel bipolar plates are produced by forming methods like stamping or hydroforming. But

since the flow fields of metallic bipolar plates require quite fine structures of gas channels in the millimeter range, these requirements pose some challenges to the forming process, as well as to the coating process. An alternative to channel-type flow fields is the use of open-pore metal foams for distribution of the gaseous reactants and for water removal. But metal foams also require corrosion-protective coatings to be successfully applied in fuel cells. Coating is related to time consume and additional costs. Actually, nowadays coated metal bipolar plates seem to have achieved corrosion stability for the relatively short operation times of automotive applications. Several car manufacturers use metallic bipolar plates in their automotive fuel cell stacks [1].

For stationary applications space and weight restrictions of fuel cells are less severe, but durability requirements are usually much higher. Therefore, graphitic materials are preferred as bipolar plate materials for this purpose. Pure graphite-based bipolar plates offer the advantages of excellent chemical resistance and good thermal and electrical conductivity combined with a lower density than metal plates. Also machining the flow fields into pure graphite plates is complicated, expensive and time-consuming. Pure graphite plates are brittle and porous, so graphite is not gas-tight enough to separate hydrogen and air from the cooling channels. For this reason, composite materials based on graphite with polymer binders are used. Composite materials are often the best solution when very diverse requirements are imposed to the material. Forming processes have to be developed or at least adapted to the new material combinations. For stationary applications of fuel cells, bipolar plates made of graphite composite materials are the only alternative, showing good long-term stability [1]. But large-scale application of graphite composite bipolar plates for fuel cells requires further improvement in terms of lifetime and price.

The most significant disadvantage of graphite composite bipolar plates produced by injection molding is not sufficient electrical conductivity. The reason is the non-conductive binding polymer, especially on the contact surfaces of bipolar plates. To solve this problem mechanical milling of the surface was used. But high cost, time consuming and the risk to cause significant mechanical damages

to the structure of the surface of bipolar plates pushed into looking for alternative methods of removal of polymer from the surface and hence improvement of electrical conductivity of bipolar plates.

One of such methods investigated here could be remote plasma treatment of the surface. This method showed to remove polymer from the surface relatively quickly without any damage of the structure of the flow-field of bipolar plates and it is not related to high costs. Besides this, plasma treatment by atmospheric air and at atmospheric pressure may be the best solution for industrial application of this method, due to its time- and cost-efficiency. Plasma treatment of bipolar plates with a view to improve their electrical properties is not studied yet. Therefore, the aim of this works is scientific investigation of plasma treatment of bipolar plates for fuel cells as a replacement of mechanical milling in order to improve their electrical conductivity.

2 Approach

A very expensive plasma system was selected for the surface modification. This system is characterized by:

- It can be operated in an extremely wide pressure range (from <1 mbar up to atmospheric pressure);
- The energy is fed into the system by microwaves without electrodes, therefore any gas can be processed in the system, in particular oxygen-containing gases;
- Due to the suitable design and the vacuum system the plasma device can be operated using dangerous gases like hydrogen.

In addition, a detailed OES plasma diagnostics was integrated.

The electrical contact conductivity of bipolar plates before and after plasma treatment was the final parameter of this research. Since electrical conductivity is determined by structural properties, structural analysis is used to determine the influence of the plasma treatment and to compare different treatment methods. Because sample composition may influence its electrical conductivity, besides the variation of the plasma parameters additionally foils of different composition were used. The foils can also be regarded as electrodes in fuel cells, they do not have any surface pattern and it is not so complicated to produce foils with different content of PP, graphite and carbon black, therefore they are used for some investigations in this work.

Considering the analysis of the samples, every available analytical method was used. Apart from the measurements of electrical conductivity, which obviously

confirmed the efficiency of plasma treatment from the beginning of the experimental work, the most interesting analytical results were expected from the methods, which allow to understand the mechanism of plasma influence on the surface: FTIR spectroscopy for investigation of the changes in heteropolar bonds and Raman spectroscopy for investigation of the changes in homopolar bonds with no transfer of charge. FTIR and Raman investigation methods, together with the investigation of the electrical conductivity of bipolar plates and foils, are the main focus of this research work. The analysis of Raman spectra led to unexpected results: that plasma influences not only the polymer, but also the graphitic particles, changing their structure.

Besides this, such simple changes as the mass change and the water wettability change due to plasma treatment were described to show the influence of plasma treatment on the samples. Chemical analysis of the surface was conducted by XPS, AES methods in the nano-range and by EDX method in the micro-range. For the sake of completeness of the investigation morphology and topography research was conducted by SEM, stylus profilometry, AFM and confocal microscopy methods.

The selected gases (argon, air, carbon dioxide, oxygen, nitrogen) differ in interaction with the sample. Argon and nitrogen have practically only physical interaction with the surface. In air physical interaction is combined with chemical interaction of the oxygen part. In carbon dioxide there is a mixed etching effect and in oxygen – pure chemical interaction. Plasma treatment by air at atmospheric pressure is especially interesting, because this kind of treatment is omitting the time-consuming pumping, the costs and the equipment for keeping a stable pressure, therefore it can be easily and effectively used in industry.

It is known that high-energy ions are abundant at low pressures [5], therefore the experiments were conducted predominantly at low pressures.

Investigating the plasma treatment of bipolar plates, the following demands were regarded:

- the treated bipolar plates have as high electrical conductivity as possible
- the treatment process is as cheap as possible (using atmospheric air as the working gas)
- the treatment process is as quick as possible (the most intensive treatment conditions, which do not destroy the sample, using air at atmospheric pressure as the working gas)
- samples of different sizes and chemical content require different sets of treatment parameters, which must be found experimentally for the plasma device used (described in Chapter 5) and the results must be reproducible
- a scientific explanation of the results must be given
- a conclusion about successful or unsuccessful replacement of mechanical milling by plasma treatment must be made.

A considerable part of this work was devoted to find the best experimental parameters, which would allow the samples to have the best possible electrical properties and would be the most cost- and time-efficient. The right combination of such experimental parameters as plasma chemistry, treatment time, gas flow, power and working pressure of the gas in the chamber is responsible for the efficiency of the etching process. Experimentally it was found in this work that bipolar plates reach the best electrical conductivity after approximately 20 minutes of plasma treatment by oxygen-containing gases at low pressures. For the foils the treatment duration and other parameters are different and must be varied depending on the content of the foil. The lower the working pressure is and the higher the gas flow is, the more mass is being removed from the surface during the plasma treatment process. The experiments were conducted at simultaneous plasma control by the method of OES.

3 Fundamentals

3.1 Fuel Cells

Taking into account the problem of high carbon dioxide emissions into the atmosphere, which is of a special scientific interest in recent years, the challenge is to develop new efficient and ecological energy sources. Recently there has been an increase in the pace of the development of hydrogen energy, which is environmental friendly, efficient and renewable, therefore it can be regarded as a perspective aim of scientific research and ecological energy development. The main task is to produce fuel cells and to use hydrogen to generate electricity [6, 7].

Hydrogen fuel cells are electrochemical devices, which convert the energy of the chemical reactions of combination of hydrogen and oxygen directly into electrical energy. The efficiency of the fuel cells is quite high, because there are no energy losses on inefficient combustion processes [7]. Proton exchange membrane (PEM) fuel cells are very promising nowadays. A schematic view of a single PEM fuel cell is presented in Fig. 3.1 [8].

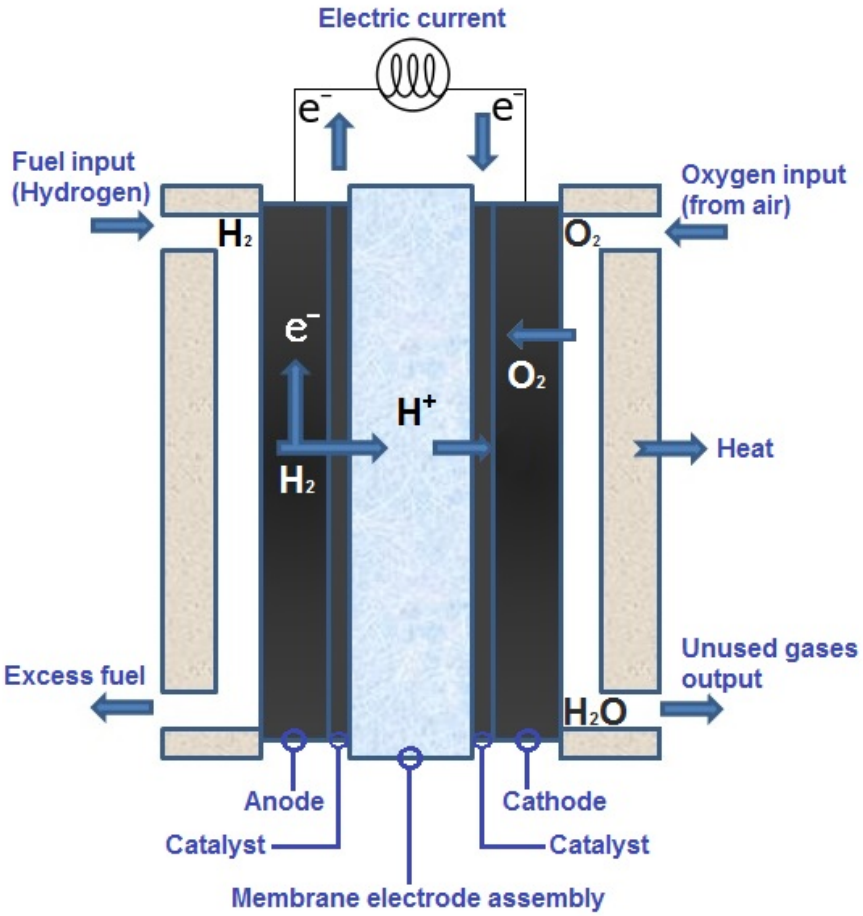

Figure 3.1: Schematic view of a single PEM fuel cell.

Chemical reactions in a fuel cell take place between the electrodes with flow channels. The electrodes are situated in a stack, so that a cathode is the anode of the following cell and thus these electrodes are called bipolar plates (BPP). The BPP are activated by a catalyst (usually based on platinum or other metals of the platinum group), according to the following scheme: hydrogen atoms are decomposed into electrons and protons at the anode of the fuel cell.

$$H_2 = 2e^- + 2H^+ \tag{3.1}$$

Electrons enter the external circuit, creating electric current. Protons, in turn, pass through the PEM to the cathode side, where they meet oxygen and electrons

from the external electrical circuit with the formation of water:

$$4H^+ + 4e^- + O_2 = 2H_2O \tag{3.2}$$

The by-products of the reaction are thus heat and water vapor [7]. Since the output volatage of a single fuel cell is given by the reactants used, in the case of hydrogen and oxygen it is upto 0.8 V at full load, thus it is necessary to connect several cells to a stack, like it is shown in Fig. 3.2. Because the anode of a cell is the cathode of the next cell these are called bipolar plates. By doing this, the values of the voltage of each cell are added together producing a higher total voltage. However the internal resistance of each cell as well as the resistance of the interconections between the cells is adding up too, decreasing the produced power of the stack. To minimize this effect, it is important to get as low internal resistances of the fuel cells and the interconnecting bipolar plates as possible, what is the aim of this work.

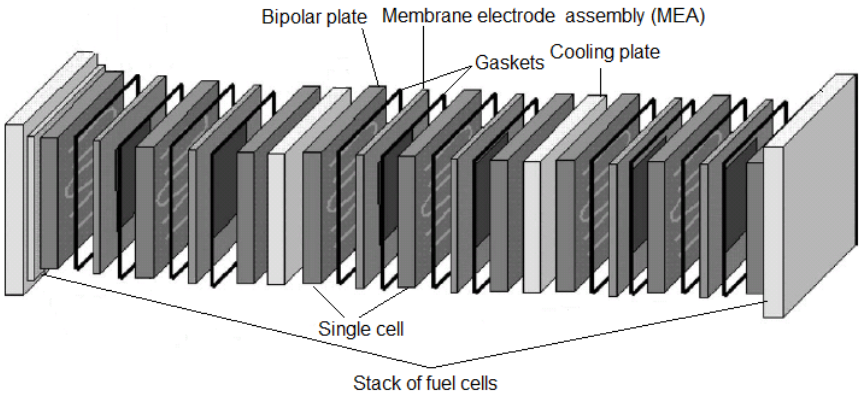

Figure 3.2: Schematic view of a PEM fuel cell stack in seriall connection to achieve higher output voltages (adapted from [3]).

The proton exchange membrane (PEM) is the heart of a fuel cell. Typically, PEM is a polymer film that combines a hydrophobic backbone and side fragments containing acid groups – hydrophilic part [7]. Membrane electrode assembly (MEA) in Fig. 3.1 is an assembled stack of PEM [9]. The MEA has the same external dimensions and media feedthrough holes as the bipolar plate. In the area of the active surface it is coated by the catalyst material. In the active

area, which comes in contact with the catalyst, it is covered from both sides by gas diffusion layers (GDLs, made of GoreTM Carbel® CL carbon cloth) and externally – by two gaskets [10], as shown in Fig. 3.3

It should be noticed that BPP are sometimes alternatively called bipolar half-plates (BPHP) to underline that one fuel cell has two electrodes.

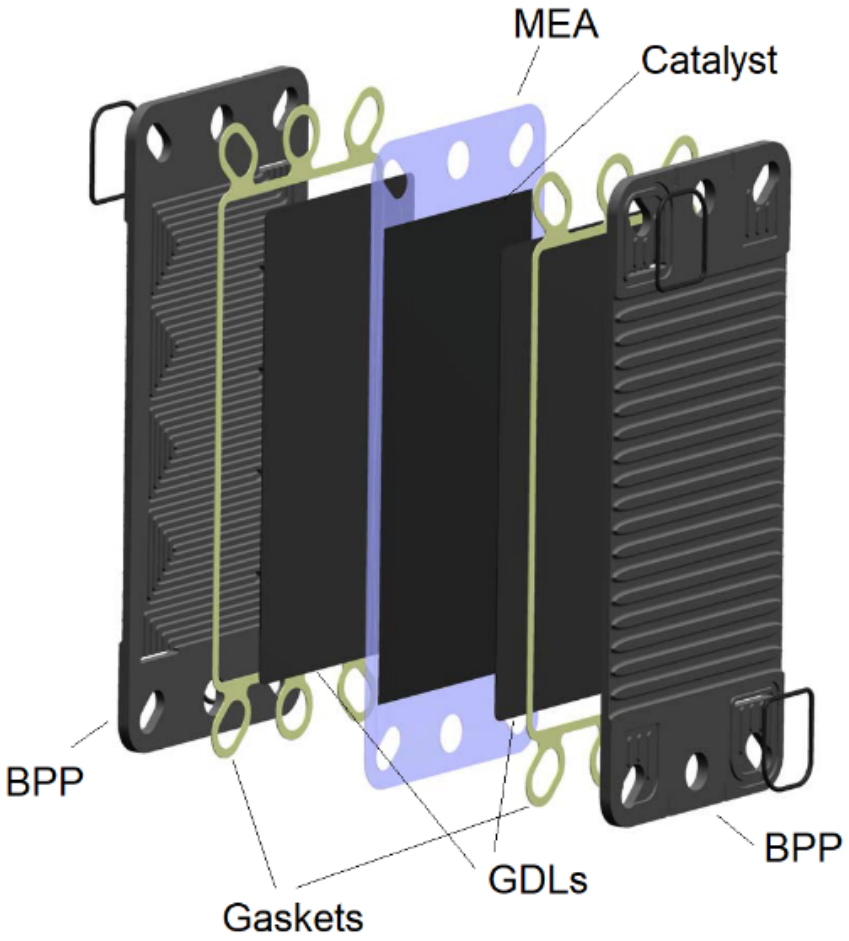

Figure 3.3: 3D view of the components of a single cell (adapted from [10]).

3.2 Bipolar Plates (BPP)

BPP are considered to be one of the most problematic parts of a fuel cell [3]. There are strict requirements for the general development of BPP, such as: good electrical conductivity, high thermal conductivity, high chemical and corrosion resistance, mechanical stability toward compression forces, low hydrogen permeability, low-cost material being processable with mass production techniques, low weight and volume and also usage of recyclable materials [1]. These requirements are related to the functions of BPP in a fuel cell stack: to distribute the fuel and oxidant within the cell, to facilitate water management within the cell, to separate individual cells in the stack, to carry current away from the cell and to facilitate heat management [4]. The authors of [11] and [12] suggested the specific properties a BPP must have to be considered as an element of a functioning fuel cell, among these criteria there is also a requirement to the area specific resistance of BPP, which must be below 0.01 $\Omega \cdot cm^2$ [4].

The BPP investigated in this work have a size of 137.5x62x2.8 mm^3 [10]. In Fig. 3.4 (left) one can see the flow field on the surface of a BPP to supply the reactant gases to the gas diffusion electrodes. The effectiveness of reactant transport depends partially on the flow-field design [3, 13].

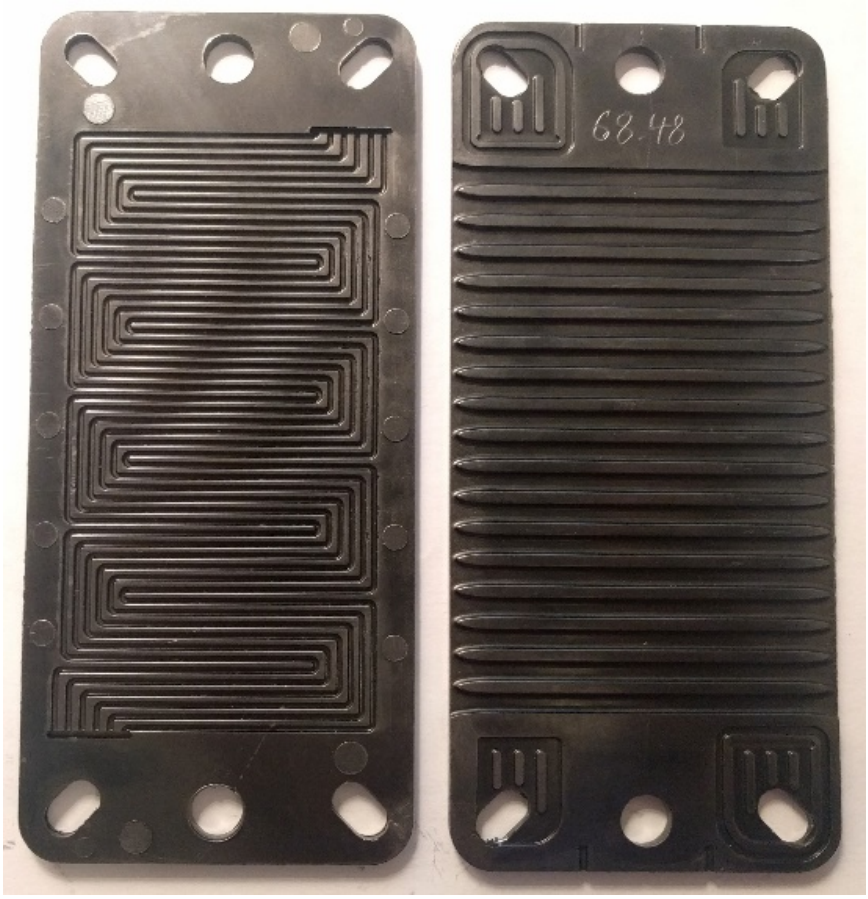

Figure 3.4: Injection molded BPP made of graphite composite material in ZBT, Duisburg.

The BPP are produced in ZBT (Zentrum für BrennstoffzellenTechnik ZBT GmbH, Duisburg) by injection molding, based on thermoplastic and carbon compounds [14, 15]. These BPP consist of filler additives (roughly 80 $wt\%$), graphite is the main filler, binder – polypropylene (PP) Adstif HA840R from Lyondell-Basell and conductive carbon compound – carbon black, in different proportions. The exact composition is the know-how of ZBT, therefore, it cannot be published, however it was taken into account in the investigation presented in this work. A. Heinzel and colleagues report in [1]:

> „The conducting particles form a percolation network within the polymer matrix. Owing to the polymer matrix, the composite material, at least partly, retains the processability of the polymer. To obtain a

> mechanically stable bipolar plate with low gas permeability, a good quality of dispersion of the conductive component particles within the polymer binder is required.“

To study the properties of carbon-PP composites of different content foils were also investigated. They are easily produced, because they do not have any flow-field design, as shown in Fig. 3.5 Like BPP, the foils are also produced in ZBT and have from 29 $wt\%$ to 35 $wt\%$ of PP in the content.

Figure 3.5: View of a carbon-PP composite foil.

Carbon-polymer composites are relatively low-cost materials and suitable for mass production of BPP, because the flow-fields can be molded directly in an established mass production process [3].

Many scientific researches focus on investigation of the properties of carbon-polymer composites and the properties of polymers at interfaces. The results of such researches allow to understand and predict the changes in physical and chemical properties of BPP under the influence of plasma, hence they play an important role for this study. Jun-Feng Zou et al. [16] reported about the relationship between the structure of carbon black and the conductivity of polymer composites. It was documented that the structure of carbon black plays an important role in conduction mechanism, as important as carbon black content does

[16]. The structure of polymer materials is bulk-inhomogeneous. The properties of the layer at the interface may differ to a large extent from the bulk polymer state [17, 18]. Formation of the interface bonds leads to significant and sometimes complicated changes of the initial polymer state due to the processes of restructuring the supramolecular polymer structure, change of the chemical composition and structure of macromolecule, for example due to oxidation process and polymer crosslinking or thermal destruction [17].

The composition of the studied BPP is optimal to meet the mechanical and thermal requirements [11, 12], but electrical conductivity deteriorates due to relatively high amount of PP on the surface of BPP. To solve this problem mechanical milling was used up to now. But this method has serious disadvantages: it is time-consuming, expensive and it damages the surfaces of BPP. Plasma treatment is devoid of these disadvantages, it allows to remove PP from the surface of BPP quickly and causing no harm to the surface, therefore it is a perspective and promising method to solve the problem of low electrical conductivity of BPP.

Thus, the main objective of this work is optimization of the surface properties by plasma to improve the electrical conductivity of BPP.

3.3 Plasma Treatment

The processes of interaction between plasma and surface, considered in this work, are limited by surface and near-surface layers of material, because the kinetic energies of plasma particles do not exceed several eV. By such energies the thickness of the surface layer where interactions between atoms, molecules, radicals, electrons, positive and negative ions and the material of the surface take place, does not exceed several nanometers, because it is limited by a few dozens of atomic layers near the surface. These interactions can be generally divided into physical (exchange of energy and kinetic moment in elastic collisions of atomic particles leads to sputtering of the material from the surface, etching or cleaning the surface) and chemical (inelastic collisions with the exchange of electrons between atoms lead to chemical reactions on the surface). In real plasma processes it is

not possible to distinguish exactly between the kinetics of physical and chemical interactions, but usually it is possible to single out the preferred mechanism determining the efficiency of the selected type of plasma treatment. The efficiency of the processes of physical sputtering and chemical interaction does not depend much on the charge of a particle, while energy (kinetic or potential) of the particle plays the definitive role. At a distance of a few tenths of a nanometer near the surface being treated, ions are neutralized by electrons, which are torn from the material by the electric field of the ions [19]. Fig. 3.6 shows the probable interactions between the surface and a particle, depending on the energy of the particle. The energies of around 1 eV allow to start the processes of chemical activation of the surface, which are often the preferred processes. The energies of ca. 10 eV are best to deposit a coating on the surface. Higher energies are responsible for sputtering and etching and also for ion implantation.

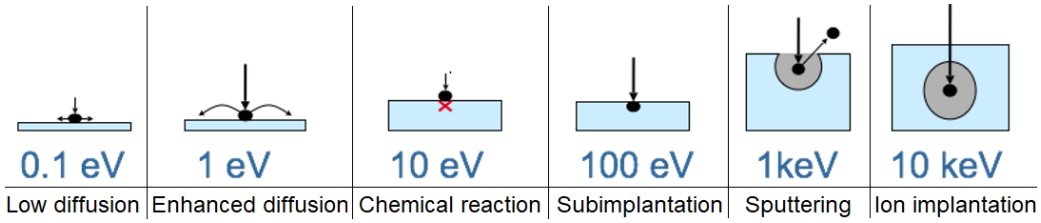

Figure 3.6: Different energies of electrons and ions result into different kinds of interaction with the surface: low diffusion, enhanced diffusion, chemical reaction, implantation, sputtering, ion implantation.

In the present work remote plasma treatment was used, so that the samples were not in contact with the plasma. Plasma was the source of chemically active particles. Therefore, energies higher than 10 keV (and therefore deep implantation) are not expected. In this particular case, when remote plasma interacts with PP on the surface of BPP, it can be supposed that the following processes may take place on the surface:

- diffuse surface activation;
- cross-linking (structuring) of the polymer;
- adsorption;

- introduction of the particles formed in plasma into the surface layer;
- remote plasma etching by atoms, radicals and ions results into destruction of macromolecules: breaking the macromolecule, forming volatile products and fragments with new bonds, what leads to removal of PP from the surface.

As it was mentioned above, these processes depend on the energies of the particles, which, in turn, depend on the experimental parameters, such as gases used (plasma chemistry), pressure, gas flow, power, distance between the sample and the plasma and, of course, treatment duration.

3.3.1 Plasma Diagnostics by Optical Emission Spectroscopy (OES)

To create and use plasma, it is necessary to understand the properties of the plasma and the processes that take place within the plasma. One of the most important and easy applicable methods to investigate plasma is optical emission spectroscopy (OES). This method does not interfere with the plasma itself and does not influence the plasma processes [20].

Optical emission spectra depend on plasma chemistry and plasma temperature. The intensity of the spectrum of radiation emitted by the plasma is measured as function of the wavelength in OES.

OES method is based on the ability of atoms and molecules in excited state to emit a photon of a specific wavelength, as the electron returns back to a lower energy level from a higher one [21]. The energy of the emitted photon, and hence its wavelength, is determined by the difference between the energy levels. A certain element emits photons with certain frequency, in accordance with the formula:

$$E_{ph} = h\nu \tag{3.3}$$

where E_{ph} – is the energy of the photon; h – Planck constant and ν – frequency. The emission spectrum of an atom or a molecule consists of several emission

lines, which correspond each to a particular electron transition.

The advantages of OES method are that it is easy to apply, it does not influence the processes in plasma and it is not complicated to analyze the spectra. However, OES has some considerable disadvantages. For example, if plasma is not spatially uniform, for OES all the light, which is captured by the glass fiber, will be subjected to analysis and is therefore not suitable for an area specific analysis. The solution of this problem can be a specific configuration of two lenses, offered in [22]. Another disadvantage of OES is related to the fact that the intensity of emission in OES depends on excitation and nonradiative deexcitation rates as well as radiative decay rates, therefore the emission intensities usually can only provide a limited insight into the plasma parameters [21]. It means that OES method usually does not allow to analyze the plasma quantitatively. But in some cases it is possible, like it is shown in [23], where the authors found a linear correlation between the optical emission intensity of the $d3\Pi \rightarrow a3\Pi$ (0,0) vibrational band of the C_2 Swan system with the absolute C_2 concentration in $Ar/H_2/CH_4$ plasma [21]. Other possibilities of quantitative analysis by OES are derivation of the electron temperature for equilibrium plasmas [24, 25] and derivation of excitation temperature for non-equilibrium plasmas [20, 26, 27]. Optical emission spectra were used to measure the plasma temperature in [21]. Since the composition of emission spectra gives an insight into the ongoing plasma chemistry [27], OES method is always applicable to implement for process control.

4 Sample Analysis Techniques

4.1 Spectroscopic Measurements

4.1.1 Fourier Transform Infrared Spectroscopy (FTIR)

In IR spectra strong absorption bands come from heteropolar bonds [28], therefore it is a good method to investigate the changes in CH_x bonds in BPP. (Whereas Raman spectroscopy is especially suitable to investigate homopolar bonds).

FTIR method is used in this work to study the changes occurring in the surface layer of the polymer under the influence of plasma. The method of FTIR spectroscopy allows establishing the formation of functional groups of different chemical nature or the changes in their amounts, fixing the release of hydrogen atoms and crosslinking in the surface layer, and also formation of a thin layer on the surface.

The data obtained by FTIR spectroscopy require the mathematical process of Fourier transform [29, 30] to be converted into the actual spectrum. This is where the term of Fourier-transform infrared spectroscopy originates from. A significant advantage of an FTIR spectrometer over a dispersive spectrometer is the ability to collect the data of high spectral resolution in a wide spectral range simultaneously [31].

The most interesting characteristics of the spectrum for the analysis are the following: the amount of the absorption bands (the amount of maximums), their position on the wavenumber scale (i.e. the wavenumber in nm for the maximum of absorption), the height of the peak (the value of the molar ratio of the

maximum of absorption ε_{max}), the intensity of the absorption band (absorption integral), the width and the shape of the band. These characteristics should be compared in the analysis of the spectra of the samples before and after plasma treatment. It allows to draw conclusions about the changes, which take place under the influence of the active plasma particles on PP on the surface of the samples.

The absorption of radiation in the infrared region of the spectrum is related to the vibrations of the molecule and its fragments. The interactions between the separate groups (parts) of the molecule affects the vibrational frequencies.

In compounds with low molecular weight there is a direct link between the vibrational spectrum of the compound, its structure and the forces of intermolecular interaction. In polymeric compounds the influence of the structure of macromolecules and their interactions are less pronounced. For polymers the influence of the physical factors, which alter the conformation of macromolecules and supramolecular structure of the polymer is typical.

The purpose of the analysis of bipolar plates for fuel cells by FTIR spectroscopy method is to find out how does the plasma treatment of the samples change the molecular structure of the surface. In the present case FTIR is a good technique to investigate first of all the influence of plasma treatment on PP on the surface of the samples.

Orbital Hybridization

In carbon-containing materials the atoms of carbon can be found in different hybridized states. This determines the wide range of properties of these materials. sp^3 hybridization corresponds to diamond (3D structure), sp^2 hybridization corresponds to layered graphite (2D structure) and sp hybridization corresponds to linear acetylenic carbon – carbyne (1D structure).

The axes of sp^3 hybrid orbitals are directed to the vertices of a regular tetrahe-

dron. The tetrahedral angle between the axes is 109°28′. These orbitals form four bonds with other atoms or they are filled with unshared electron pairs. There are other forms of elemental carbon, which are considered as transitional and, which, in turn, are divided into mixed and intermediate forms. This means that plasma treatment can lead to the formation of a complex layer with the participation of carbon atoms in different states on the surface of the BPP.

Carbonization

Carbonization is another process, which may take place on the surface of BPP during the plasma treatment. This possibility is endorsed by the increase of electrical conductivity of the samples after plasma treatment. F. I. Grigorjev in his book „Ion-plasma treatment of polymeric materials in microelectronics technology“ [32] writes:

> „One of the most important consequences of ion implantation is the appearance of electrically conductive properties in initially dielectric polymers. The electrical conductivity of polymers irradiated with ions appears due to the formation of carbon-containing structures in the ion-implanted layer. As the dose of ion irradiation accumulates in the implanted layer a system of conducting islands separated by potential barriers appears. Since the conducting phase in the ion-implanted layer is formed by discrete carbon clusters and their associates, the appearance of the electrically conductive properties in the irradiated polymer with the accumulation of the implantation dose has a threshold nature. The conductivity of the ion-implanted layer strongly depends on the details of the structure of the carbonized phase (the size of the carbon clusters, the nature of their binding to aggregates, the presence of heteroatoms). Therefore, the electrical resistance of various polymers, subjected to ion implantation under identical conditions, can differ by several orders of magnitude.“

Absorption of Polymer Structures

The PP molecule $[-CH_2 - CH(CH_3)-]_n$ has $C - H$ bonds of methyl group CH_3, methylene group CH_2 and methine group CH (Fig. 4.1 [33]). All of these groups are connected by $C - C$ bonds. There are the peaks of $C - H$ bonds in the FTIR spectra of PP, although the peaks of these bonds may also appear in a hydrogenated carbon layer. But taking into account the treatment conditions, it is unlikely that the formation of such a layer could take place for the considered samples.

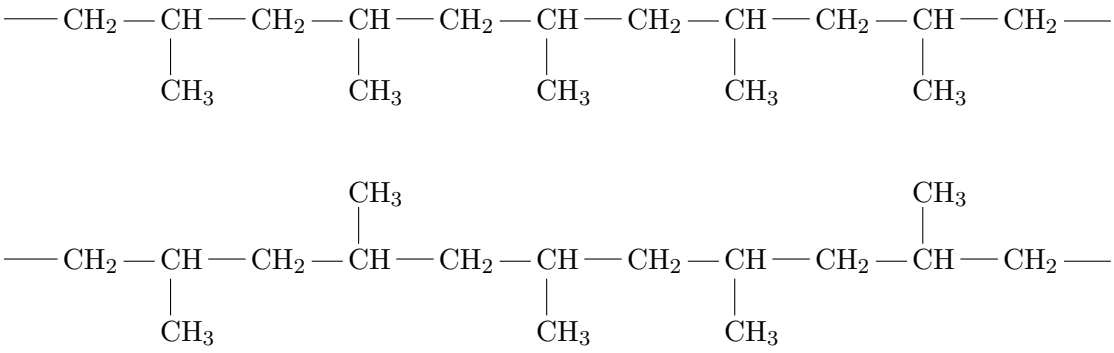

Figure 4.1: Isotactic (top) and atactic (bottom) PP [33].

In Fig. 4.2 the FTIR spectrum of a PP film is presented [34].

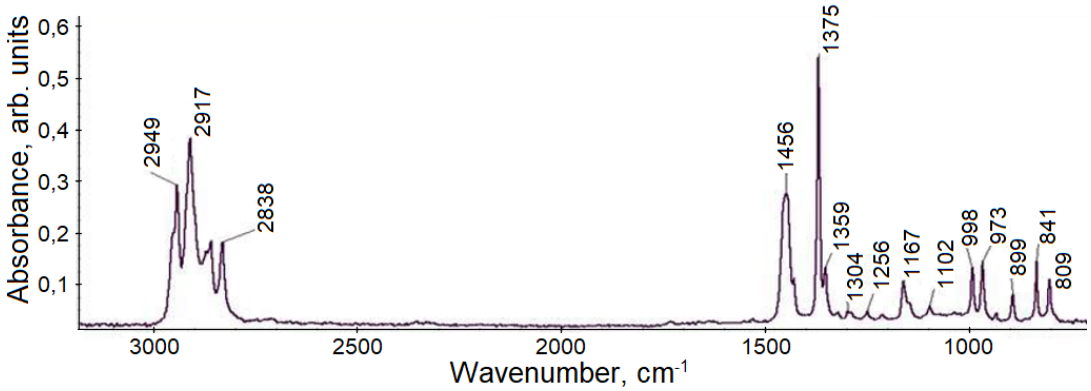

Figure 4.2: FTIR spectrum of a PP film [34].

Spectra of PP have been studied in a number of works, an interpretation of the absorption bands is given below:

1. **D. V. Kuznetsov et al.** Investigation of the stability of polymer composites based on polypropylene after UV radiation, Modern Problems of Science and Education 6 (2012) (in Russian) [35].
   Equipment used: Spectrometer Thermo Nicolet 380, Smart ITR with diamond crystal for FTIR; Resolution: 4 cm^{-1}, measured 32 times.
   Subject: PP with nanotubes in it (the thickness – not more than 30 nm, the length – not more than 5 mm) was studied.
   Peaks: PP after the UV radiation has the peaks, typical for PP:
   3310 – hydroxyl groups;
   2498 and **2866** – (sym and asy stretching vibrations of CH_3-groups);
   1450 and **1375** – bending vibrations of CH_3-groups;
   2916 and **2837** – stretching vibrations of methylene groups CH_2;
   1116, 998, 974, 900, 841, 809 – bands of regularity or crystallinity of PP;
   1735 – $C = O$ due to a slight oxidation of PP;
   1650-1600 – $C = C$ (appeared after UV treatment of PP).
   After the modification by boron nitride and UV irradiation:
   2498 and **2866** – no changes;
   1450 and **1375** – merge with the bands in 1600-900;
   2916 and **2837** – no changes;
   1710 – $C = O$ appears.

2. **Yu. Gorokhovatskii et al.**, Experimental Physics, IR-spectroscopy of electrets on the basis of polythene and polypropylene (2004) 69-75 (in Russian) [36].
   Equipment: Spectrophotemeter IKS-29 (4000-400 cm^{-1}), two beam scheme.
   Subject: PP films with the thickness of 15 μm.
   Peaks: **1300, 1255, 1160, 998, 976, 835-840**;
   Some peaks present in the areas of **700-800** and **600-500**;
   968 – a flat zigzag in a crystal with orthorhombic or triclinic symmetry or in an amorphous phase.

3. **B. Wunderlich**, The ATHAS database on heat capacities of polymers, Pure & Appl. Chem. 67(6) (1945) 1019-1026 [37].

Absorption bands of isotactic crystalline PP:
2950 – CH_3 stretching, asy;
2921 – CH_3 stretching, sym;
2922 – CH stretching;
2879 – CH_2 stretching, asy;
2868 – CH_2 stretching, sym;
2838 – CH_2 stretching, sym;
1435 – CH_2 scissoring;
1460 – CH_3 bending, asy;
1454 – CH_3 bending, asy;
1378 – CH_3 – bending, sym;
1340-1270 – CH bending.
The main bands of PP, which do not depend on its structure, i.e. they can be observed in crystalline and amorphous forms of PP: **1460** and **973**.
The intensity of the bands **1168, 995** and **842** depends on the structure of PP.
Isotactic PP: intensive bands at ≈ **1380** with a shoulder at **1360** and at **1460, 1153, 974** with a shoulder at **995**.
Atactic PP: intensive bands at ≈ **1380** with peaks at **1360** and at **1460**; many bands in the region of **800-1350** with intensive peaks at 1168 with a shoulder at **1153, 995, 974, 842**.

- The spectra of a PP sample with the thickness of 200 μm have two bands of low-intensity in the area of **1700-1600**; two intensive bands at ≈ **1455** and ≈ **1380**; four less intensive bands at **1320-1220**; an intensive band at ≈ **1170**; a doublet at **980-100**; bands at **895, 840, 810**.
- The spectra of a PP sample with the thickness of 300 μm after the irradiation by fast electrons (500 Mrad) have a new band, which appeared at **1645**; the same bands at **1500-1000**, but just the higher-frequency part in the doublet is decreased; bands at **910, 890, 855 and 816**.
- When the sample was irradiated by a dose of 4000 Mrad, except band

at **1645**, another weaker band has appeared at **1665**, which probably relates to the internal double bonds:

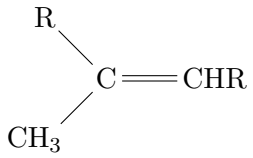

This is consistent with the bands in the region of **815-855**, which relate to the vibrations of $C - H$ with a double bond.

4. **V. L. Karpov**, Radiation chemistry of polymers, Nauka, Moscow (1966) (in Russian) [38].
   Subject: IR spectra of unirradiated and irradiated PP films.
   After UV irradiation of PP the following bands appear in the IR spectra: **965** – double bonds of trans-vinylene type ($R_1HC = CHR_2$); **850** – double bonds such as $R_qR_2C = CHR_3$; **1650** – vinylidene groups $RR_1C = CH_2$.

5. **A. N. Elliot**, Infrared spectra and structure of organic long chain polymers, Acta Cryst. B26 (1970) 1387 [39].
   Subject: H- and D forms of isotactic (crystalline) PP:

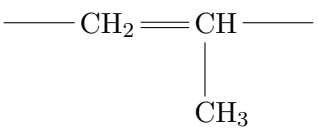

   Peaks: At $\approx$ **2900** – fragment; two intense bands at around **1400** and a number of bands in the low frequency region of the spectrum.
   The dependence of the intensity of a number of bands on the polarization of the incident radiation is found.

6. **L. I. Kravets et al.**, Research of the surface and electrochemical properties of polypropylene track membrane modified by non-polymerizing gas plasma, Electrochemistry, Dubna (2012) (in Russian) [40].
   Equipment: FTIR Spectrophotometer "Bruker Equinox 50S" with MIRacleTM with ZeSe crystal, 100-fold accumulation; increment 2 cm^{-1}.

Peaks of PP track membrane before plasma treatment:
Four bands in the region of **3000-2800**: **2950, 2919, 2868, 2839**;
Two intensive bands at **1456** and **1375**;
Weak bands at **1200-750**.
The spectrum of the membrane after nitrogen plasma treatment had the same absorption bands as before plasma treatment, i.e. the plasma treatment did not cause any changes in the spectrum.
The spectrum of the membrane after oxygen and air plasma treatment had the bands, caused by the vibrations of oxygen-containing groups.

4.1.2 Raman Spectroscopy of Carbon and Carbon-Containing Materials

Raman spectroscopy is used in this work especially due to the characteristic frequencies produced by the stretching modes of homopolar covalent bonds $C-C$ [28]. For this reason, this method provides a possibility to watch the changes of carbon structure due to the plasma impact.

Raman spectroscopy is a good non-destructive technique for analyzing different carbon and carbon-containing materials. It can provide important information about the crystallinity, defects, presence of sp^2 and sp^3 hybridization, bonding structure, chemical impurities of the surface and so on. This method is also sensitive to the possible restructuring in sp^2 clusters of carbon [41]. The comparison of Raman spectra of different carbon materials is shown in Fig. 4.3 [42–44].

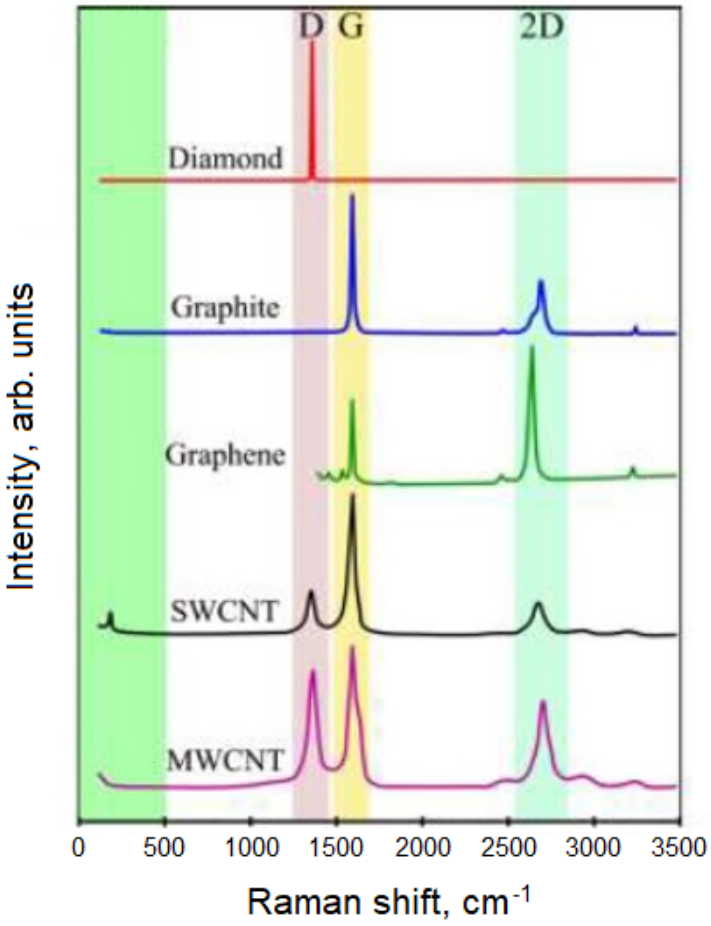

Figure 4.3: Raman spectra of carbon materials [42], where SWCNT is single-walled carbon nanotubes; MWCNT is multi-walled carbon nanotubes.

Diamond has the only one mode at 1332 cm^{-1} [Fig. 4.3]. Unlike single crystal graphite, which has a single Raman active mode at ∼1580 cm^{-1}, "G" mode for "graphite", disordered graphite has another mode at ∼1350 cm^{-1}, labelled "D" mode for "disorder" [43] for visible excitation. The higher the D peak, the more defects are present in the sample, i.e. the smaller the crystals are. This peak can also indicate the presence of graphite nanoclusters in carbon structure [41]. Fig. 4.4 [45–47] shows the Raman spectra of (A) diamond, (B) single crystal graphite and (C) microcrystalline graphite. Besides, J. Robertson in [43] reports:

„An unusual and significant fact is that the Raman spectra of most

disordered carbons remain dominated by these two G and D modes of graphite, even when the carbons do not have particular graphitic ordering."

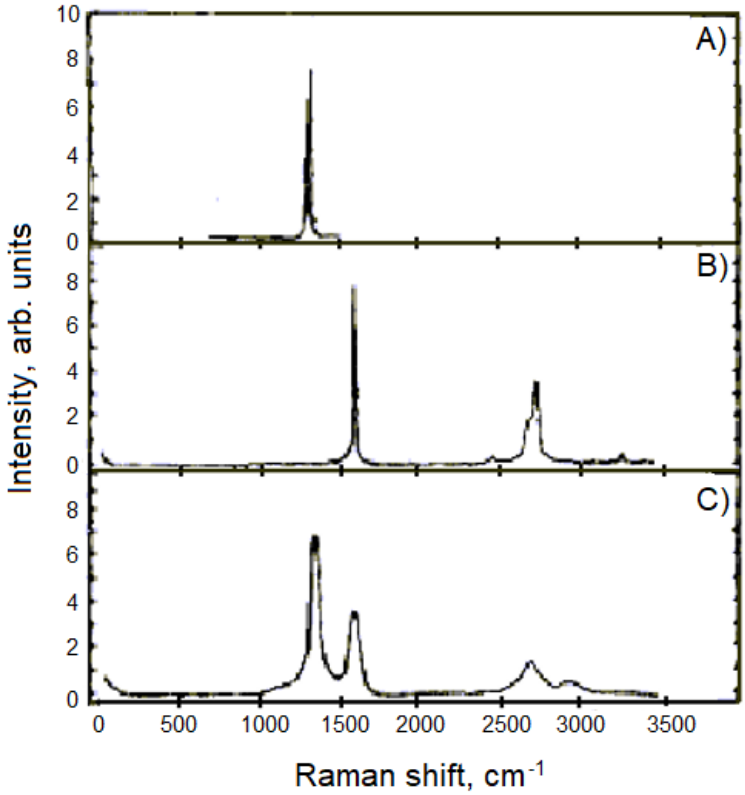

Figure 4.4: Raman spectra of: (A) single crystal diamond (B) graphite and (C) microcrystalline graphite [45] (adapted from Reference [46]).

The G mode is related to in-plane vibrations of sp^2 hybridized atoms of carbon [42]. The G band is present in Raman spectra of the samples with any organization of sp^2 bonds of carbon. And the shorter the chain, or the smaller the ring cluster, the stronger are the carbon bonds and, consequently, higher the frequency $\Delta\omega^G_{max}$ (the maximum of G) [41]. The authors in [41] report that any disorder in ring structures leads to the decrease of $\Delta\omega^G_{max}$ concerning the G band in graphite and also to a significant increase of the width of both G and D bands. A. Ferrari and J. Robertson in their work [48] have reported:

> „The G and D peaks are due to sp^2 sites. The G peaks is due to the bond stretching of all pairs of sp^2 atoms in both rings and chains. The D peak is thus due to the breathing modes of sp^2 atoms in rings.“

It is important to notice, that the effect of sp^2 sites dominates in all Raman spectra, excited by visible photons, because of much greater cross-section of sp^2 sites than sp^3 sites. It is so because the higher lying σ states ($C-C$ bonds) are not excited by visible light, they need higher energies [43, 49]. The information about the sp^3 sites content can be received from the position of “T“ peak, found at $\sim$1060 cm^{-1} in UV Raman spectra, and from the I(T)/I(G) intensity ratio [21, 48].

Another prominent band of graphite samples at $\sim$2700 cm^{-1} is visible in Fig. 4.3 and Fig. 4.4 (B) and (C), historically named G'. This band refers to the second order of the D peak, therefore it is now commonly called 2D [49]. This band is well observable for defect-free sp^2 carbons [42]. Graphene and bulk graphite have different shapes of the 2D peak [49], this can also be noticed in Fig. 4.3. In bulk graphite this peak consists of two components, approximately 1/4 and 1/2 the height of the G peak: $2D_1$ and $2D_2$ (Fig. 4.5). The Raman spectrum of graphene has a sharp and single 2D peak, approximately four times more intense than the G peak. Thus Raman spectroscopy allows to distinguish between graphene and graphite and to identify a single layer of graphene, bi-layer and so on up to 5 layers of graphene [49, 50].

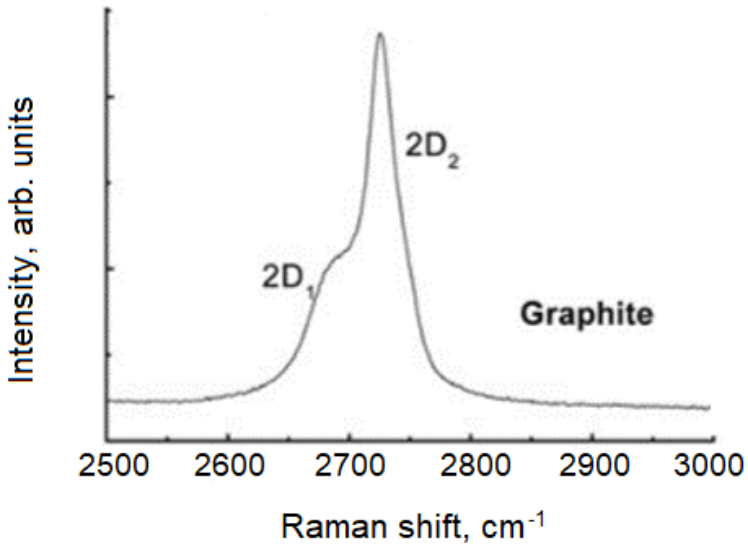

Figure 4.5: 2D peak in graphite (adapted from Reference [49]).

As an example, the small sharp peak at $\sim$3250 cm^{-1}, well definable in the Raman spectra of graphite and graphene (Fig. 4.3), is the second order of D' peak, i.e. 2D' peak [49]. The consideration of Raman spectra of BPP, regarding the most important peaks for characterization of graphite-containing materials like BPP, namely G and D peaks, is complicated by the factors, illustrated in Fig. 4.6, which can alter the relative intensity of these peaks and shift them to both directions. However, Raman for visible photons does not see the $C-H$ bonds significantly [43].

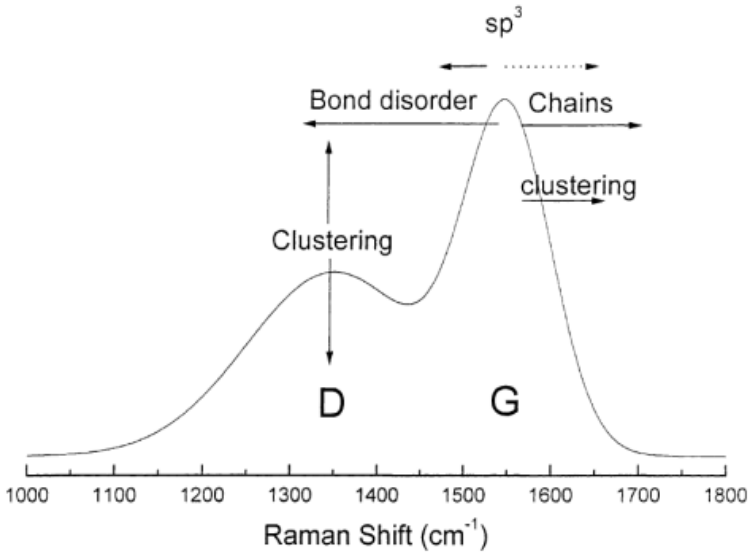

Figure 4.6: Schematic view of the factors affecting the Raman G and D peaks [43]).

In addition to that, for amorphous carbon such parameters as the full width of half maximum of the G peak and the shift of the G peak to the higher wavenumbers with the decrease of the excitation wavenumber from IR to UV region (dispersion of G peak) correlate with the disorder [21].

Visual examining of vibrational spectra can often provide an important information about the structure of the molecules. Due to Raman and IR spectroscopy data it is possible to identify the form of some molecules [51]. Some functional groups of organic compounds and the corresponding frequency regions are listed in Table 4.1 [52].

Table 4.1: Frequency regions with associated functional groups of organic compounds.

Frequency $[cm^{-1}]$	**Functional groups**
3700 - 3100	OH, NH and $\equiv CH$
3180 - 2980	aryl, olefinic, and three-membered ring CH
3000 - 2700	aliphatic CH
2300 - 1900	$C \equiv C$ and $C \equiv C \equiv C$
2000 - 1700	aryl and olefinic overtones
1900 - 1550	$C = O$
1700 - 1550	$C = C$ and $C = N$
1660 - 1500	NH_2, CNH
1620 - 1420	aromatic and heteroaromatic rings
1500 - 1250	CH_3 and CH_2
1350 - 1150	CH_2 and CH wag
1300 - 1000	$C - O$
1000 - 600	olefinic and acetylenic wag
900 - 700	aromatic wag

4.1.3 Auger Electron Spectroscopy (AES)

The fundamental principles of AES and XPS techniques are similar [53–55]. Both techniques can damage a sensitive surface: AES by an electron beam and XPS by X-rays. The interpretation of XPS spectra is easier, XPS does not require conductive substrates, unlike AES, but the main advantage of AES is a better spatial resolution. Also for some elements AES can be more sensitive to chemical state than XPS. Both, AES and XPS techniques provide information about the near-surface layers of nanoscale, unlike EDX, which allows to investigate the surface in micron range of the depth.

Underlying the Auger electron spectroscopy (AES) is the Auger effect. A primary electron beam strikes an electron of a surface atom out of its atomic shell, so that a core hole is created. The state of the atom becomes unstable and in a fairly short time the vacancy is filled by an electron from a higher energy level. The released energy is transferred to another electron from the same shell without radiation. The kinetic energy of this electron only depends on the energy

difference between the atomic shells and is independent of the primary energy of the electron beam. This electron is released from the atom. Such electron is called Auger electron. Thus, an electron beam is used to excite the electronic subsystem and Auger electrons are released from the atom [56–60]. Auger electrons have a kinetic energy which is element-specific and thus the spectroscopic examination of the emitted electrons allows to draw a conclusion on the chemical composition of the surface [61–63].

Auger electron emission process involves three electrons, therefore the elements, which have less than three electrons in atom, namely H and He, cannot be detected by AES. In this research mainly carbon and oxygen are of interest, thus only KLL transactions are regarded. The principle of AES is also well described in [64]:

> „. . . a KLL transition involves initial ionization of the K shell and relaxation of an electron from the L shell into the K vacancy. Energy released in this process is transferred to another L electron, which is consequently ejected from the specimen with characteristic energy and can be identified as an Auger electron.“

For quantitative analysis of the surface it is important to determine the depth of the electron yield: the distance that electrons of a certain energy can pass without loss of energy. Usually, the energies of the emitted Auger electrons are in the range of 20 up to 2000 eV. These values are comparable with the binding energies of electrons in atoms. Only those electrons that are excited along the surface at a distance less than the mean free path can exit the solid without losses and contribute to the corresponding Auger peak. The electrons, which yield from deeper layers of the surface experience inelastic collisions and lose energy moving from the ionization point to the outer surface, they leave the solid with less energy and contribute to the background or the “tail“of the signal, which can shift up to several hundred eV down from the main peak. Thus, the depth of the analyzed surface layer in the electron Auger spectroscopy method is determined by the average depth of the electron yield with a certain energy. Here the depth of electron yield is considered as a synonym for the mean free

path, which depends on the electron energy and has a roundish minimum located between 50 and 100 eV, as shown in Fig. 4.7 The graphs of the dependence of the mean free path on electron energy are called universal curves. The mean free path is to some degree insensitive to the substance in which the electrons move (usually it has values about 0.2 – 5 nm). Therefore, the AES method has high surface sensitivity [65–68].

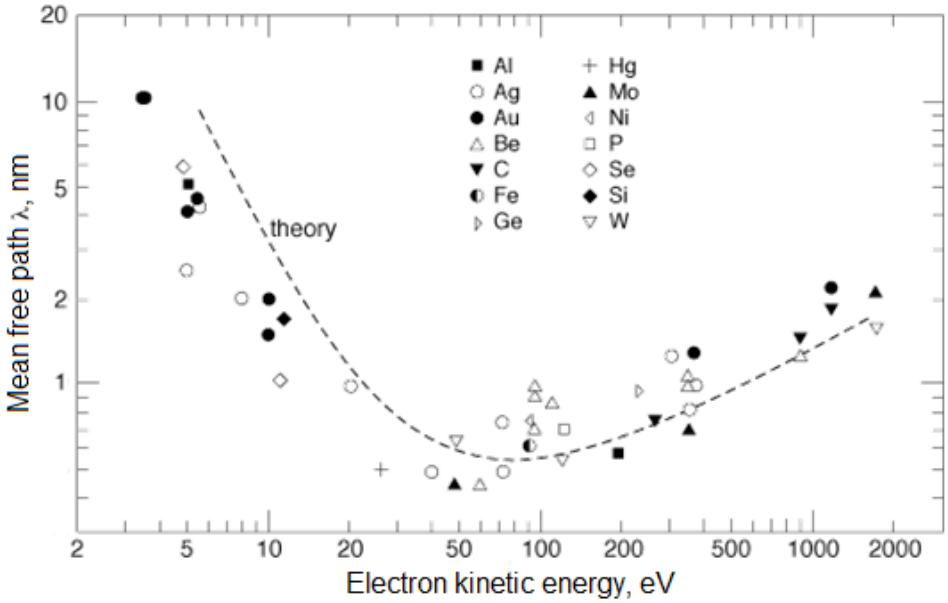

Figure 4.7: A universal curve of the inelastic mean free path of the electrons in solid (adapted from [68]).

AES is being traditionally carried out under ultra-high vacuum (UHV) environment (10^{-7} – 10^{-12} mbar) [69].

Auger electrons can be defined by small peaks (number of Auger electrons) on the energy distribution curve on a strong background of secondary electrons. The selection of the Auger electrons spectrum against this background is a difficult experimental problem. The method, in which Auger electrons, excited by an electron beam, are used to identify the components on a surface, was proposed by J. J. Lander in 1953 [70], but the extensive use of Auger spectroscopy for chemical analysis began after 1968, when L. A. Harris [71] proposed to take

the derivative of the energy distribution curve to suppress the background of secondary and inelastically scattered Auger electrons [72]. Nowadays the differential form of the spectrum is commonly used for Auger spectra.

AES can be used for some experimental investigations of PP and other polymers [73]. For instance, such as polymer-radiation interactions, the Auger spectrum of PP is of interest [74].

4.1.4 X-Ray Photoelectron Spectroscopy (XPS)

Among all the surface chemistry analytical techniques XPS, as a method for quantitative elemental analysis of surfaces, is one of the most widely used [75–77]. But its ability to detect and quantify some functional groups is limited [78, 79]. As it is reported in [78],

> „in several cases, relative chemical shifts of different groups are below the energy resolution attainable, even by the new generation XP spectrometers, due to the existence of significant intrinsic peak widths [80]. Therefore, the data has only limited value for the determination of the concentration of a particular functional group. ... Carbon atoms can be distinguished according to the number of bonds to neighboring oxygen atoms. ... However, the differentiation of hydroxyl groups from ethers, peroxides and epoxides due to their C1s binding energies is not possible [81]...“

Even though XPS method does not require conductive substrates, in terms of count rate and resolution, the best performance of an XPS spectrometer is generally obtained with conducting samples. For conductors charging problems are absent and good energy resolution can be obtained [82].

The XPS technique is based on the phenomenon of external photoelectric effect. To obtain the XPS spectra the investigated surface is irradiated by X-rays and simultaneously the kinetic energy of electrons, which escape from the surface, is measured. The process of interaction between radiation and a sample atom can

be treated as "collision" of a photon with an electron in the atom with subsequent energy transfer to the electron [51]. Since radiation with a known wavelength is used to excite the photoemission, the binding energy of the emitted electrons can be found from the equation:

$$E_B = h\nu - E_{Kin}, \tag{4.1}$$

where E_B is the binding energy of the electron; E_{Kin} is the kinetic energy of the emitted electron and is the energy of the used X-ray photons [83–86].

X-ray photon does not have a charge but, as an electromagnetic wave, it consists of oscillating electric and magnetic fields, which interact with the charge of the orbital electrons, but this interaction is not so strong as the interaction of the orbital electrons with a particle having a fixed charge. Therefore, X-rays penetrate matter more easily than electrons. Electron scattering is useful only for studying the surface layers of materials [30].

The C1s peak, which appears in XPS spectra of PP, consists of two components at the values of binding energy of 285.16 eV and 285.00 eV [82]. C1s spectra for polymers tend to have symmetric peak components. Extended delocalised electrons can result in satellite structure, which can be found several eV to higher binding energy of the main peak. Binding energies of common chemical states in polymers are presented in Table 4.2 [87]. The energies of XPS are comparable

Table 4.2: Binding energies of common chemical states [87].

Chemical state	**Binding energy C1s** $[eV]$
$C-C$	284.8
$C-O$	≈286
$C=O$	≈289

with AES, because in both methods the primary beam excites the electrons at the depth of 0.5 – 5 nm, therefore both methods are surface-sensitive.

4.1.5 Energy-dispersive X-Ray Spectroscopy (EDX)

EDX of SEM technique allows to investigate the surface depth of several μm, unlike AES and XPS, which give information only in nano-range. This method allows to find out whether plasma treatment of the surface can also influence on deeper levels than several atomic layers of the surface. Therefore, the results of AES, XPS and EDX investigations are expected to differ.

The EDX spectroscopy method allows to study the spectrum of X-ray radiation, which arises when the sample is irradiated by accelerated electrons. The X-ray spectrometer is usually combined with a scanning electron microscope (SEM), which allows to conduct a local elemental analysis of the sample surface [88, 89]. The method of X-ray spectral analysis, based on Moseley's empirical law (the square root of the frequency of the X-ray, emitted from an atom of a chemical element, is proportional to the atomic number), allows to detect the presence of a defined chemical element (except H and He) on the sample surface. X-ray spectroscopy is widely used and often described in research literature, for example in [90–96].

Vacuum in SEM systems is needed to allow the electrons to travel within the instrument unimpeded. Poor vacuum levels shorten the life of the electron emission source due to the electrical discharges in the gun assembly of the SEM [97].

Practically for conventional imaging in the SEM, at least the surface of the specimens must be electrically conductive. When the primary electron beam interacts with the sample, the electrons lose energy by repeated random scattering and absorption within the interaction volume – a teardrop-shaped volume of the sample (see Fig. 4.8) [98], which extends up to approximately 3 μm into the surface, as shown in Fig. 4.8. The excitation volume is defined by the primary beam energy and is larger than the primary electron beam spot on the sample [69]. The size of the interaction volume depends on the atomic number of the sample, the sample's density and, as mentioned above, on the electron's landing energy. The interaction between the incoming primary electrons and the surface

or near-surface of the material at different levels of penetration results in the reflection of electrons with different energies and electromagnetic radiation, mainly X-rays [99].

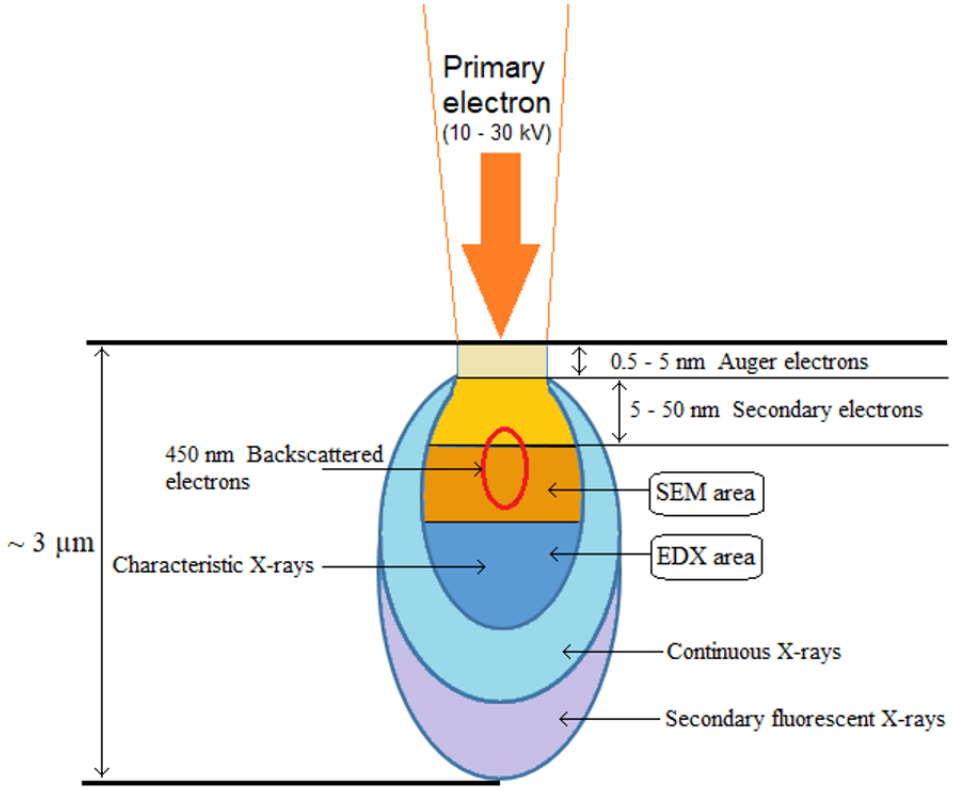

Figure 4.8: Cross section of the interaction volume (adapted from [100]).

For the reason of several μm penetration of the primary electron beam into the surface, EDX of SEM is a good technique to analyze materials at the micron scale of depth. Nanoscale characterization using EDX would require a reduction of the primary electron energy, what would mean that the K shells of many elements could no longer be excited and the analysis would rely on L and M shell excitations. The peaks of these levels are often close together, so the quantification is difficult [69].

The phenomenon of the X-rays emission is caused by the excitation of the inner shells of an atom by incident electrons. Under the influence of high-energy

electrons, an electron from the core-shell is excited to a higher energy level, the vacancy in the core-shell is filled with an electron from the higher energy level, which leads to the emission of the characteristic X-ray radiation with the energy equal to the energy difference between these two energy levels [101–103].

In quantum mechanics it is proved that the probability of the interaction between the exciting electron and the internal electron of the atom increases with the density of the spatial distribution of the electron density: with the square of the modulus of the wave function of one-electron state $|\Psi|^2$. Consequently, most likely is the interaction of the exciting electron with the electrons from 1s shell, with the principal quantum number n = 1. If the kinetic energy of the exciting electron exceeds the binding energy of the inner electron, the inner electron can break away from the atom. There is ionization of the atom in K layer and a vacancy is formed in the electron shell 1s. Due to the ionization, the atom is in an excited state. The excitation of the atom can be removed by filling the vacancy by an electron from another shell, which has a higher energy, and the energy difference can be carried away from the atom by a photon. The energy ε of such a photon can be defined by the equation:

$$\varepsilon = En_2 - En_1, \tag{4.2}$$

where En_2 and En_1 are the energies of the stationary states, where the electron transition occurred. In this case the energy of the atom decreases by the energy difference between the upper and lower stationary states. Since each atom has a certain discrete set of one-electron stationary states, the spectrum of the emitted photons is a line spectrum. Thus, the characteristic X-ray radiation is formed by radiative transitions of electrons, which fill the vacancies in inner electron shells. Since a specific energy corresponds to each element, the elements of the investigated sample can be identified. Measuring the integrated intensity of the peak it is possible to determine the quantitative content of the elements in the substance [101].

4.2 Characterization of Surface Morphology and Topography

The contact between BPP in a fuel cell occurs only at the irregularities of the rough surface. Since atmospheric air is insulating, the contact resistance is defined by the electron flow through these contact areas [104–106]. Therefore, surface roughness should be investigated due to its impact on electrical properties of the surface [107–109].

4.2.1 Roughness and Roughness Parameters

Roughness determines operational properties and characteristics of a solid. It is defined by the presence of micro- and nano-irregularities on the surface. Mechanical friction and wear and plasma treatment may change the roughness.

The change in surface roughness can lead to the change of the surface wettability, because it affects the contact angle due to the increased area of solid–liquid interface and due to the effect of sharp edges of rough surfaces [110, 111].

Surface roughness measurement methods include linear roughness measurement and areal roughness measurement. There are contact (stylus directly touches the surface of the sample) and non-contact (light emitted from the instrument is reflected and read, to measure without touching the sample) types of roughness measurement devices [112].

A detailed overview of the roughness parameters is presented in Appendix A [113–120].

4.2.2 Stylus Profilometry

A profile of the surface in order to quantify the roughness can be measured by a profilometer. Stylus profilometry is a contact method, therefore can be destructive for some surfaces. It is very sensitive and provides high Z resolution,

but slower than non-contact techniques. The stylus moves along the examined surface and oscillates when the surface is uneven. The oscillations are transmitted to the sensor where they are converted into small electric currents, which, in turn, are amplified and recorded. These records are displayed and give an idea of the studied surface profile [121, 122].

4.2.3 Scanning Electron Microscopy (SEM)

The technique of SEM is used in this work for completeness of the investigation with a view to get a visual idea about the changes on the surface after the plasma treatment. Using SEM with different magnifications gives qualitative information about the surface and can be useful as primary investigation to see whether plasma treatment at the specific conditions leads to any visual changes on the surface.

SEM method is based on the principle of interaction of the electron beam with the surface studied. This method allows to characterize the surface in the nano-range, it is non-destructive and does not need any special sample preparation, therefore SEM is regarded as good and high-performance morphology imaging technique. However, despite the fact that the diameter of the electron beam of the SEM can reach nanometers, the size of the collection area of secondary electrons can reach several tens of nanometers due to scattering processes. This leads to a discrepancy between the size of the particle, determined by the SEM video signal profile, and its real size [123]. The problem of determining the error and uncertainty of the results of measurements of linear dimensions using the SEM method does not have a generally accepted solution and is often ignored by the manufacturers of the measuring equipment. So, SEM images only map the intensity of scattered electrons, while the real surface may differ from the SEM image. Scatter-measuring instruments are not directly comparable to profile-measuring instruments [124].

4.2.4 Atomic Force Microscopy (AFM)

Atomic Force Microscopy (AFM) is a suitable technique to obtain a real 3D image of the surface. Nowadays, atomic force microscopes (AFM) are commonly used for investigating the surface topography and nanoscale surface properties [124–133]. AFM is a type of Scanning Probe Microscopy (SPM) [134], it has a resolution on the order of fractions of a nanometer, allows to estimate the exact nano-roughness, to obtain 3D images of the surface and to measure the forces between the probe and the sample as a function of the distance between them.

The surface of a sample is scanned by the AFM cantilever with a sharp tip (the probe) that deflects interacting with the sample surface [135]. Typical force microscopes are equipped with a detector that measures the displacement of the cantilever and feedback electronics to maintain a constant imaging parameter such as force or tip-sample separation [128]. Surface scan is performed by means of a piezoelectric actuator, which is able to perform minimal displacements of the order of 0.1 nm with high precision up to displacements of the order of 100 μm [135]. The most versatile and simple to implement method of detection of cantilever deflections in AFM is optical lever deflection, described in [128] and [135].

The basic AFM operation modes are defined by the motion of the cantilever: the contact (static) mode, and two dynamic modes – tapping mode and non-contact mode [136]. Fig. 4.9 (adapted from [137]) A) shows an AFM cantilever in constant contact with the surface and the surface image obtained above, B) cantilever is in tapping mode and C) shows the failure of non-contact mode of operation when the water droplet is reported as part of the surface.

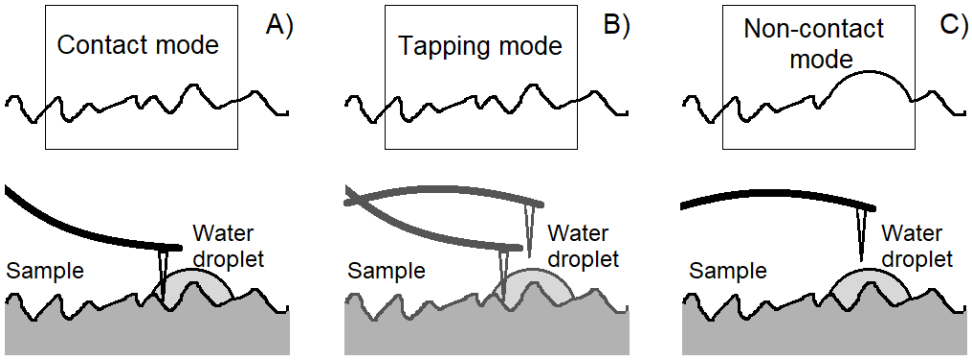

Figure 4.9: AFM scanning modes (adapted from [137]).

Fig. 4.10 shows the dependence of interatomic forces on the distance between the tip and sample [137, 138].

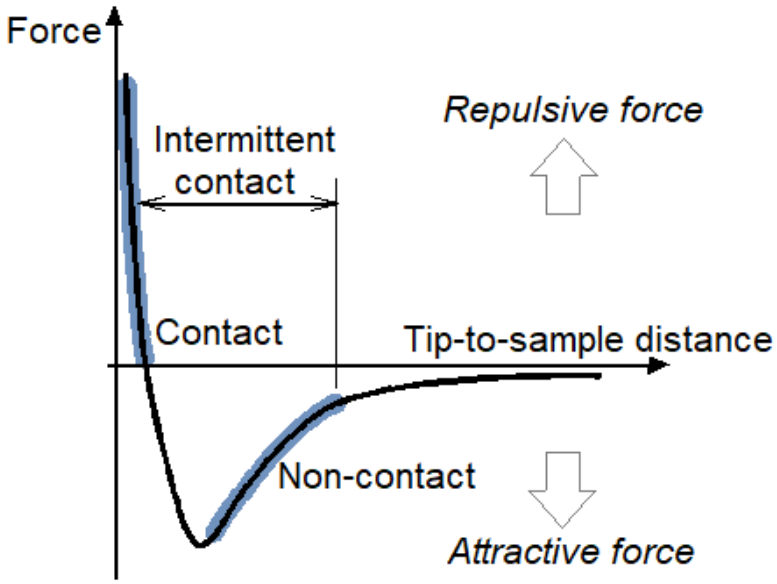

Figure 4.10: Tip-sample separation curve illustrating the main interaction during AFM scanning (adapted from [137, 138]).

The forces between the cantilever tip and the sample surface, which depend on the distance between them (i.e. the operation mode), are described in detail in [139].

4.2.5 Confocal Microscopy

Confocal microscopy is a form of optical sectioning microscopy [140] with a high contrast and spatial resolution, which can be reached by means of a spatial pinhole to block out-of-focus light in formation of the image [141]. Optical sectioning process – capturing images at different focal planes, allows to reconstruct the 3D structure.

Contrary to the SEM technique, confocal microscopy offers quantitative data in true three-dimensional coordinates. No previous sample preparation is required for measurements. Confocal microscopes operate without contact and do not cause the destruction or damage of the surface, therefore the hardness of the material to be examined is irrelevant [142].

In this work NanoFocus confocal microscope with μsurf sensor technology was used. The μsurf sensor technology is based on the Confocal-Multi-Pinhole technology of NanoFocus. It allows to acquire topography, roughness and layer thickness in the micro- and nanometer ranges within seconds. The NanoFocus confocal microscope consists of a light-emitting diode (LED) light source, a rotating multi-pinhole disc, an objective lens with a piezo drive and a CCD (charge-coupled device) camera. The LED source is focused through the multi-pinhole disc and the objective lens onto the sample surface. The light is reflected from the surface and reduced by the pinhole of the multi-pinhole disc to that part, which is in focus, and this falls on the CCD camera. In contrast to an image from a conventional optical microscope, which contains sharp and blurred details, in the confocal image the unfocused details are filtered out by the operation of the multi-pinhole-disc. Only the light from the focal plane reaches the CCD camera. Due to this, the confocal microscope is capable of high vertical resolution in the nanometer range. Capturing the images - horizontal slices through the topography of the sample, at different focal heights produces a stack of such images, achieved by the confocal microscope through precise vertical displacement of the objective lens by means of a piezo drive. Within a few seconds up to 400 confocal images can be captured, then the software reconstructs an exact 3D image of the

surface from the stack of confocal images [142].

In [143] the authors also compare different methods of roughness measuring, including confocal microscopy, and explain the possible reasons of different results obtained by different methods and also within the same method. An increase of working distance of a confocal microscope results into a decrease of the numerical aperture and leads to a decrease in lateral resolution and depth resolution. Even different magnifications may lead to the difference of roughness values due to the difference in optical resolution and in the size of the field of view. So, the comparison of the results obtained by different methods should be carried out taking into account the features and limitations of these methods. Therefore, none of the methods can be considered a reference one [143].

4.3 Electrical Resistance of BPP

4.3.1 Area Specific Resistance

Usually area-normalized resistance, or area specific resistance (ASR), is used for BPP for fuel cells discussing ohmic losses. Generally, resistance scales with area, so, to compare the fuel cells of different sizes their resistances must be compared on a per-unit-area basis and current density should be used instead of current [144].

ASR of a fuel cell is its resistance normalized by its area. It carries units of $\Omega \cdot cm^2$. A fuel cell can be regarded as a good one if its ASR is below 0.1 $\Omega \cdot cm^2$. To calculate ASR it is necessary to multiply a fuel cell's ohmic resistance R by its area A:

$$ASR = R \cdot A \tag{4.3}$$

Ohmic losses can be calculated by multiplying ASR by current density:

$$\eta_{ohmic} = ASR \cdot j \tag{4.4}$$

By definition, resistance is inversely proportional to area:

$$R = \rho \frac{l}{A} \tag{4.5}$$

where ρ is electrical resistivity of the material, l is the length of the conductor and A is the cross-sectional area of the conductor. It means that the resistance of a large fuel cell with big square would be lower than the resistance of a smaller one. On a per-unit-area basis their resistances should be about the same. To get area-independent resistance multiplication by area is used [144].

4.3.2 Measuring Technique

Four-point probes method was used to measure the resistance of two BPP, which form a single fuel cell. This method uses two separate pairs of electrodes and provides more accurate measurements than the two-point technique [145]. This measuring method is well-known and not complicated, it is described in detail in [10]. The main features of the four-point probes method applied to this research are described in this chapter.

The measuring device used in this work to measure electrical conductivity of BPP is schematically presented in Fig. 4.11 [10]. It is important that this method can only be used if the conductivity of the sample is isotropic.

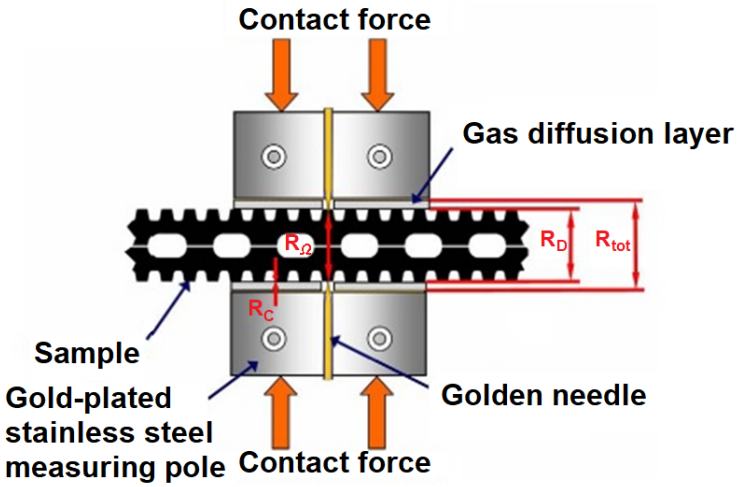

Figure 4.11: Schematic view of the device for measuring the resistance of BPP: R_{tot} – total resistance, R_D – contact and bulk resistance, R_Ω – bulk resistance, R_C – contact resistance (adapted from [10]).

Measuring the resistance of two connected bipolar plates the following resistances should be taken into account: resistance of the gas diffusion layer (GDL), contact resistance between BPP and GDL (from both sides), bulk resistance and internal contact resistance between two bipolar plates [8]. Plasma modification reduces the contact resistance by modifying the surface and removing PP. The contact resistance can be calculated using the following expression:

$$R_C = \frac{R_D - R_\Omega}{2} \tag{4.6}$$

where R_D is contact and bulk resistance (total resistance exclusive of the resistance of GDL) and R_Ω is bulk resistance. The contact resistance R_C, in turn, consists of contact resistance between BPP and GDL R_K, bulk resistance of GDL R_B and contact resistance between GDL and the measuring pole $R_{GDL_{Pole}}$:

$$R_C = R_K + R_B + R_{GDL_{Pole}} \tag{4.7}$$

The bulk resistance of GDL (R_B) and the contact resistance between the GDL and the measuring pole ($R_{GDL_{Pole}}$) have been analyzed elsewhere [10], so R_K can be found from equation (4.7).

Fig. 4.12 schematically shows that the value R_K (and hence R_C) may depend on the contact area between the porous GDL and rough surface of BPP (since air is an insulator [146]) and on the conductivity of the BPP surface. The applied pressure of the measuring pole (Fig. 4.11) on BPP was 20 bar, what increases the contact area, and plasma treatment allows to improve the transmissional contact.

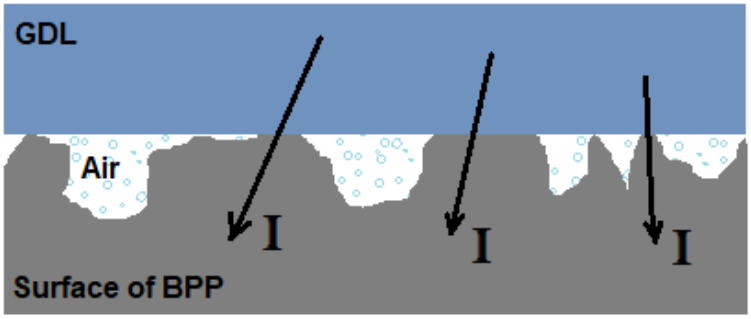

Figure 4.12: Schematic view of the contact between BPP and GDL (R_K).

Electrical scheme of the resistance measuring device from Fig. 4.11 is presented in Fig. 4.13.

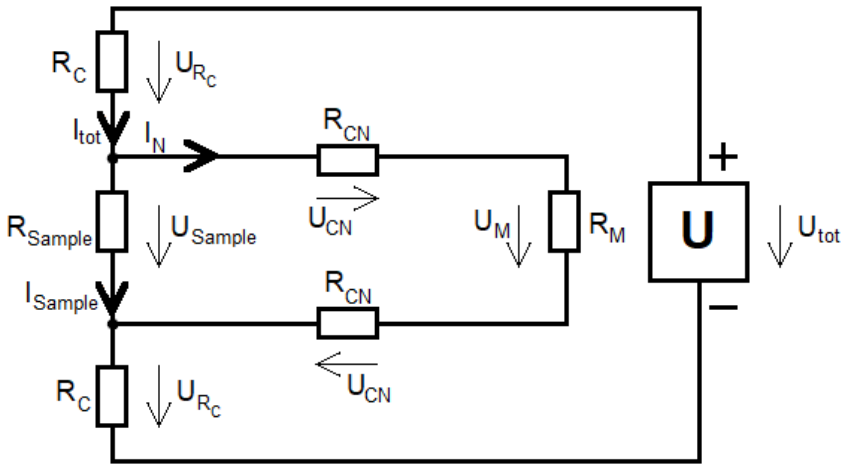

Figure 4.13: Electrical scheme of the resistance measuring device.

The values of I_{tot}, U_{tot} and U_M are measured. From Fig. 4.13:

$$U_{Sample} = U_M + 2U_{CN} \tag{4.8}$$
$$I_{tot} = I_N + I_{Sample} \tag{4.9}$$
$$U_{tot} = U_{Sample} + 2U_{RC} \tag{4.10}$$
$$U_{RC} = R_{CN} \cdot I_N \tag{4.11}$$
$$U_{CN} = R_{CN} \cdot I_N \tag{4.12}$$
$$U_M = R_M \cdot I_N \tag{4.13}$$

Substituting equation (4.12) into (4.8) and (4.11) into (4.10):

$$U_{Sample} = U_M + 2R_{CN}I_N \tag{4.14}$$
$$U_{Sample} = U_{tot} - 2R_C I_{tot} \tag{4.15}$$
$$\tag{4.16}$$

In Fig. 4.13 and in the formulae (4.8) – (4.15): I_{tot} is the total current running though the complete assembly; I_{Sample} is the current running though the sample (two BPP); I_N is the current running though the golden needles and the digital multimeter (DMM), bypassing the BPP; R_{Sample} is the resistance of the sample (two BPHP, including the contact resistance between them, or a single foil); R_C is the resistance, which includes contact resistance between BPP and GDL, bulk resistance of GDL and contact resistance between GDL and the measuring pole (4.7); R_{CN} is the contact resistance between the sample and the golden needle (the golden needle does not contact with the GDL due to a hole in the GDL, which allows the direct contact between the needle and the sample (BPP), as shown in Fig. 4.11); R_M is the internal resistance of the DMM; U_{tot} is the total applied voltage; U_{Sample} is the potential difference from the two sides of the sample; U_{RC} is the potential difference between one measuring pole and one side of the sample next to it; U_{CN} is the potential difference between one golden needle and one side of the sample next to it; U_M is the voltage measured by the DMM.

Since area specific contact resistance R_C (measurement by the pressing pole)

should be comparable to the area specific contact resistance R_{CN} (measurement by the golden needle) and, because typical internal resistance of a DMM is at least 10 MΩ, which is five or more orders of magnitude higher than the resistance of R_{Sample}, the value of U_{Sample}, which can be calculated by the formula (4.14), is much more exact than this from (4.15). Considering the fact that I_N is generally very small, it follows that: $U_{Sample} \approx U_M$. Therefore, the method of four-point probes is preferable over the two-point method.

It is not possible to measure R_{Sample} and R_C directly, therefore it is necessary to calculate these values from the measured values of I_{tot}, U_{tot} and U_M. By Ohm's law:

$$R_{Sample} = \frac{U_{Sample}}{I_{Sample}} \tag{4.17}$$

$$R_C = \frac{U_{RC}}{I_{tot}} \tag{4.18}$$

Considering equation (4.9) and the fact that $I_N \ll I_{tot}$, it follows that $I_{tot} \approx I_{Sample}$

$$U_{RC} = \frac{U_{tot} - U_{Sample}}{2} \tag{4.19}$$

Taking U_{Sample} from (4.14) and calculating U_{RC} by the formula (4.19), it is possible to calculate the values of interest – R_{Sample} (bulk resistance of BPP), and R_C, which can be regarded as "contact resistance":

$$R_{Sample} \approx \frac{U_M}{I_{tot}} \tag{4.20}$$

$$R_C \approx \frac{U_{tot} - U_M}{2I_{tot}} \tag{4.21}$$

It should be taken into account that the "contact resistance", investigated in this work, is actually R_K – the contact resistance between the sample and GDL, which can be deduced from the equation (4.7):

$$R_K = R_C - R_B - R_{GDL_{Pole}} \tag{4.22}$$

where R_B (bulk resistance of GDL) and $R_{GDL_{Pole}}$ (contact resistance between GDL and the measuring pole) are known [10]. In case of measuring BPHP, when two plates are connected together and regarded as one sample, the internal contact resistance between these two plates cannot be measured by the method used. So, as well as bulk resistances of both plates, the internal contact resistance between the plates is regarded as a component of bulk resistance – R_{Sample}. Thus, the overall performance of this stack is regarded and discussed for technical application.

5 Experimental Setup and Parameters

5.1 CYRANNUS® Microwave Plasma Source

The treatment of BPP by plasma was conducted using IPLAS CYRANNUS® I - 6“ (Cylindrical Resonators with Annular Slots) microwave plasma device (IPLAS GmbH, Germany) [147] with the operating frequency 2.45 GHz. This system was chosen because it allows to variate the biggest amount of experimental parameters, such as chamber geometry, mixture of the gases, pressure of the process, treatment duration and so on. The choice of these parameters defines the efficiency and the result of plasma treatment. A schematic picture of the system is given in Fig. 5.1 [148]. It is not complicated to operate this system and there were only few modifications (such as choosing and installing a suitable pump, gas flow controllers, sample holder and etc.) done to start plasma treatment of BPP using this device.

A substrate holder was custom designed and inserted into the chamber from the bottom [21]. In this work the sample holder was an aluminum cylinder, its position in the chamber could be changed along the vertical axis, so that the sample could be situated at the distance from 0 up to 6 cm from the bottom of the plasma chamber for remote plasma treatment. In this case the plasma is just a source of the particles, which take part in the process of treatment [8].

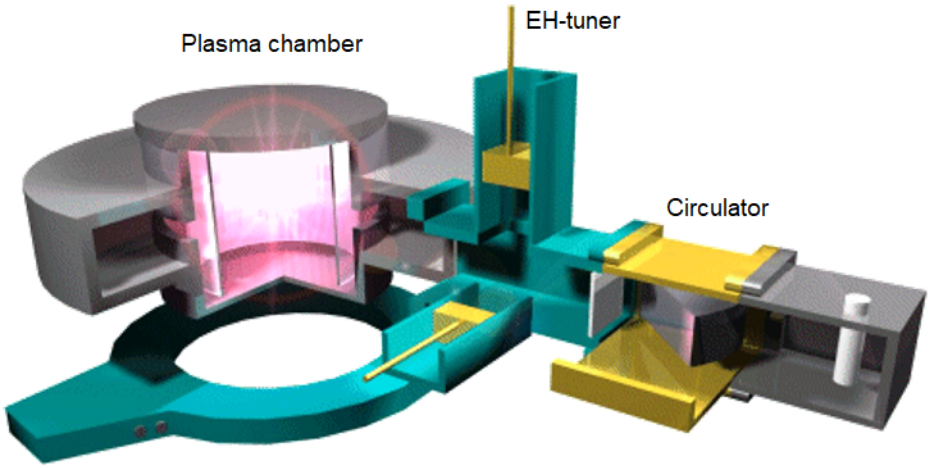

Figure 5.1: Schematic view of IPLAS CYRANNUS® I microwave plasma source (adapted from [148]).

The microwaves coming from the generator are fed into the chamber, passing though the microwave circulator and the E-H tuner. The circulator works as a semitransparent mirror leading the microwaves into the chamber, preventing the reflected microwaves turning back to the generator and leading them into the cooling water load instead. Cylindrical configuration of the resonator operating in TM 012 mode enables the generation of a freestanding plasma in a shape of a sphere in the center of the quartz cylinder independent of pressure, because the microwave power density is higher in the center of the chamber and lower at the glass cylinder [8, 21, 149]. The quartz cylinder is cooled by air flowing between it and the ring resonator.

An EH-tuner (Magic-T) has a variable shorting plunger in each of the E- and H-arms. The E stands for electric field and the H stands for magnetic field. The two arms terminated in adjustable plungers are used for impedance transformation [149]. By adjusting the plunger positions and therefore changing the impedance of the system it is possible to minimize the reflected microwave power. It should be noticed that microwave impedance of the system depends on several experimental parameters, such as pressure, plasma chemistry and geometry of the resonator (position of the sample holder and the sample inside the chamber).

Changing one of those parameters changes the impedance of the system, which has to be compensated by adjusting the plungers of the EH-tuner appropriately. Fig. 5.2 shows the dependence of reflected power for air plasma at the pressure of 10.6 mbar on the position of the plungers of the EH-tuner.

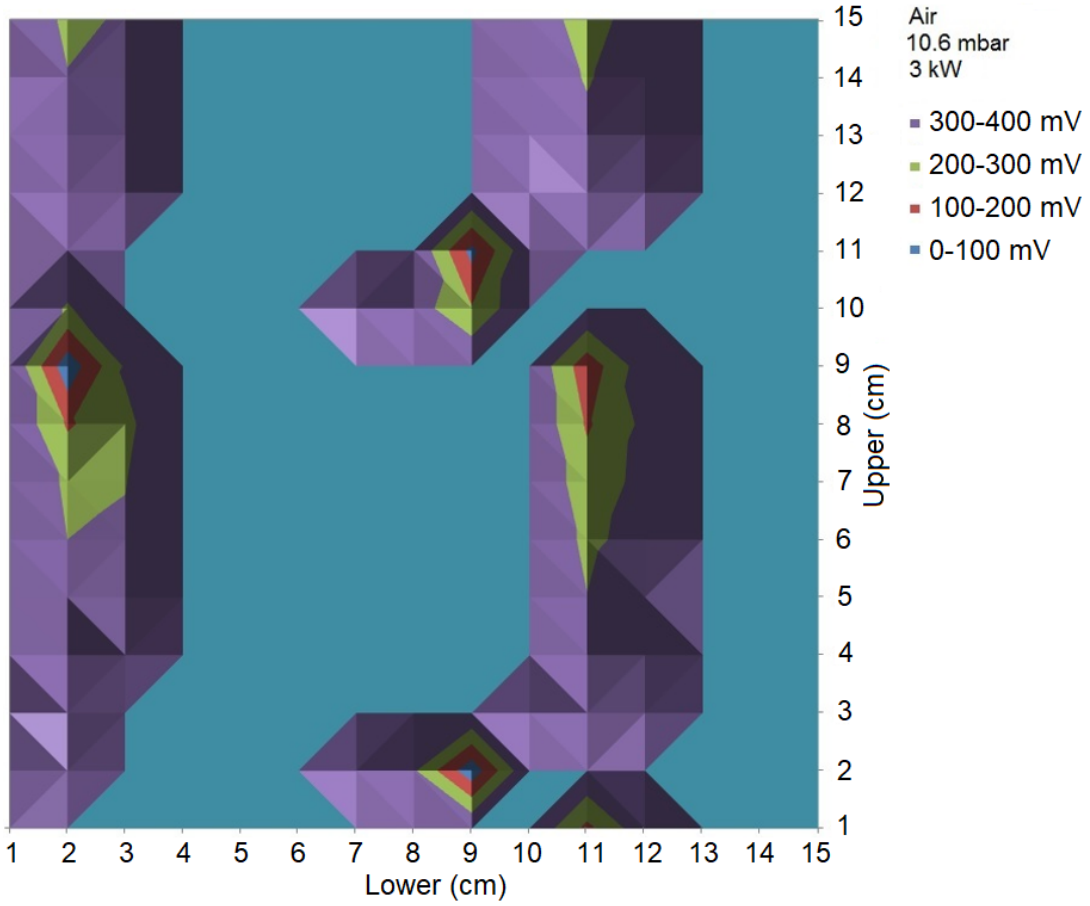

Figure 5.2: Reflected microwave power for air plasma at 10.6 mbar, 3 kW.

In Fig. 5.2 one can see that there are several spots where the reflected microwave power is minimized: (11; 9), (9; 2), (9; 11) and (2; 9). It means that in those positions of the EH-tuner plungers the minimum of the microwaves is reflected and most of the microwave power is delivered to the chamber. In this case the optimal position of the plungers would be (11; 9) in the center of the map in Fig. 5.2, because in case of impedance change due to the changes of pressure or plasma chemistry this position provides a possibility to adjust the position of

both plungers in a wide range.

5.2 Experimental Parameters

In the beginning of the work on plasma modification of the electrical surface properties of BPP it was an important task to choose appropriate experimental parameters. The choice was not evident because there are many parameters to vary: plasma chemistry (gases to use), gas flow, process pressure, treatment time, position of the sample (distance between the plasma sphere and the sample) and power of the microwave generator. The optimal set of parameters for IPLAS CYRANNUS® I microwave plasma source used (for BPP and foils with 29 wt% – 35 wt% of PP) was found experimentally.

The power of the microwave generator was set at 3 kW – the maximal for the device used. An oilfree scroll vacuum pump (Scrollvac SC15D) was evacuating the system achieving the residual pressure of $2{\cdot}10^{-2}$ mbar, after that gases were fed into the chamber.

The etching properties of different gases result in different efficiency of plasma treatment. For example, plasma treatment by oxygen-containing gases (oxygen, carbon dioxide, air) leads to PP reduction and, consequently, the improvement of the conductive properties of the surface already after 5 minutes of plasma treatment. While the treatment by other gases was not so effective, it could improve the surface conductivity only very insignificantly. Argon (the inert gas) plasma treatment causes the least significant changes of the surface conductivity. Therefore, study of plasma treatment by oxygen-containing gases (mainly air and CO_2) was in focus. The experiments conducted included plasma treatment of BPP and foils by such gases as carbon dioxide, air, oxygen and argon. But the main attention was paid on atmospheric air plasma due to time- and cost-efficiency and on carbon dioxide plasma due to high efficiency of the treatment.

The gas flow was varied from 100 sccm up to 17 slm. Some experiments with atmospheric air were conducted by letting some air into the chamber by opening

a needle valve, controlling the pressure in the chamber.

The pressure variation range depended on the gas used. For example, for air the pressure was varied in the range of roughly 10^{-2} mbar up to atmospheric pressure (∼1000 mbar); for carbon dioxide – from 0.1 mbar up to 34 mbar; for oxygen – from 8 up to 34 mbar; up to 85 mbar for nitrogen and up to 980 mbar for argon.

The duration of plasma treatment was varied depending on other experimental parameters from 3 up to 60 min for BPP and from 3 up to 15 min for foils.

The distance between the sample and the bottom of the plasma chamber was varied from 0 up to 6 cm for BPP, but in most experiments ≈ 4 cm. Foils were always treated at the optimal distance of 6 cm. It should be noticed that this distance and the distance between the sample and the plasma ball are not the same. Since the plasma ball is situated approximately in the center of the chamber and the distance is measured from the sample to the bottom of the chamber, it should be taken into account that the distance between the sample and the plasma ball is a few centimeters longer than the distance presented here, which can be measured.

The samples of different composition (foils) require specific sets of experimental parameters. In case of plasma treatment of foils another important variable parameter appears – the composition. It must be taken into account choosing the parameters of the treatment. In this work a suitable and effective mode of plasma treatment was found experimentally for each foil composition investigated.

6 Elemental Analysis of Plasma by OES

OES is used in this work to reduce trial and error varying plasma treatment conditions as much as possible, but the idea not to lose plasma conditions leading to a good performance at variation of parameters was only partly successful at such big difference of plasma conditions used. Optical emission spectra were obtained during the plasma treatment of the samples by different gases (air, carbon dioxide, nitrogen and argon). Since the pressure was varied from 0.1 mbar up to atmospheric by air plasma treatment, also the comparison of optical emission spectra of air plasma at different pressures was done.

The measurements were done by optical emission spectrometer Avantes AvaSpec-3648, with the microwave power of the plasma source of 3 kW. The spectra were analyzed using the following sources: [27, 150–153].

Since many experiments were conducted using atmospheric air as working gas and the pressure is an important parameter which influences the result of plasma treatment, it was necessary to investigate the change of air plasma at different pressures. The result of such investigation by OES is presented in Fig. 6.1. Air plasma at the pressure of 0.1 mbar has a bright pink color, characteristic for nitrogen. Changing the pressure up to atmospheric the temperature of the plasma changes and hence the color of plasma also changes. At the atmospheric pressure air plasma had white color. The color reflects the spectral composition of the radiation.

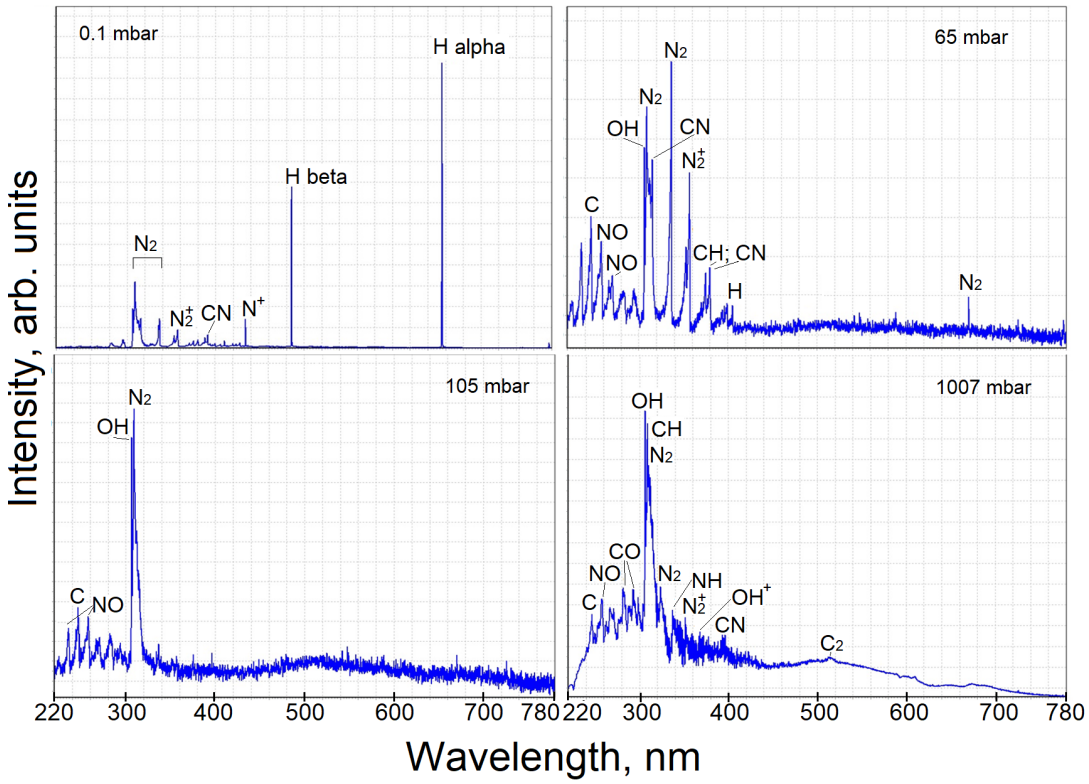

Figure 6.1: Emission spectra of air plasma at different pressures.

At the pressure of 0.1 mbar (Fig. 6.1 (top left)) one can see the lines, which belong to the second positive system of nitrogen N_2 $(C^3\Pi_u, \nu') \rightarrow (B^3\Pi_g, \nu'')$ with the wavelengths of 282.0; 297.5; 315.9; 337.1; 380.5 nm, and so on. A weak line of ion of molecular nitrogen, which belongs to the first negative system of N_2^+ $(B^2\Sigma_u^+, \nu') \rightarrow (X^2\Sigma_g^+, \nu'')$ at 391.4 nm $(\nu' = 0, \nu'' = 0)$ is also recognizable at the pressure of 0.1 mbar (Fig. 6.1 (top left)) and 65 mbar (Fig. 6.1 (top right)). The intensity of this line decreases with the increase of the pressure of air. At the pressure of 0.1 mbar the lines of atomic oxygen are absent, what indicates a low rate of ozone formation under such treatment conditions [151]. It also means that at low air pressure nitrogen ions give significant contribution to the surface treatment process.

Increase of the pressure up to 65 mbar and more leads to the appearance of the

emission line of the molecule OH (308; 313 nm and so on) and also H_2 and NO from the region of 200-300 nm, wherein the lines of hydrogen are not recognizable at the pressure of 105 mbar and higher. The authors in [151] have noticed that the lines H_2 and NO appeared only due to water, what means that H_2O molecules (not molecular oxygen), are responsible for the formation of nitrogen oxides [151, 154].

The spectrum of air plasma at atmospheric pressure (Fig. 6.1 (bottom right)) shows the lines of atoms, molecules and ions on the continuous "noise"5spectrum of thermal, braking and recombination plasma radiation. The lines of N_2 are still very intensive at atmospheric pressure, at the same time there are intensive lines of OH radical, formed from water vapors, which are present in ambient air and NO radical, formed from O_2 and N_2 that dissociate at temperatures above 1600 K or by electron impact [27].

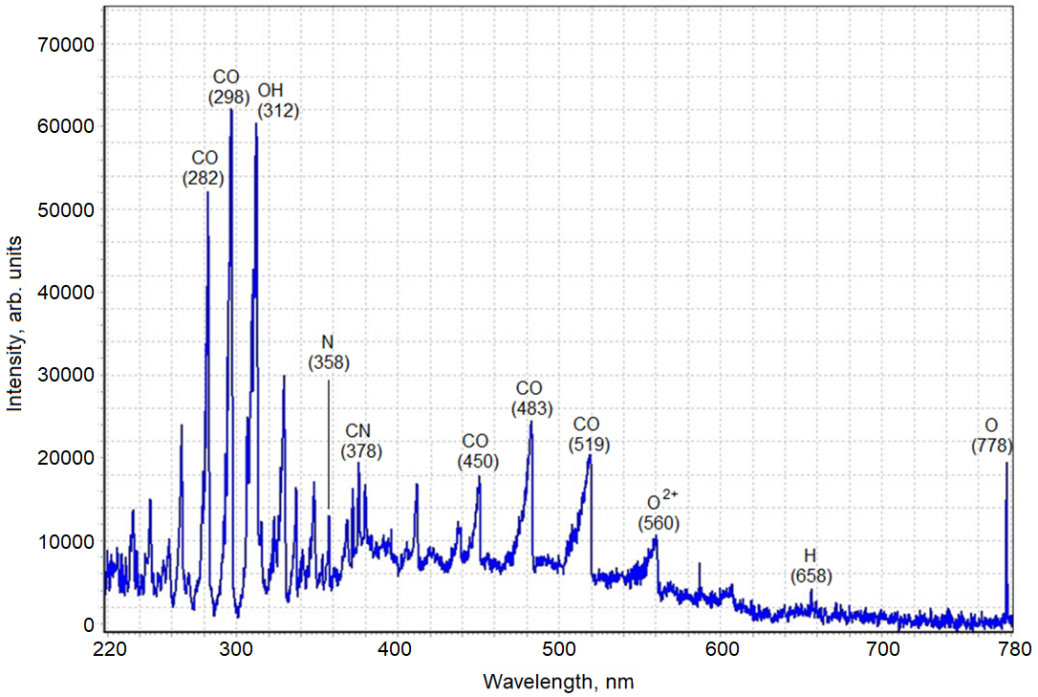

Figure 6.2: Emission spectra of carbon dioxide plasma.

In the spectrum of carbon dioxide plasma at the pressure of 8.5 mbar in Fig. 6.2

one can see dominating CO and OH lines, also well definable CN lines. CN radicals are formed from N_2 (probably from residual air in the chamber) and carbon-containing impurities (apparently from the sample). Atomic lines N, O and H initiate further plasma chemical processes, such as formation of ozone (O_3), peroxyl radicals (HO_2), and other reactive species [27], responsible for successful plasma treatment.

In the spectrum of nitrogen plasma at the pressure of 10 mbar (Fig. 6.3) except the lines of N_2, N and nitrogen ions, CN and OH lines and are visible. Some minor NO bands can also be detected in the region of approximately 200-295 nm, what was also reported in [20] and [155] where only pure nirtrogen was used as a process gas. Even small admixture of oxygen or water vapor into nitrogen plasma dramatically changes plasma chemistry and thus emitted spectra, decreaseing CN emission and enhancing the emission of NO and NH radicals [27]. So unwanted water in the plasma chamber can be recognized by orange or yellow color of the plasma ball.

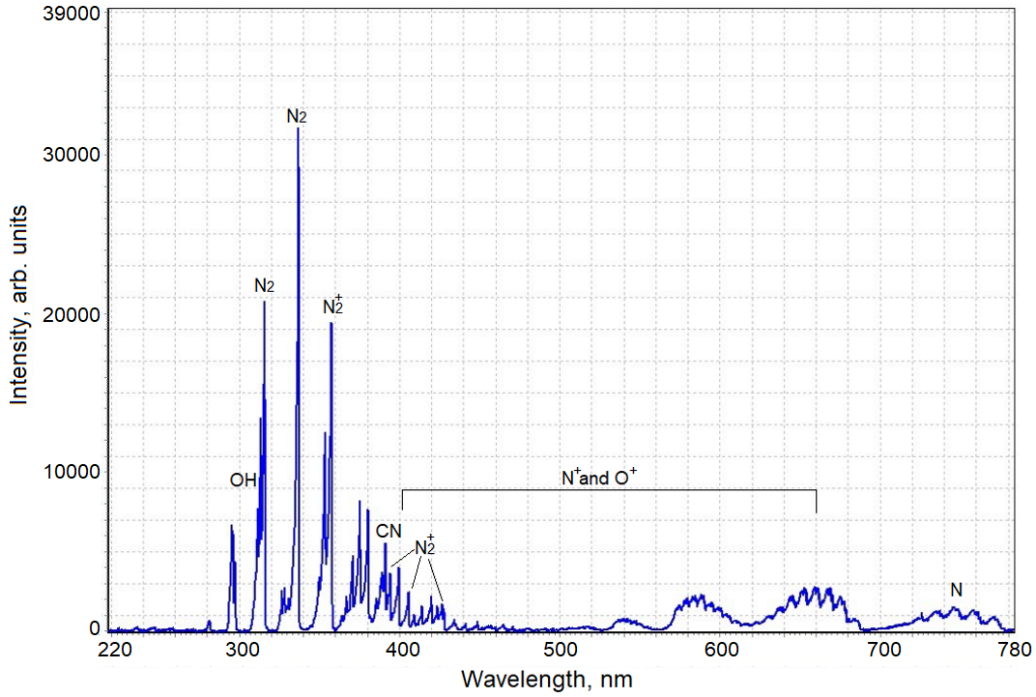

Figure 6.3: Emission spectra of nitrogen plasma.

Emission spectrum of argon plasma, presented in Fig. 6.4, has dominating argon lines and the lines of insignificant intensity of OH and CH radicals. At low pressure (4 mbar) the color of argon plasma was pink-purple, likely because of the remains of the atmospheric air in the chamber. The residual pressure before argon input was $3.2{\cdot}10^{-3}$ mbar. Increase of argon pressure up to 150 mbar leads to the change of plasma color to more purple, the plasma ball loses the brightness. Argon plasma ball at the atmospheric pressure is light-purple. The time of plasma treatment did not significantly influence the emission lines, changing only the general intensity of the spectrum.

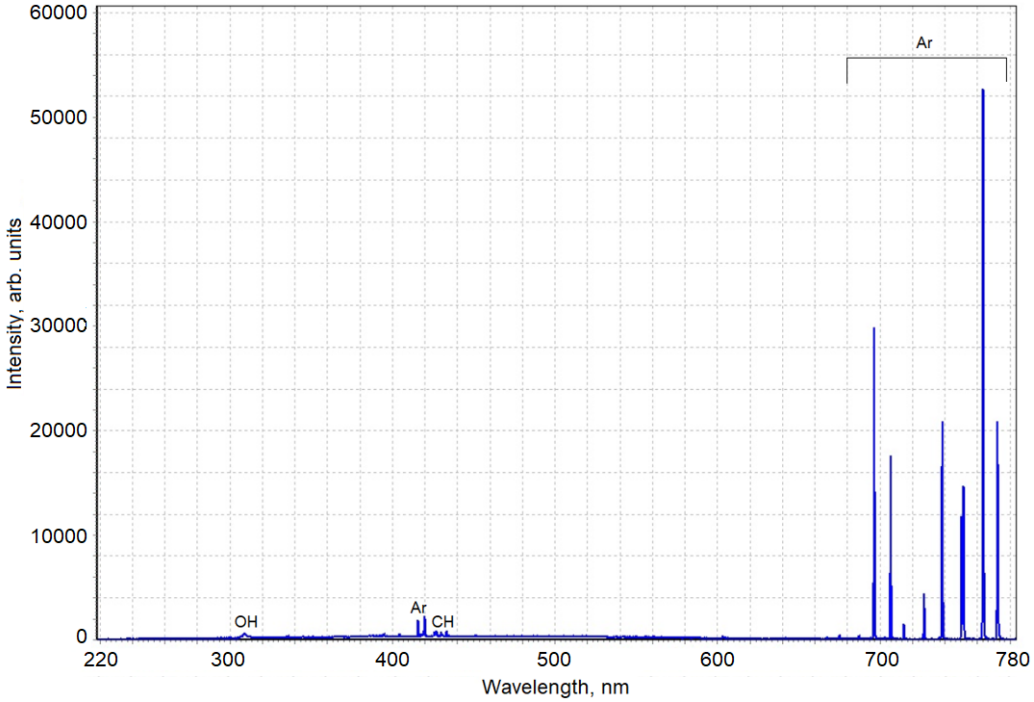

Figure 6.4: Emission spectra of argon plasma.

7 Analysis of BPP

7.1 FTIR Investigation of the Surface

One of the main highlights of this work is FTIR spectroscopy, because it allows to see the changes in absorption bands of heteropolar bonds, hence to monitor the removal of PP from the surface of BPP. The result of this monitoring will be reported later in this chapter. The vibration bands of $C-H$ bonds for sp^2-carbon allow to state the presence of graphite fragments of the carbon-containing layer.

7.1.1 Description and Definition of the Peaks of FTIR Spectra

The FTIR spectra were obtained using Varian 670-IR FTIR spectrometer. The analysis of the FTIR spectra was conducted for the samples treated in plasma by different gases: carbon dioxide, oxygen, air and argon. To estimate the impact of plasma treatment on the surface of BPP the intensity ratios of the peaks typical for polymer and graphite structures for untreated and treated samples were compared.

The survey FTIR spectra of the untreated bipolar plate sample and of the sample treated in carbon dioxide (20 minutes, 4 cm, 100 sccm, 5.8 mbar), are shown in the Fig. 7.1. The extended peak analysis, presented in this work below, is done for these samples. In Fig. 7.1 the clearly visible and definable absorption bands are the following: 1250-1700 cm^{-1}; 2400 cm^{-1}; 2700-3100 cm^{-1} and slight 3600-3900 cm^{-1}, which refers to H_2O absorption [156, 157].

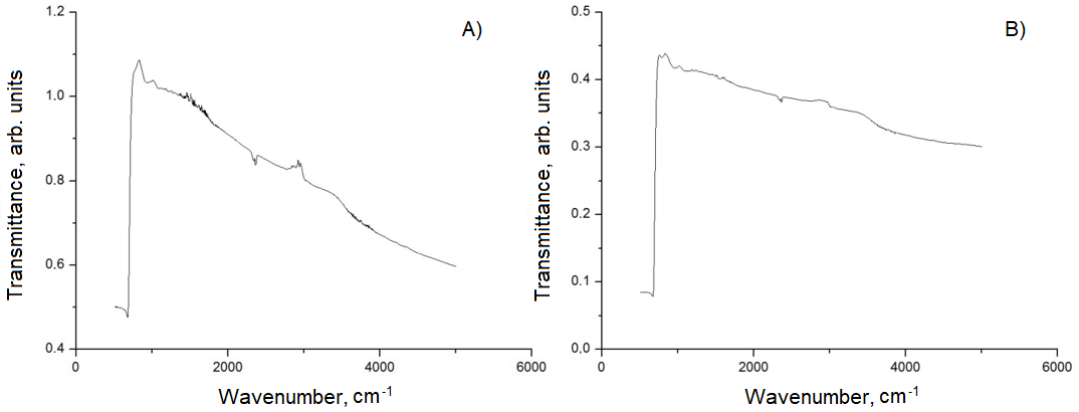

Figure 7.1: Survey FTIR spectra of: A) untreated sample and B) sample treated 20 min with a carbon dioxide plasma.

The absorption peaks from the spectra in Fig. 7.1 of the untreated sample were picked and compared with the peaks of the treated one.

Description of the Spectral Peaks of the Untreated Sample

The spectrum of the untreated sample (Fig. 7.1 (A)) contains the absorption bands of CH_3, CH_2 and CH groups. The data decryption can be found in a number of scientific papers [35, 37, 39, 40, 158–160], including the well-known work of J. Ristein [156]. The most intensive absorption peaks (2960, 2925 and 2840 cm^{-1}), which are well visible in Fig. 7.2 (C), correspond to the stretching vibrations of $C-H$ bonds for carbon in tetrahedral environment, i.e. carbon in sp^3 - state. In the absorption range of 2800-3100 cm^{-1} there are peaks related to asymmetric (2960 cm^{-1}) and symmetric (2870 cm^{-1}) vibrations of the $C-H$ bonds in the CH_3 group; asymmetric and (2878 cm^{-1}) and symmetric (2840 cm^{-1}) vibrations of the $C-H$ bonds in the CH_2 group. For the CH_3 group the asymmetric vibrations can be planar and nonplanar. The stretching vibrations of the CH group are characterized by the peak at 2900 cm^{-1}. In the region of 1300-1500 cm^{-1} there are bands of bending vibrations of $C-H$ bonds: asymmetric (1456 cm^{-1}) and symmetric (1375 cm^{-1}) in CH_3 group; scissoring (1435 cm^{-1}) and olefinic (1419 cm^{-1}) vibrations of $C-H$ bonds in CH_2 group. The range of 617-750 cm^{-1} is the range of vibrational energy of $C-C$ bonds, which forms

the skeleton of the organic compound. Carbon dioxide absorbs in the range of 2300-2400 cm^{-1}.

Description of the Spectral Peaks of the Sample after Carbon Dioxide Plasma Treatment

After carbon dioxide plasma treatment of the sample (Fig. 7.1 (B)) the following changes of the spectrum can be noticed:

- In the range of 3000-2800 cm^{-1} the absorption bands are merged. Decomposition using Origin 9.0 software showed that the most intensive absorption bands of CH_3 group remaine (2960 and 2870 cm^{-1}). The absorption band of CH group (2906 cm^{-1}) is also remained, but its intensity decreased comparing to the intensities of the absorption bands of the bonds in CH_3 group.

- The absorbance increase for the wavenumbers over 3000 cm^{-1}. $C-H$ groups in aromatic (ring structures) and olefinic (one or several double bonds in the chain) structures absorb in this region (see [156]). This suggests that changes in composition and in structure of the surface layer take place. Unsaturated bonds and aromatic cycles appear as a result of abstraction of hydrogen atoms.

- In the range of 1300-1500 cm^{-1} the bands of $C-H$ vibrations in CH_3 group (1456 cm^{-1} and 1375 cm^{-1}) are remained. The band of olefinic vibration of $C-H$ bonds in CH_2 group (1416 cm^{-1}) is also remained.

- The appearance of an intense band at 1465 cm^{-1}, next to the band of 1452 cm^{-1}, happened partly due to the bending vibrations of the CH_3 group. CH_3 bending vibrations are inherent in several bands [156].

- The absorption bands around 1700 cm^{-1} and 3250 cm^{-1} refer to H_2O [156].

Definition of the Peaks of PP and Graphite Structures

The absorption bands of 1300-1500 cm^{-1} and of 2800-3100 cm^{-1} refer to $C-H$ bending modes and $C-H$ stretching modes, respectively. The peaks, typical

for PP, as well as the peaks of graphite structures, can be found in these ranges. Fig. 7.2 shows the absorption regions for $C-H$ bonds of bending vibrations (1300-1500 cm^{-1}) and stretching vibrations (2800-3100 cm^{-1}) for the untreated sample and the treated one in carbon dioxide plasma (Gaussian fitting).

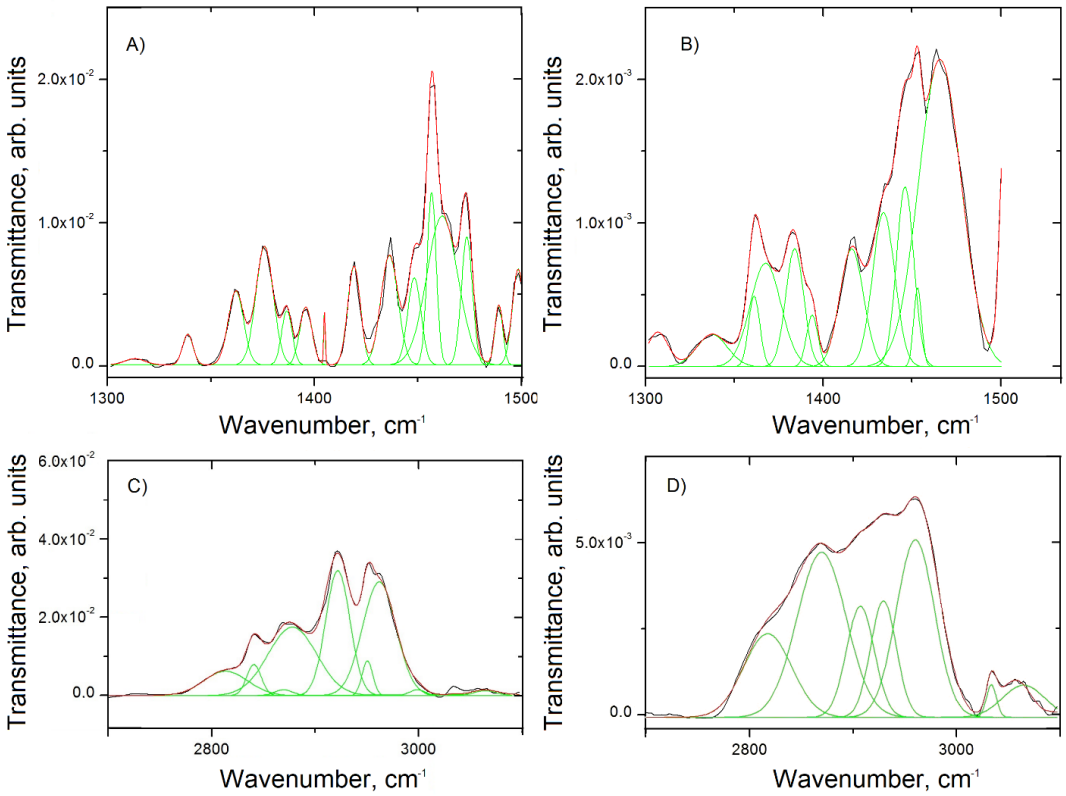

Figure 7.2: FTIR spectra of : A) untreated sample (1300-1500 cm^{-1}); B) treated in CO_2 sample (1300-1500 cm^{-1}); C) untreated sample (2700-3100 cm^{-1}); D) treated in CO_2 sample
(2700-3100 cm^{-1}).

Analyzing the FTIR spectra of BPP which consist of carbon and PP can be problematic due to the difficulty of distinguishing the PP peaks from the graphite structures peaks unambiguously. For this reason, first of all the intense peaks, known from the literature, typical for PP and for graphite structures, were analyzed. These peaks are listed for PP and for graphite structures in Table 7.1 and in Table 7.2, respectively.

Table 7.1: Description of the PP peaks of the spectra.

Range cm^{-1}	**Peak** cm^{-1}	**PP C-H stretching modes**	**References**
2800-3100	2949	sp^3CH_3 asy	[37, 40, 156]
	2917	sp^3CH_2 asy	[35, 39, 40, 156]
	2838	sp^3CH_2 sym	[35, 39, 40, 156]
		C-H bending modes	
1300-1500	1456	sp^3CH_3 asy	[35, 37, 40, 156]
	1435	sp^2CH aromat, CH_2 scissor	[37, 156]
	1375	sp^3CH_3 sym	[35, 37, 40, 156, 161]
	1359	$2CH$	[37]

Table 7.2: Description of the peaks of graphite structures.

Range cm^{-1}	**Peak** cm^{-1}	**Graphite structures C-H stretching modes**	**References**
2800-3100	3030	sp^3CH sym / sp^2CH aromat	[41, 156]
	2960	sp^3CH_3 asy	[41, 156]
	2925	sp^3CH_2 asy	[41, 43, 156]
	2900	sp^3CH	[41, 43, 156]
	2870	sp^3CH_3 sym	[40, 41, 43, 156]
		C-H bending modes	
1300-1500	1490	sp^3CH_3 asy	[156]
	1473	sp^3CH_2	[156, 162–165]
	1361	CH_2 wag	[166]

Absorption Bands of Graphite and Polymer Structures

The intensity of the peaks of 1361-1362 cm^{-1}; 1473 cm^{-1} and 1490 cm^{-1} (these peaks are merged with the neighboring one) increases after the plasma treatment. Graphite-like structures absorb in these regions.

J. V. Gulmine and others have reported the presence of a double peak in the region 1473-1463 cm^{-1} for low-density polyethylene in their work on polyethy-

lene characterization by FTIR [167]. This doublet can be seen also in the FTIR spectrum of the untreated bipolar plates (Fig. 7.2 (A)). After 20 minutes of CO_2 plasma treatment the doublet merges into one (Fig. 7.2 (B)).

For polymeric material a small but discernible satellite at 1398 cm^{-1} appears. This satellite is part of a doublet into which the 1375 cm^{-1} (1372 cm^{-1} in [156]) line splits when two or three CH_3 units are bonded to the same carbon atom, i.e., in the case of $C(CH_3)_2$ and $C(CH_3)_3$ units [156].

Absorption of CO_2 and H_2O

The small peaks in the region of 2300-2400 cm^{-1} (Fig. 7.1) indicate that the surface of the sample contains dissolved CO_2. Cooling the plate after CO_2 plasma treatment did not lead to any changes in the spectrum, new lines did not appear, CO_2 absorption remained the same. Perhaps some absorption increase in the region of 3500 cm^{-1} indicates the presence of water on the surface. It is known [168] that the bands of physically sorbed water (nonrotating water molecule) lie in the region of 3825 and 3965 cm^{-1}.

Hydrogen on the Surface

The intensity ratio of the peaks, which refer to different amount of hydrogen, for example I(CH_3)/I(CH), is different before and after the plasma treatment of the samples. This difference can be associated to the change of the amount of hydrogen on the surface of the sample.

Since the peak of 2900 cm^{-1}, well visible in the spectrum of the treated sample (Fig. 7.2 (D)), seems to be completely merged with the neighboring ones in the spectrum of the untreated sample (Fig. 7.2 (C)), it is difficult to evaluate the intensity ratio I(CH_3)/I(CH) for this peak. J. Ristein in his work regarding hydrogenated amorphous carbon films [156] has reported:

> „For one of the vibrational modes a direct determination of its contribution to the absorption spectrum is not possible. This is the sp^3CH stretching mode, which is completely masked in all samples by the

> asymmetric stretching mode of the sp^3CH_2 groups. Thus only one absorption band at around 2925 cm^{-1}, which covers both modes, the asymmetric sp^3CH_2 vibration and eventually the sp^3CH band, can be fitted into the spectra. Nevertheless, one can extract the contribution of the sp^3CH stretching mode to the IR spectra of the DLC material by an indirect method by assuming that the concentration of sp^3CH groups is negligible in the polymerlike material... This assumption can be justified by the chainlike structure... sp^3CH groups would imply a three-dimensional cross linking of the chains, which is obviously hardly realized in those films.“

However, the intensity ratio I(CH_3)/I(CH) was calculated for the following peaks:
2870 cm^{-1} (CH_3 sym), 2960 cm^{-1} (CH_3 asy), 3030 cm^{-1} (CH aromat), 3062 cm^{-1} (CH aromat), 2998 cm^{-1} (CH olef). The intensity ratio I(CH_3)/I(CH) in Fig. 7.3 shows the decrease of CH_3 and the increase of CH groups on the surface after plasma treatment.

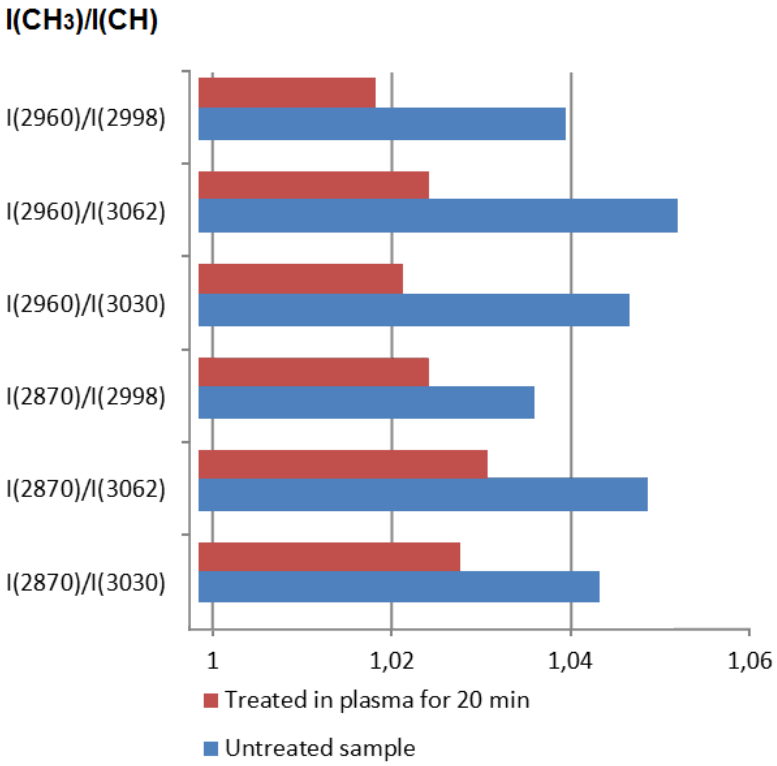

Figure 7.3: Intensity ratio of CH_3 and CH groups before and after the plasma treatment.

Plasma treatment destroys the macromolecules of PP and removes its monomer items and parts, clearing the graphite surface. The structure of the graphite surface is porous, the size of the pores separating the hexagonal crystals of graphite is around a nanometer [169], several crystals can be united into "granules", separated by the pores of a micrometer size. AFM and SEM measurements showed that the size of the pores in plasma-treated BPP is 0.5 – 3 μm. A hydrogen molecule H_2 with the size of 0.23 nm can easily fill the micro- and nanopores of graphite and even infiltrate into the crystal lattice of graphite. Remaining water molecules in the chamber are decomposed to hydrogen and oxygen. Therefore, the pores of the graphite surface can be filled by hydrogen. When the chemical bonds in $C-H$ and $C-C$ complexes are breaking, the reverse process – physical desorption can take place. Atoms of hydrogen are chemically very active, they form different complexes, like $C-H$, and this way easily sorb into graphite [169].

The processes of dissociation of hydrogen molecules on graphite defects also play an important role in formation of different chemical bonds of hydrogen and graphite [169]. The authors of [169] (in Russian) report:

> „The reaction: $C + H_2 = CH + H$ with the formation of atomic hydrogen and a non-volatile CH complex takes place on the graphite surface. Atomic hydrogen fills the defects of graphite crystal and dissolves in it... But the dissociation should also take place in the bulk of graphite in nanopores, accumulating hydrogen in chemical $(C - H)$ and physical (atomic H) forms. However, the kinematics of these processes has almost not been studied in practice."

The thermal impact of the plasma of chemically active gases, like oxygen and air, on the surface of the samples leads to removal of carbon in volatile oxides form (CO, CO_2) and in the form of hydrocarbons (methane CH_4, ethylene C_2H_4 and other C_xH_y) from the pores of graphite. High temperatures in plasma during the treatment of graphite surfaces also lead to a significant change in the distribution of pores, i.e. to the change in sorption and desorption properties of the surface [169]. This dynamism of the properties of graphite complicates the investigation of sorption and desorption processes of hydrogen.

Table 7.3 and Fig. 7.4 show the increase of the intensity ratio I(CH_3)/I(CH_2) after plasma treatment. At the same time the ratio I(CH_3)/I(CH) decreases after plasma treatment. Probably it is so because depolymerization process in plasma (detachment of methyl groups from the ends of the polymer chain) is slower than the process of methylene groups removal CH_2. Disappearance of the CH_2 vibrations of PP with increasing the duration of plasma treatment was also mentioned in [170].

Table 7.3: Comparison of the intensity ratio I(CH_3)/I(CH_2) before and after the plasma treatment.

I(CH_3)/I(CH_2)	**Before plasma treatment**	**After plasma treatment**
I(2949)/I(2917)	0.99241	0.99764
I(2960)/I(2925)	0.99038	0.99761

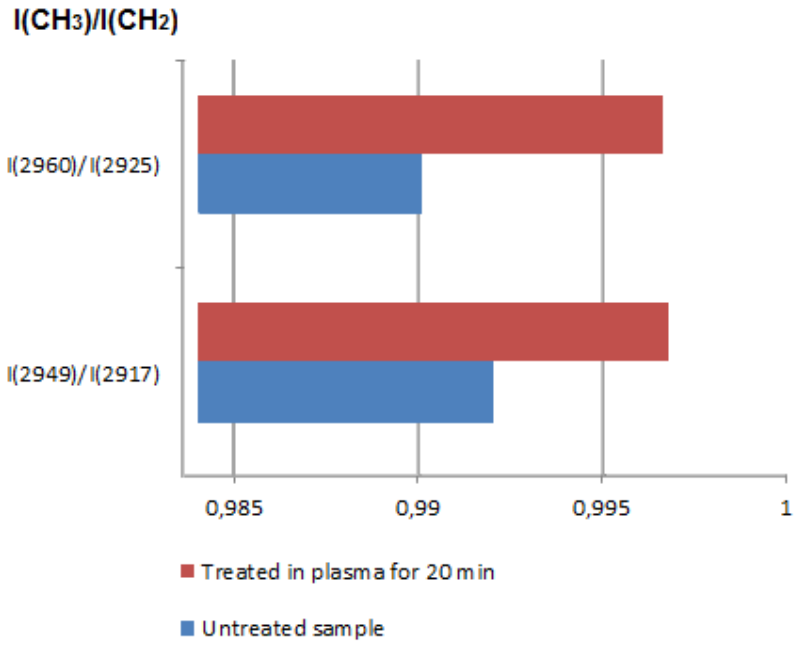

Figure 7.4: Intensity ratio of CH_3 and CH_2 groups before and after the plasma treatment.

Indeed, it would be logical to suppose that hydrogen should be removed from the surface in plasma, hence the intensity ratio I(CH_3)/I(CH_2) should decrease after treatment, but it does not happen. This contradiction can be explained by precise measuring of the masses of the samples in every stage of the investigation.

7.1.2 Removal of PP from the Surface

As it was mentioned before, the FTIR technique allows analyzing absorption of polymers and investigating the polymer-containing surfaces, because it shows the strong absorption bands of heteropolar bonds. Comparison of the intensity ratio

of PP and graphite structures before and after the plasma treatment shows how the amount of PP changes on the surface.

In the spectrum of PP (Fig. 7.5) there are two very well definable peaks: 1375 cm^{-1} and 1456 cm^{-1}, which are also present in the spectra of the BPP surfaces (Fig. 7.6). These peaks refer to the bending vibrations of CH_3 groups in PP [35, 37, 40, 156, 161, 171]. The other two peaks, marked in Fig. 7.6: 1361 cm^{-1} and 1473 cm^{-1} refer to the bending modes of $CH2$ groups in graphite structures [35, 156, 172]. The intensity ratio of the PP peaks and graphite peaks, shown in Fig. 7.7, decreases after the plasma etching, what indicates the reduction of PP on the surface after the treatment.

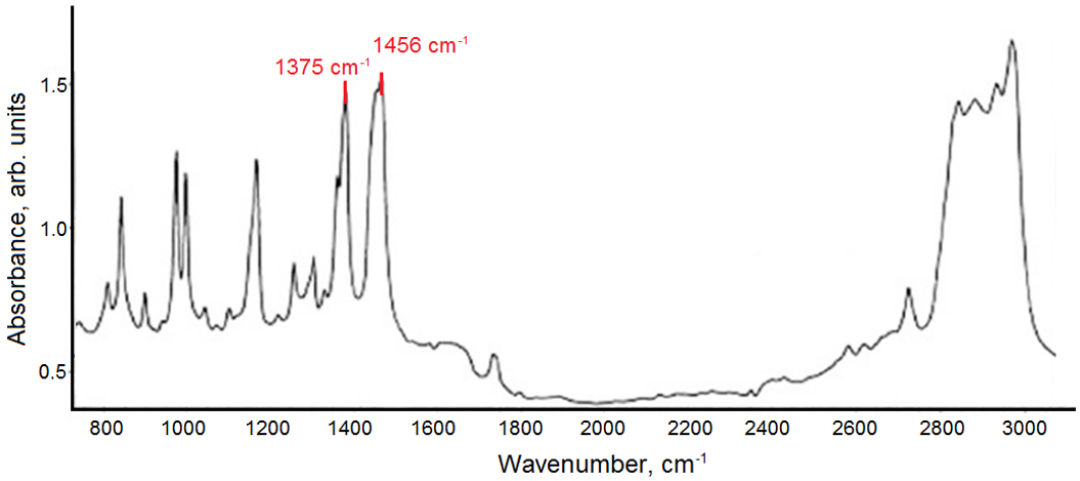

Figure 7.5: FTIR spectrum of PP.

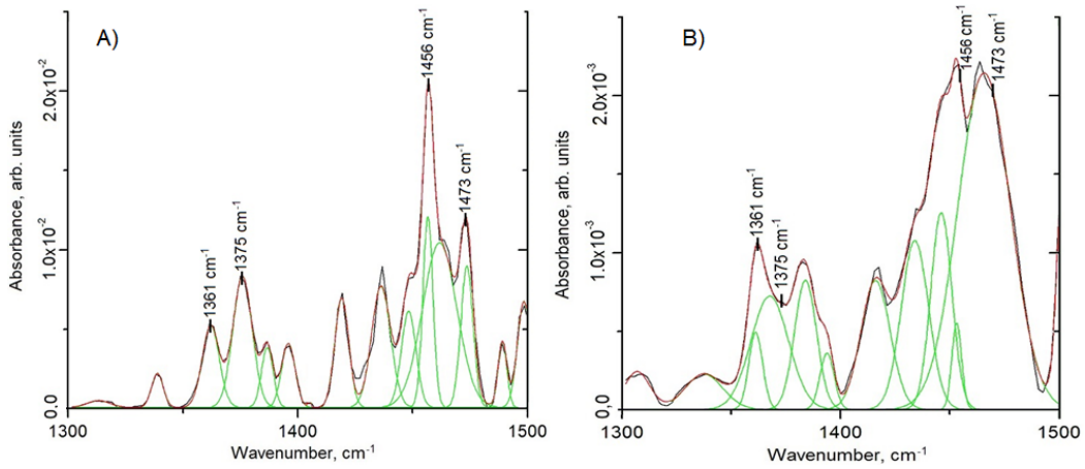

Figure 7.6: FTIR spectra of A) untreated BPP and B) treated 20 minutes in CO_2 plasma with marked peaks of PP (1375 cm^{-1} and 1456 cm^{-1}) and carbon structures (1361 cm^{-1} and 1473 cm^{-1}).

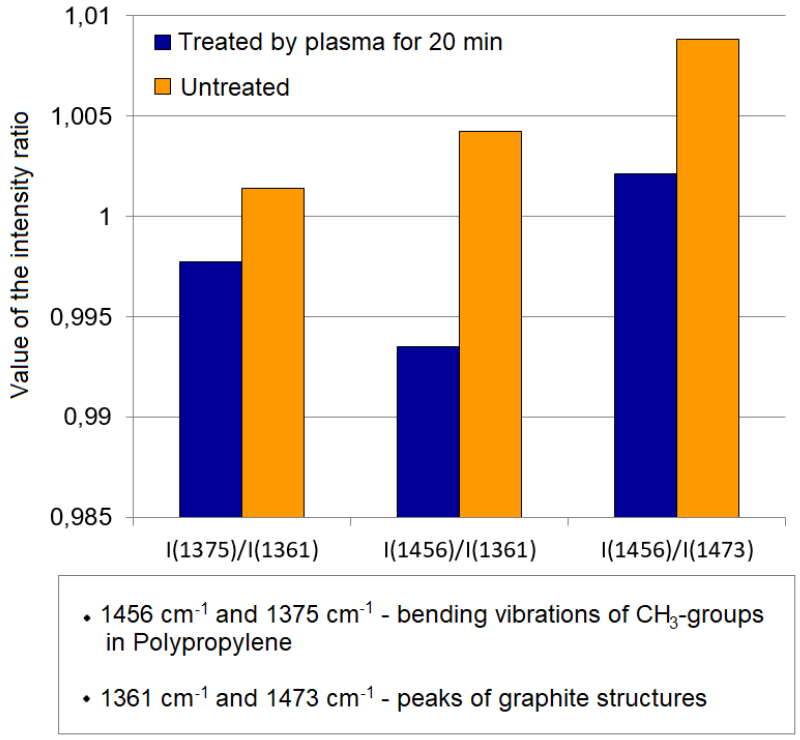

Figure 7.7: Intensity ratios of the peaks, typical for PP and graphite structures before and after plasma treatment.

The dependence of the intensity ratio $I_{PP}/I_{Graphite}$ on the duration of plasma treatment is fairly predictable and presented in Fig. 7.8 and Table 7.4. The longer the etching time, the less PP remains on the surface, hence the lower is this intensity ratio.

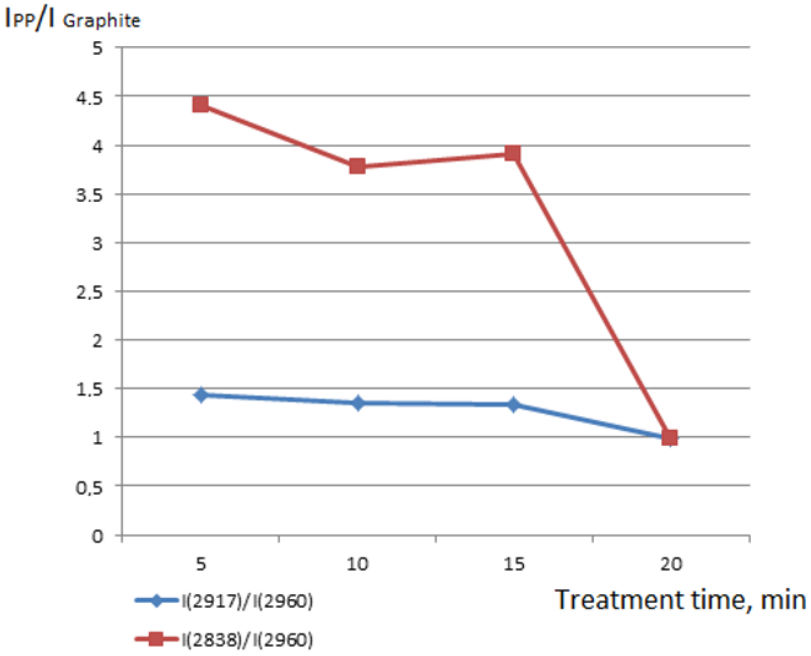

Figure 7.8: Dependence of the intensity ratio of the PP and graphite peaks on treatment duration.

Table 7.4: Dependence of the intensity ratio of the PP and graphite peaks on time of plasma etching.

$I_{PP}/I_{Graphite}$ cm^{-1}	**Treatment time** 5 min	10 min	15 min	20 min
I(2917)/I(2960)	1.430	1.350	1.340	0.997
I(2838)/I(2960)	4.410	3.780	3.910	0.994

The comparison of the intensity ratio of the peaks of sp^3- and sp^2-hybridized atoms of carbon before and after plasma treatment shows the increase of the content of sp^2-hybridized carbon atoms (Fig. 7.9), therefore the increase of the content of conductive graphite phase on the surface of the etched sample.

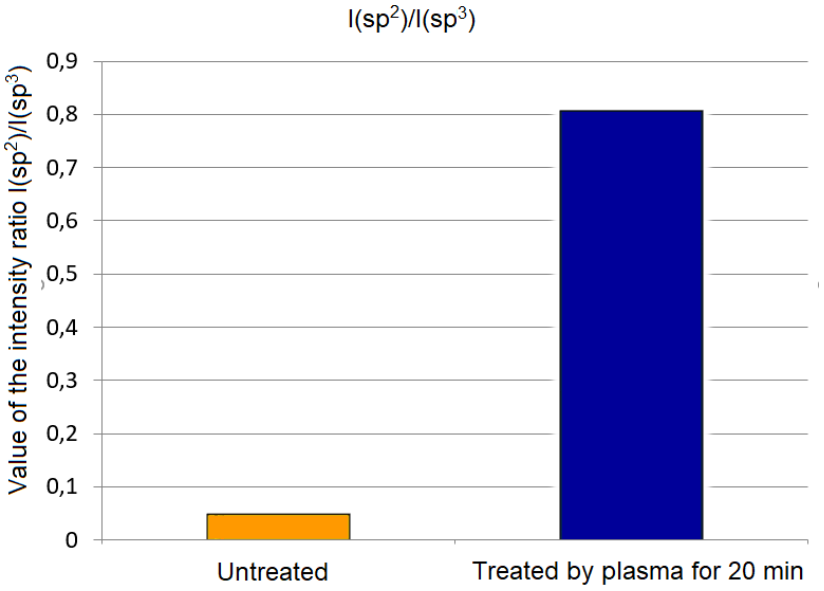

Figure 7.9: Change of the intensity ratios of the peaks of sp^3- and sp^2-hybridized atoms of carbon before and after plasma treatment.

So, the change of the intensity ratios of the peaks, typical for PP and graphite, and the intensity ratio of sp^2/sp^3 shows the decrease of PP and appearance of graphite on the surface. Hence, plasma etching of BPP should be an effective method of improvement of electrical conductivity of BPP.

7.2 Changes of the Mass

The mass of the samples was measured before and after plasma treatment to estimate the etching rate. Several measurements after the treatment allowed to notice the increase of mass during the first two minutes after extracting the sample from the plasma chamber. The mass changes of the treated samples over time are described in this chapter.

The chemical bonds of the surface atoms become uncompensated during the etching process, providing the possibility of the formation of new chemical bonds (oxidation, hydroxyl groups OH) when the sample is taken out of the chamber. Weakly bound carbon and water on the surface are removed in plasma, forming

volatile products, such as carbon dioxide, which are transported out of the chamber by the process gas, ultimately reducing the mass of the sample. The mass of the complete BPP was measured before, during and after the process. The results of mass change of the sample, etched in air plasma for 30 min at ambient pressure are shown in Fig. 7.10.

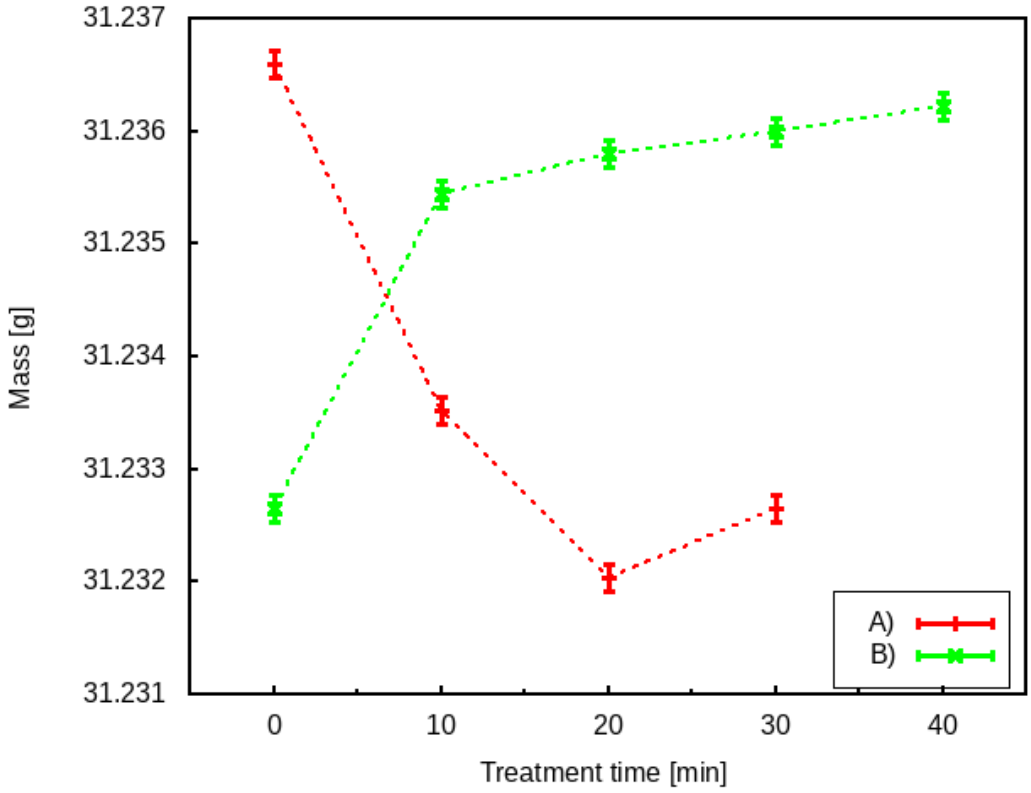

Figure 7.10: Mass change of a BPP, etched in air plasma for 30 min at ambient pressure (A) during the etching process, (B) after the etching process.

A slight mass increase in Fig. 7.10 (A) after 20 minutes of plasma treatment can be explained by chemical modification of the surface, i.e. appearance of polar hydrophilic groups on the surface, which takes place mainly between 15 - 20 minutes of plasma etching in oxygen-containing gases. For this reason, the modified surface actively absorbs molecular water from the environment as soon as the sample is extracted from the chamber. Since the main absorption takes place immediately, in the first minutes after the extraction of the sample from the

chamber (Fig. 7.10 (B)), the time of measuring the sample mass in the ambient conditions was enough to gain more mass via absorption than to loose during the next 10 minutes via plasma etching (Fig. 7.10 (A)).

The measurement of the mass of the samples directly after the plasma treatment shows that it noticeably decreases during the treatment, but increases very fast and almost reaches the initial value in approximately 2 - 3 minutes, as shown in Table 7.5 (error of the scales is 0.1 mg). Plasma etching of the surface leads to the formation of structures with reduced content of hydrogen. But as soon as the sample appears in ambient conditions, the molecules of water from the air diffuses into the graphite surface and the mass of the sample increases (Table 7.6) until some "saturation" value. The absorption takes place mainly during the first minutes when the sample is taken out of the chamber. After approximately 24 hours the mass does not change significantly.

Table 7.5: Mass change.

Sample	**Pressure** mbar	**Gas flow** slm	**Etching time** min	
1.1	960	17	5	
1.2	990	17	10	
1.3	990	17	15	
2.1	990	17	5	
3.2	990	2	3	
3.3	990	7	3	
4.1	10	0.5	3	
4.2	10	2	3	
4.3	10	7	3	
	Mass before and after etching			
	before g	**directly after** g	**2 min after** g	**24h after** g
1.1	4.6397	4.6377	4.6382	4.6387
1.2	4.4696	4.4657	4.4670	4.4675
1.3	4.5912	4.5879	4.5892	4.5899
2.1	3.5767	3.5734	3.5751	3.5756
3.2	4.2497	4.2476	4.2488	4.2492
3.3	4.3138	4.3057	4.3080	4.3099
4.1	5.2063	5.2024	5.2042	5.2048
4.2	5.2462	5.2138	5.2170	5.2194
4.3	4.9309	4.8505	4.8538	4.8617

The schematic view of the mass change during the etching process is shown in Fig. 7.11.

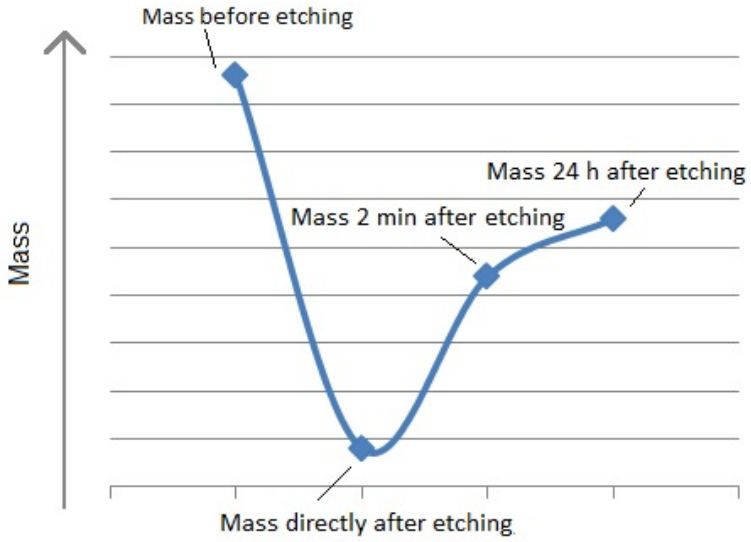

Figure 7.11: Schematic view of the mass change during the etching process.

Table 7.6: Etched mass in plasma and the increase of the sample mass in two minutes after etching.

Sample	**Etched mass** mg	**Mass increase** mg
1.1	2.0	0.5
1.2	3.9	1.3
1.3	3.3	1.3
2.1	3.3	1.7
3.2	2.1	1.2
3.3	8.1	2.3
4.1	3.9	1.8
4.2	32.4	3.2
4.3	80.4	3.3

7.3 Water Wettability

Water wettability of the surface usually depends on the liquid, material of the surface and the roughness of the surface. Change of the surface wettability shows that plasma treatment changes the roughness and leads to chemical modification of the surface (Fig. 7.12).

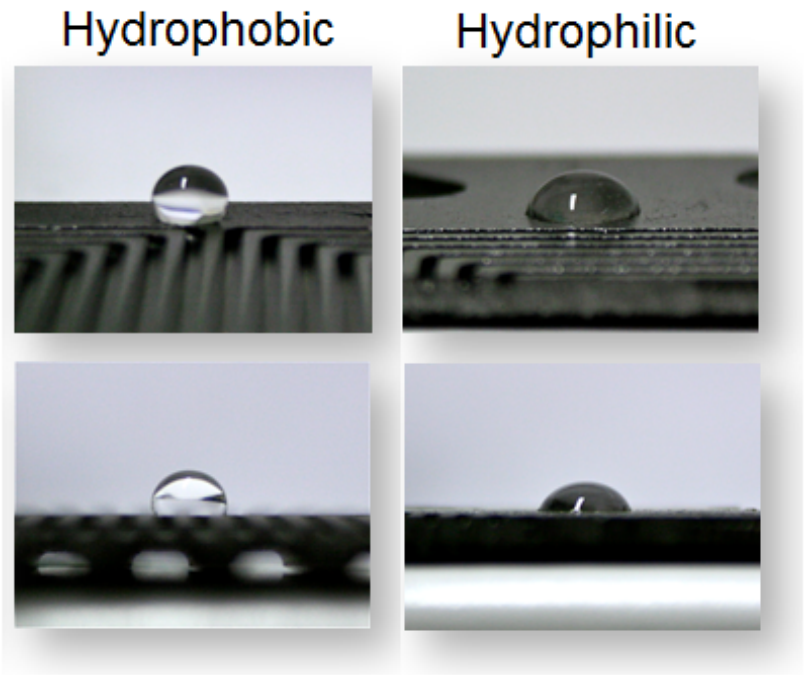

Figure 7.12: Hydrophobic (left) surface of BPP before plasma treatment and hydrophilic (right) after treatment.

The molecule of PP is composed of only carbon and hydrogen (not polar) atoms, it has pendant CH_3 groups, CH and CH_2 groups along its backbone (Fig. 4.1), therefore PP, unlike water, is nonpolar and hence hydrophobic. Thus the surface of untreated BPP is also hydrophobic.

The contact angle measurements were conducted using SURFTENS Universal measuring instrument from OEG with accuracy of $\pm 0.5°$, water droplet volume of about 10 μL. The wettability of the BPP changes already after 3 min of plasma treatment. The contact angle changes, depending on the duration of plasma

treatment, as it is shown in Fig. 7.13. For oxygen-containing gases it decreases and reaches the minimal values for treatment duration of around 20 min, indicating a good hydrophilicity of the surface (Fig 7.14 – for plasma treatment in CO_2). Further etching leads to the increase of contact angle again.

A decrease of the static water contact angle on the surface of carbon/PP BPP with increasing the duration of oxygen plasma treatment was also studied by M. Schade et al. in [170] and by J. H. S. Yang and K. Teii in [173], but the increase of the contact angle after a certain treatment time was not shown there. Probably because of softer treatment conditions (microwave power of 90 W and working gas pressure of 0.5 mbar instead of 3000 W and 5 mbar up to ambient pressure, regarded in this work) the treatment time of 45 min was not enough to reach this effect.

The authors in [170] have also reported that the improved wettability of the BPP surfaces depends on the duration of plasma treatment, but in any case this effect is not stable over time. However, the experimental investigations showed that the wettability does not significantly influence the electrical conductivity of BPP, i.e. worsening of the wettability does not mean worsening of the conductive properties of the surface, therefore the change of the wettability during the aging of plasma-treated samples in ambient air was not regarded in this work.

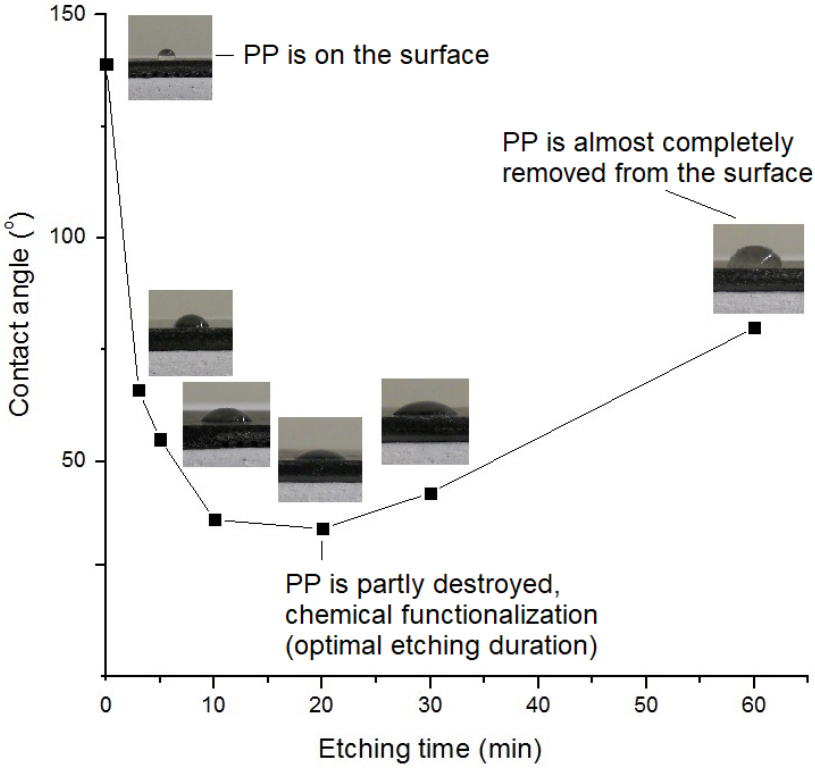

Figure 7.13: Contact angle dependence on etching duration in CO_2.

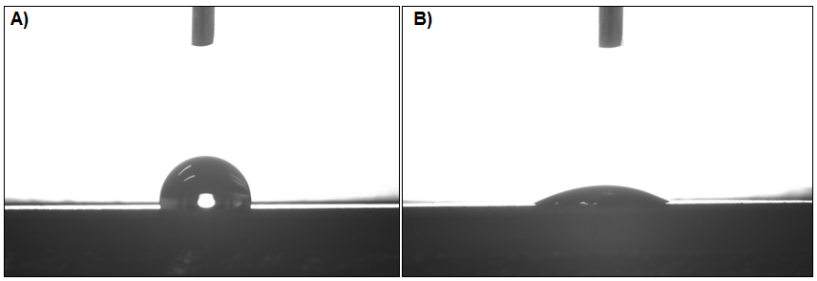

Figure 7.14: Water drop on the BPP surface A) before plasma treatment; B) after 20 min of CO_2 plasma etching.

Change in contact properties of the surface, including wettability of the surface, is one of the results of chemical modification of the surface. The improvement of the adhesion properties of polymers under the influence of plasma is related to surface cleaning, i.e. removal of different contaminations by plasma, and forma-

tion of hydrophilic groups of different chemical nature. Just breaking the bonds in PP in plasma would not lead to such an effect, because the broken bond cannot remain in the torn state. If there are no components, which can react with the radicals formed on the surface, then there will be polymer fragments remaining on the surface, which will be hydrophobic, like the original PP. Polar hydrophilic groups on the surface, for instance oxygen-containing groups, which appear during the etching in oxygen or air, provide the hydrophilicity of the surface. Nitrogen-containing groups (amino-, amido-, imino- and etc.) appear during the plasma etching in ammonia or its mixtures with hydrogen.

In this case, when the samples were etched in CO_2 plasma, the surface has been cleaned, because plasma etching contributes to the "molecular polishing" of the surface, and CO_2 interacted with hydrocarbon radicals with the formation of oxygen-containing groups. The known processes of carboxylation and carbonylation of organic compounds by carbon oxides took place leading to chemical functionalization of the surface and as a consequence – to the hydrophilicity of the surface.

This supposition is confirmed by the results of investigation of the wettability of the BPP treated in the noble gas – argon. The surface of the samples treated in argon plasma, independent of the treatment parameters, remained hydrophobic, with only minor decrease of the contact angle with the change of the treatment conditions to harsher ones: increase of treatment duration, working pressure and gas flow and decrease of the distance between the surface of the sample and the edge of the plasma ball. Most probably this minor change took place due to the formation of defects in PP on the surface. So, the chemical functionalization of the surface of BPP in oxygen-containing plasma makes the biggest contribution to the change of water wettability.

Taking into account the results of investigation by FTIR method, presented in Fig. 7.7 and Table 7.4, it can be concluded that the PP has been destroyed and partly removed from the surface along with the chemical functionalization of the surface. The increase of the contact angle for the samples, treated in plasma

longer than 20 minutes, can be explained by almost complete removal of PP and functional groups from the surface, what makes the surface more hydrophobic, compared to the surface treated for 20 minutes in plasma, but the surface does not become so hydrophobic as before any plasma treatment.

Varying the experimental parameters it was found that the increase of the distance between the sample and the plasma leads to the shift of the line in Fig. 7.13 to the right, what means the same results are achieved by longer duration of the plasma treatment. The distance increase up to 4 cm means that the best wettability (the minimal contact angle) would be achieved after 30 minutes of plasma treatment. Further increase of the distance does not lead to the required electrical conductivity, therefore it was not considered.

Summarizing the previous conclusions, plasma treatment causes the destruction of macromolecules with rupture of the bonds, removal of hydrogen and formation of unsaturated bonds, and carbonization of the layer.

7.4 Raman Investigation of the Surface

It was surprising and unexpected that plasma treatment also changes the structure of graphite on the surface of BPP. This will be demonstrated by Raman spectroscopy in this chapter. Therefore, Raman technique turned out to be as important as FTIR for this research.

To confirm and refine the results obtained using green diode laser (532 nm) additionally red diode laser was used (633 nm), because the crosssection for excitation depends on the wavelengt used. Thus, some specialties of Raman spectra, like for example the peak at 1620 cm^{-1} merged with G peak, which appears due to the presence of sp^2 bonds, are better defined using red laser.

Since oxygen-containing gases provide the most efficient plasma treatment, Raman spectra of BPP treated by oxygen, air, carbon dioxide and the spectra of untreated BPP are compared.

Microscope images showed the inhomogeneity of the surface, therefore Raman spectra were obtained in different spots of the surface. This was done for the surfaces of BPP untreated and treated by oxygen-containing gases (oxygen, air and carbon dioxide) with a view to compare their Raman spectra and to define whether the deeper areas and spots of the inhomogeneous surface are exposed to plasma treatment or not.

Raman spectra reaffirm the influence of treatment duration and gas flow on the resulting electrical conductivity. Raman spectroscopy allows to find out that plasma treatment at atmospheric pressure can be very effective if the gas flow value is high enough.

Spectra of foils of different composition show that the composition of a sample, namely the amount of PP in the composition, has a meaningful impact on the change of graphite structure during the plasma treatment.

7.4.1 Raman Investigation of Plasma Influence On Surface Structure and Electrical Conductivity of BPP

Renishaw inVia Confocal Raman Microscope and Spectrometer was used for this research. The microscope focuses a laser source onto specific areas of a sample then collects the light scattered off the surface of the sample and directs it through a Raman spectrometer. This Raman device is using 532 nm (green) diode laser with 1800 lines/mm grating as a standard set-up [174]. The laser is the instrument for excitation of the oscillations of atoms and groups of atoms. The change of the energy of the laser photons can lead to a shift of the spectral range and to intensity changes of some peaks. In this research the spectra of the samples were additionally obtained using 633 nm (red) diode laser. This will be explained in detail in Chapter 7.4.2.

Besides this the device allows to set the grating to 2400 lines/mm to obtain more precise spectra in a smaller range of wavenumbers. But in the present

research the standard grating of 1800 lines/mm was used for all the samples, because the peaks, which are interesting for this research: D, G and 2D peaks of carbon, are situated in a wider range than the grating of 2400 lines/mm allows to obtain.

Raman spectra were obtained for BPP and foils of different composition untreated and treated in atmospheric air, CO_2 and O_2 plasma. Raman spectrum of the untreated BPP (Fig. 7.15) has peaks typical for carbon materials: D peak at 1332 cm^{-1}, G peak at 1591 cm^{-1} and 2D peak at 2674 cm^{-1}. The position of the D peak at 1332 cm^{-1} shows the presence of tetrahedrally coordinated carbon in graphite.

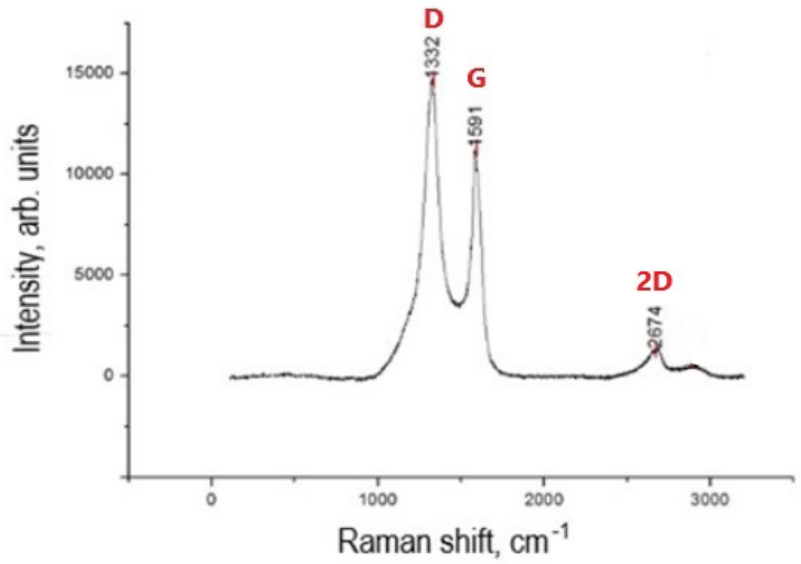

Figure 7.15: Raman spectrum of an untreated BPP.

Raman spectrum of PP used for production of BPP (Adstif HA840R, Basell Ultra Polymers) in Fig. 7.16 looks similar to the FTIR spectrum of a PP film (Fig. 7.5). Regularity bands of PP are well definable in the range of 800-1300 cm^{-1}. In the range of 1300-1500 cm^{-1}, where bending vibrations of $C-H$ bonds in functional groups CH_3 and CH_2 appear, the peak at 1332 cm^{-1} (D peak

in carbon materials) is also definable. There is also a peak at 2650-2725 cm^{-1} (where in carbon materials 2D peak would be situated), but no peaks at the frequencies of G peaks in carbon materials. A wide band at the range of 2600-3000 cm^{-1} refers to hydroxyl groups, bonds with heteroatoms or some macromolecules in oxidized state.

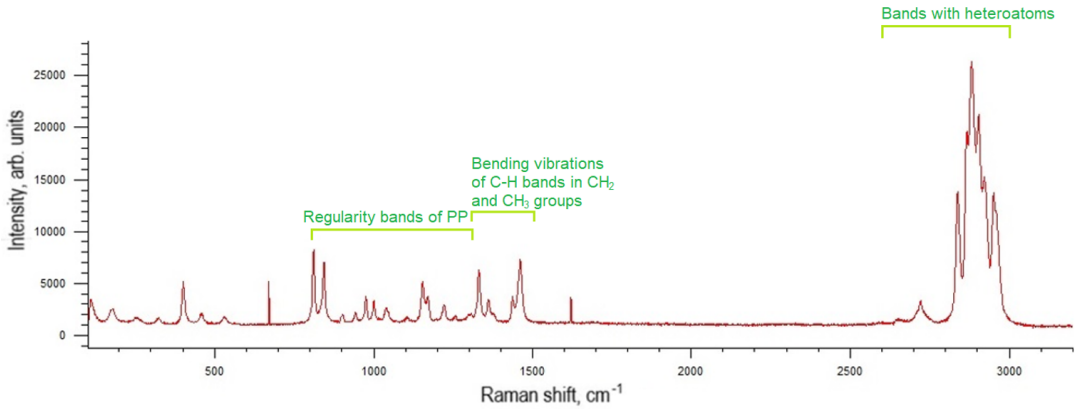

Figure 7.16: Raman spectrum of PP.

Comparing the spectra of the samples treated by different oxygen-containing gases (Fig. 7.17 (B), (C), (D)) with the spectrum of the untreated sample (Fig. 7.17 (A)), it is easy to notice the changes after the plasma treatment, which are common for plasma treatment by different gases. These changes are: the shift of the G peak to the smaller values of wavenumbers, the change of the intensity ratio of D and G peaks and the intensity increase of the 2D peak of carbon. Such changes indicate the removal of the PP from the surface of the samples as expected, but even the etching of nanocrystalline carbon from the surface since the Raman spectra are indicating bigger crystals after the plasma treatment [8].

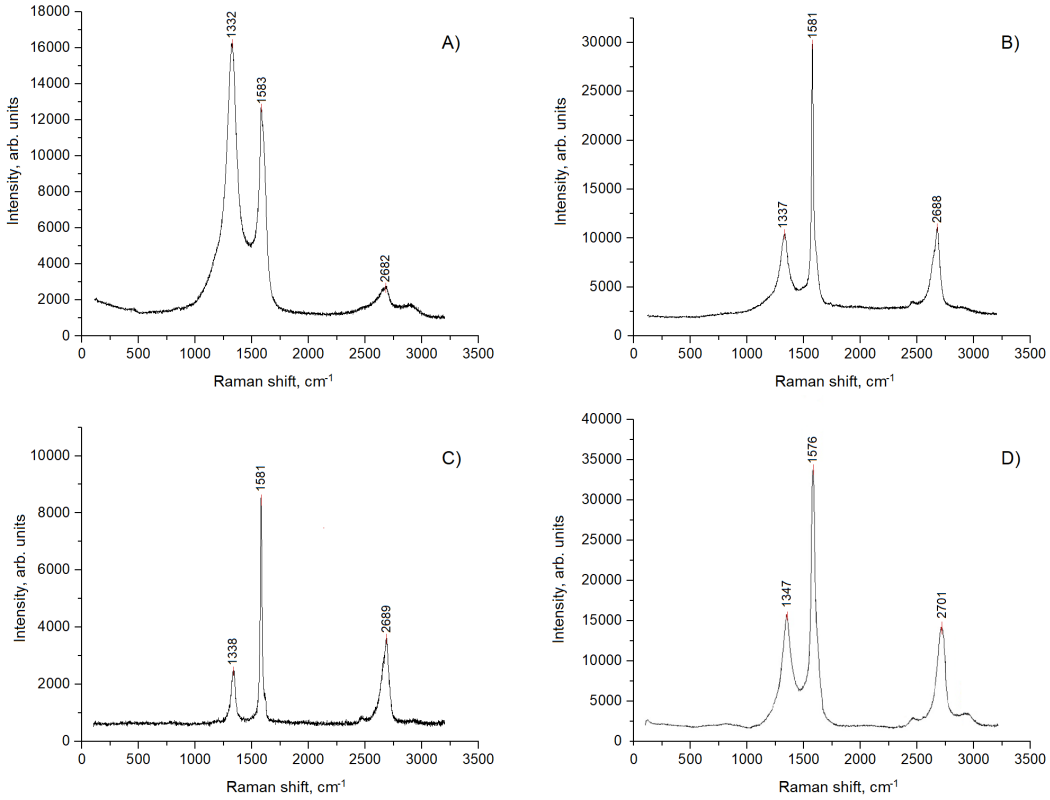

Figure 7.17: Raman spectra of: A) the untreated sample; B) the sample, etched by CO_2 for 20 min; C) the sample, etched by air for 20 min; D) the sample, etched by O_2 for 7 min.

The spectra of the samples treated in plasma show a noticeable shift of the G peaks to the smaller values of the wavenumbers: from 1591 cm^{-1} to 1576 cm^{-1} and 1584 cm^{-1} (Fig. 7.17). Zolkin A. S. and Yurkovskaya E. S. report in [41] about the shift of the G peak in Raman spectra of carbon films to 1600 cm^{-1}. This shift indicates the crushing of graphite monocrystals to micro- and nanocrystals. This shift of the G peak is also described in [175] and mentioned in [176]. Thereby the shift of the G peaks in the spectra of the treated samples in Fig. 7.17 can indicate the change of the structure of graphite on the surface: the increase of the crystals size. This assumption is also confirmed by analyzing the changes of the intensity of the D peak with respect to the intensity of the G peak.

Another change in Raman spectra after plasma treatment visible in Fig. 7.17

is a significant decrease of the intensity of D peak comparing to the intensity of G peak. Such change indicates the increase of the crystals size [41] on the surface of the treated samples and the decrease of the amount of defects. This conclusion is also confirmed by the diagram in Fig. 7.18 adapted from the works of J. Robertson [43] and A. Ferrari [48]. Fig. 7.18 shows how the graphite on the surface of the samples, treated for 20 minutes in CO_2 plasma, changes the structure from partly nanocrystalline to polycrystalline.

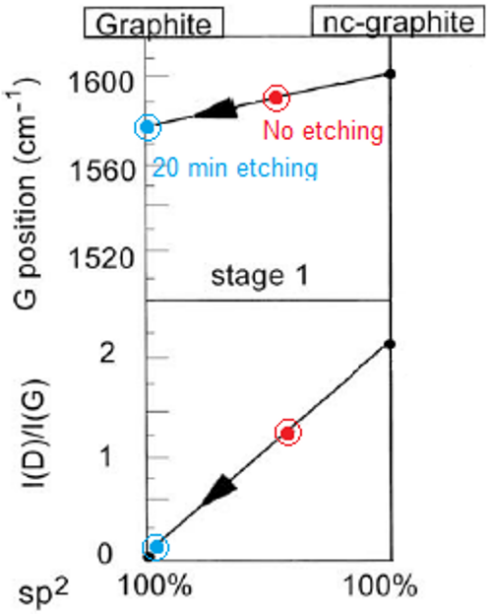

Figure 7.18: Structural change of the graphite on the surface after CO_2 plasma treatment for 20 minutes (adapted from References [43] and [48]).

Fig. 7.19 explains and completes the diagram in Fig. 7.18 for the particular example of CO_2 as a working gas for plasma etching.

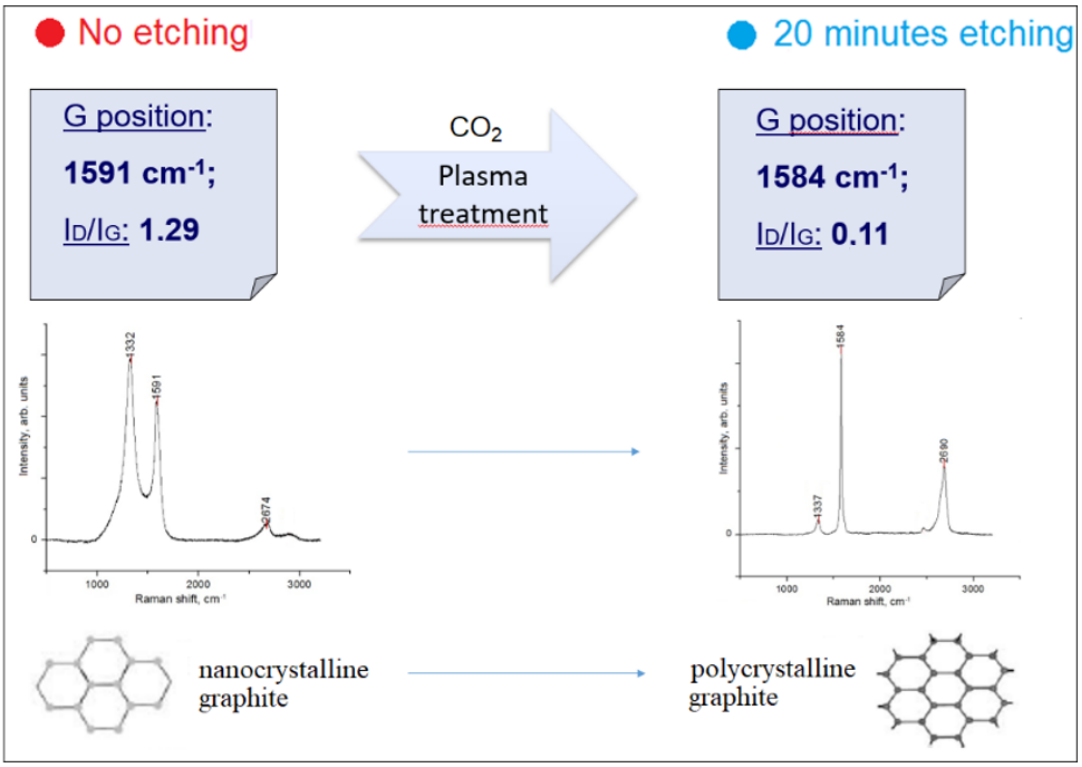

Figure 7.19: Schematic view of the changes of Raman spectrum and graphite structure on the surface of a BPP after CO_2 plasma treatment for 20 minutes .

Graphite has e-type electrical conductivity. Electron scattering takes place on thermal vibrations and on defects. Since the crystalline structure of graphite changes and the close packing does not change, the electrical conductivity of the samples increases together with the increase of the crystals size. It is so because the bigger the crystals, the fewer interfaces are there between them, and, consequently, the fewer interfaces are there between the crystals, the less is the scattering of electrons, hence the conductivity of the etched samples with polycrystalline structure is better than the conductivity of the untreated samples [8].

7.4.2 Influence of the Experimental Parameters On Raman Spectra

As it was mentioned above (in Chapter 7.4.1), the lasers with the wavelengths of 532 nm (green) and 633 nm (red) of the Raman spectrometer were used for this investigation. Fig. 7.20 shows some differences in Raman spectra, obtained with the use of different (red and green) lasers. These are the spectra of a foil with 29 wt% of PP in its composition.

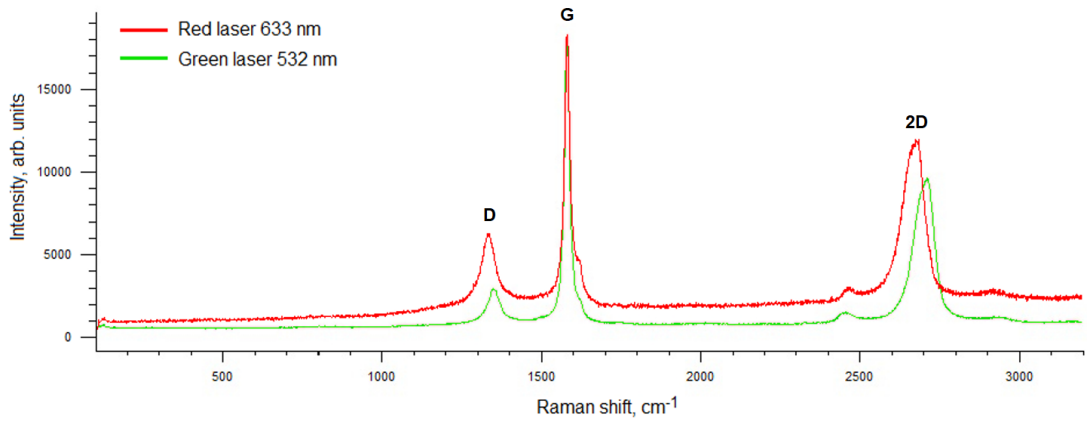

Figure 7.20: Comparison of Raman spectra of a foil, obtained with red and green laser of the Raman spectrometer.

It is easy to see in Fig. 7.20 that with the increase of the incident radiation wavelength (the red laser compared to the green one) the D peak and the 2D peak become more intense and they both shift to the smaller wavenumber values, while the G peak does not change its intensity and position at all. Moreover, a distinctly noticeable shoulder appears near the G peak at around 1620 cm^{-1}. Since both spectra were obtained for the same untreated sample, the graphite matrix, the structure, the packing of atoms and the crystals size remain unchanged, therefore the G peak does not shift and does not change the intensity. The shift of the D peak, as well as the shift of the 2D peak, can be explained by the change in the energy of the excitation quantum $\hbar\omega_{exc}$ [176, 177]. According to [176], for the same reason the small additional band at 1620 cm^{-1} appears next to the G peak, which does not change (Fig. 7.20 and Fig. 7.21). J.

Robertson in [43] mentions the olefinic origin of the peak at 1620 cm^{-1}. Usually this peak is more intensive and merged with the G peak, noticeably changing its contour, in the spectra, obtained with the red laser (Fig. 7.20). It is also present in the spectra obtained with the green laser, but less intensive; it is absent or merged with the G peak in the spectra of the foils (Fig. 7.20) and it has a sharp peak at 1620 cm^{-1}, noticeably separated from the G line, for the BPP treated in air plasma (Fig. 7.22). At that the more effective the air plasma treatment is, the more distinctively this peak separates from the G peak (Fig. 7.23), (even though its intensity remains relatively small), what indicates the presence of sp^2 bonds on the treated surface. Conductive graphite has a sp^2-hybridized crystal structure [178], what may be another evidence of the improved electrical conductivity of the BPP treated in plasma. However, as it was already mentioned, such a dependence of the shape of the peak at 1620 cm^{-1} on the plasma treatment influence on the surface was established only for air-etched BPP. For the BPP and foils treated with other gases this dependence was not observed.

Bi-Gaussian fitting of the Raman spectrum obtained with red laser from Fig. 7.20 is shown in Fig. 7.21.

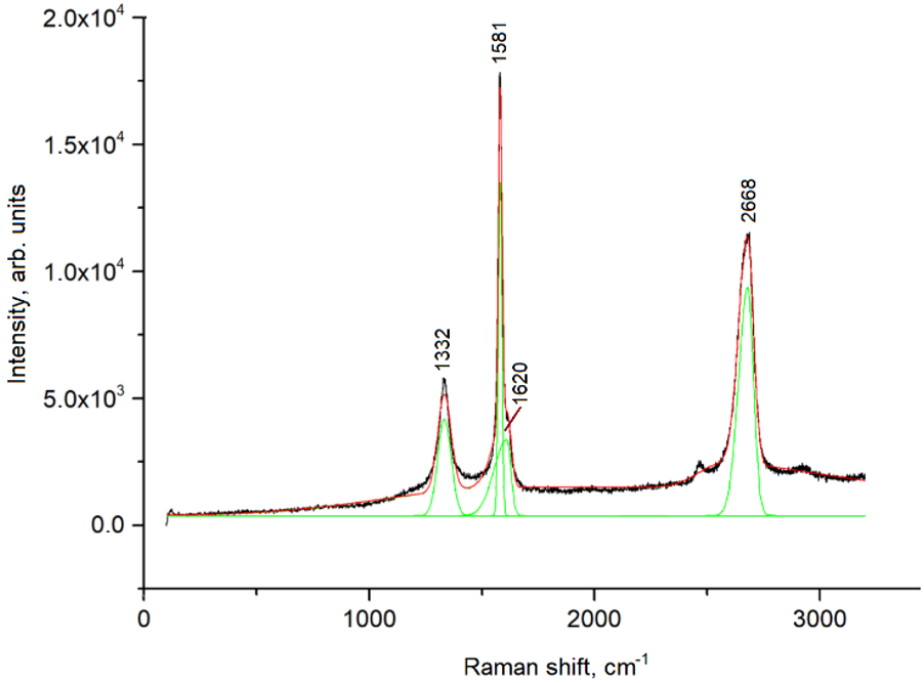

Figure 7.21: Bi-Gaussian fitting of the Raman spectrum of the foil, obtained with red laser.

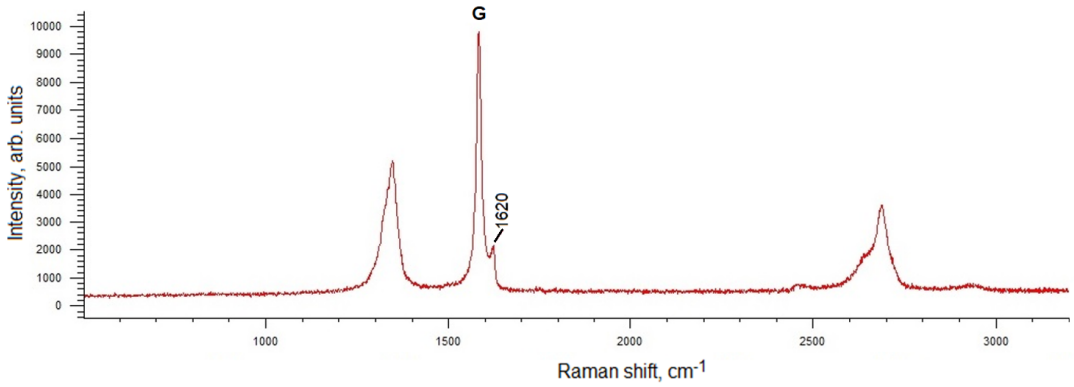

Figure 7.22: Raman spectrum of the BPP, 20 min treated in air plasma at the pressure of 0.019 mbar.

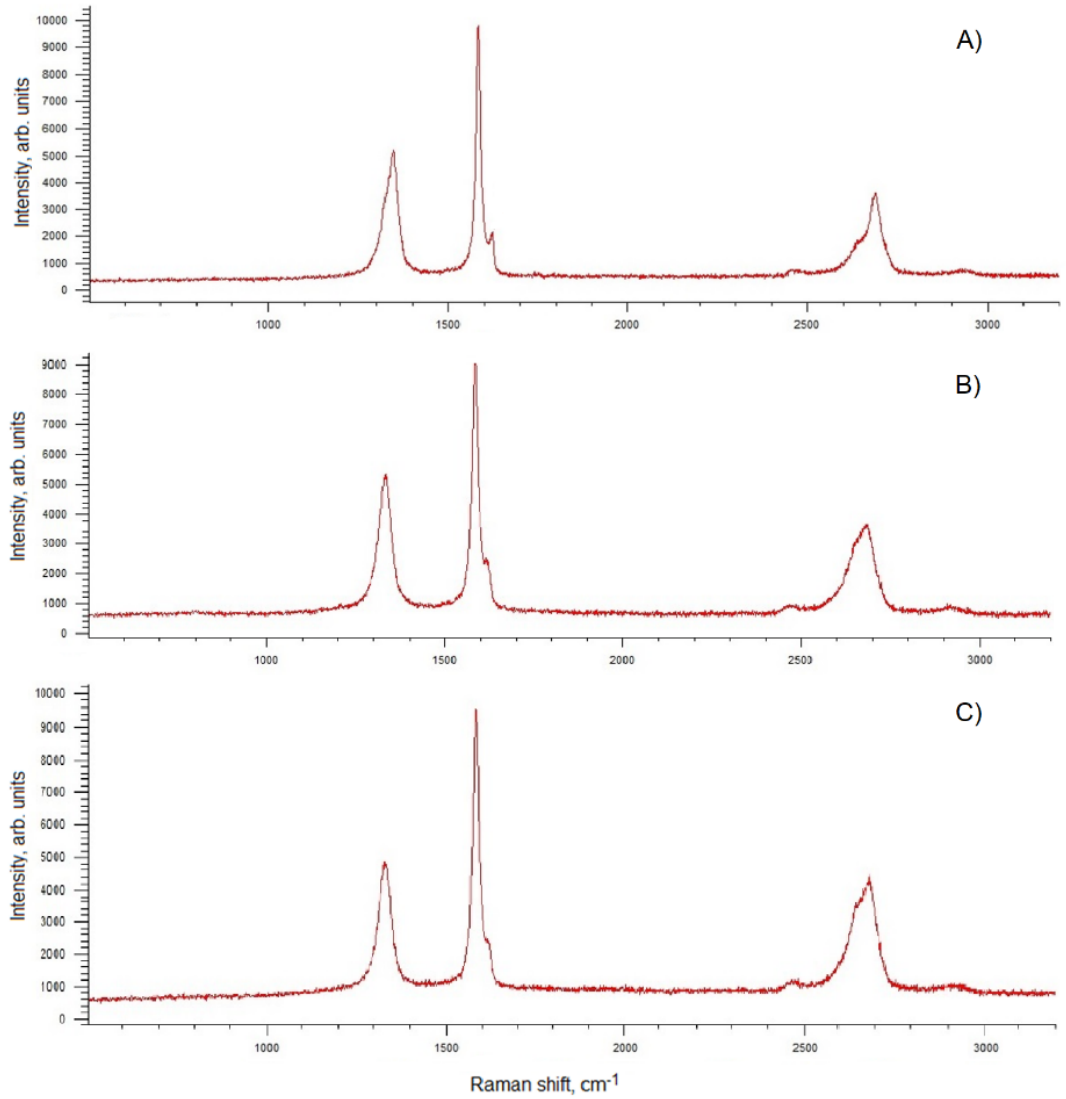

Figure 7.23: Raman spectra of the BPP, 20 min treated in air plasma at the pressure of: A) $1.9{\cdot}10^{-2}$ mbar; B) 30 mbar; C) 60 mbar.

Unsaturated $C=$ bonds absorb at 1600 cm^{-1}. Mono-olefins (containing one $C=C$ bond) have a characteristic band in the region of 1640-1675 cm^{-1} [179]. The conjugation of two $C=C$ bonds can lead to the appearance of two absorption bands in the region of 1560-1650 cm^{-1} region.

Comparing the Raman spectra of the foil (29 wt% PP) treated in air plasma

for 7 min at the pressure of 0.19 mbar and the distance between the sample and the plasma chamber of 6 cm, obtained with red and green lasers, one can notice the same differences, which are observable for the untreated sample: the shift of the D and 2D peaks to smaller wavenumber values, while the G does not change its position and intensity, and the higher severity of the peak at 1620 cm^{-1} in the spectrum, obtained with the red laser (Fig. 7.24). The only difference is that in case of the treated sample (Fig. 7.24) the peaks D and 2D almost do not change their intensity, unlike in case of the same sample before plasma treatment (Fig. 7.20), where these peaks look more intense in the spectrum, obtained by the red laser.

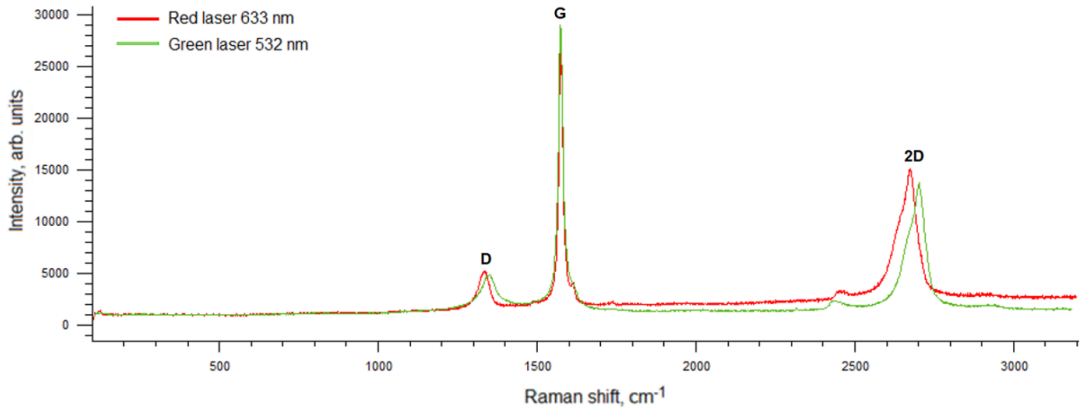

Figure 7.24: Comparison of Raman spectra of the foil treated in air plasma, obtained with red and green laser of the Raman spectrometer.

Fig. 7.25 shows the Raman spectrum of another foil (35 wt% of PP) 20 minutes treated in air plasma at the pressure of 0.13 mbar and the distance between the sample and the plasma chamber of 4 cm, obtained with green laser. Visually it is not different from the spectrum of the sample treated in air plasma for shorter time and at bigger distance in Fig. 7.24, but the intensity ratio I(D)/I(G), presented in the Table 7.7, shows the difference between these spectra.

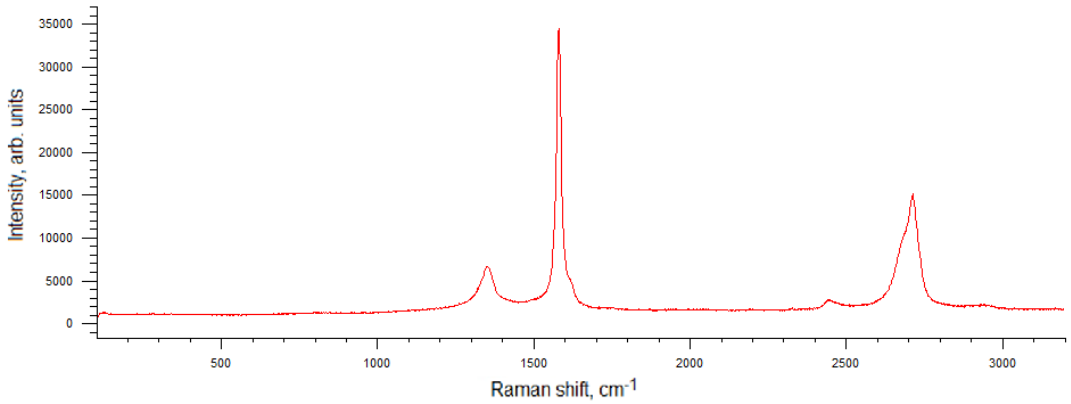

Figure 7.25: Raman spectrum of the foil, 20 min treated in air plasma.

Table 7.7: Raman spectrum of the foil, 20 min treated in air plasma with Pressure **P**, Treatment duration **t** and Distance between the sample and the chamber **L**. Foil 1 is the untreated reference.

Foil	**Amount of PP** wt%	**Gas** mabr	**P** min	**t** cm	**L**	**I(D)/I(G)**
1	29	-	-	-	-	1.07
2	29	Air	0.19	7	6	0.15
3	35	Air	0.13	20	4	0.19

Longer treatment duration of foil 3 compared to foil 2 and a shorter distance to the plasma should have led to a smaller value of I(D)/I(G), because the graphitic surface should be more intensively cleared from the PP. On the other hand, the amount of PP is higher in the composition of foil 3 than in the composition of foil 2. The result of the comparison of the I(D)/I(G) ratios in the Table 7.7 shows that the I(D)/I(G) ratio of foil 3, which was treated longer and at shorter distance to the plasma chamber but has more PP in its composition, is higher than the I(D)/I(G) ratio of foil 2. This result can also be explained considering the experimentally established fact that generally foils need "softer" conditions of plasma etching: bigger distance and shorter treatment duration than BPP to reach the necessary electrical properties. At the treatment parameters which were chosen for foil 3, the plasma has partly removed PP from the surface, but

also started to etch and destroy the graphitic surface, what lead to the increase of disorder and amount of defects on the sample surface, and consequently to the increase of the D peak intensity compared to the intensity of the G peak.

Renishaw inVia Confocal Raman Microscope, which was used for this research, allows to make scans of the surface and chose the point, which should be scanned for the spectrum. The pictures of the surfaces of a BPP and a foil before and after a successful air plasma treatment are presented in Fig. 7.26. It is easy to see that even the surfaces of the plasma-etched samples (Fig. 7.26 (B), (D)) are inhomogeneous, therefore the view of the Raman spectra can depend on the point, where the spectrum was taken. Higher spots of the surface look brighter in Fig. 7.26.

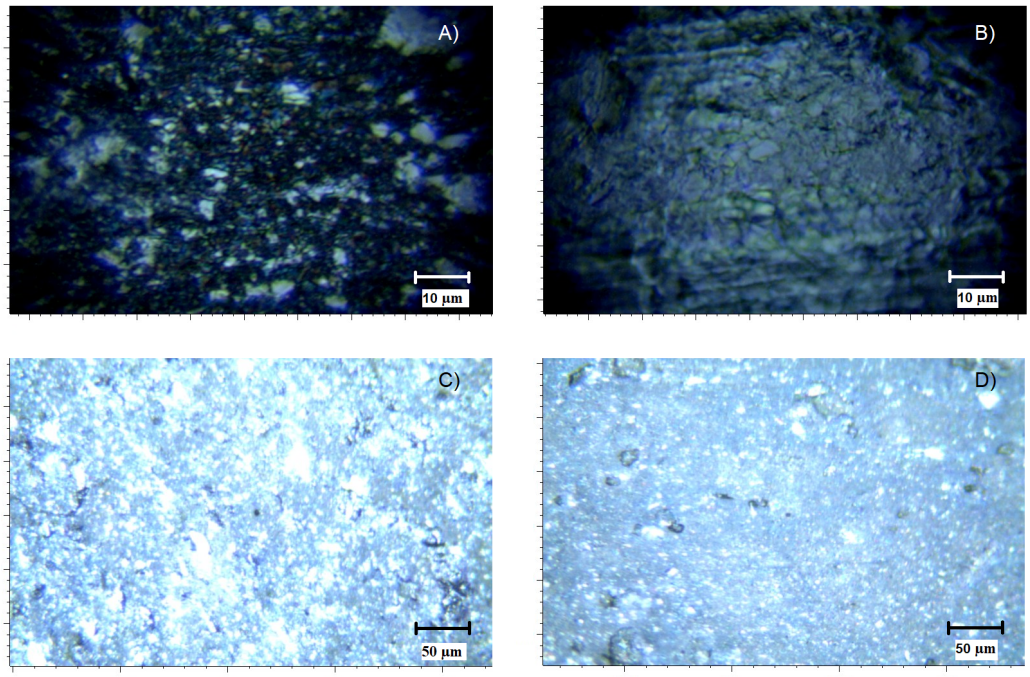

Figure 7.26: Raman microscope pictures of the surface of: A) a BPP before plasma treatment; B) the BPP after air plasma treatment; C) a foil before plasma treatment; D) the foil after air plasma treatment.

Spectra of BPP strongly depend on the spot of the surface (“low“ (dark) or

"high" (bright)), where they are taken. Fig. 7.27 (A) shows the view of the surface of a BPP, 20 minutes treated in air plasma at the pressure of $1.9 \cdot 10^{-2}$ mbar and at the distance from the plasma chamber of 4 cm; and two spots (dark and bright) on the surface where the spectra were taken. The Raman spectra, corresponding to these spots, are shown in Fig. 7.27 (B). The spectrum, which was taken in the dark spot of the surface looks rather like the spectrum of an untreated sample (Fig. 7.17 (A)) and even visually differs a lot from the spectrum of the bright spot, what allows to make a conclusion that the roughness of the BPP is too high for homogeneous surface etching with the method used and the conditions of plasma treatment.

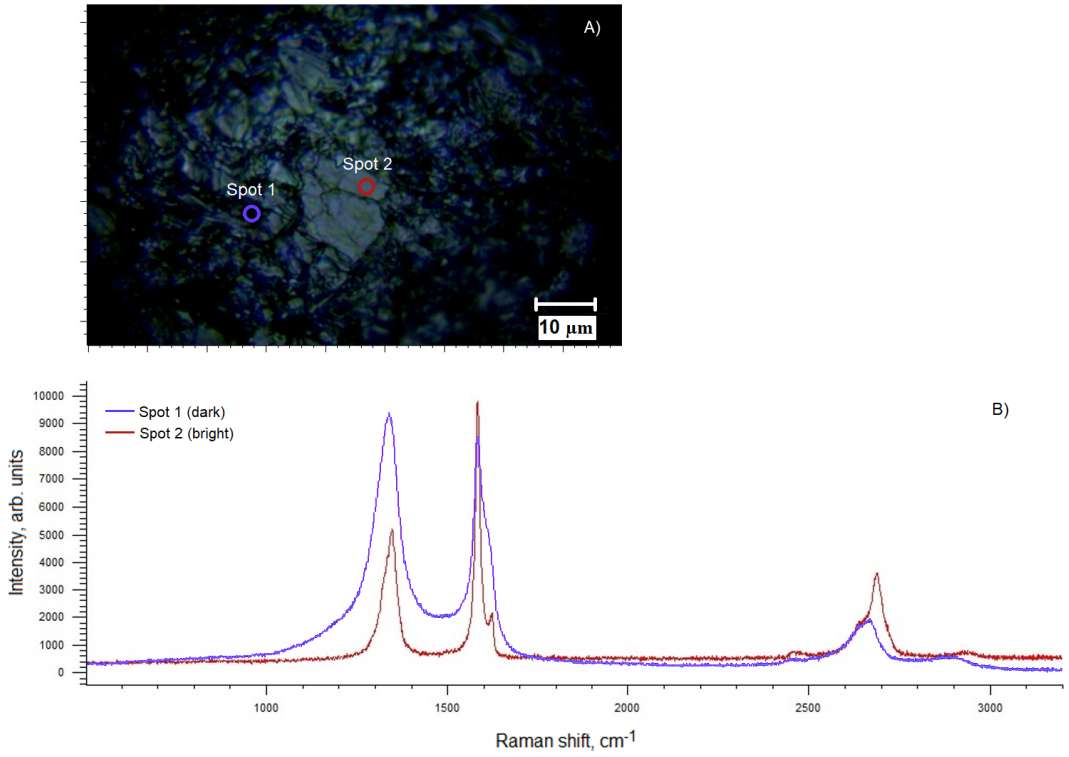

Figure 7.27: A) View of the surface of a BPP treated in air plasma; B) Raman spectra taken in two different spots of the surface.

The thickness and the roughness of the surface of BPP is much higher than those of foils. Therefore, it is not difficult to find the experimental parameters,

by which the surface of a foil would be evenly etched. The view of the plasma-treated surface and the comparison of the Raman spectra, taken in two different spots, of a foil (33 wt% of PP), 20 minutes treated in oxygen plasma at the pressure of 8.2 mbar and at the distance from the plasma chamber of 4 cm, are shown in Fig. 7.28.

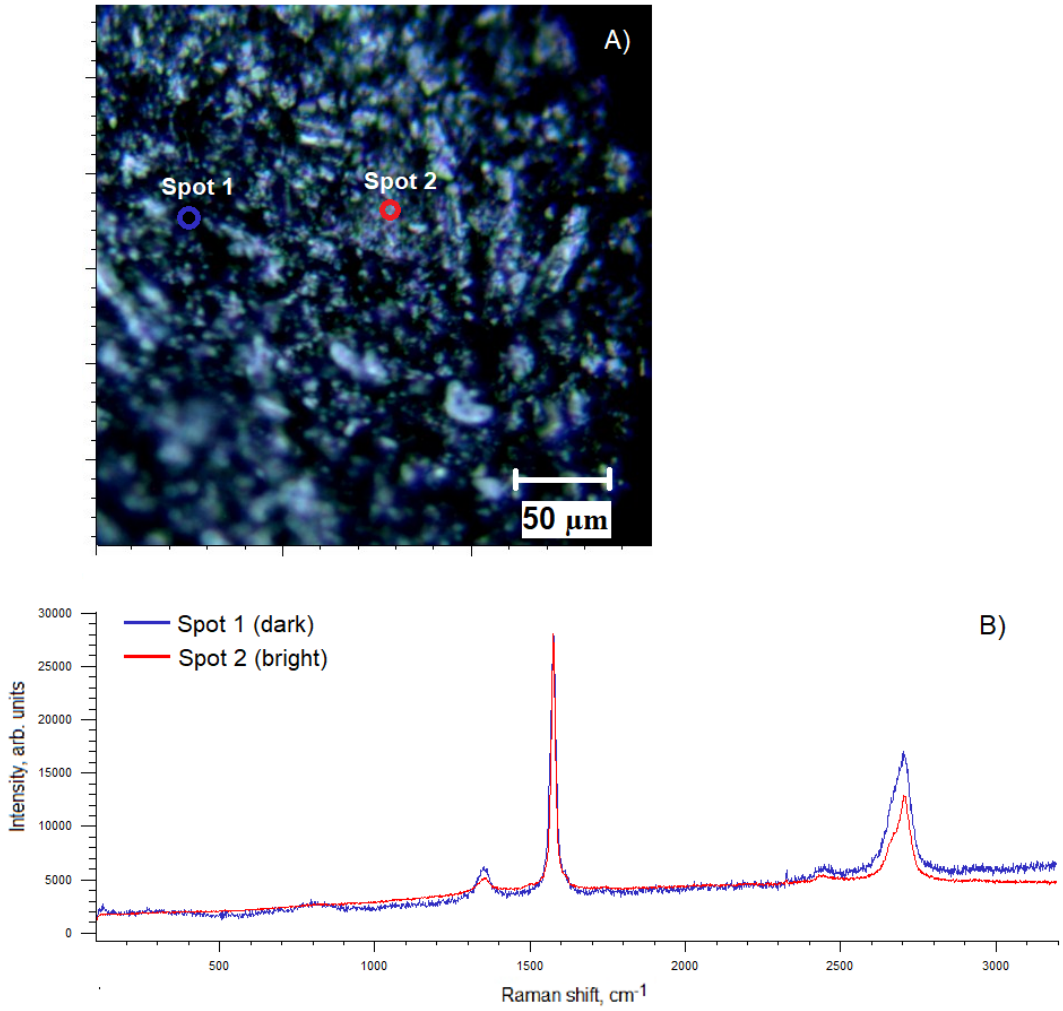

Figure 7.28: A) View of the surface of a foil 20 min treated in oxygen plasma; B) Raman spectra taken in two different spots of the surface.

Using oxygen as a working gas allows to shorten the time of plasma treatment, to increase the distance between the sample and the plasma chamber (to avoid

the possibility of combustion of the sample) and to achieve the required surface conductivity values not damaging the surface. Fig. 7.29 shows the spectra taken in a dark spot and in a bright spot of a foil treated in oxygen plasma for 7 min at the distance of 6 cm from the chamber. These experimental parameters do not allow to etch the surface of the foil evenly in all the structure spots, but at these parameters the surface is treated well enough to meet the required properties.

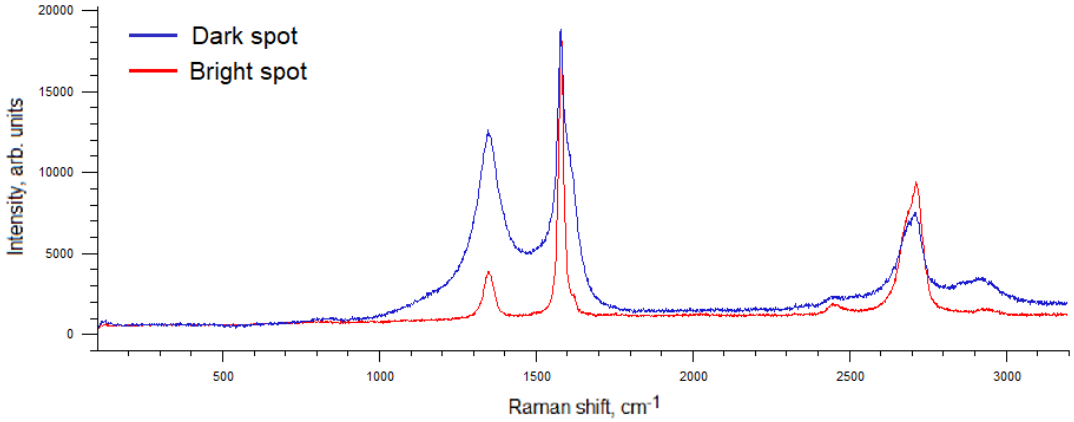

Figure 7.29: Raman spectra of a foil treated 7 min in oxygen plasma, taken in two different spots of the surface.

Fig. 7.30 shows the spectra of two BPP treated in carbon dioxide (Fig. 7.30 (A)) and in air plasma (Fig. 7.30 (B)) for 20 min. The value of $I(D)/I(G)$ of the sample treated in CO_2 ($I(D)/I(G)_{CO_2}$=0.1197) is lower than this of the sample treated in air ($I(D)/I(G)_{Air}$=0.3519). Both values show a significant decrease comparing to the $I(D)/I(G)$ value of an untreated sample ($I(D)/I(G)_{Untreated}$=1.2617). However, air is the preferred gas for plasma treatment application, because of its availability and the possibility to conduct the experiments much faster and cheaper than using other gases.

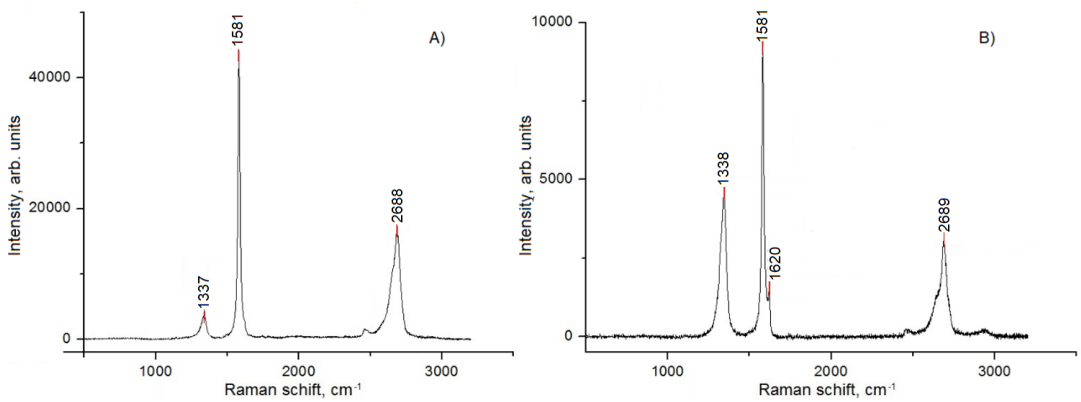

Figure 7.30: Raman spectra of BPP 20 min treated in: A) CO_2; B) air.

The change of the intensity ratio I(D)/I(G) value with the increase of the treatment duration (3 to 30 minutes) for BPP treated in CO_2 (8 mbar; 4 cm; 3.85 slm, 3 kW) is presented in Fig. 7.31. The I(D)/I(G) value increases when the sample is treated for longer than 20 minutes. The dependence of the G peak shift on the treatment duration was not observed, but for all the treated BPP the shift of the G peak to the smaller values of wavenumbers took place, as it is presented in Table 7.8.

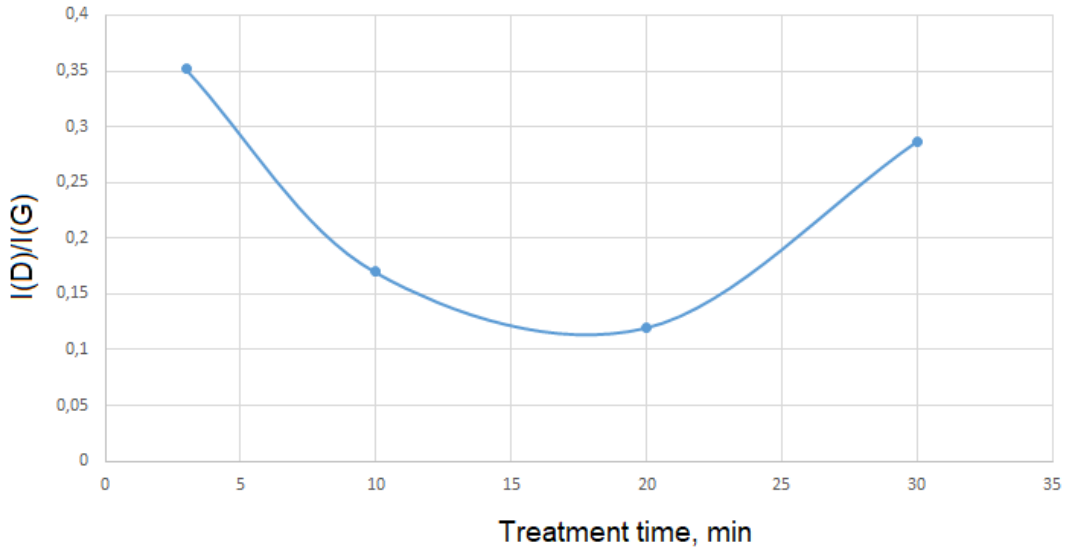

Figure 7.31: Dependence of the I(D)/I(G) ratio value on treatment duration for BPP treated in CO_2.

Numerical data for the dependence of the I(D)/I(G) ratio on treatment duration for BPP, treated in CO_2 plasma, are presented in Table 7.8.

Table 7.8: Numerical data for the dependence of the I(D)/I(G) ratio and the positions of the peaks D and G on the treatment duration for BPP, treated in CO_2 plasma.

Sample	**Duration** min	**G peak** cm^{-1}	**D peak** cm^{-1}	**I(D)/I(G)**
Untreated BPP	0	1583	1332	1.26
1	3	1576	1332	0.35
2	10	1571	1327	0.17
3	20	1581	1337	0.12
4	30	1576	1353	0.29

Raman spectra of the samples treated in a very large pressure range (from 10^{-2} mbar up to atmospheric pressure) show the chande of the I(D)/I(G) ratio values with the decrease of the working pressure, as it is shown in Fig. 7.32.

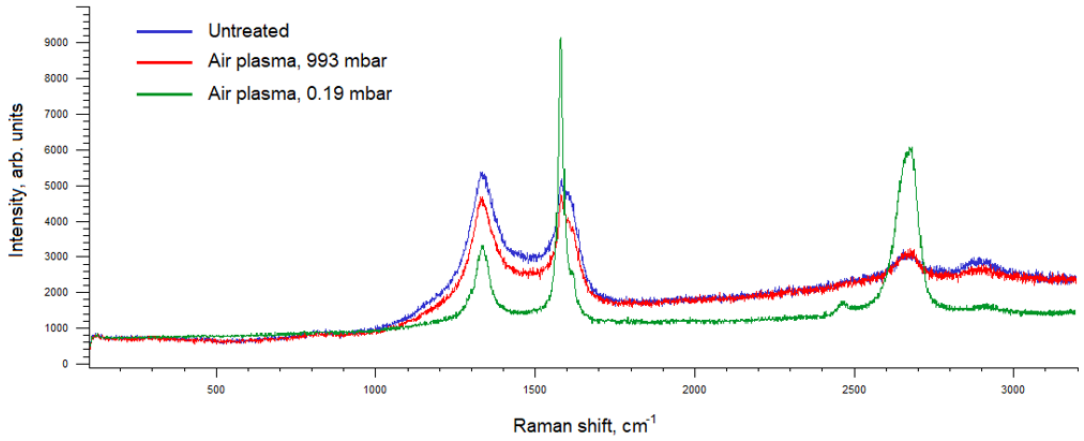

Figure 7.32: Comparison of Raman spectra of the untreated and the treated at different pressures foil.

The Raman spectra of foils (29 wt% of PP), obtained with red laser, in Fig. 7.32 illustrate the higher efficiency of 7 minutes long plasma treatment by air at low pressure (0.19 mbar), comparing to ambient pressure, when all the other experimental parameters remain the same. The intensity ratios I(D)/I(G) and the positions of the G peak of the spectra in Fig. 7.32 are presented in Table 7.9.

Table 7.9: I(D)/I(G) ratio and G peak position from the Raman spectra of the untreated and the treated at different pressures foils.

Plasma treatment	**Pressure** mbar	**G peak** cm^{-1}	**I(D)/I(G)**
Untreated foil	-	1583	1.07
Air plasma	933	1581	1.04
Air plasma	0.19	1579	0.15

The data presented in Table 7.8 and Table 7.9 generally confirm the assumption about the dependence of the result of plasma treatment on the treatment duration and on the gas pressure during the treatment and correspond to the results in Chapter 9. Another important experimental parameter, which influences the efficiency of plasma treatment is gas flow. Fig. 7.33 shows how the Raman spectrum changes when the gas flow changes. These are the spectra of the foils

(29 wt% PP) 3 minutes treated in air plasma with the pressure of 10 mbar at the distance from the chamber of 6 cm.

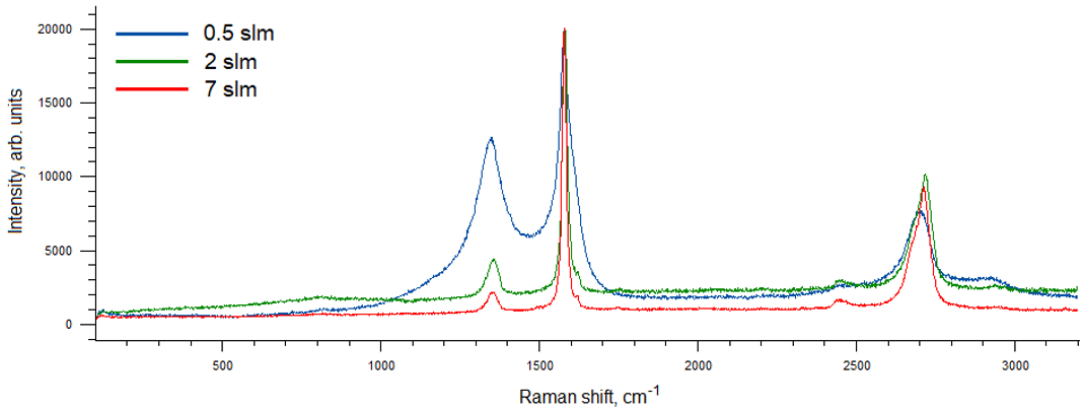

Figure 7.33: Raman spectra of a foil treated in air plasma at different gas flows.

The Raman spectra in Fig. 7.33 show that the increase of the gas flow results into more efficient plasma treatment, what is also mentioned in Chapter 7.2 (Table 7.5).

7.4.3 Influence of the Foil Composition on Raman Spectra

Foils consist of graphite, PP and carbon black in different percentages. The result of plasma treatment strongly depends on the composition of the foil. Therefore, certain experimental parameters must be selected for each foil composition. The exact compositions cannot be presented because of data protection, in this connection only the percentage by mass of PP of the researched foils are shown in Table 7.10.

Table 7.10: Amount of PP in the composition of the researched foils.

Foil	**PP** wt%
F1	35
F2	33
F3	31
F4	29

Raman spectra of the untreated foils, described in Table 7.11, are presented in Fig. 7.34.

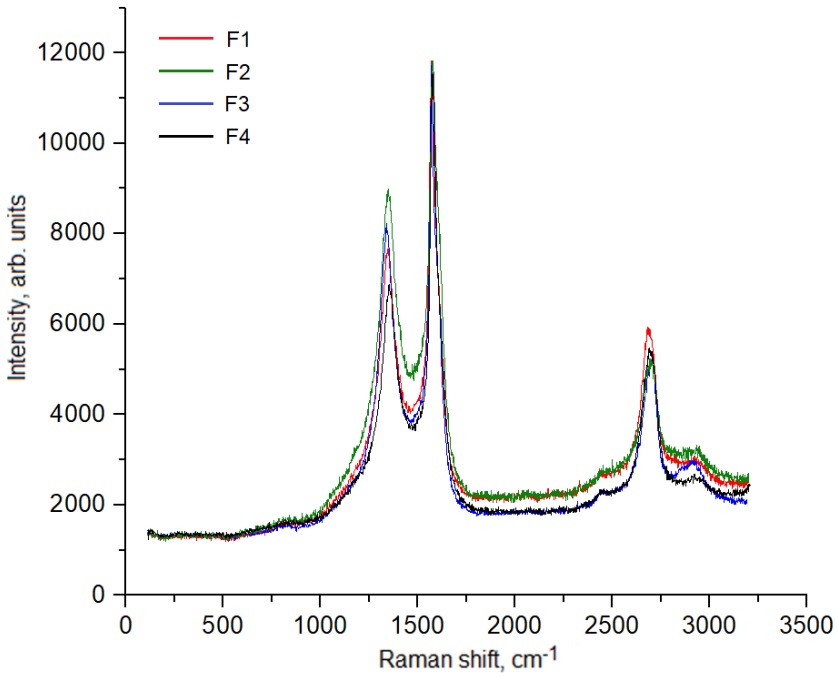

Figure 7.34: Raman spectra of the untreated foils.

Four Raman spectra, obtained with green laser, of the foils with different compositions and treated in plasma at different parameters are presented in Fig. 7.35. The data in Table 7.11 show that the I(D)/I(G) ratio of foil F4 (see Table 7.10) with the smallest amount of PP in its composition (29 wt%) in Fig. 7.35 (A) has the value 0.1548 and it is the smallest value for the spectra presented in Fig. 7.35, in spite of a shorter treatment duration, compared to the sample F1 (35 wt% of PP). Thus, the composition of a sample has a big influence on the result of the plasma treatment, therefore must always be taken into account and surely it should affect the choice of the treatment parameters.

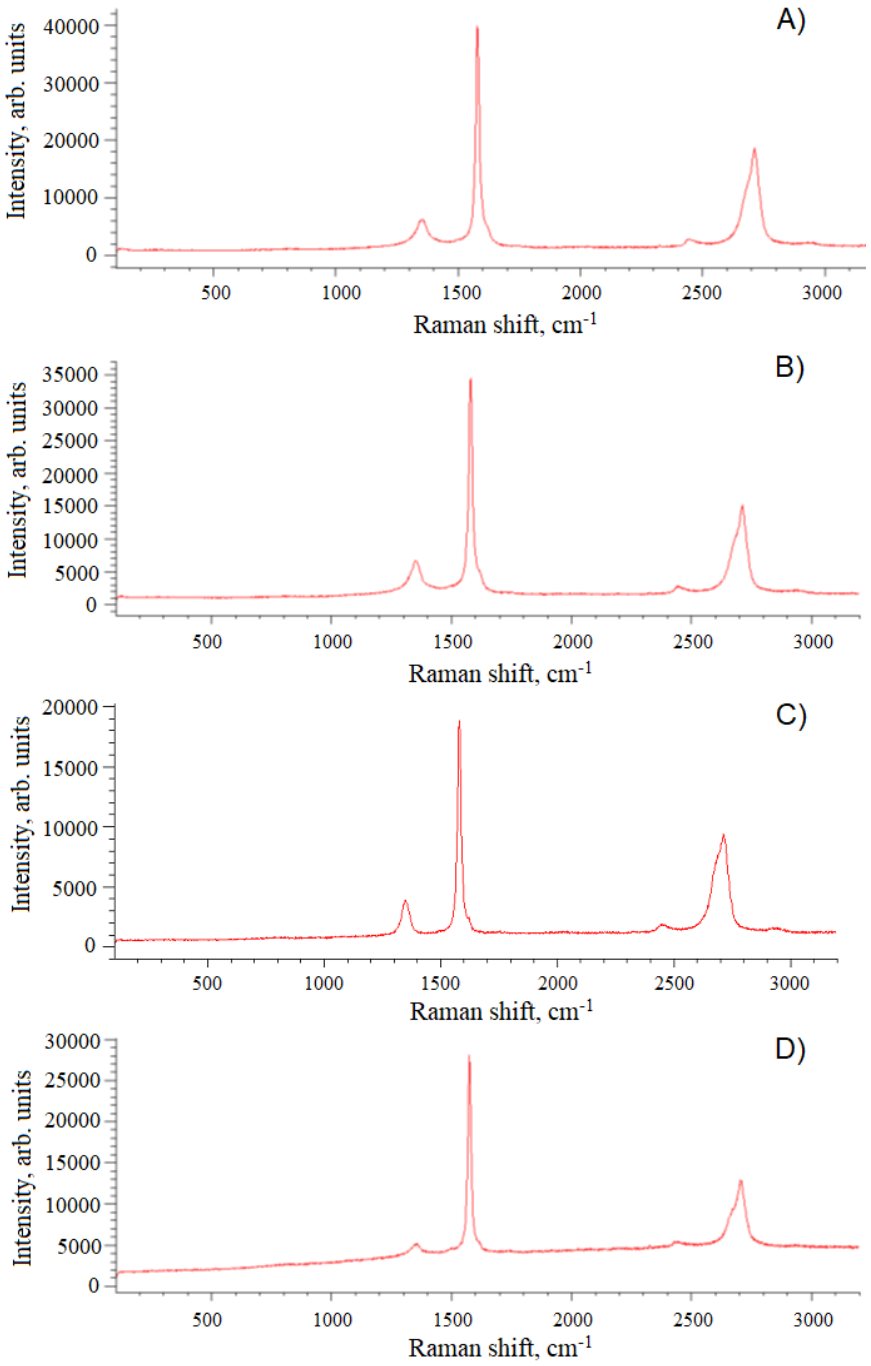

Figure 7.35: Raman spectra of the foils: A) F4 treated in air plasma, 7 min, 0.19 mbar; B) F1 treated in air plasma, 20 min, 0.13 mbar; C) F3 treated in O_2 plasma, 7 min, 8 mbar; D) F2 treated in O_2, 20 min, 8 mbar.

The sample F2 with 33 wt% of PP in Fig. 7.35 (D) has the biggest shift of the G peak position and has lower than F3 (31 wt% of PP) value of the I(D)/I(G) ratio what is also shown in Table 7.11. In this case longer treatment duration in oxygen let obtain a better result in spite of higher content of PP in the sample.

Table 7.11: I(D)/I(G) ratio, G peak position and plasma treatment parameters from the spectra in Fig. 7.35.

Sample	**PP content** wt%	**Parameters**	**G peak** cm^{-1}	**I(D)/I(G)**
F1	35	Air, 20 min, 0.13 mbar	1581	0.19
F2	33	O_2, 20 min, 8 mbar	1576	0.18
F3	31	O_2, 7 min, 8 mbar	1578	0.50
F4	29	Air, 7 min, 0.19 mbar	1579	0.15

Table 7.12 shows the I(D)/I(G) ratio values and the positions of the G peak for the untreated and treated in air plasma at ambient pressure without gas flow foils (993 mbar, 6 min, 6 cm).

Table 7.12: I(D)/I(G) ratio and G peak position from the spectra of the untreated and treated in air plasma at ambient pressure without gas flow foils.

Sample	**PP content** wt%	**G peak** cm^{-1}	**I(D)/I(G)**
Untreated F1	35	1583	1.54
Untreated F2	33	1583	1.15
Untreated F3	31	1583	1.09
Untreated F4	29	1583	1.07
F1	35	1581	0.82
F2	33	1581	0.89
F3	31	1581	1.03
F4	29	1581	1.04

The results presented in Table 7.12 show that plasma treatment at ambient pressure is inferior in effectiveness to the low pressure treatment (see Table 7.11), even though it also allows to see the changes in Raman spectra after the plasma treatment: the decrease of the values of I(D)/I(G) ratio and the shift of the G

peak. It is interesting that at the same treatment conditions using no gas flow, the samples with higher content of PP are treated more intensively, as evidenced by the I(D)/I(G) in Table 7.12: the foil F1, which has the highest PP content, has lower I(D)/I(G) value after the plasma treatment than the other foils. This phenomenon allows to suppose that first of all PP is being removed from the surface during the plasma treatment and graphite disorder increases faster in the samples with higher PP amount.

Raman spectra of three foils, 5 minutes treated in air plasma at the pressure of 990 mbar with the gas flow 17 slm at the distance to the chamber of 6 cm are shown
in Fig. 7.36. Table 7.13 shows the values, describing these spectra.

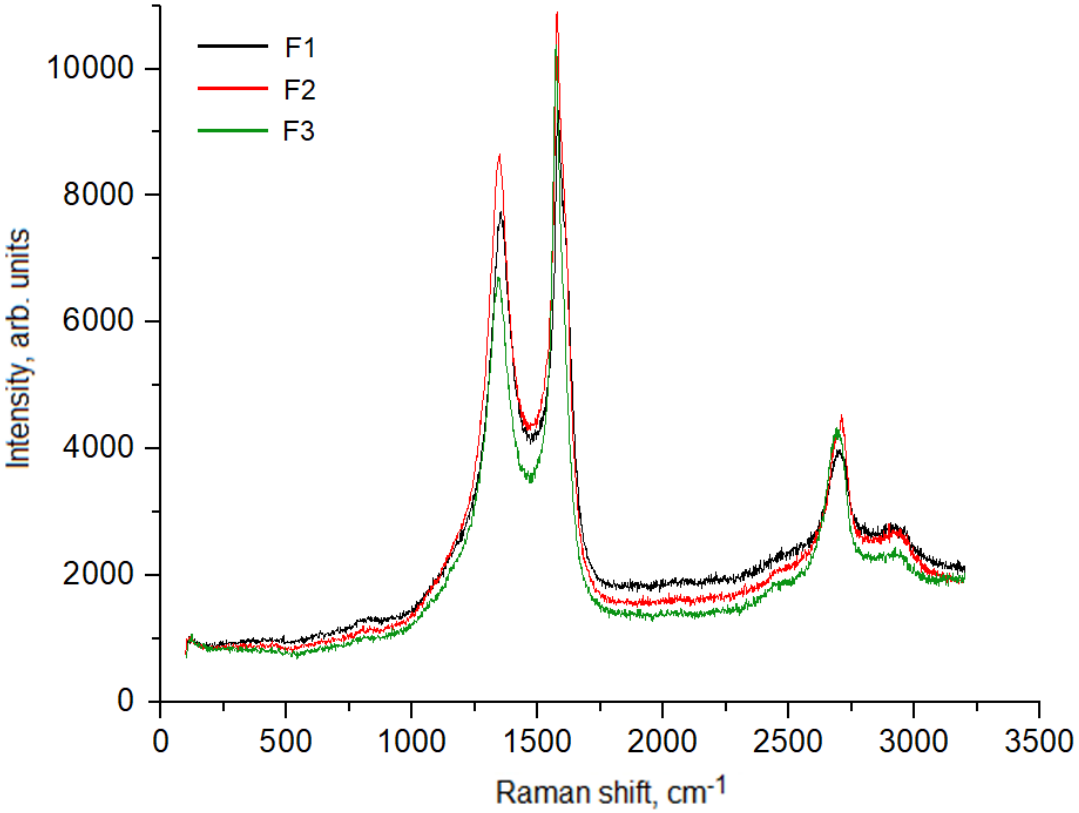

Figure 7.36: Raman spectra of different foils, 5 minutes treated in plasma with the gas flow of 17 slm.

Table 7.13: I(D)/I(G) ratio, G peak position and content of PP from the spectra in Fig. 7.36.

Sample	**PP content** wt%	**G peak** cm^{-1}	**I(D)/I(G)**
F1	35	1581	0.82
F2	33	1581	0.79
F3	31	1575	0.66

The results, presented in Table 7.13, obviously show that using high values of the gas flow (17 slm) leads to very intensive plasma treatment and the sample with lower PP amount have lower I(D)/I(G) values. For foil F3 also the shift of the G peak is observed. The sample F4 could not be regarded in Table 7.13, because the treatment conditions were too hard for this sample, the sample was burned and crumbled during the experiment. The edges of the sample F3 were also crumbled, even though the sample could still be investigated, practically the plasma treatment conditions used are not suitable for the samples F3 and F4 with relatively low amount of PP in their composition (see Table 7.10).

The samples F1 and F2 were treated for longer time: 10 and 15 minutes. The spectra of these samples after the treatment are presented in Fig. 7.37. The numerical values of I(D)/I(G) and the position of the G peak for these spectra are shown in Table 7.14.

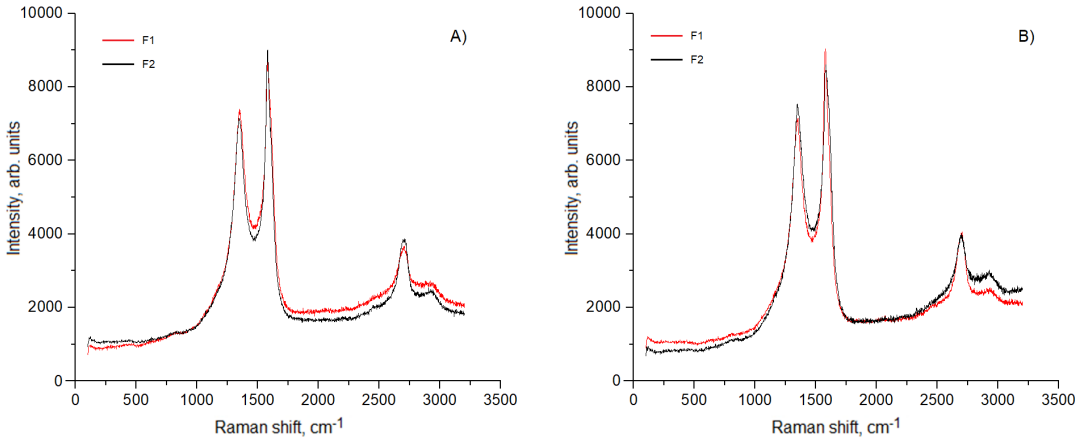

Figure 7.37: Raman spectra of the foils F1 and F2, treated in air plasma with the gas flow of 17 slm for: A) 10 min; B) 15 min.

Table 7.14: I(D)/I(G) ratio and G peak position from the spectra in Fig. 7.37.

Sample	**Duration** min	**PP** wt%	**G peak** cm^{-1}	**I(D)/I(G)**
F1	10	35	1581	0.85
F2	10	33	1581	0.79
F1	15	35	1578	0.79
F2	15	33	1584	0.88

The sample F2, treated for 15 minutes, also started to crumble at the edges. Only the sample F1 with 35 wt% of PP in its composition could be successfully treated in air plasma at ambient pressure with the gas flow of 17 slm for 15 minutes without being damaged. However even the most intense plasma treatment of foil F1 did not let the sample reach the required electrical conductivity, even though it was significantly improved after the plasma treatment.

An example of the common influence of such parameters as pressure, gas flow, and the composition of the foil is shown in Table 7.15. The foil F3 (31 wt% of PP) was treated in air plasma for 3 minutes at the distance of 6 cm from the plasma chamber, varying the gas flow and the pressure of the gas. The smallest value of the I(D)/I(G) ratio was achieved using the strongest gas flow at ambient

pressure (9 slm, 990 mbar), but the lower pressure at lower value of the gas flow (2 slm, 300 mbar) was more efficient than 7 slm gas flow at ambient pressure. It should also be noted that only the sample, treated at the gas flow of 7 slm at ambient pressure with the highest I(D)/I(G) value in Table 7.15 (0.7862) was not damaged and not crumbled at the edges after the plasma treatment.

Table 7.15: I(D)/I(G) ratio and G peak position of F3, treated in air plasma at different conditions.

Sample	**PP** wt%	**Conditions**	**G peak** cm^{-1}	**I(D)/I(G)**
F3	31	9 slm, 990 mbar, 3 min	1575	0.66
		2 slm, 300 mbar, 3 min	1575	0.68
		7 slm, 990 mbar, 3 min	1578	0.79

7.4.4 Summary of the Results of Raman Spectroscopy

The most interesting and unexpected result obtained by Raman spectroscopy is the fact that oxygen-containing plasmas not only remove PP from the surface, but also change the micro structure of graphite from nanocrystals to microcrystals. This is evidenced by the shift of G peak to smaller wavenumbers and by decrease of the intensity ratio of D and G peaks after oxygen-containing plasma treatment. These changes indicate the increase of size of graphite crystals, what positively influences the electrical conductivity of the samples.

The width of the D band at half maximum height (FWHM), which implies the disorderness of graphite, depends on the excitation energy. The changes of FWHM were not regarded in this work.

Additional investigation using red laser confirmed the results obtained by green laser. The absence of changes in position and intensity of G peak mean that graphite matrix, structure, packing of atoms and the size of the crystals are not changed. The change of excitation energy leads to shifts of D and 2D peaks. Nevertheless, the investigation using red laser allowed to see the peak at 1620 cm^{-1} merged with G peak, especially well recognizable in the spectra of BPP treated

in air plasma. This peak indicates the presence of sp^2 bonds responsible for electrical conductivity of graphite.

Inhomogeneity of the surface of BPP can be seen in microscope images in Fig. 7.26. Therefore, several spots of the surfaces of BPP untreated and treated by oxygen-containing gases (oxygen, air and carbon dioxide) were investigated by the method of Raman spectroscopy. The results showed that after 20 min of oxygen plasma treatment almost no differences between the spectra taken in different spots of the surface remain (see Fig. 7.28).

Plasma treatment by carbon dioxide appeared to be more efficient than by air. Using the spectra of BPP treated by CO_2 plasma as an example the change of the value of intensity ratio I(D)/I(G) with increase of treatment duration from 0 to 30 min is shown. It allows to define the optimal treatment duration of BPP by this gas.

Raman spectra of BPP treated by air at different pressures showed the high efficiency of low pressure plasma treatment compared to high pressure. Also high values of gas flow lead to more efficient plasma treatment.

Investigation of Raman spectra of foils showed that plasma treatment by air at atmospheric pressure can remove PP and improve the conductivity of BPP ver efficently if the value of gas flow is high enough and the higher the value of the gas flow, the higher is the efficiency of plasma treatment.

Raman spectra of foils of different composition allow to state that the composition of the sample influences the result of plasma treatment very much. Comparison of intensity ratios I(D)/I(G) of different foils showed that the structure of the graphite matrix of the foils with the maximal amount of PP in their composition (35 wt%) is changed from nanocrystalline to polycrystalline more significantly than the structure of the graphite matrix of the foils with smaller amount of PP in their composition. Oxygen-containing plasma removes PP from the surface of the samples with higher amount of PP relatively fast, after that the graphite

disorder increases. This process appeared to be faster for the samples with higher PP amount.

7.5 XPS Investigation of the Surface

In this research VersaProbe II^{TM} from Ulvac-Phi was used for the XPS investigation. The technical data of the device are described in [180].
The XPS quantitative evaluation of the surface chemistry of BPP untreated and treated in air plasma is presented in Table 7.16. The description of the samples used for XPS investigation is also presented in Table 7.16.

Table 7.16: Quantitative evaluation of chemical composition of the untreated and treated in air plasma BPP, showing the gas type, the distance from the sample to the chamber **L**, treatment duration **t** and the pressure **P**. Also the data for the untreated sample 0 are shown.

BPP	**Gas**	**L** cm	**t** min	**P** mbar	**XPS evaluation**
0	-	-	-	-	97 at% carbon, mostly sp^3-hybritized; 3 at% oxygen; minimal silicon contamination
1	Air	4	20	1004.80	91 at% mostly sp^3-hybritized carbon with small amounts of $C-O$ bonds; 7 at% oxygen; 2 at% nitrogen; minimal silicon contamination
2	Air	4	3	0.15	93 at% carbon with small amounts of $C-O$ bonds; 5 at% oxygen; 2 at% silicon; (no nitrogen detected)

The results of the quantitative chemical analysis, presented in Table 7.16, may suggest that the values of the atomic percent of oxygen after plasma treatment are higher than the value before plasma treatment. But considering the error of the method, the values of atomic percent of oxygen may also decrease or remain

unchanged. Blue, purple and green lines in Fig. 7.38 show the possible change of the value of atomic percent of oxygen after air plasma treatment.

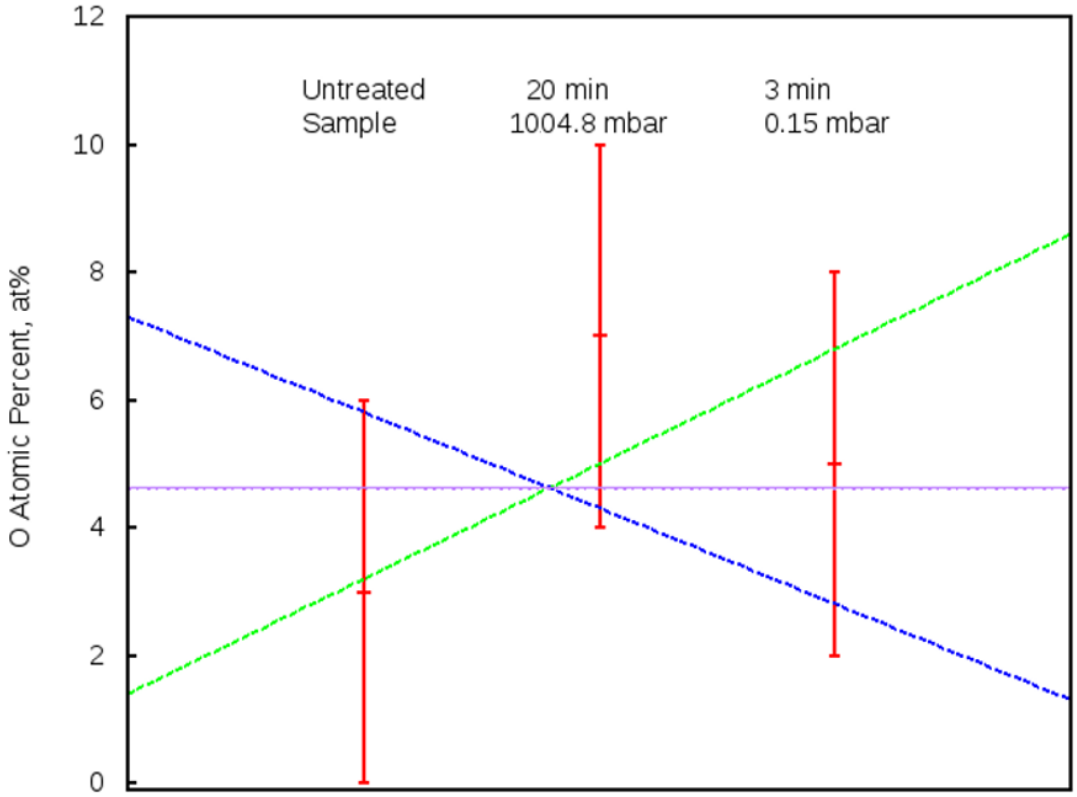

Figure 7.38: XPS values of atomic percentage of oxygen of the untreated and treated in air plasma BPP, considering the error.

Since the error for atomic percentage is roughly ±3 at% in XPS, the quantitative results, obtained by XPS method, are very approximated and should be regarded on the basis of more precise methods for this research, such as FTIR and Raman spectroscopy methods.

As it was already mentioned, experiments showed that plasma treatment at low gas pressure is usually more effective than the treatment at high pressures. Plasma treatment by air leads to oxidation, to appearance of nitrogen on the surface and to oxidative destruction of the polymer.

Minor contaminations were found on all the investigated surfaces. It is also difficult to make a conclusion about the reduction of sp^3- hybridized carbon after the plasma treatment, because on the surface of the sample, treated in plasma at ambient pressure, mostly sp^3-hybritized carbon was found. Nevertheless, a significant increase of sp^2 hybridization compared to sp^3 is demonstrated by FTIR spectroscopy method.

Nitrogen 1s peak of the sample 1 from Table 7.16 has quite small intensity and is shown in Fig. 7.39.

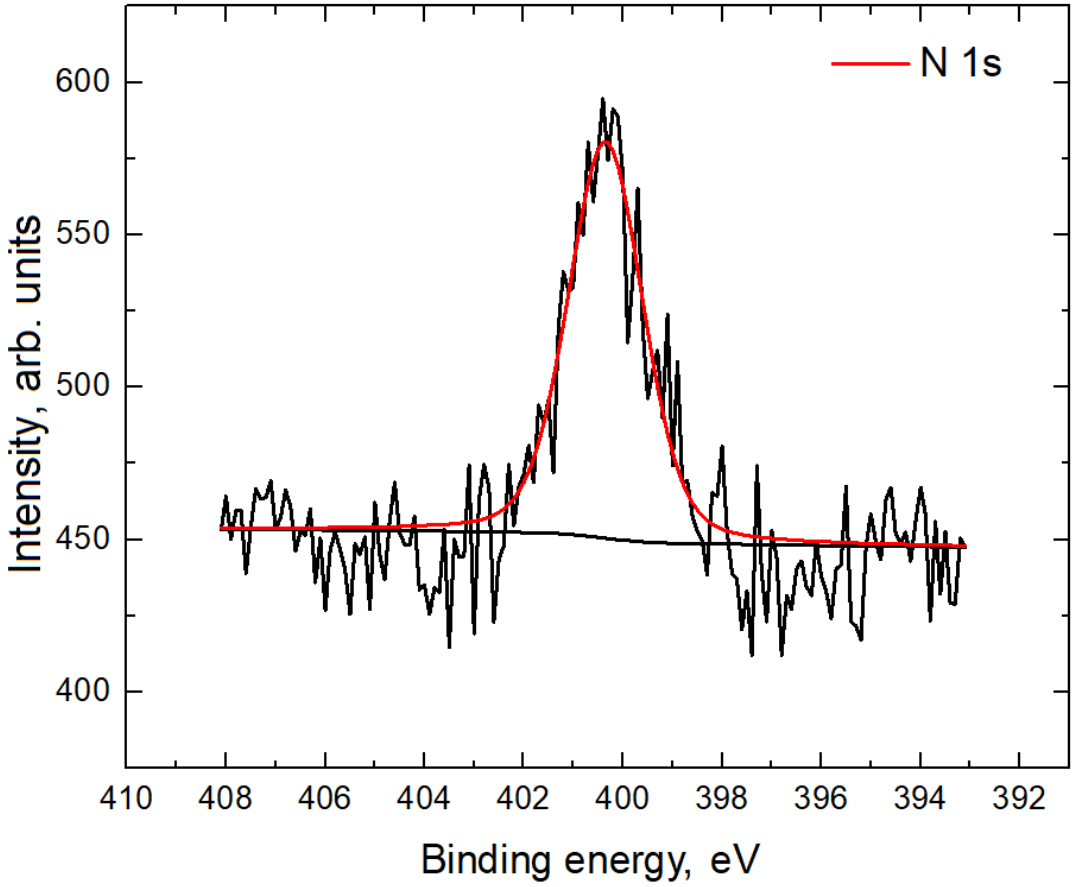

Figure 7.39: XPS analysis of nitrogen in sample 1 (see Table 7.16).

Nitrogen from the air can interact with carbon, oxygen and hydrogen on the surface of BPP during the air plasma treatment. A small amount of nitrogen

may be present on the surfaces of the samples, treated by air. It is known that nitrogen is capable of forming three covalent bonds with other atoms, according to the exchange mechanism. When an atom of nitrogen has a valence of 3 it can act as a donor of a pair of electrons, forming the fourth bond by the donor-acceptor mechanism. In this case, nitrogen acquires a valence of 4. The tetravalent nitrogen atom has a positive charge and can participate in the formation of ionic bonds [181].

T. Homola et al. in [110] reported about the small amount (up to 3 at%) of nitrogen on poly(ethylene terephalate) – PET samples treated by air plasma at atmospheric pressure, but the atomic percentages of nitrogen are too small within the XPS accuracy. Also decrease of carbon concentration and increase of oxygen concentration with the increase of plasma treatment time from 1 to 10 seconds was described in [110]. Other investigations report that more $C-O$ and $C=O$ present on the surface of polymers after exposure to atmospheric-pressure oxygen-containing plasma [182].

The XPS peaks of carbon 1s and oxygen 1s are presented in Fig. 7.40 and Fig. 7.41, respectively. The peak in C 1s spectrum of the BPP, treated at low pressure (Sample 2 in Table 7.16), shown in Fig. 7.40 (C), is asymmetric and has a satellite feature towards higher binding energy from the main C 1s peak, what implies high concentration of sp^2 carbon in the sample [87]. The peak in the spectrum of the BPP, treated at low pressure (Sample 1 in Table 7.16), shown in Fig. 7.40 (B), also has a satellite feature, but at lower binding energy values. This peak has an asymmetric tail towards higher binding energy on its top, while the peak of the untreated BPP in Fig. 7.40 (A) is more symmetric. If the sample has a high concentration of sp^3-bonded carbon, the C 1s peak has a symmetric shape and can be slightly shifted to higher values of binding energy [87].

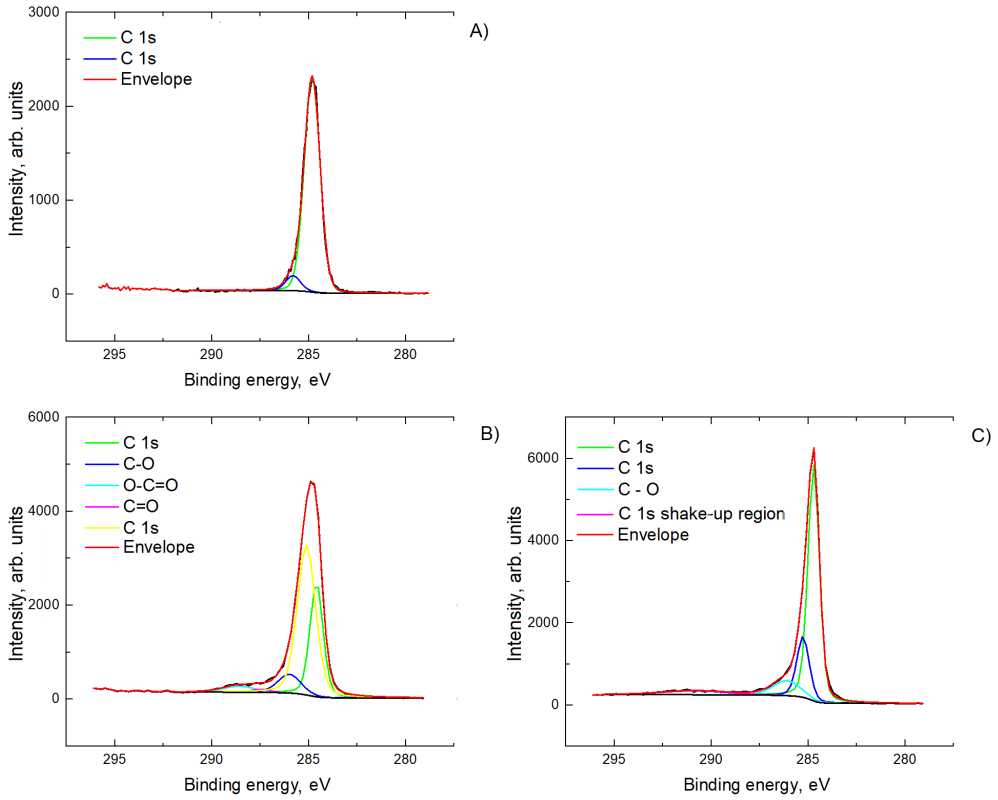

Figure 7.40: XPS analysis of carbon in BPP (see Table 7.16): A) Sample 0; B) Sample 1; C) Sample 2.

The shape of the C 1s peaks also depends on the amount of nitrogen on the surface. The higher the concentration of nitrogen on the surface, the higher is the full width of the peak at half maximum height (FWHM) and the wider is the peak C 1s [183].

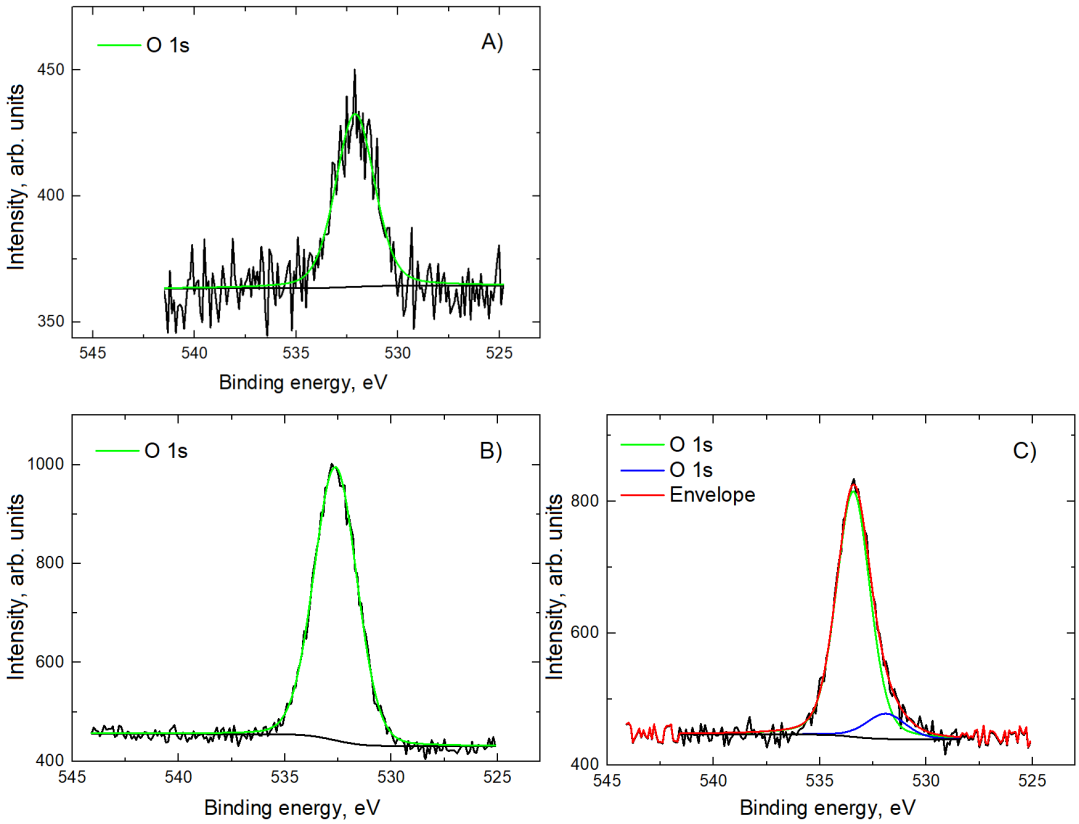

Figure 7.41: XPS analysis of oxygen in BPP (see Table 7.16): A) Sample 0; B) Sample 1; C) Sample 2.

The peak O 1s in Fig. 7.41 can be deconvoluted into two components: 531.9 eV (attributed to $C = O$) and 533.43 eV (attributed to $C-O$). The peaks in Fig. 7.41 have similar shapes. Generalizing the data in Fig. 7.40 and Fig. 7.41, more $C-O$ and $C = O$ bonds present on the surface after plasma treatment at the described conditions.

Since XPS gives information about the chemical composition in the depth of nm, oxygen may appear on the surface due to absorption or oxidation after the plasma treatment. Nevertheless, the inhomogeneity of the BPP surface should be taken into account, what means that the results of the XPS analysis may differ in a certain range in different spots of the surface.

7.6 AES Investigation of the Surface

AES analysis of BPP untreated and 20 min treated in CO_2 plasma (5.8 mbar, 4 cm, 100 sccm, 3 kW) was conducted to compare the results of CO_2 plasma treatment with the results of air plasma treatment, obtained by XPS method.

For this investigation the Scanning Auger System PHI 660 from Physical Electronics was used [184]. The voltage of the electron beam was chosen to be 10 kV. The high energy resolution (0.7%) provides the possibility to define the exact peak position and the shape of the peak, which depend on the chemical surrounding of the element [184]. Images of the surfaces of the investigated samples, obtained by this device, are presented in Fig. 7.42. The surface of the sample etched in plasma (Fig 7.42 (B)) is more inhomogeneous and rough than the surface with PP of the untreated sample (Fig 7.42 (A)).

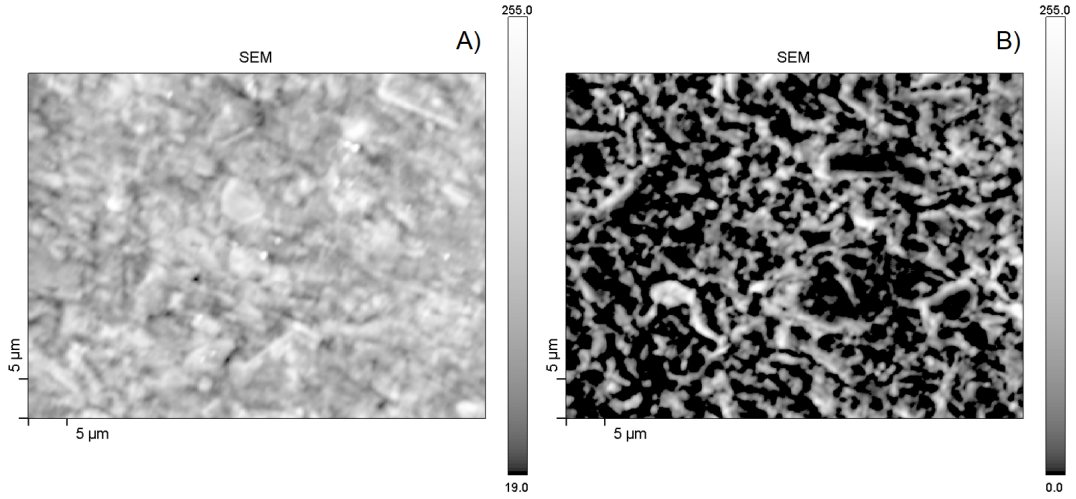

Figure 7.42: SEM pictures of BPP: A) untreated; B) 20 min treated in CO_2 (5.8 mbar, 4 cm, 100 sccm, 3 kW).

Auger spectra of the BPP untreated and 20 min treated in carbon dioxide plasma are shown in Fig. 7.43. The treatment conditions of the second sample allow to achieve the required electrical conductivity.

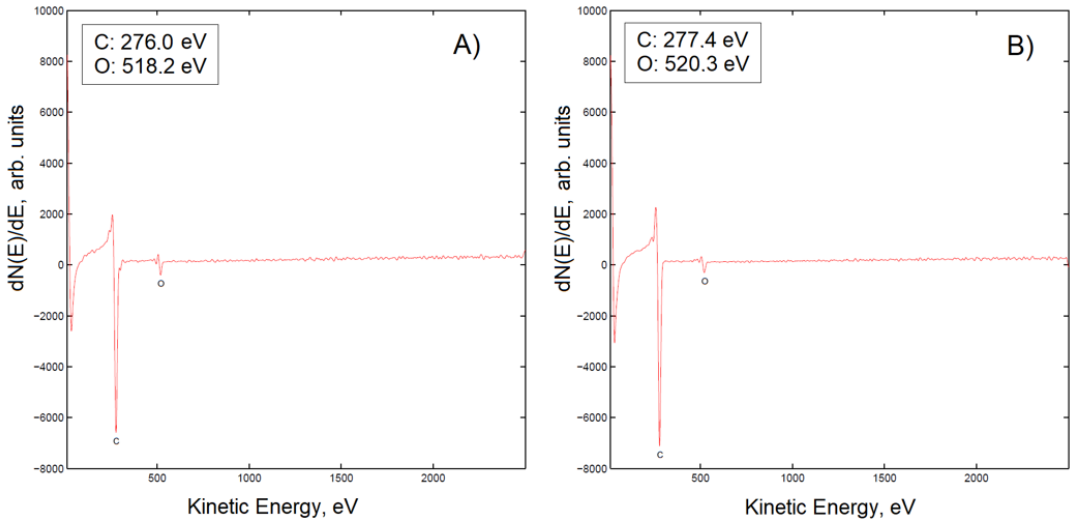

Figure 7.43: Auger spectra of BPP: A) untreated; B) 20 min treated in CO_2 (5.8 mbar, 4 cm, 100 sccm, 3 kW).

In [170] the carbon peak is defined at 278 eV for C KLL transition, while 272 eV for this transaction is mentioned in [64]. As it is shown in Fig. 7.43, the BPP, investigated in this work, exhibit the peaks of carbon at 276 eV before plasma treatment and 277.4 eV after CO_2 plasma treatment (1.4 eV shift) and the peaks of oxygen – at 518.2 eV and 520.3 eV (2.1 eV shift), respectively, instead of 516 eV, mentioned in [64]. The peak shifts of a few eV often occur due to chemical bonding [64]. These shifts may be related to high electronegativity of oxygen in carbon-oxygen bonds [185].

Measurements using AES show that the carbon content increases and the oxygen content decreases after 20 min of etching in carbon dioxide plasma. The value of the intensity ratio of carbon and oxygen content in the untreated sample (I(C)/I(O)=10.57) is smaller compared to this ratio of the sample, treated in CO_2 plasma (I(C)/I(O)=15.04). In [170] Auger spectra of carbon/polymer composite samples show a significant increase of the oxygen content on the surface after 6 s of oxygen plasma treatment at low microwave power of 2 kW. Such treatment conditions can be regarded as plasma activation and described by the authors as

> „very useful for chemical functionalization of the carbon/polymer composite samples“ [170].

Much longer treatment time and much higher microwave power removes PP and also oxygen-containing functional groups from the surface, therefore in the present case the intensity of the oxygen peak in Auger spectra decreases after the CO_2 plasma etching. Considering the increase of the intensity of carbon peak after plasma treatment, the authors of [170] report:

> „Etching predominantly removes polypropylene. Indeed, at even longer treatment times selective etching of polypropylene becomes evident by the formation of graphitic powder on the surface.“

Graphite plays an important role in the improvement of the electrical conductivity of BPP, targeted in this work. Graphitization of the surface contributes to the decrease of the surface resistance. If carbon dioxide is chosen as the working gas instead of oxygen or air, then the carbonization process appears to be more intensive than oxidation. AES quantitative evaluation showed that the sample treated in CO_2 plasma has roughly estimated 97.7 at% of carbon and 2.3 at% of oxygen. It should be noticed that the atomic percentages of oxygen and nitrogen are too small within the accuracy of the method, therefore no conclusion about the concentration of these elements on the surface can be made. Chemical analysis by AES method was done for completeness of the work.

7.7 EDX Investigation of the Surface

Since EDX method allows to investigate the depth of several μm, it was the most interesting method of chemical analysis. Since plasma influences only the surface layers of the material (see Fig. 3.6), no significant changes of EDX results after the plasma treatment were expected. It was unexpected to find out that the amount of oxygen changes after the plasma treatment, what will be shown below.

An untreated BPP and the BPP treated in CO_2 plasma for 3, 5, 10 and 20 min at the pressure of 0.1 – 8.5 mbar and using gas flows of 100 sccm and 3.85 slm,

and also foils with 35 wt% and 29 wt% of PP were used for EDX investigation. The EDX method was used for chemical characterization of BPP in JEOL JSM-7500F Field Emission Scanning Electron Microscope (SEM), where the sample is investigated using a focused electron beam of high energy, equipped with Bruker XFlash® detector 5030 for EDX analysis. As mentioned in Chapter 4.1.5, the primary electron beam penetrates into the surface and reaches several μm depth. For this reason, measurements by EDX method damages the sample (especially polymer on the surface). To analyze the data, the software Bruker Quantax 200, Esprit 1.9 was used. Additional investigation was conducted using SEM Stereoscan-360 from Cambridge Instruments, equipped with EDX system AN 10000 from Link Analytical; ZAF-4/FLS software provided by Link Systems was used for quantitative analysis. The error is defined by the measurement device, it depends on the intensity and is specific for each element. For the measurement, presented below, the error does not exceed 11.1 wt% for carbon and 0.5 wt% for oxygen.

Since electrical properties of crystals depend on the amount of atoms of the constituent components of the crystal, atomic percent (at%) is often used to define concentrations of the components. Weight percent (wt%) can be converted to atomic percent and vice versa [186]. So the data can be presented in at% or wt%, depending on the specific research need.

EDX analysis of the untreated and treated for 5 min and 20 min in CO_2 plasma with the gas flow of 100 sccm BPP, keeping the pressure of the gas at 8.5 mbar, at the distance from plasma chamber of 4 cm and microwave power of 3 kW, showed that during the first 5 min plasma treatment with the described parameters leads to the decrease of oxygen on the surface, then it slightly increases (see Fig. 7.44). Slight fluctuations of the atomic percent of oxygen may take place depending on the spot of the surface where the EDX spectrum is taken. Fig. 7.45 shows two different values of atomic percent of oxygen in two different spots of the surface. The spot with a lower value is obviously a graphite structure, while the second spot may contain contaminants. Also the quantitative evaluation is very approximate due to the big error of the method. In this case such a

change of the atomic percent of oxygen (Fig. 7.44) cannot be regarded as an effect, which depends on the duration of plasma treatment. Taking into account the investigated spot on the SEM image of the surface in Fig. 7.44 (C) (left) and some peaks of contaminants Fig. 7.44 (C) (right), which were not regarded, probably this minor increase is related to oxidation of the contaminants on the surface [187].

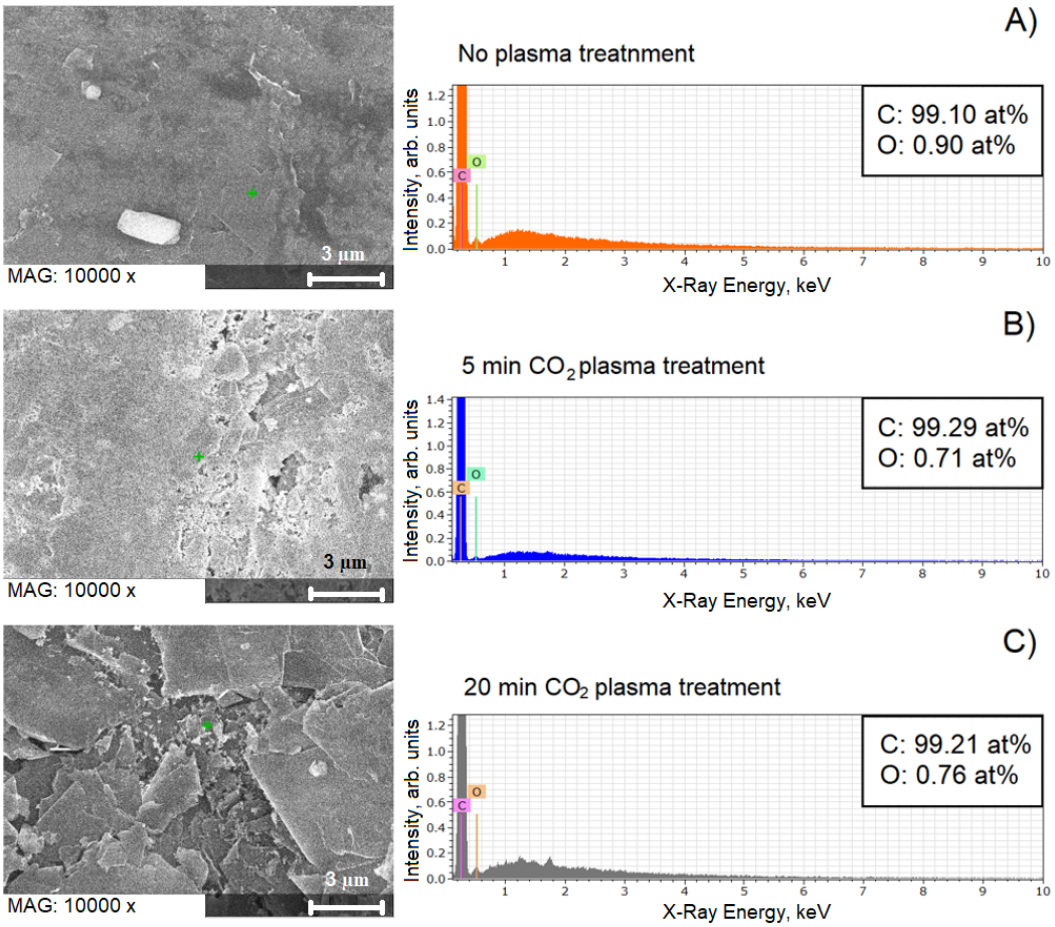

Figure 7.44: SEM images of the surfaces (left) and EDX spectra (right) of: A) untreated BPP; B) treated 5 min in CO_2 plasma at the gas flow of 100 sccm BPP; C) treated 20 min in CO_2 plasma at the gas flow of 100 sccm BPP.

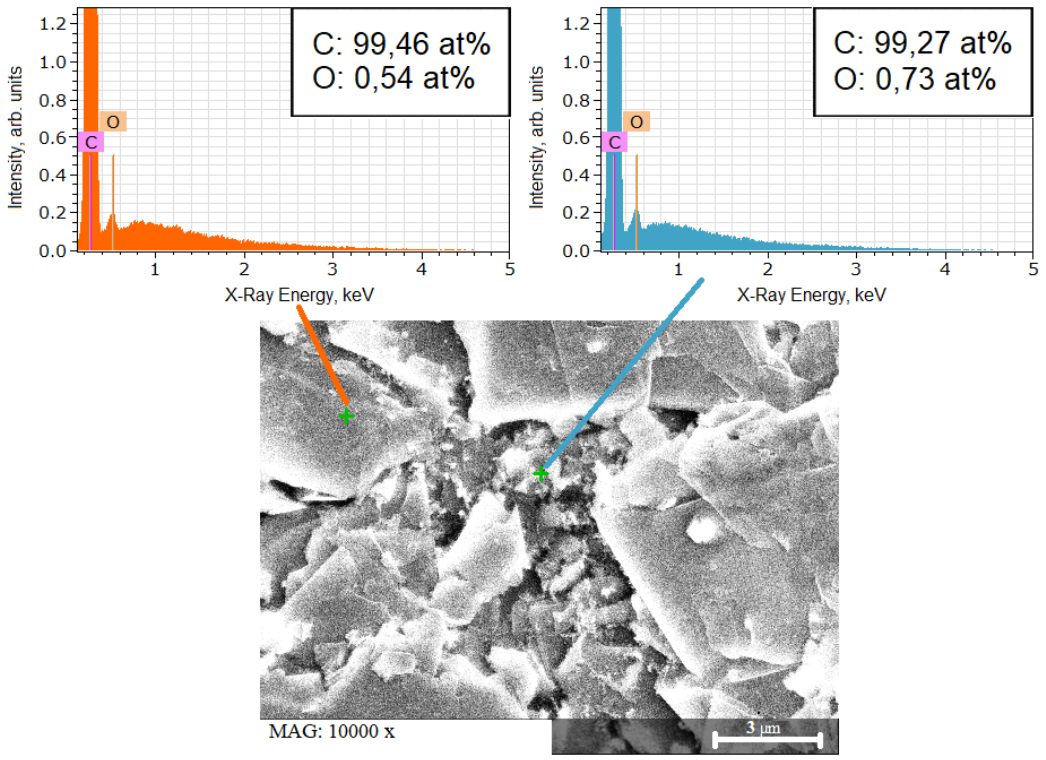

Figure 7.45: EDX spectra (top) and a SEM image (bottom) of the BPP treated 20 min in CO_2 plasma at the gas flow of 100 sccm BPP in two different spots of the surface.

The application of BPP as a part of a fuel cell does not suppose any special storage conditions of the BPP. All the samples were equally transported in new paper envelops and in plastic boxes, nevertheless, chemical analysis shows the presence of contaminants, especially on the surface of the BPP, treated in plasma for 20 minutes. Perhaps it is so because a complete or almost complete PP removal from the surface, provided by the mentioned treatment conditions, leads to the formation of graphitic powder on the surface, what is also mentioned in [170]. Even though the sorption capacity of this graphitic powder was not studied in the present work, since carbon materials (like porous graphitic carbon [188]) are known as good sorbents [189–192], it can be supposed that every contact of the graphitic surface with paper or plastic and etc. may cause the appearance of contaminants on the surface. PP in BPP is a binder for graphite, therefore the amount of contaminants on the surfaces of untreated samples and samples,

which still have enough PP on the surface, is lower than on the graphitic surfaces with insignificant amount of PP or without PP.

In some spots of the surface of BPP, treated in CO_2 plasma for 20 minutes, significant contaminants with the size from several micrometers to a few tens of micrometers were found on the surface (Fig. 7.46).

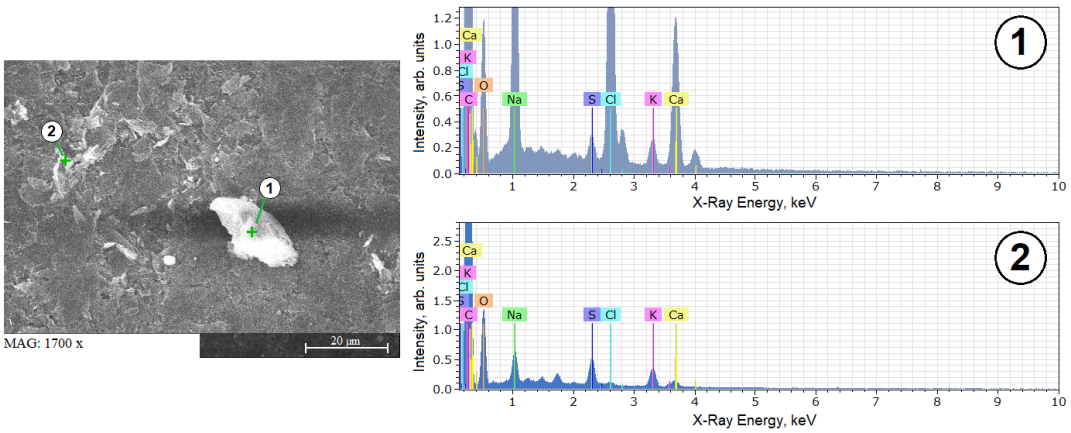

Figure 7.46: SEM image and EDX spectra of contaminations on the surface of BPP, treated in CO_2 plasma for 20 minutes.

The BPP treated in CO_2 plasma for 5 minutes is of interest because PP is still present on the surface, but it is already partly removed enhancing the graphitic surface. Fig. 7.47 shows SEM images and EDX spectra of three different spots on the surface of this sample: A) graphitic part of the surface; B) the part of the surface with carbon black and probably remains of PP; C) deepening of the surface. EDX spectrum, obtained in the clean graphite spot of the surface, shows no definable contamination peaks (Fig. 7.47 (A)), some minor contaminations can be defined on the surface part with carbon black (Fig. 7.47 (B)) and on the deeper surface part (Fig. 7.47 (C)), which was reached by less plasma particles than the higher areas of the surface during the plasma treatment. More contaminated spots of the surface usually have higher content of oxygen.

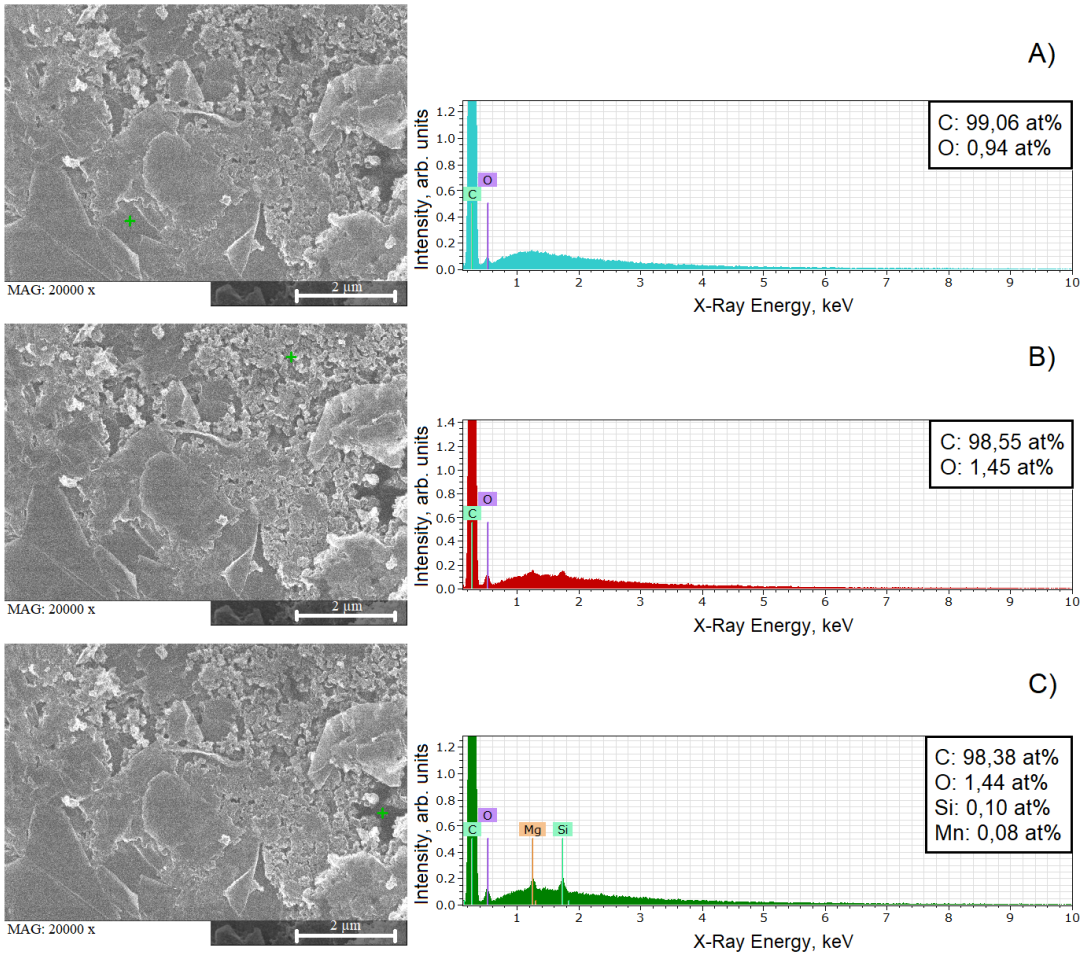

Figure 7.47: SEM images of the surfaces (left) and EDX spectra (right), taken in three different spots of the surface of the BPP, 5 min treated in CO_2 plasma: A) graphitic part of the surface; B) the part of the surface with carbon black and remains of PP; C) deepening of the surface.

Some contaminants as single particles are also present on the surface of the untreated sample, usually their size range is from one to several micrometers. For example, two well-definable particles in the SEM image of the surface of the untreated sample in Fig. 7.44 (A) (left) represent calcium oxide. The surfaces of untreated BPP are mainly covered by PP, so high surface potential of some surface areas can be provided by polar groups, terminal elements of macromolecule, radicals and etc. on the surface [193]. Chemically reactive polymer groups interact with oxides and hydroxides on the surface (at the interface), also

the formation of molecular chemical bonds with contaminants may take place [194]. Such contaminations are inevitable, considering the practical application of BPP. On the surfaces of the investigated samples the total amount of contaminations did not exceed 3 at%, what can be regarded as insignificant, considering the influence on the electrical conductivity of BPP.

SEM image and EDX spectrum of another BPP, 3 min treated in CO_2 plasma at the gas flow of 3.85 slmare presented in Fig. 7.48. Several surface spots were scanned and the maximal defined amount of contaminants did not exceed 0.15 at%. High values of the gas flow allow to etch the surface quickly and intensively, successfully removing PP and contaminations even from the deeper areas of the surface, but it is much more difficult to control the process for it is progressing much faster than at low values of the gas flow. However, even at high gas flow value, 3 min of plasma treatment is a relatively short duration for BPP, so, presumably, there is still a lot of PP on the surface.

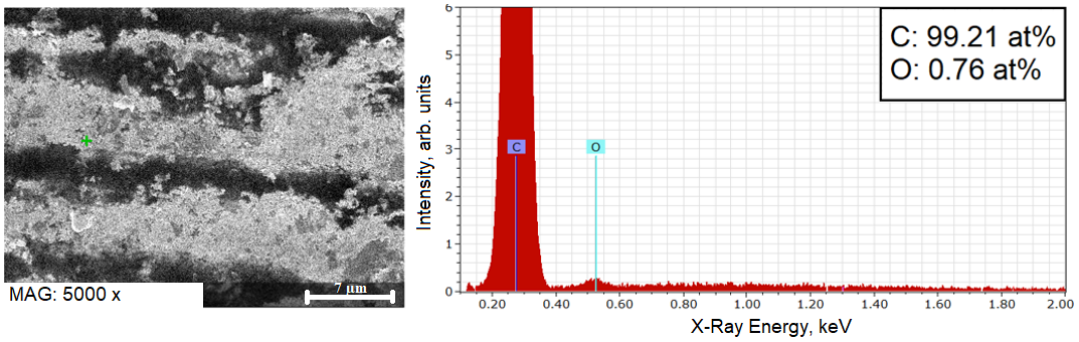

Figure 7.48: SEM image of the surface and EDX spectrum of the BPP, treated for 3 min in CO_2 plasma at the gas flow of 3.85 slm.

The elemental maps of the of the BPP, treated for 3 min in CO_2 plasma at the gas flow of 3.85 slm are presented in Fig. 7.49. They allow to evaluate the content of carbon and oxygen visually.

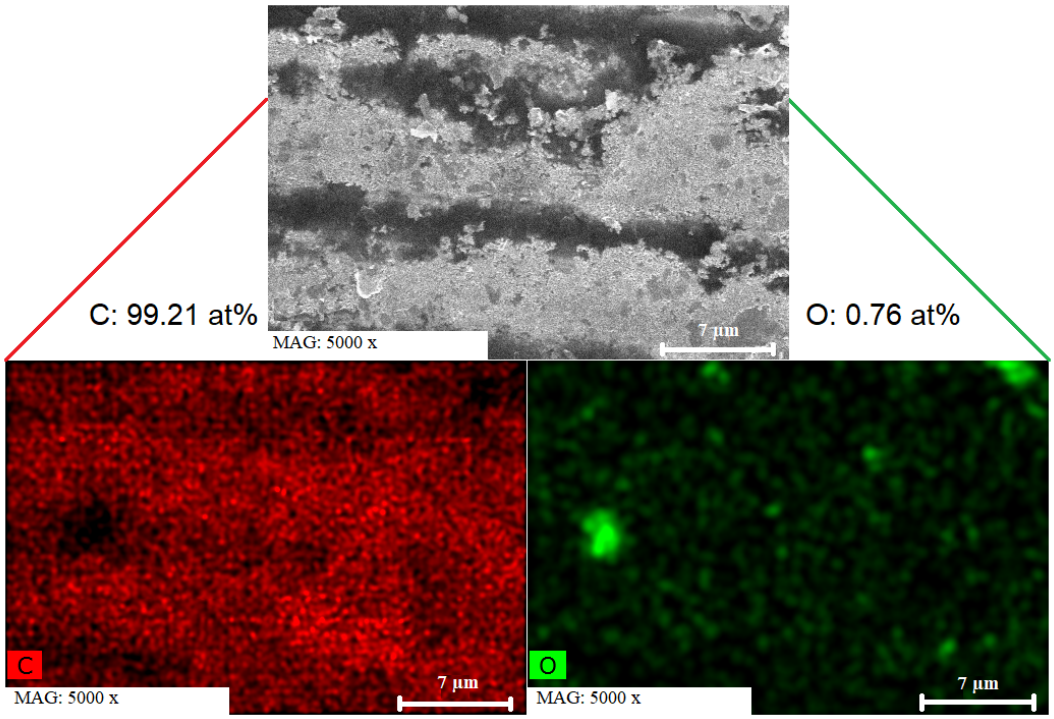

Figure 7.49: SEM image of the BPP, treated for 3 min in CO_2 plasma at the gas flow of 3.85 slm(top), and EDX mapping scan of C (bottom left) and O (bottom right).

Investigation of the elemental composition was also performed by the SEM Stereoscan-360 (Cambridge Instruments), equipped with AN 10000 from Link-Analytical for microanalysis.

As it was mentioned before, usually the values obtained by EDX quantitative analysis may be inaccurate and can only be used as rough approximations. Elemental analysis of the BPP, treated in CO_2 plasma for different time, was used to approximately trace the dependence of the sample composition on the plasma treatment duration (Fig. 7.50).

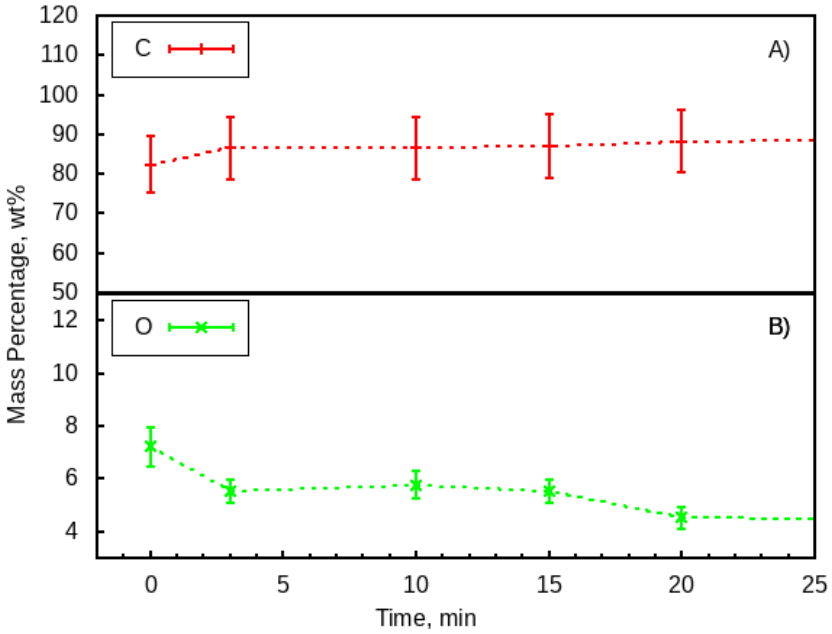

Figure 7.50: Change of the percentage by mass of: A) carbon and B) oxygen on the surface of BPP with increase of the duration of CO_2 plasma treatment.

EDX analysis showed an insignificant increase of the percentage by mass of carbon on the BPP surface with the increase of the duration of plasma treatment in CO_2. Since this increase is smaller than the error range, it cannot be considered (Fig. 7.50 (A) and Fig. 7.51 (A)).

It is shown in Fig. 7.50 (B) that the percentage by mass of oxygen tends to decrease with the increase of the duration of CO_2 plasma treatment. The value of the percentage by mass of oxygen of the sample, treated for 10 min, increases comparing to this of the sample, treated for 3 min. The surface of BPP is not homogeneous and, as it was mentioned above, oxygen is unevenly distributed on the surface, therefore the percentage by mass strongly depends on the investigated spot of the surface. Also relatively small amount of oxygen and the error ranges do not allow to investigate the dynamic of oxygen decrease with the increase of the duration of plasma treatment exactly. Nevertheless, the experimental data allow to state that such the decrease takes place (Fig. 7.50 (B) and Fig. 7.51 (B)).

An effect of plasma on polymers, along with the generation of radicals and new functional groups, is the formation of double bonds and crosslinks. Crosslinks change the average molecular weight of the polymer, its mechanical characteristics and reduce the diffusion coefficients of low molecular weight substances [195]. Oxygen from the air causes oxidation of PP, catalyzed by light. Carbon black is an effective light stabilizer, which can be introduced to PP in the amount of 1.5 wt% [196]. Therefore, one can make an assumption that due to the oxidation of PP on the surface of BPP during the storage at ambient air the surface of the untreated sample contains more oxygen than the surfaces of the treated in plasma samples. In the process of plasma etching the oxidized superficial layer of PP is being removed and the remaining PP accumulates oxygen-containing functional groups, increasing the degree of oxidation [197], what may be related to the peak at 10 min point on the curve in Fig. 7.50 (B).

Definition of nitrogen was complicated by a continuous spectrum, formed by inelastically scattered primary electrons [198].

> „The bombarding electrons also give rise to a continuous X-ray spectrum, as well as producing characteristic X-ray lines, which limits the detachability of small peaks, owing to the presence of 'background' “ [199].

However, the percentage by mass of nitrogen was enough to define it on the surfaces of the samples, treated in air plasma.

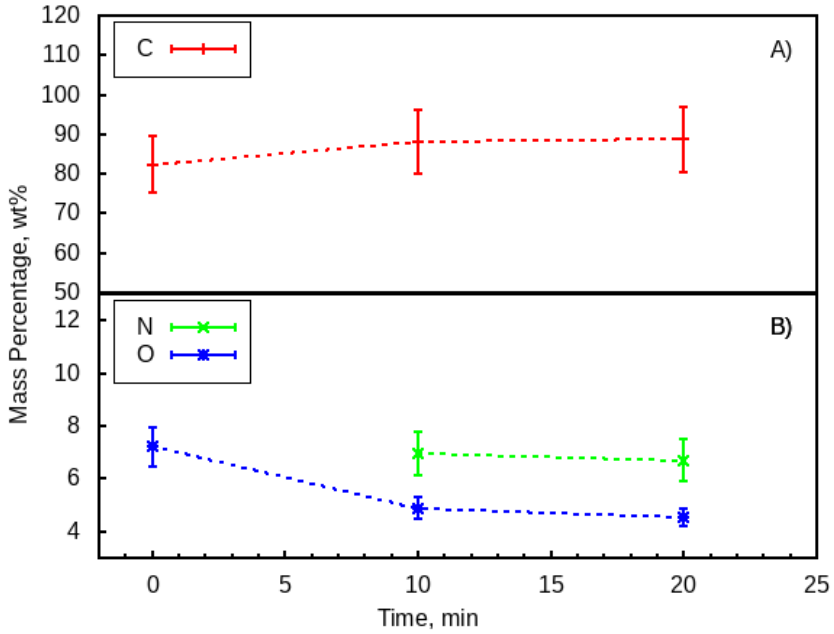

Figure 7.51: Change of the percentage by mass of: A) carbon and B) oxygen and nitrogen on the surface of BPP with increase of the duration of air plasma treatment.

The results of the quantitative analysis of carbon, oxygen and nitrogen in BPP, treated in air plasma at the pressure of 8.5 mbar and at the distance from the plasma chamber of 4 cm, are shown in Fig. 7.51. The values of the percentage by mass of nitrogen were generally higher than those of oxygen on the surfaces of the samples treated in air plasma.

Fig. 7.52 also shows that the percentage by mass of oxygen decrease after plasma treatment. The values of percentages by mass of oxygen and nitrogen of the sample, treated at the pressure of 8 mbar, and the sample treated at 0.1 mbar are comparable in the error range.

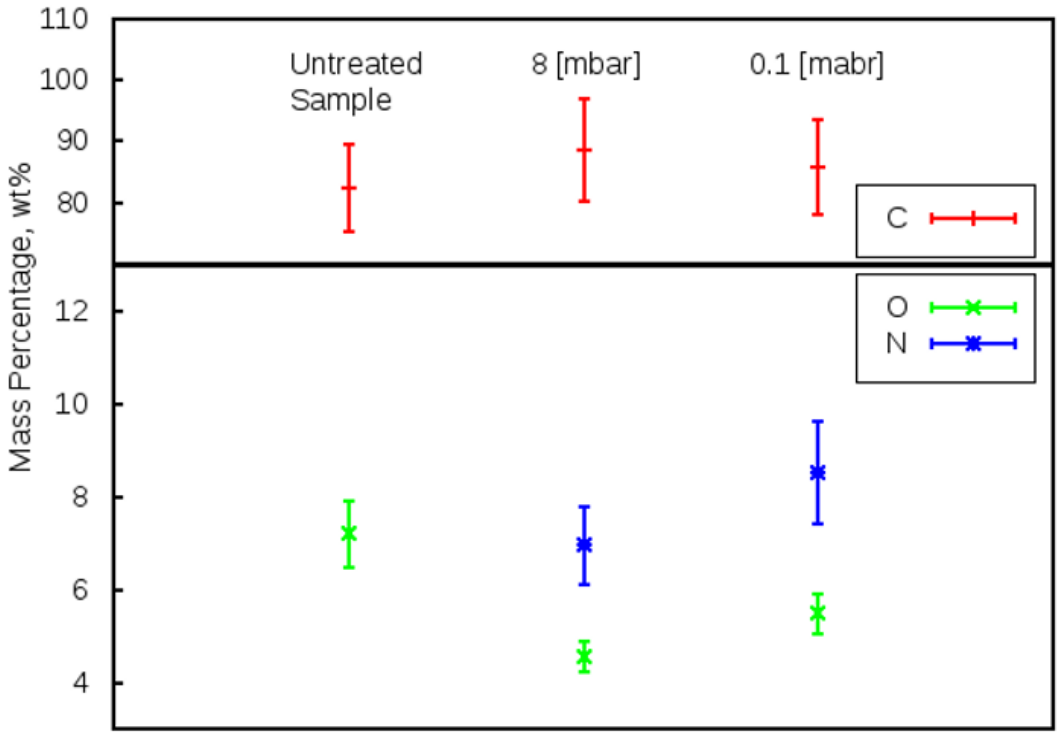

Figure 7.52: Differences of the mass percentages of carbon, oxygen and nitrogen on the surfaces of untreated BPP and BPP 20 min treated in air plasma at different pressures (8 mbar and 0.1 mbar).

EDX investigation of the surfaces of the foils F3 and F4 (Table 7.11 in Chapter 7.4.3)

6 minutes treated in air plasma at atmospheric pressure showed nitrogen and some minor contaminations on the surface (Fig. 7.53 and Fig. 7.54). The spectra of both foils have a considerable background, but definable nitrogen peaks.

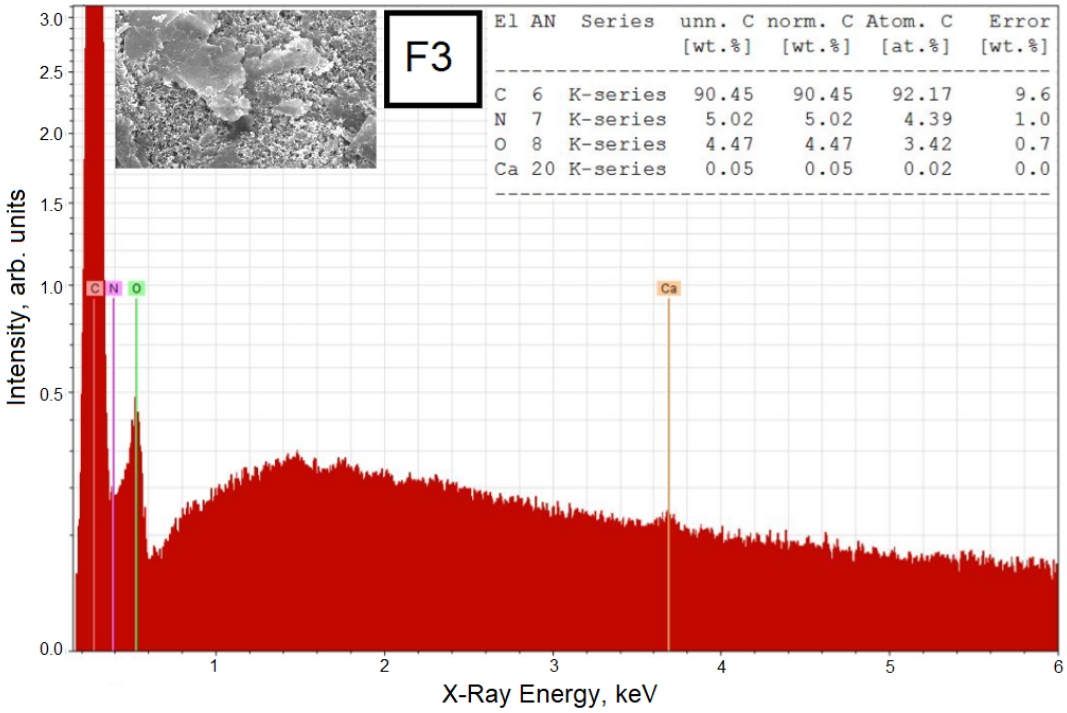

Figure 7.53: EDX spectrum and chemical analysis of the foil F3.

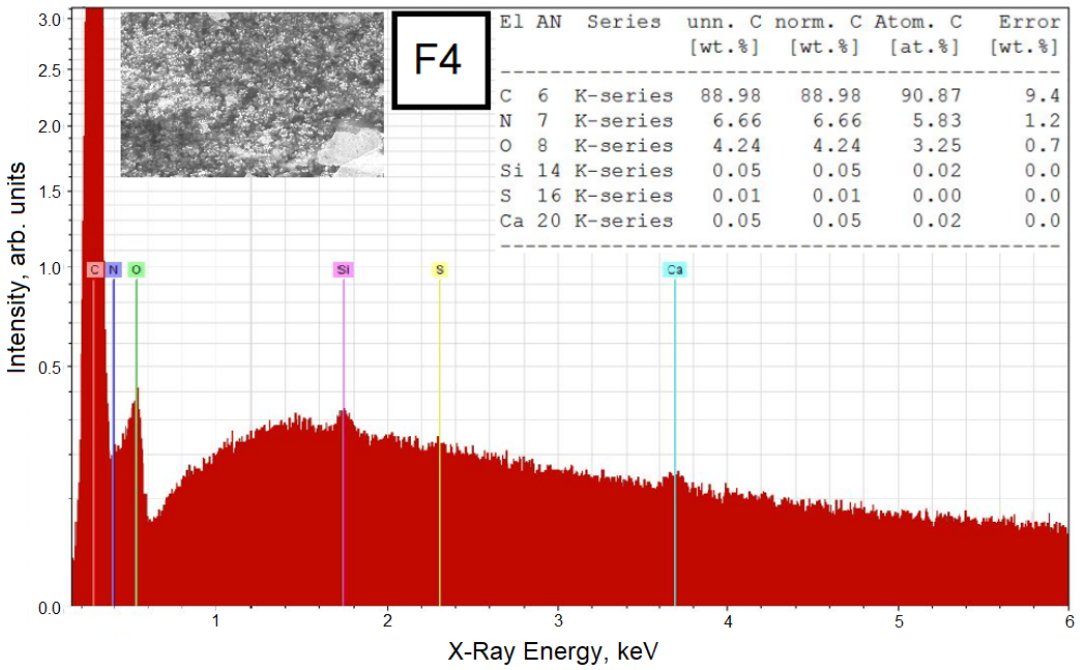

Figure 7.54: EDX spectrum and chemical analysis of the foil F4.

The change of oxygen amount after plasma treatment defined by EDX was unexpected, therefore it is interesting to look through similar investigations. In [170] is was shown that the surface chemistry has been changed only if the polymer-containing sample is treated in oxygen-containing plasma for short time (< 1 min), therefore the content of oxygen increases on the surfaces of the plasma activated samples, compared to the untreated samples [110, 170, 182], whereas longer treatment time changes the topography of the surface by etching [170, 200] and removing PP. The surface chemistry of the samples, investigated in this work, has been changed up to 20 minutes of plasma treatment, depending on other experimental parameters (see Chapter 7.1 and Chapter 7.3). The required electrical conductivity of a fuel cell can be achieved if the BPP are treated for around 20 minutes in oxygen-containing plasma, when the content of PP on the surface becomes insignificant. But as long as the destruction of PP takes place, the surface chemistry may change [197].

Considering the information above, one can conclude that the content of oxygen

may change during the etching of PP in graphite matrix by oxygen-containing gases. When a significant amount of PP is removed from the graphitic surface, no new functional groups are formed and the surface chemistry does not change anymore, but further etching changes the topography of the graphitic surface, the decrease of oxygen content in the depth of the micro-range can be detected by EDX.

8 Surface Morphology and Topography

Roughness of the surface and its shape can have a strong impact on electrical properties of the sample [201]. For this reason, investigation of the influence of plasma treatment on morphology and topography of the surfaces of BPP and foils was conducted.

Scanning electron microscopy (SEM) was chosen for the initial qualitative evaluation of morphology of the surfaces. JEOL JSM-7500F Field Emission scanning electron microscope and Stereoscan-360 from Cambridge Instruments were used for this investigation. Quantification of surface topography was done by Veeco Dektak 6M Stylus Profilometer with stylus radius of 12.5 μm and stylus force of 3 mg; by Solver PRO and Veeco D3000 (with the radius of the cantilever tip of 20 nm and tip height of 2.5 – 3.5 μm) high resolution atomic force microscopes (AFM) and by 3D confocal microscope μsurf Custom from NanoFocus.

8.1 Morphology

Investigation of the surfaces of untreated and treated BPP (in CO_2 for 3 – 20 min and in air for 20 min) and foils with 29 wt% and 35 wt% of PP by SEM method was conducted for completeness of this work.

SEM images of untreated BPP samples with different magnifications are shown in
Fig. 8.1. At high magnification (x30000 and x10000) one can see carbon black particles [150, 202–204] on graphite surface [202, 205–207]. Magnification up to x1000 allows to see the binding PP on the surface [208–210].

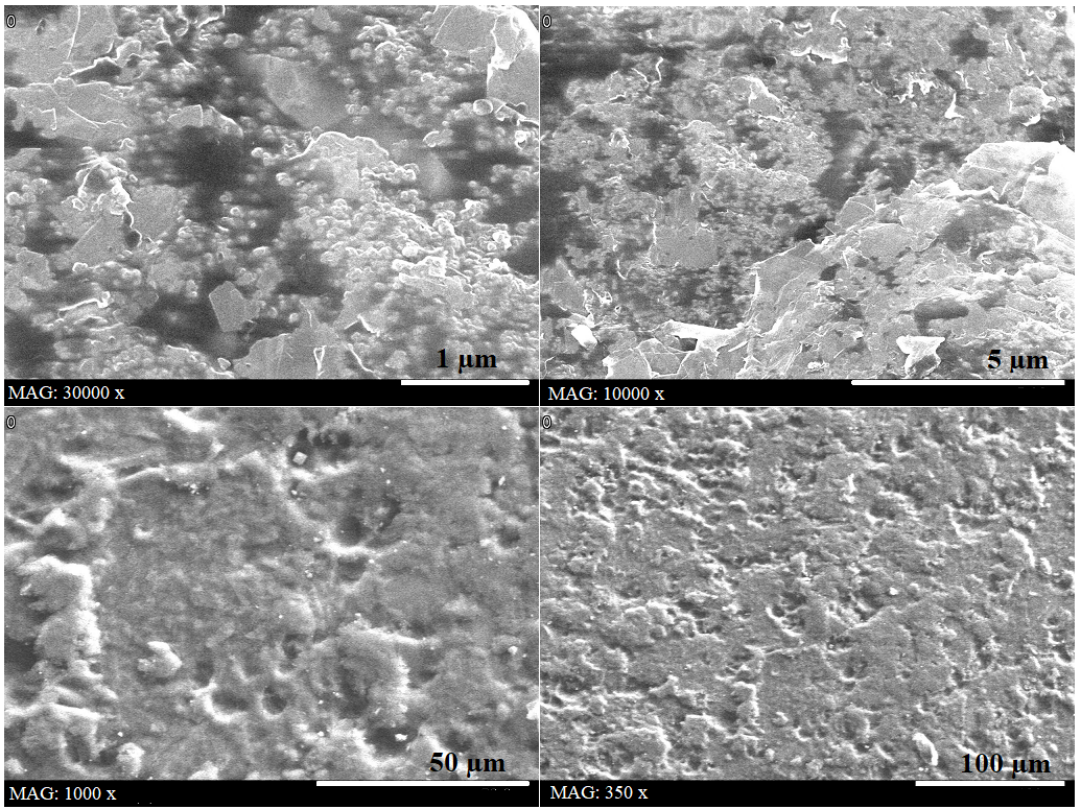

Figure 8.1: SEM images of untreated BPP.

The particles of carbon black are visible at x10000 magnification in Fig. 8.2 (B), but higher magnification (x100000) in Fig. 8.2 (A) allows to see that carbon black is bound by PP. SEM images of pure PP used in the composition of BPP and foils are shown in Fig. 8.3.

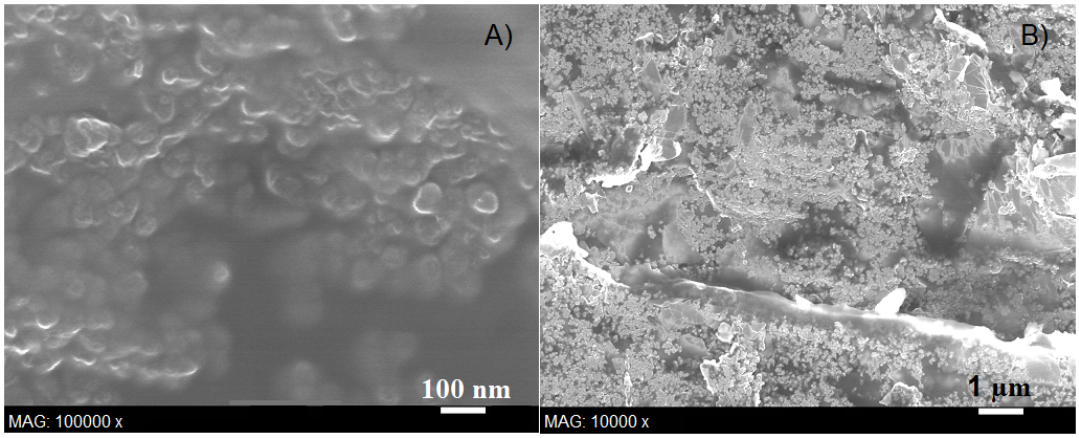

Figure 8.2: SEM images of untreated BPP with magnification of: A) x100000; B) x10000.

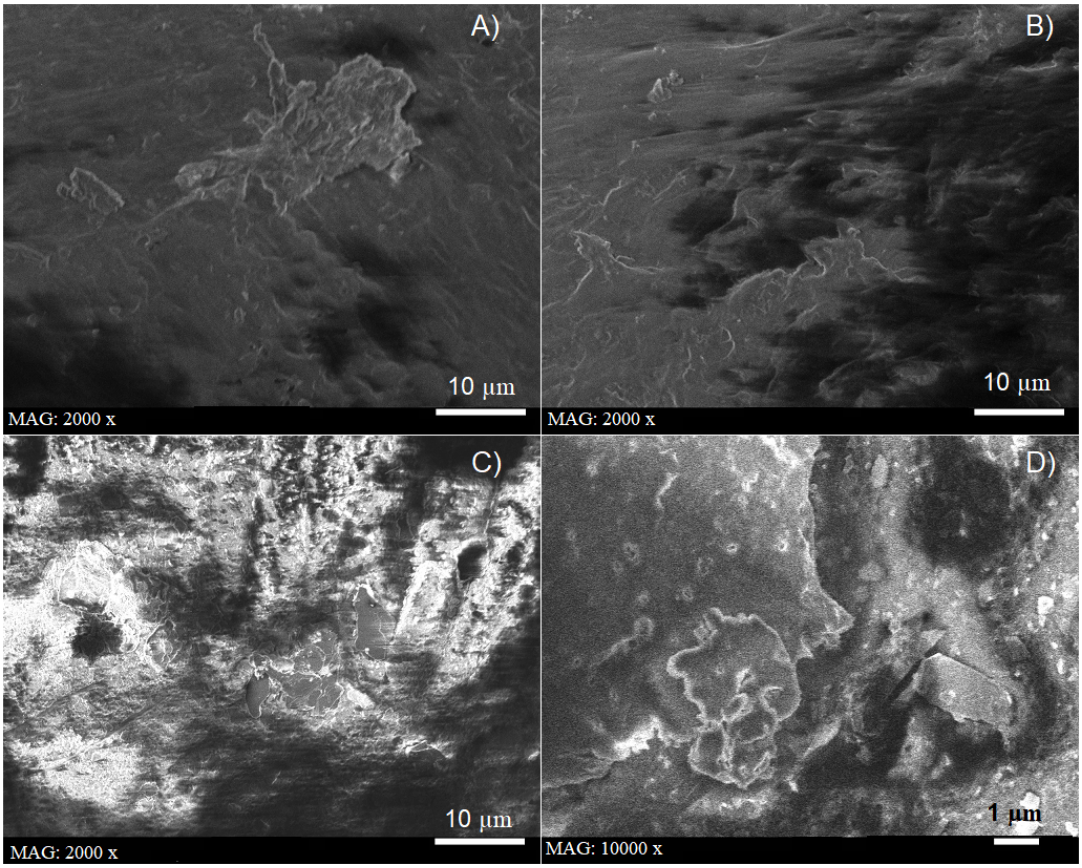

Figure 8.3: SEM images of PP.

Fig. 8.4 shows the surface of a BPP 20 min treated in air plasma: magnification x3300 (left) and x43000 in two different spots of the surface (center and right). The left image with lower magnification shows a graphitic surface of BPP intensively treated in plasma, while the images with higher magnification allow to see constantly distributed particles in a range of diameters from several up to around 50 nm. Presumably these are graphite nanoparticles and remained parts of PP bound carbon black. Though, clarification of the reason of such distribution of the particles after air plasma treatment requires more detailed studies.

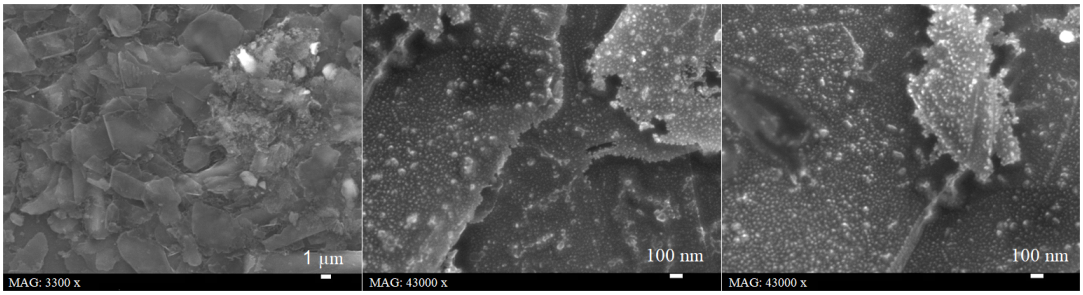

Figure 8.4: SEM images of BPP treated by air plasma (60 mbar; 20 min; 4 cm).

The change of the morphology of the samples, as well as the change of electrical resistance due to plasma treatment, strongly depends on chosen experimental parameters, which, in turn, depend on chemical composition of the sample. So, the surface in
Fig. 8.5 of a foil with 35 wt% of PP treated in oxygen plasma for 7 min still has PP bound carbon black in contradistinction to the surface in Fig. 8.6 of a foil with 29 wt% of PP treated in air plasma at the same conditions, which has a lot of unbound carbon black particles.

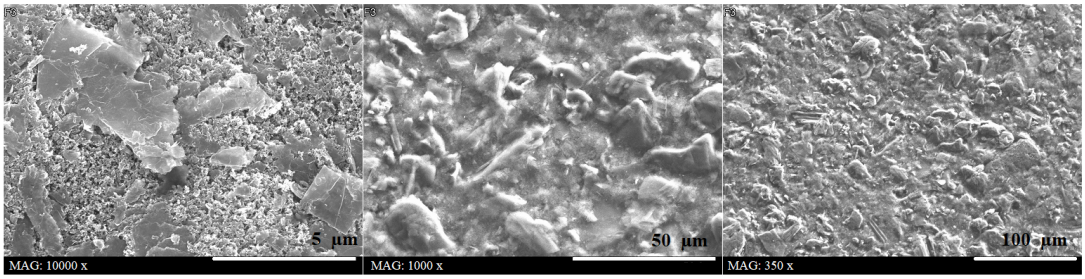

Figure 8.5: SEM images of a treated foil with 35 wt% of PP.

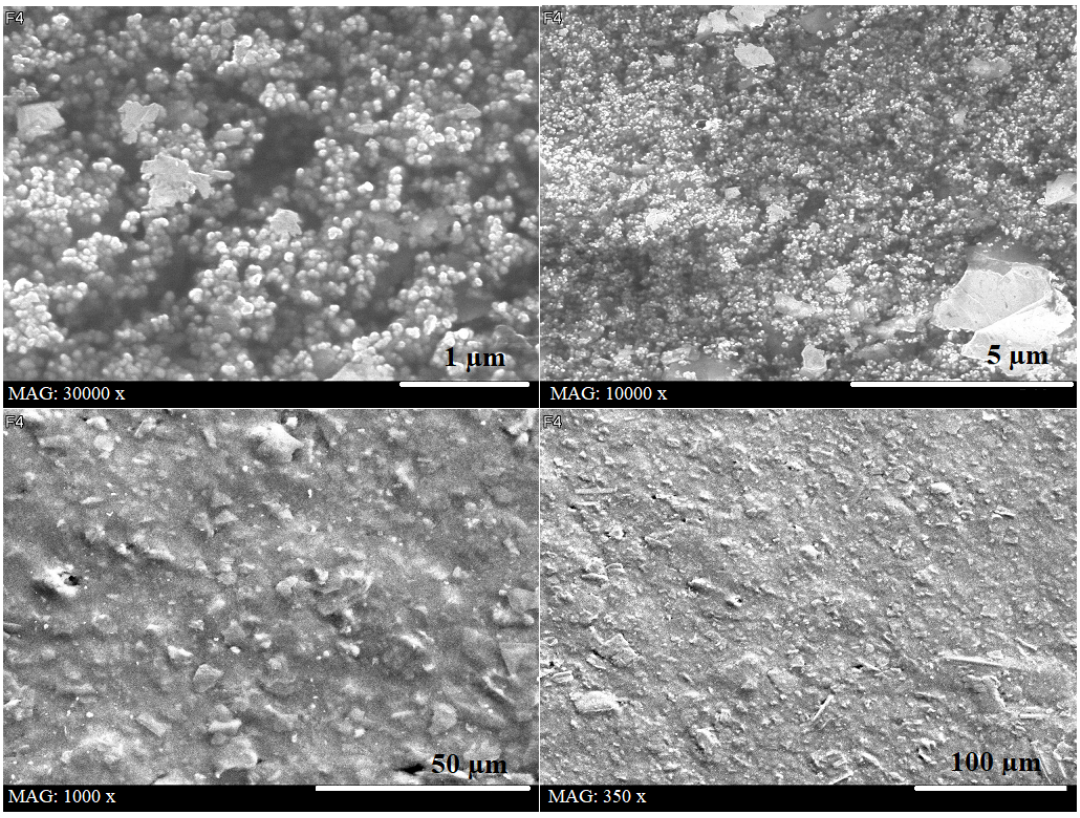

Figure 8.6: SEM images of a treated foil with 29 wt% of PP.

Air plasma treatment appeared to be less intensive than CO_2 plasma treatment at the same conditions. Although the right selection of experimental parameters makes air plasma treatment as effective as CO_2 plasma treatment for the present application, the surfaces of BPP treated by air differ from those treated by CO_2

at a high magnification.

Carbon black bound by PP is still well definable at high magnification SEM images (Fig. 8.7 (A) and (B)) of BPP treated in CO_2 plasma for 5 min at the distance from plasma chamber of 4 cm and with gas flow of 100 sccm.

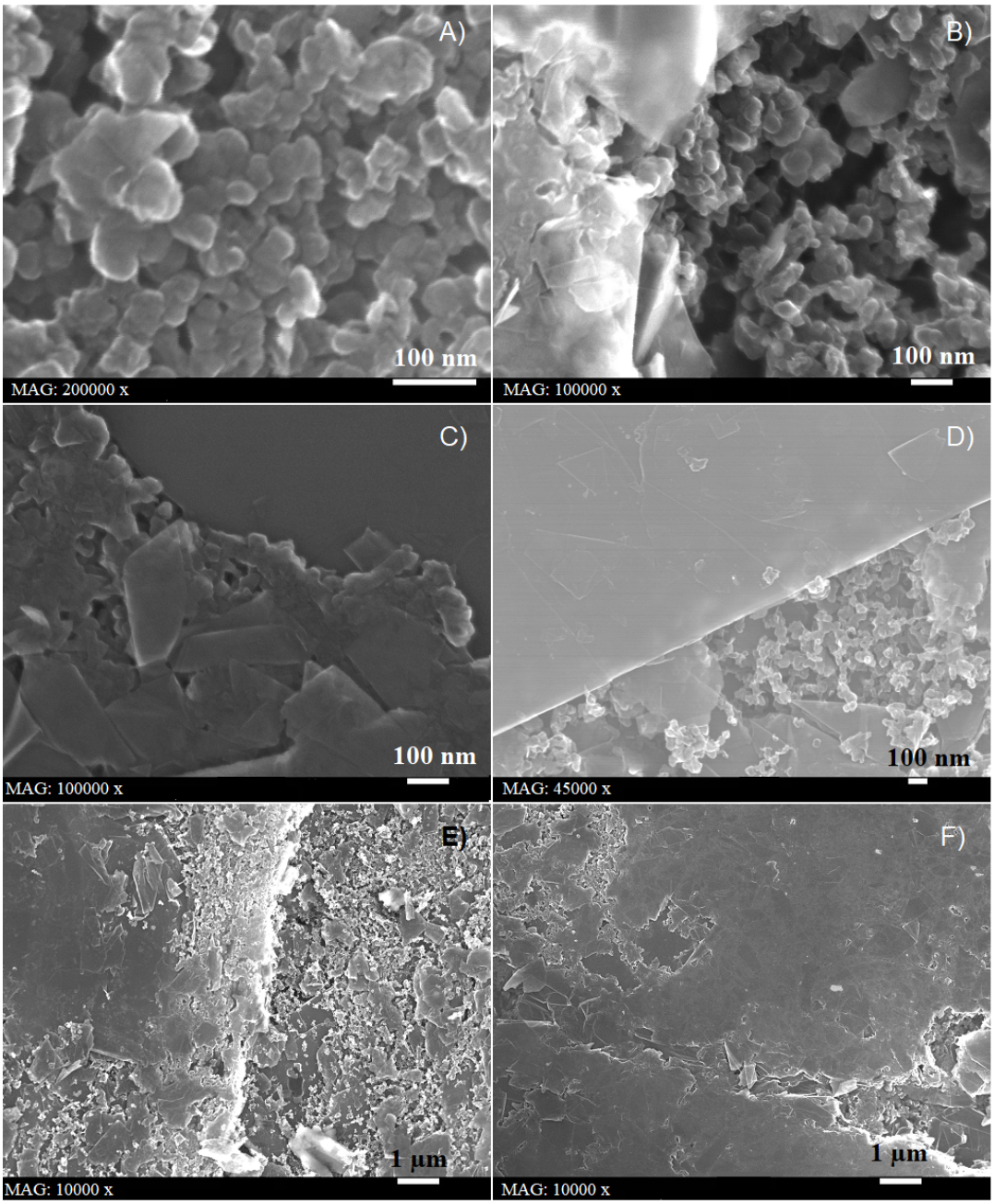

Figure 8.7: SEM images of the BPP 5 min treated in CO_2 plasma with magnification of: A) x200000; B) and C) x100000; D) x45000; E) and F) x10000.

The magnification of x45000 (Fig. 8.7 (D)) also allows to recognize bound carbon black particles, but, as well as Fig. 8.7 (C) with x100000 magnification,

it also shows that the surface, 5 min treated in plasma, is partly free from PP and carbon black. These areas look rather like surfaces of commercially available graphite [211–215]. The comparison of the SEM images with magnification of x10000 in Fig. 8.2 (B) (untreated BPP)
Fig. 8.7 (E) and (F) (5 min treated in CO_2) allows to see that the carbon black bound by PP has been partly removed by plasma treatment during 5 minutes, but can still be found on the irregularities of the surface. This fact explains a significant improvement of wettability of BPP after 3 – 5 min CO_2 plasma treatment (Fig. 7.13 in Chapter 7.3): considering the presented SEM images, the amount of hydrophobic PP on the surface significantly decreases in the first minutes of plasma treatment.

Carbon black bound with PP is not found on the surfaces of the samples treated in CO_2 plasma for 20 min. Fig. 8.8 (A) and (B) show the graphitic surface of the 20 min treated sample. However, carbon black can be seen between the "flakes" of the graphite structure (Fig. 8.8 (C)) especially with high magnification (Fig. 8.8 (D)).

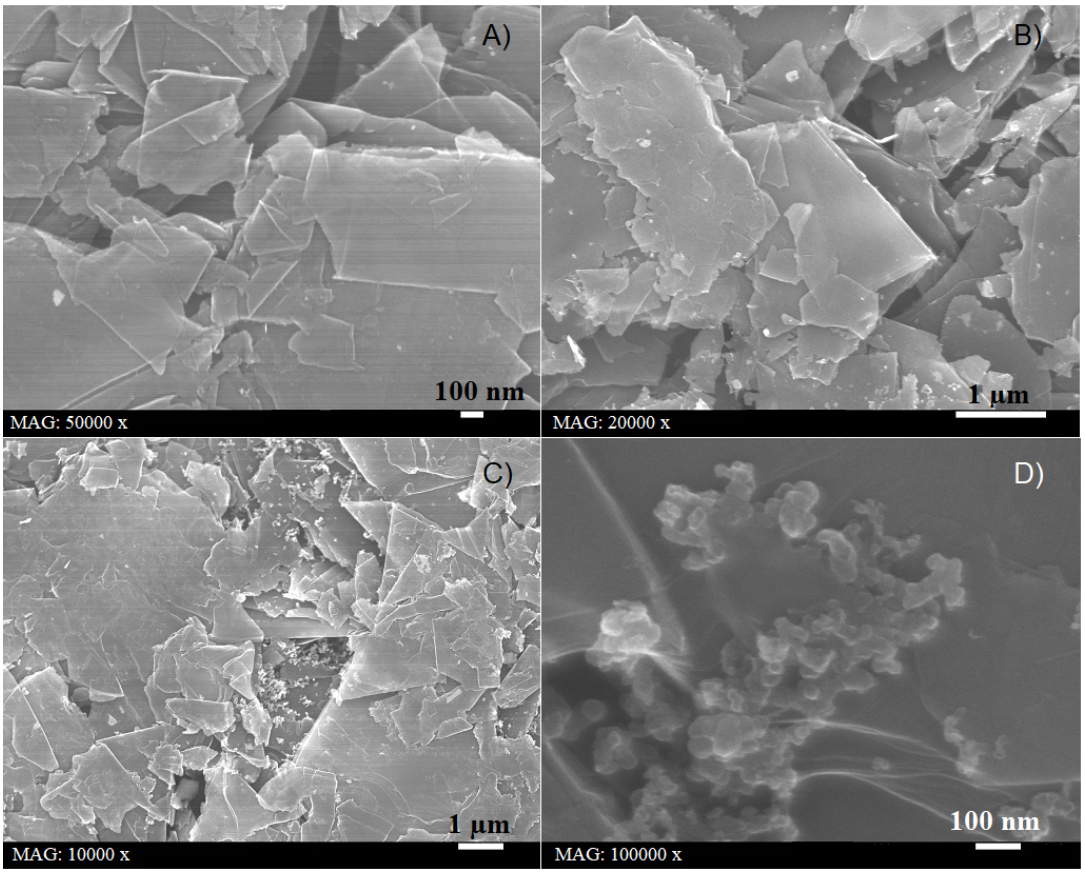

Figure 8.8: SEM images of the BPP 20 min treated in CO_2 plasma with magnification of: A) x50000; B) x20000, C) x10000; D) x100000.

The surfaces of BPP untreated and treated for 5 min and for 20 min are compared in Fig. 8.9 with x500 magnification: contaminations and surface irregularities due to PP bound carbon black, which are clearly visible on the surface on the untreated BPP (Fig. 8.9 (A)), are removed during the first minutes of plasma treatment, therefore, the 5 min treated surface (Fig. 8.9 (B)) is more homogenous and clean from contaminations, but PP still covers the surface. Whereas the surface treated for 20 min in Fig. 8.9 (C) looks graphitic and again not so homogeneous as in Fig. 8.9 (B).

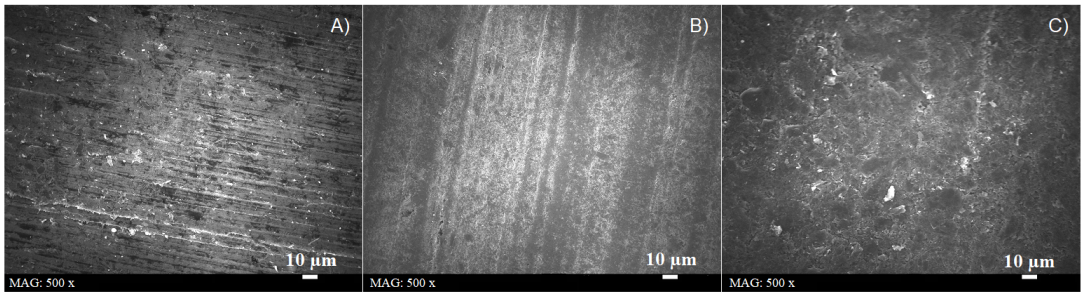

Figure 8.9: SEM images (x500) of BPP: A) untreated; B) 5 min treated in CO_2 plasma, C) 20 min treated in CO_2 plasma.

If the conditions of plasma treatment are harder, for example shorter distance to the plasma chamber and longer treatment time, the carbon black particles do not disappear completely. It can be some remained carbon black bound with PP, or particles of graphitic powder with carbon black. SEM method does not allow to distinguish between them. Fig. 8.10 shows SEM images with different magnification of the samples, treated at the distance of 2 cm from the plasma chamber for 20 and 30 min. Magnification x350 up to x1000 does not show any differences, but from x10000 to x30000 one can notice slightly less carbon black particles on the surface, treated for 30 min (Fig. 8.10 (B)), than on the surface treated for 20 min (Fig. 8.10 (A)).

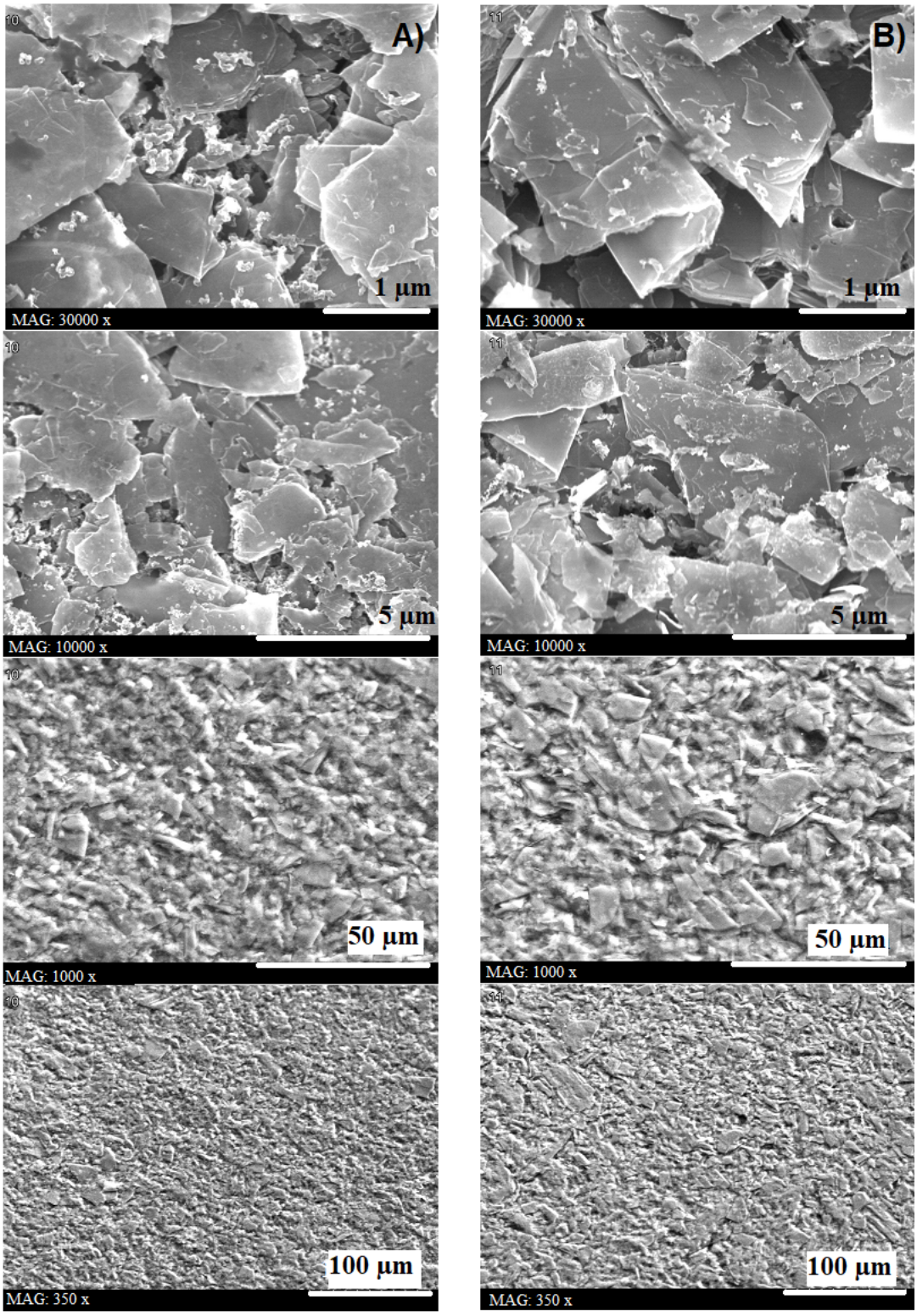

Figure 8.10: SEM images of BPP, treated in CO_2 plasma at the distance to the plasma chamber of 2 cm: A) for 20 min; B) for 30 min.

Increasing the gas flow at the same pressure does not allow to remove PP in first minutes of plasma treatment. Comparing the surface of BPP treated for 3 min in CO_2 plasma with gas flow of 3.85 slm (Fig. 8.11 (top)) with the surface of BPP treated for 5 min with gas flow of 100 sccm (Fig. 8.7 (E) and (F)), one can see the advantage of longer plasma treatment even with much smaller gas flow: less carbon black bound with PP is found on the surface which was treated for 5 min. The surface of the sample treated for 3 min at 3.85 slm with magnifications of x350 and x1000 in Fig. 8.11 (bottom) looks rather like the surface of untreated BPP covered by PP (Fig. 8.1 (bottom)).

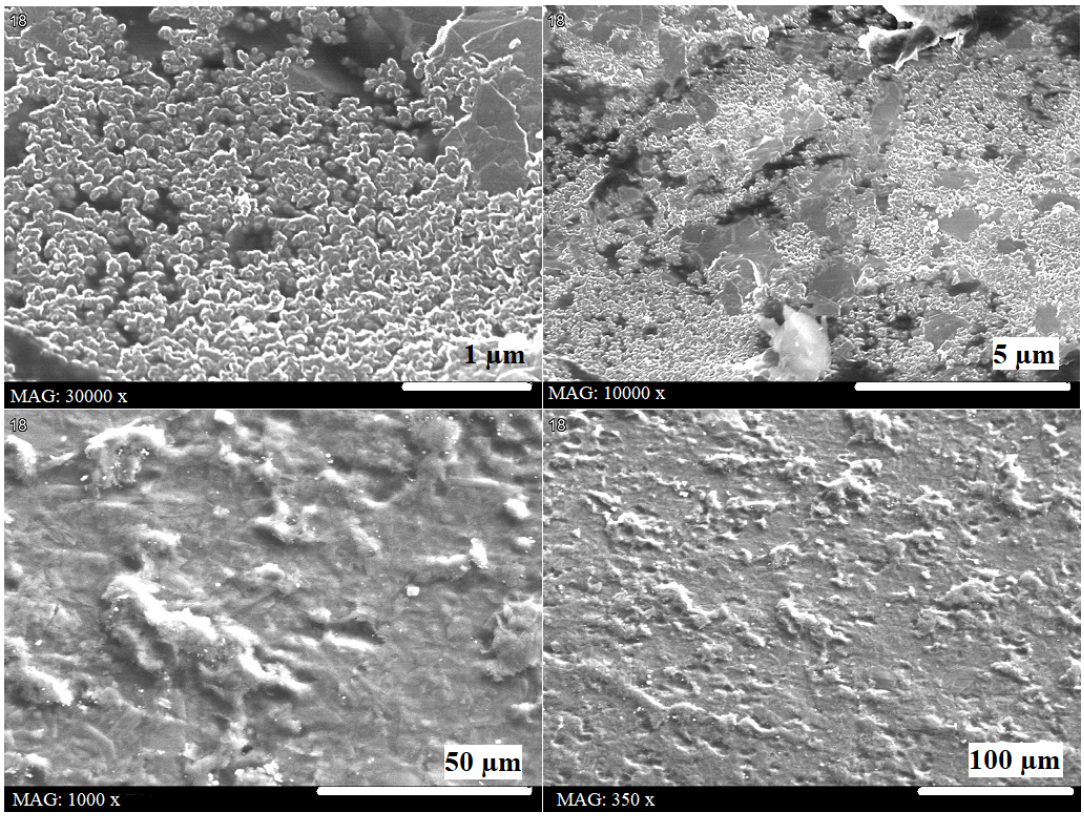

Figure 8.11: SEM images of BPP 3 min treated in CO_2 plasma (8.5 mbar; 4 cm; 3.85 slm).

Plasma treatment duration of 3 min does not remove contaminants of width about
200 nm and more from the surface, such relatively big particles (visible in Fig. 8.12)

remain on the surface, shortly treated in plasma. The results of EDX analysis of contaminative particles larger than 1 μm are shown in Chapter 7.7.

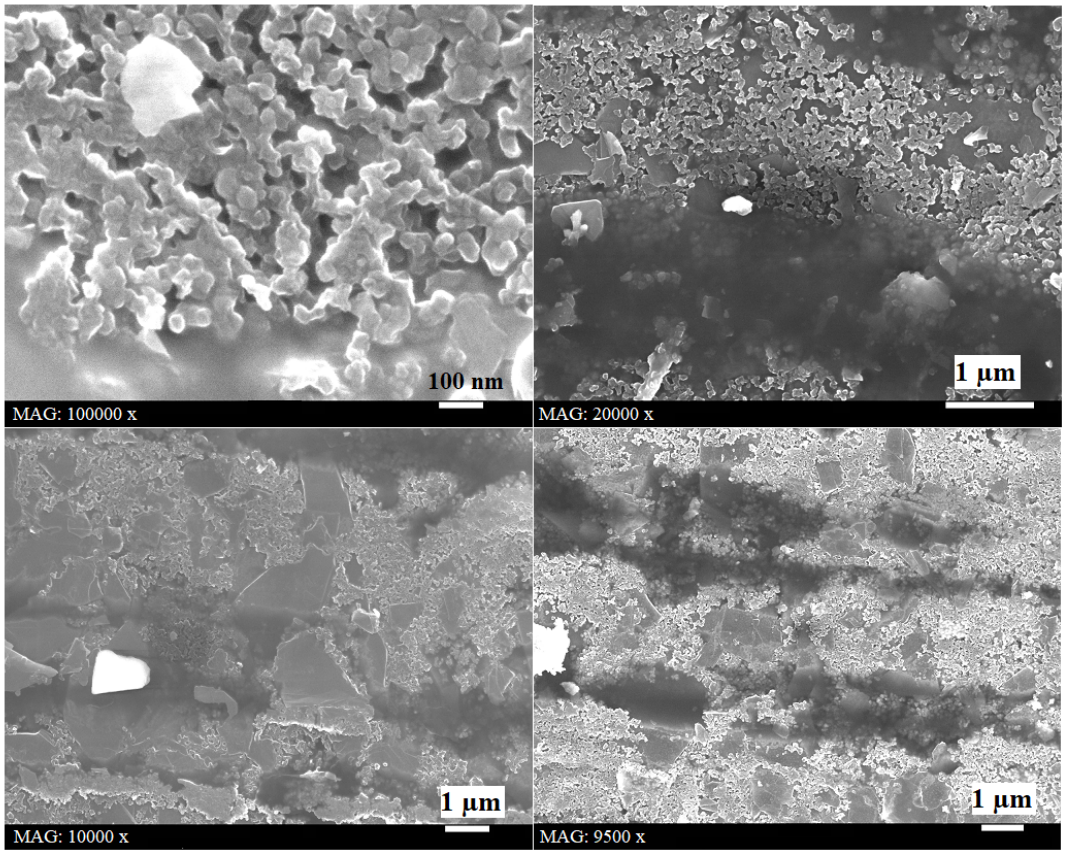

Figure 8.12: Contaminations on the surface of BPP 3 min treated in CO_2 plasma (8.5 mbar; 4 cm; 3.85 slm).

Further increase of plasma treatment duration leads to the following changes (Fig. 8.13): the surface treated for 5 min does not differ much from the surface treated for 3 min in Fig. 8.11, even though with big magnification one can see that the surface was treated in plasma; there is almost no carbon black bound with PP on the surface exposed to CO_2 plasma for 7 min, but with the magnification of x350 one can still see PP on the surface, though it looks smoother than on the surface treated for 5 min; a lot of graphite particles are seen on the surface exposed to the plasma for 15 min and even the magnification of x350 allows to recognize the graphitic structure of the surface. This magnification also allows to

see that the craters seen on the surface exposed to the plasma for 5 min disappear with the increase of plasma treatment time.

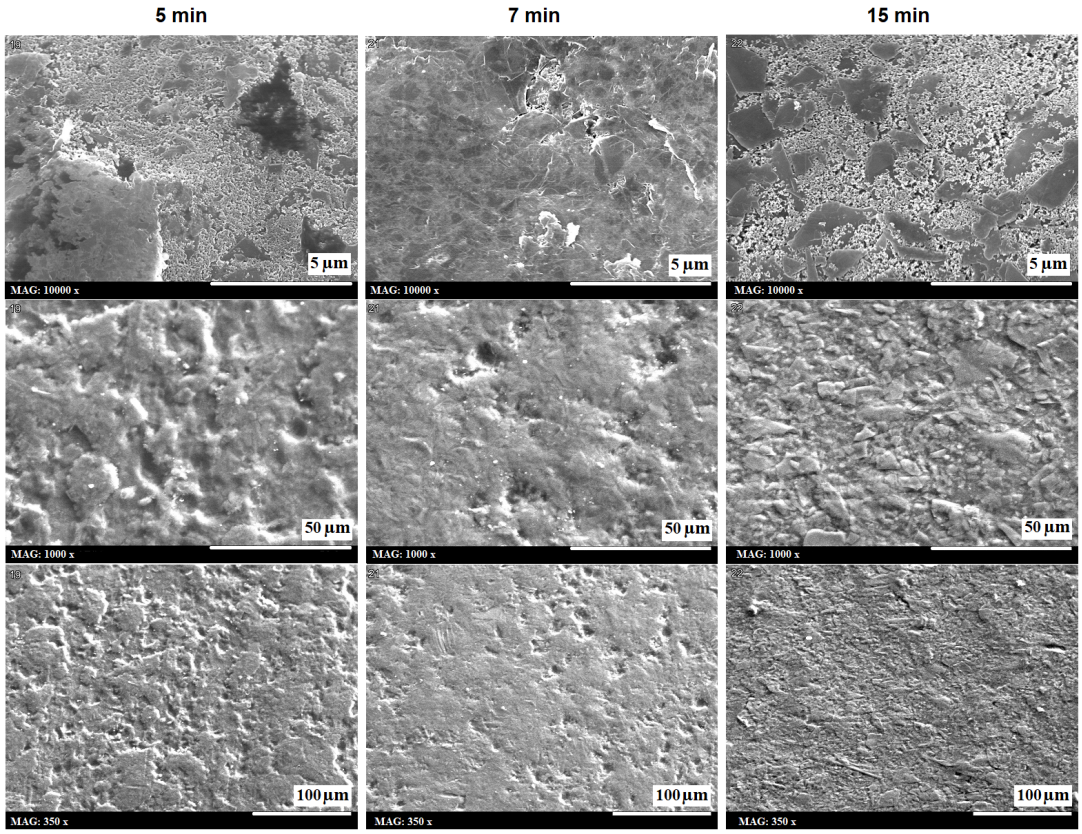

Figure 8.13: Comparison of the surfaces on BPP treated in CO_2 plasma (8.5 mbar; 4 cm; 3.85 slm) for 5 min (left), 7 min (center) and 15 min (right).

Plasma treatment for 20 min almost completely removes PP from the surface. Fig. 8.14 shows the differences of morphology of the surfaces exposed to CO_2 plasma. Carbon black and PP visible on the surface treated for 7 min are not obviously noticeable on the surface treated for 20 min. Some minor particles visible on the 20 min treated surface may be graphite powder particles or carbon black with remaining PP. The particles larger than 1 μm are definitely contaminants.

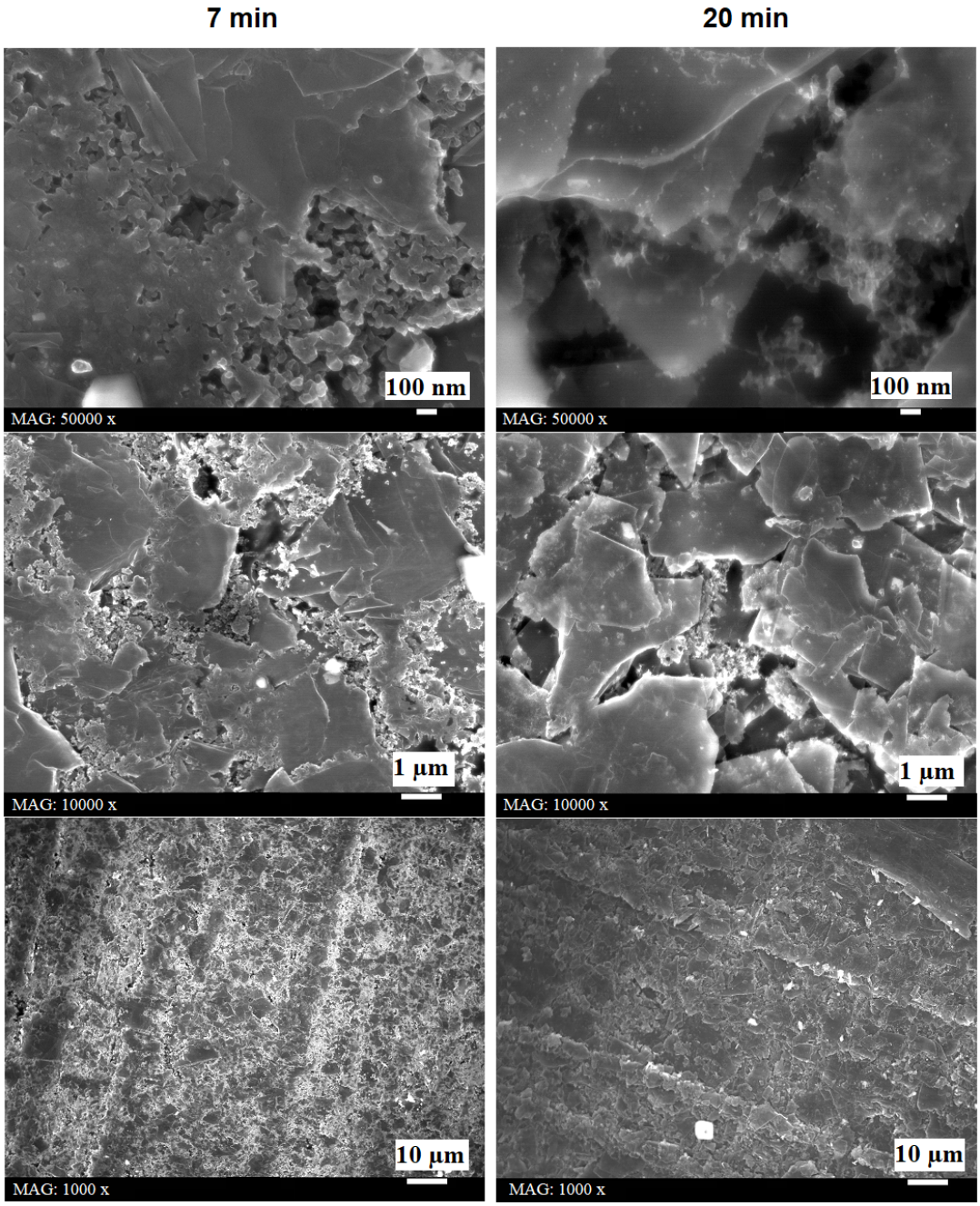

Figure 8.14: Comparison of the surfaces on BPP treated in CO_2 plasma (8.5 mbar; 4 cm; 3.85 slm) for 7 min (left) and 20 min (right).

SEM is a very suitable method to observe the process of polymer destruction

during the plasma treatment of BPP. Visual comparison of SEM images of untreated BPP in Fig. 8.2 and BPP treated for 10 min in CO_2 plasma (Fig. 8.15) allows to see the shape change of bound carbon black and presence of space between the PP boundaries of carbon black. Especially noticeable it is with the magnification of x100000: Fig. 8.2 (left) and Fig. 8.15 (bottom right).

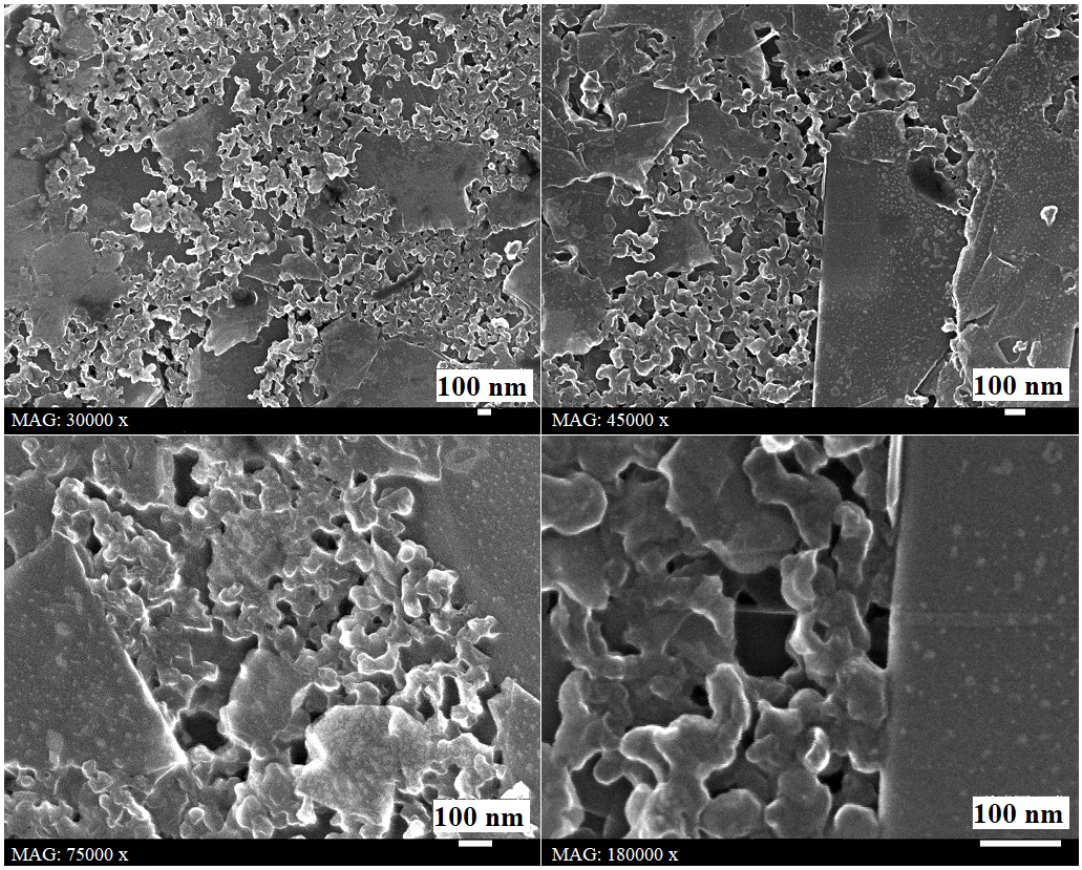

Figure 8.15: SEM images of BPP treated for 10 min in CO_2 plasma (8.5 mbar; 4 cm; 3.85 slm).

Investigation of morphology of the samples gives a good perception of the visual changes on the surface due to plasma treatment and allows to evaluate the rough sizes of the inhomogeneities, what helps to choose the suitable techniques to estimate the roughness of the surface.

It is shown how plasma treatment at different conditions changes the surface, removes PP and carbon black bound with PP from the surface until the graphitic

structure of the surface is clearly recognizable.

8.2 Roughness and Topography

Surface topography was studied by stylus profilometry, AFM and confocal microscopy methods. AFM and confocal microscopy techniques also provide a possibility to investigate the surface morphology, what gives a perception of two- or three-dimensional view of a surface.

The accuracy of the roughness measurements should be regarded within the confines of each method. For example, the stylus of profilometer with 12.5 μm or 25 μm radius cannot define the changes of nano-roughness, which are definable by AFM tip with the radius of 20 nm. However, profilometry can be more informative in case if the height of the surface changes above several μm.

The differences of the roughness parameters obtained by different methods can be explained by different physical principles of these methods. So, for example, AFM profile is a combination of the shape of the surface and the form of the probe needle, what may understate the values of roughness [143]; the values measured by profilometer may also be slightly distorted if the size of the stylus is not right for the studied surface. Also relatively large sampling lengths complicate the comparison of the results because of non-periodical form of relief. The values Ra and Rq measured by confocal microscope significantly differ from those measured by AFM and profilometer. Such mistakes as bad sample or unsuitable measurement area are excluded by the measurement of several samples, which have comparable values of amplitude parameters. This difference is related to the method of confocal microscopy and the measurement settings.

AFM investigation was conducted on randomly selected areas with the sizes of 35x35 μm^2, 40x40 μm^2 and 100x100 μm^2 of BPP surfaces. The AFM data were analyzed by the software Gwyddion 2.49. 3D AFM images of the surface morphology of BPP untreated and 20 min treated in CO_2 plasma are presented in Fig. 8.16. Profile lines of 0.14 mm of the same samples are shown in Fig. 8.17.

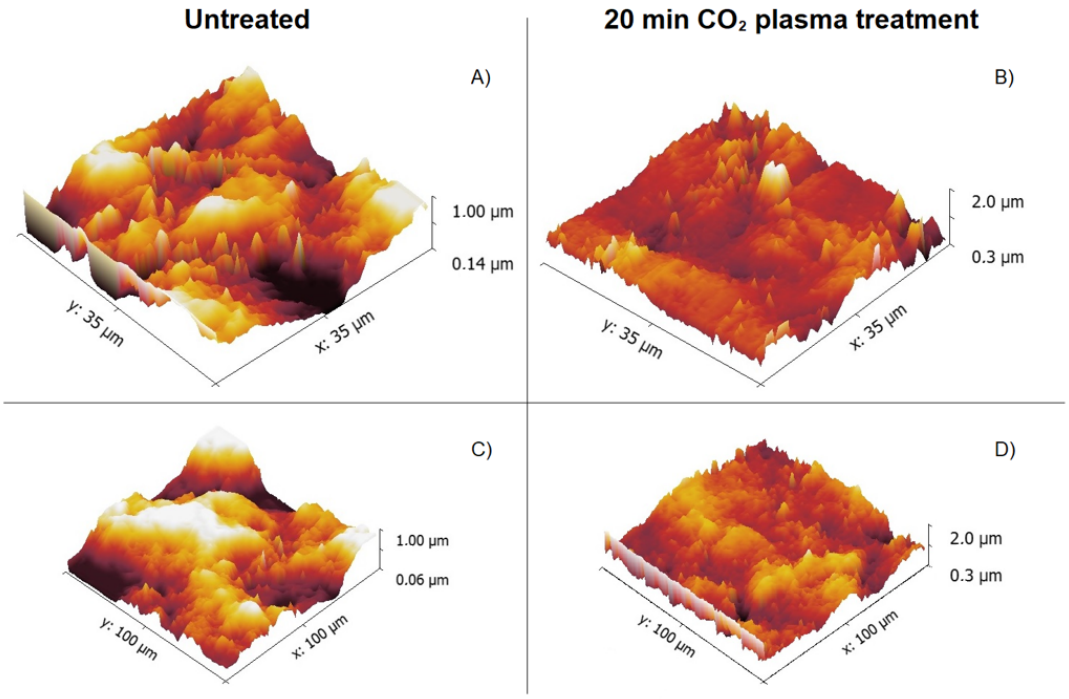

Figure 8.16: 3D AFM images of 35x35 μm^2 area for: A) untreated and B) CO_2 plasma-treated BPP; and of 100x100 μm^2 area for: C) untreated and D) CO_2 plasma-treated BPP.

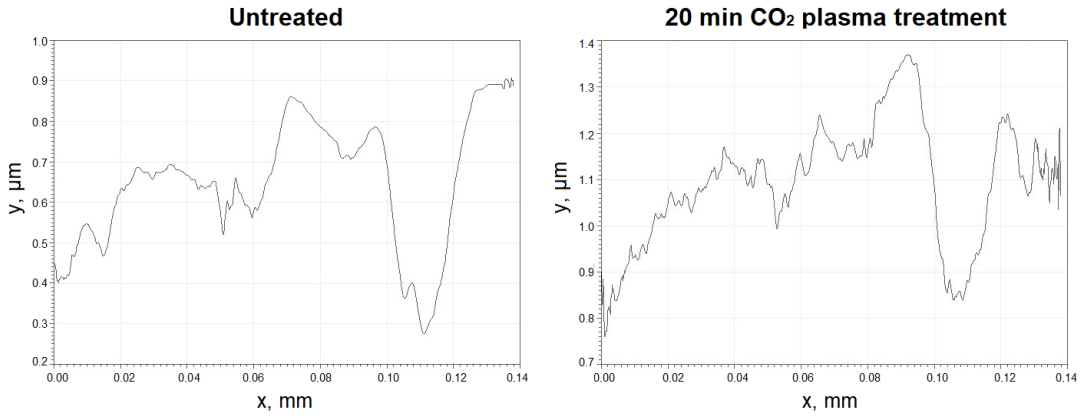

Figure 8.17: Profile lines of 0.14 mm of BPP untreated (left) and 20 min treated in CO_2 plasma (right) .

Table 8.1 shows the values of R_a and R_q obtained by AFM for untreated and treated BPP. These average values were calculated for 0.5x19 μm^2 parts of the

evaluated square. It was done due to the limitations of the roughness determination by AFM [216]. In the standard AFM technique the AFM tip typically has a radius of 5 – 50 nm [217]. Due to the finite size of the AFM tip imperfections in AFM images and thus errors in the roughness determination may take place. Such errors are especially important when imaging highly corrugated surfaces [216].

Table 8.1: R_a and R_q roughness of BPP measured by AFM.

Roughness	**Untreated** nm	**20 min treated in air** nm	**20 min treated in CO_2** nm
R_a	194.1	226.6	256.8
R_q	226.8	290.2	304.9

In the light of the above-mentioned considerations, one can state that the roughness of BPP increases in nano-range after plasma treatment.

Since the surfaces of BPP may be relatively rough, Veeco Stylus Profilomter Dektak 6M with Dektak 32 Version 8.34 software was used to define the roughness in micro-range of the scan length. Table 8.2 shows the roughness parameters obtained by the stylus profilometer with the scan length of 1800 μm. Plasma treatment by argon cleans the surface of BPP from contaminations, but inert argon does not etch the surface, therefore the roughness of the sample treated in argon plasma decreases comparing to the roughness of the untreated sample. The roughness of BPP increases after the treatment in CO_2 plasma, whereas it decreases after the air plasma treatment. This result differs from the AFM result in Table 8.1, where the untreated BPP has the smallest values of amplitude roughness parameters. Presumably the reason of higher AFM-measured roughness of the air-treated sample compared to the untreated sample is the presence of the nano-sized particles visible in SEM images of BPP treated by air plasma in Fig. 8.4, which cannot be defined by the stylus of profilometer with 12.5 μm radius within the confines of the profilometry method, but are definable by AFM.

Table 8.2: Roughness parameters of BPP untreated and treated for 20 min in different gases measured by profilometer.

Roughness	**Untreated** nm	**Air** nm	**CO_2** nm	**Ar** nm
R_a	203.2	176.0	325.2	198.1
R_q	251.1	2130.0	400.0	248.1
R_v	-611.3	-384.6	-908.5	-756.3
R_p	848.6	688.1	1176.3	571.4
R_t	1459.9	1072.7	2084.8	1327.7
R_{tm}	846.2	812.5	1624.1	783.1
R_{sk}	0.165	0.615	-0.078	-0.422

The measurement with a stylus with 25 μm radius showed slightly lower roughness: R_a of 258 nm and R_q of 332 nm, compared to the values obtained by 12.5 μm radius stylus: 325.2 nm and 400 nm, respectively, for the sample treated in CO_2 plasma. The larger stylus gives a better representation of shape by means of "filtering" out the roughness. The smaller stylus provides more accurate roughness measurement [218].

Investigation of roughness of the foils treated in plasma showed very high values of roughness on the scan length of 2500 μm (Fig. 8.18) and the increase of roughness with the increase of plasma treatment time or gas flow, as shown in Table 8.3.

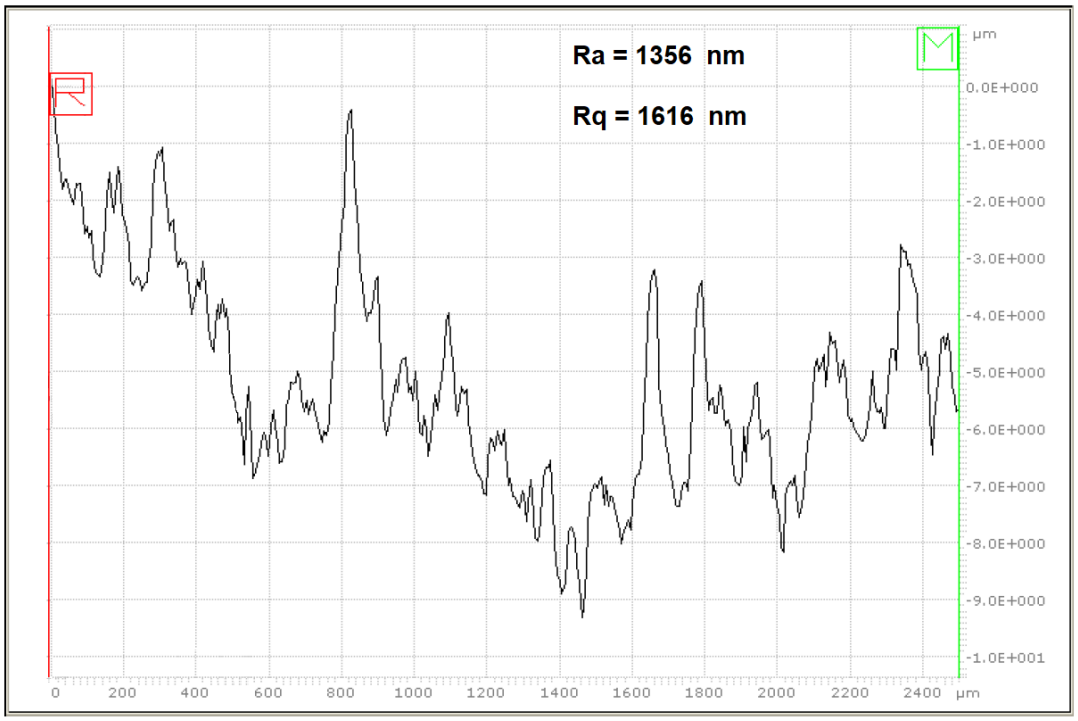

Figure 8.18: Profile line of a foil (31 wt% of PP) treated in air plasma (20 min, 990 mbar, 6 cm,
17 slm).

Table 8.3: Roughness parameters of the foils treated in air plasma, measured by profilometer.

Conditions	**PP** wt%	$\mathbf{R}_a$ nm	$\mathbf{R}_q$ nm
5 min, 960 mbar, 17 slm		1181.2	13774.7
10 min, 990 mbar, 17 slm	31	1168.2	1648.2
15 min, 990 mbar, 17 slm		1356.0	1615.9
3 min, 10 mbar, 0.5 slm		658.0	783.6
3 min, 10 mbar, 2 slm	29	1362.7	1706.0
3 min, 10 mbar, 7 slm		1372.9	1674.6

Electrical conductivity increases due to removal of PP from the surface and due to bigger contact area, what means lower values of roughness.

Plasma etching removes PP from the surface, but also etches and increases the roughness of the graphitic surface. Therefore, it is important to find suitable plasma treatment parameters and to decrease the etching duration as much as it is still enough to remove the most of PP from the surface. However, the measurements of resistance, which were conducted under the pressure of 20 bar, showed that the roughness does not influence the electrical conductivity of the samples as much as the presence of PP on the surface. PP is the main factor responsible for bad electrical conductivity. The samples treated in CO_2 plasma for longer than 20 min, despite the roughness increase, had the best conductivity performance, though such treatment conditions worsen the mechanical properties of BPP.

The data obtained by NanoFocus μsurf Custom with Gaussian filter and analyzed by μSoft Analysis Premium 5.1.1.5785 software showed the increase of roughness after treatment in air plasma (20 min, 4 cm, 8.5 mbar), as shown in Table 8.4. Random areas with the size of 150x150 μm^2 on the surfaces of BPP were investigated.

Table 8.4: Roughness parameters of untreated and treated BPP measured by confocal microscopy method.

Roughness	**Untreated**	**Treated for 20 min in air plasma**
	nm	nm
R_a	78.1	101
R_q	99.8	141
R_p	225	470
R_v	266	360
R_z	491	831
R_c	243	341
R_t	849	1220
R_{dc}	162	163
R_{sk}	0.0217	-0.0505
R_{ku}	3.30	4.73
R_{mr}	100 %	95.4 %

Another interesting observation is the increase of kurtosis of the roughness profile (R_{ku}) value after plasma treatment, what can be seen in Table 8.4. Even

though this value was not measured by other methods, the results obtained by AFM allow to observe the increase of sharpness of the profile after the exposure to plasma (see Fig. 8.17). Visually it can also be seen in Fig. 8.19. J. H. C. Yang and K. Teii in [173] describe their investigation of morphology of nanocrystalline diamond films by AFM, in particular, the generation of a large number of "fine cone-like structures" on the surface due to oxygen plasma treatment, instead of granular morphology of as-deposited films. The authors report:

> „The trend of the morphological change without nitrogen addition was similar to that with nitrogen addition."

[173], what allows to suppose that oxygen from the air is responsible for the formation of the profile sharpness after the treatment by air plasma.

It was experimentally confirmed that BPP treated in oxygen-containing plasma have the best electrical properties: the highest conductivity and the lowest values of area-specific resistance, due to the high reactivity of oxygen. For this reason, the working gas for plasma treatment of BPP should always be oxygen-containing, what should lead to more significant profile sharpness, as mentioned above. In the process of resistance measurement, described in Chapter 4.3.2, two BPP appear under the pressure of 20 bar, what, most probably, leads to the destruction of the sharp peaks of graphite structure. This destruction increases the contact areas with GDL, what, in turn, contributes to the better electrical conductivity. Therefore, no significant influence of profile sharpness of graphite on electrical conductivity of BPP was found in this investigation.

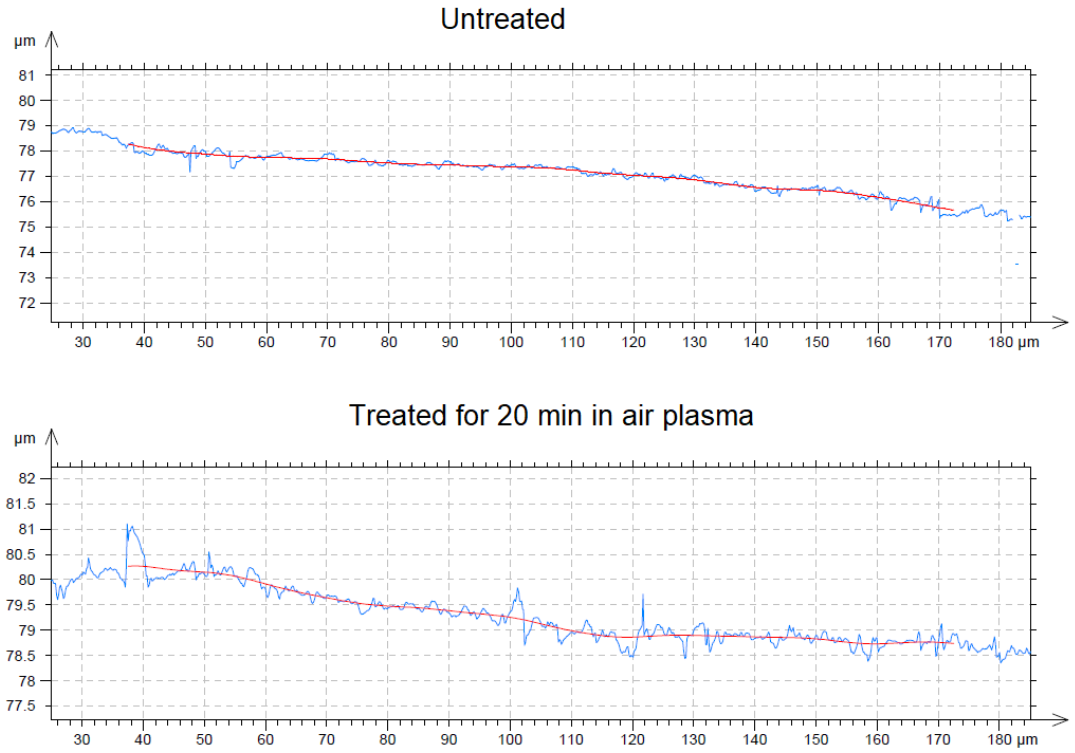

Figure 8.19: Roughness profile and waviness profile of untreated (top) and treated in air plasma (bottom) BPP, measured by the method confocal microscopy.

Table 8.5 shows the comparison of roughness of untreated and 20 min treated in air plasma BPP, measured by AFM, stylus profilometry and confocal microscopy methods.

Table 8.5: Comparison of roughness of untreated and treated in air plasma BPP measured by AFM, stylus profilometry and confocal microscopy methods with different sampeling length L.

Method	AFM	Profilometry	Confocal M.
L	19 μm	1800 μm	160 μm
R_a [nm] Untreated	194.1	203.2	78.1
R_a [nm] Air treated	226.6	176.0	101
R_q [nm] Untreated	226.8	251.1	99.8
R_q [nm] Air treated	290.2	213.0	141

Making a conclusion one can say that the average value of roughness decreases

after the plasma treatment on bigger scan lengths, as profilometry measurements show. Plasma treatment aligns the height of the surface in milli-range. Only the treatment by CO_2 leads to significant increase of roughness even in milli-range, due to the high amount of oxygen and its high chemical activity. AFM investigation in micro-range showed that the roughness of the surfaces treated by argon decreases, because plasma treatment by argon only physically influences the surface. Nevertheless, oxygen-containing plasma removes PP from the surface and etches the graphitic surface, increasing the nano-range roughness of the surface, as AFM method and the method of confocal microscopy show. Higher amount of oxygen in plasma obviously leads to higher roughness after the plasma treatment. The method of confocal microscopy allowed to define the increase of the profile sharpness of the samples treated in oxygen-containing plasma. But no negative influence of increased roughness and sharpness on electrical conductivity was found because of the possibility of profile peaks destruction and increase of contact area under the pressure of 20 bar during the measurement of area specific resistance.

9 Influence of Plasma Treatment on Resistance of BPP

The measurements of area-specific resistance (ASR) were conducted by the device, described in chapter 4.3.2 (Fig. 4.11) [10]. The resistance measurements presented in this work were done by Mario Gillmann, ZBT GmbH (Zentrum für BrennstoffzellenTechnik, Duisburg). The error of an ASR value (bulk resistance and two times contact resistance) is estimated to vary from 3% (measurement error) up to 8% due to production-related dispersion of the composition.

Total ASR value should be below 100 $m\Omega \cdot cm^2$ for BPP [144]. The ASR value of the milled BPP meets these requirements, as well as the ASR value of the sample 20 min treated in air plasma at 0.1 mbar. It means that plasma treatment is as good as mechanical milling, while plasma treatment has no shortcomings of milling.

The process pressure is an important parameter, which influences the final electrical properties of the treated BPP: reduction of the process pressure from 8.5 mbar to 0.1 mbar allows to reduce the ASR of the sample to the required value. The same can be said about the composition of the sample, which defines the initial ASR of the untreated BPP. Some deviations of the initial ASR can be explained by the fact that the injection molded BPP during the production process inevitably contacts some residual material, which has been heated for a long time and may have slightly different properties.

Fig. 9.1 shows the comparison of ASR values of untreated and plasma-treated foils with different PP content: A) the foils were treated by oxygen and air at plasma the pressure of 0.1 mbar; B) the foils were treated by air plasma at

atmospheric pressure (933 mbar).

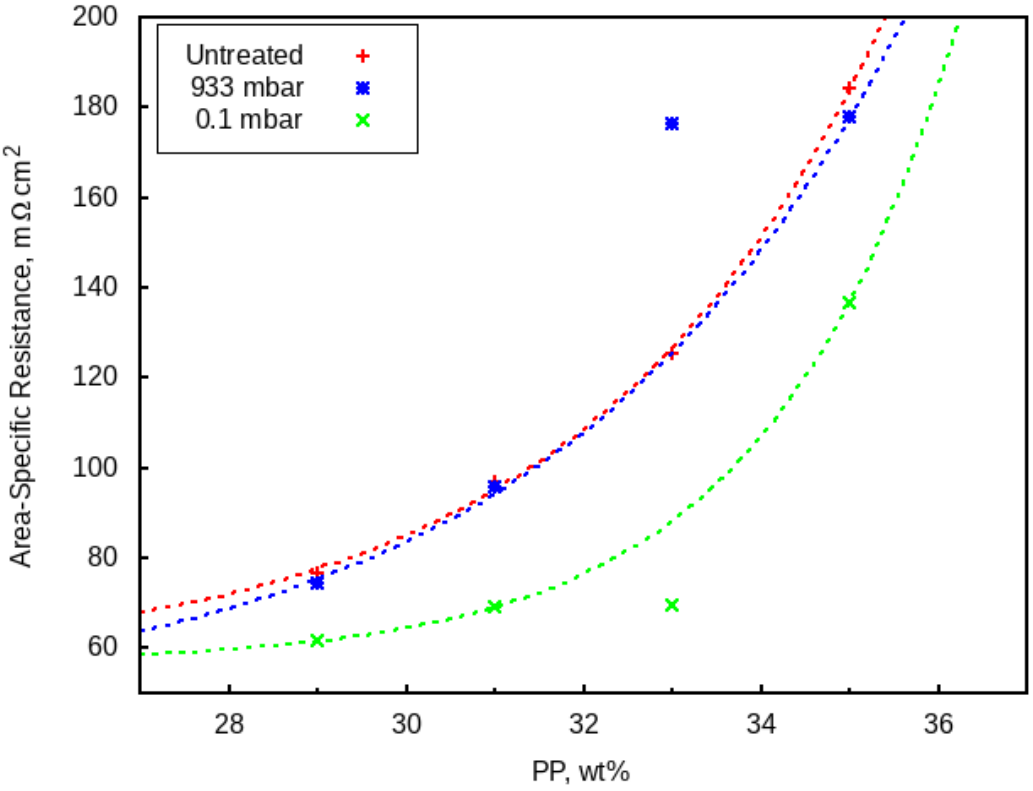

Figure 9.1: ASR dependence on PP content in foils: O_2 and air plasma treatment at 0.1 mbar; air plasma treatment at 933 mbar.

One can again see the high efficiency of low pressure plasma treatment: the ASR values of the samples treated at low pressure are noticeably lower than those of the samples, treated at atmospheric pressure, which are only slightly below the ASR values before the treatment (Fig. 9.1). But in both cases ASR value increases with the increase of PP content in the presented range. This result means that even a slight reduction of binding PP amount in the sample composition has a great positive influence on the electrical conductivity of the sample.

To achieve the required ASR by plasma treatment without mechanical treatment it is necessary to choose right experimental parameters, which can be different for samples which have different geometric sizes and chemical composi-

tion. As it is shown in Fig. 9.2, ASR of untreated samples may be equal in the error range, while ASR of the BPP treated in air plasma decreases with process pressure. Decrease of the distance between the plasma chamber and the sample obviously also leads to faster and more effective plasma treatment, but only with the correct selection of other experimental parameters and only if the treated sample has enough binding PP in its composition, otherwise such distance decrease would lead to unwanted effects (crumbling, cracking, overheating, burning). From the other hand, too big distance does not allow to achieve the required effect of plasma treatment. The optimal distances for the plasma device used were 4 cm for BPP and 6 cm for foils for plasma treatment by air, oxygen or carbon dioxide.

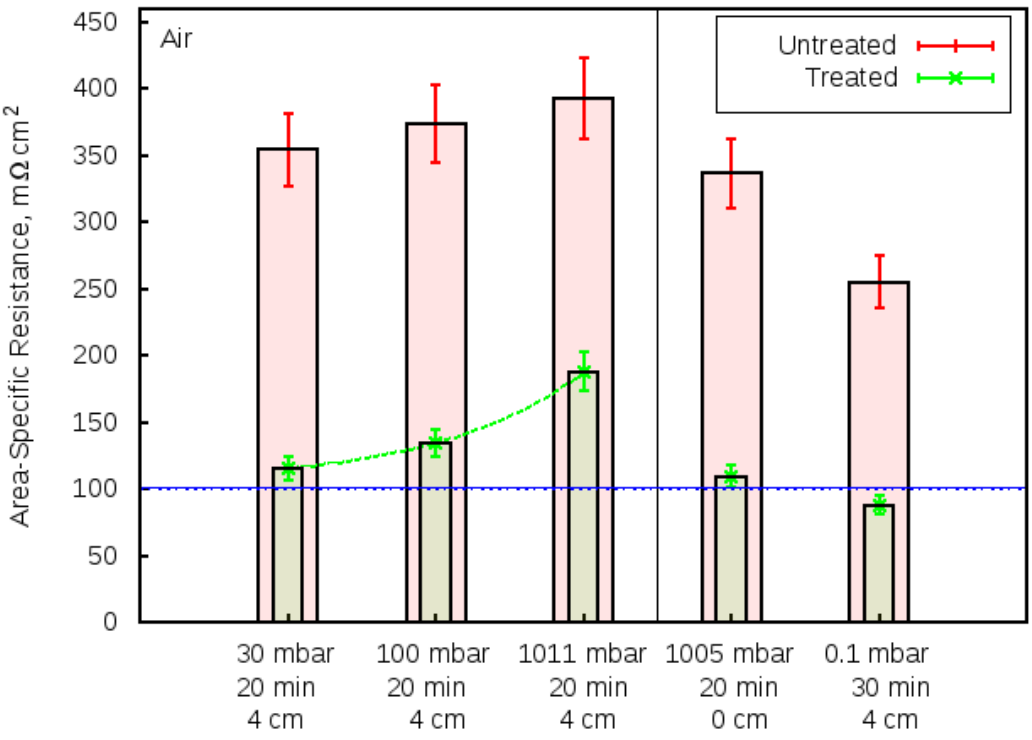

Figure 9.2: Comparison of ASR of BPP untreated and treated by air plasma BPP.

Investigation of foils, treated at different pressures, also showed much better results of plasma treatment at low pressure. For example, the decrease of ASR

of a foil with relatively low PP content (29 wt%) is shown in Fig. 9.3. At low pressure mean free paths in the plasma are longer than at high pressure, the particles have higher energies and interact with the surface more intensively than at high gas pressure.

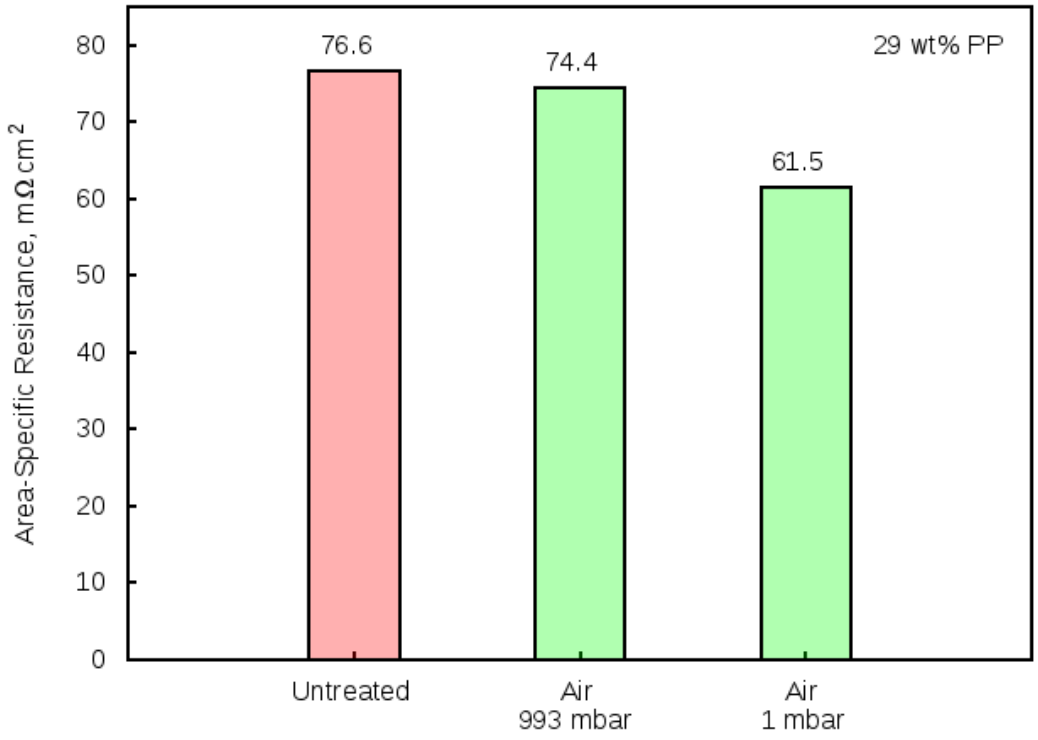

Figure 9.3: Influence of gas pressure during the plasma treatment on ASR of foils (PP 29 wt%).

Duration of the treatment process is an important parameter for the industrial use of this method. Treatment time also has an influence on the result of plasma treatment. Fig. 9.4 shows the ASR values of the BPP treated in air plasma at the pressure of 8.5 mbar and at the distance of 4 cm from plasma chamber for 10, 20 and 30 min, compared to the average value of the samples before plasma treatment. One can see the tendency of ASR decrease with the increase of the duration of plasma treatment, though ASR values do not differ significantly. Plasma treatment for 10 min is enough to decrease the ASR signif-

icantly compared to the average initial ASR value of untreated BPP, but even the treatment for 30 min at 8.5 mbar does not allow to decrease the ASR to the required value of 100 $m\Omega \cdot cm^2$. Longer treatment is not effective, especially for industrial applications, and also may lead to overheating and crumbling of the sample, therefore other process parameters should be varied to achieve the required ASR value.

Fig. 9.4 shows ASR decrease with time, even though ASR values do not differ significantly in the error ranges.

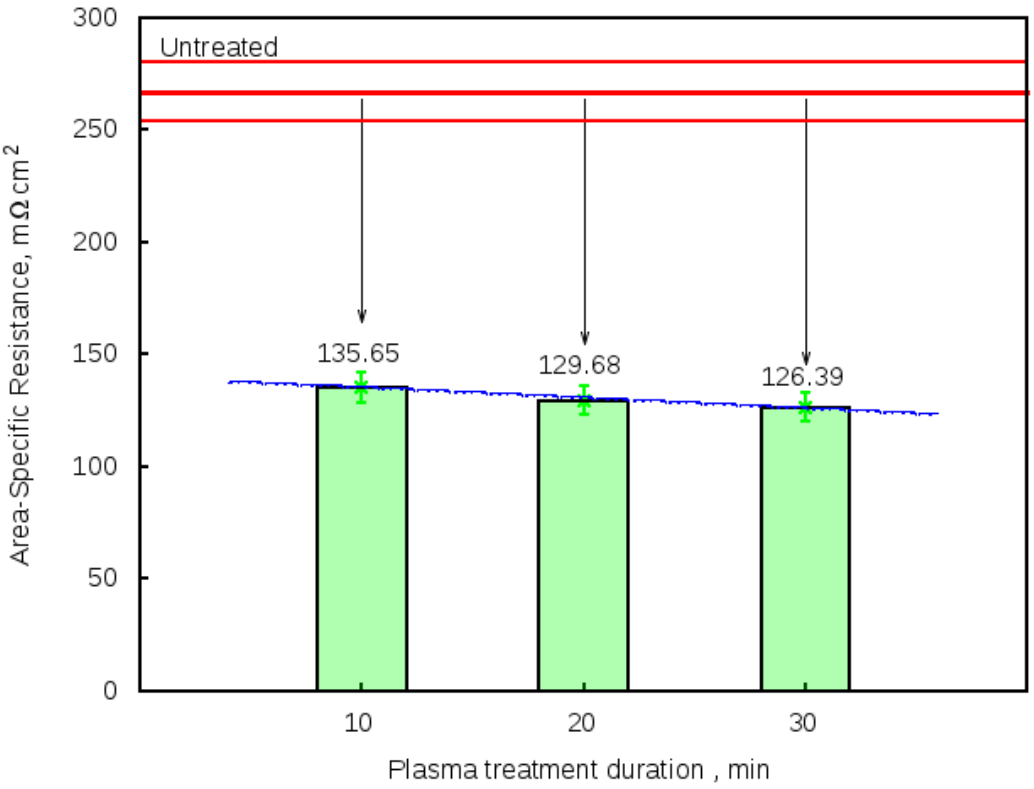

Figure 9.4: Influence of duration of plasma treatment on ASR.

The choice of the duration of plasma treatment, as well as the choice of the distance between the sample and the plasma chamber, depends on other experimental parameters: the used gas, its pressure and flow; type, size and chemical composition of the sample. It was found that ASR decreases with the increase of

plasma treatment duration until destruction of the sample. Oxygen-containing plasma effectively removes PP and after that etches graphitic surface of BPP. The longer is the treatment, the more graphitic powder appears on the surface, what provides better electrical conductivity. Thereby the treatment in plasma should be long enough to achieve the required ASR value, but not too long not to damage or destroy the sample.

The dependence of the result of plasma treatment on time and on gas flow for foils (35 wt% of PP and 29 wt% of PP) is shown in Fig. 9.5. The foils were treated by synthetic air (20.5 $\pm$ 0.5% O_2 in N_2) at the distance of 6 cm from the plasma chamber: 960 mbar, 17 slm – Fig. 9.5 (left); 10 mbar, 3 min – Fig. 9.5 (right).

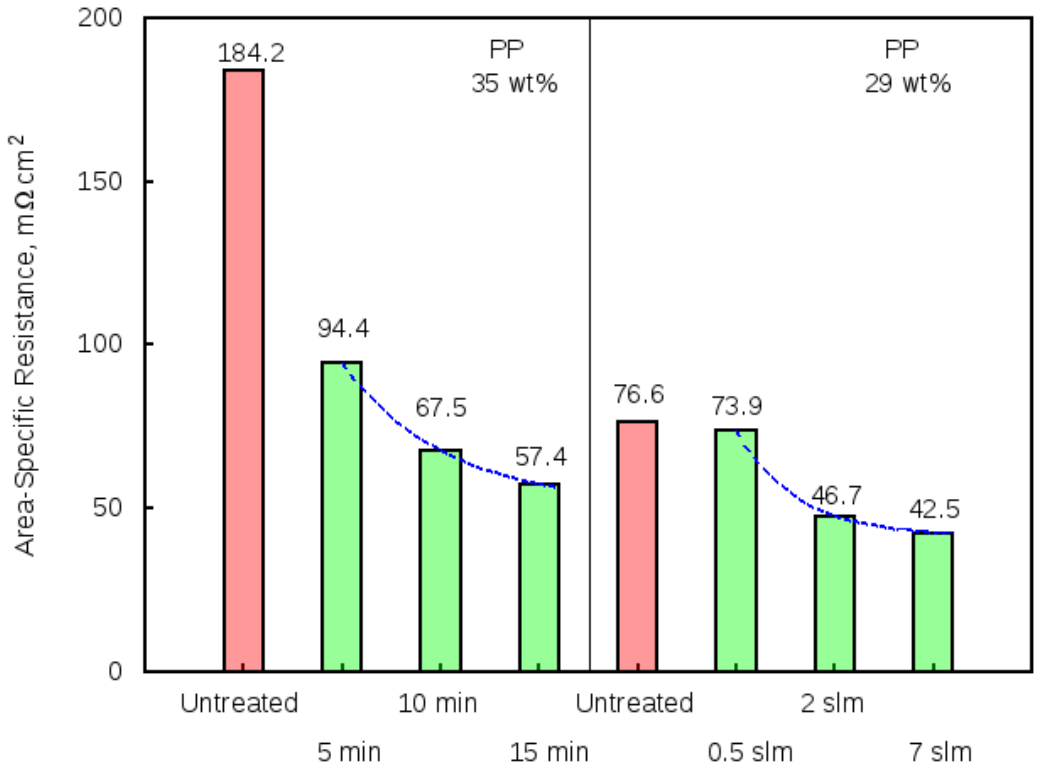

Figure 9.5: ASR dependence on treatment time and on gas flow.

Carbon dioxide plasma treatment is more effective than air plasma treatment because of much higher oxygen content in CO_2 than in air. However, air plasma treatment with the right set of experimental parameters also allows to obtain the required value of ASR, as shown in Fig. 9.6. This value is comparable with ASR of BPP treated in CO_2 and with ASR of the milled sample.

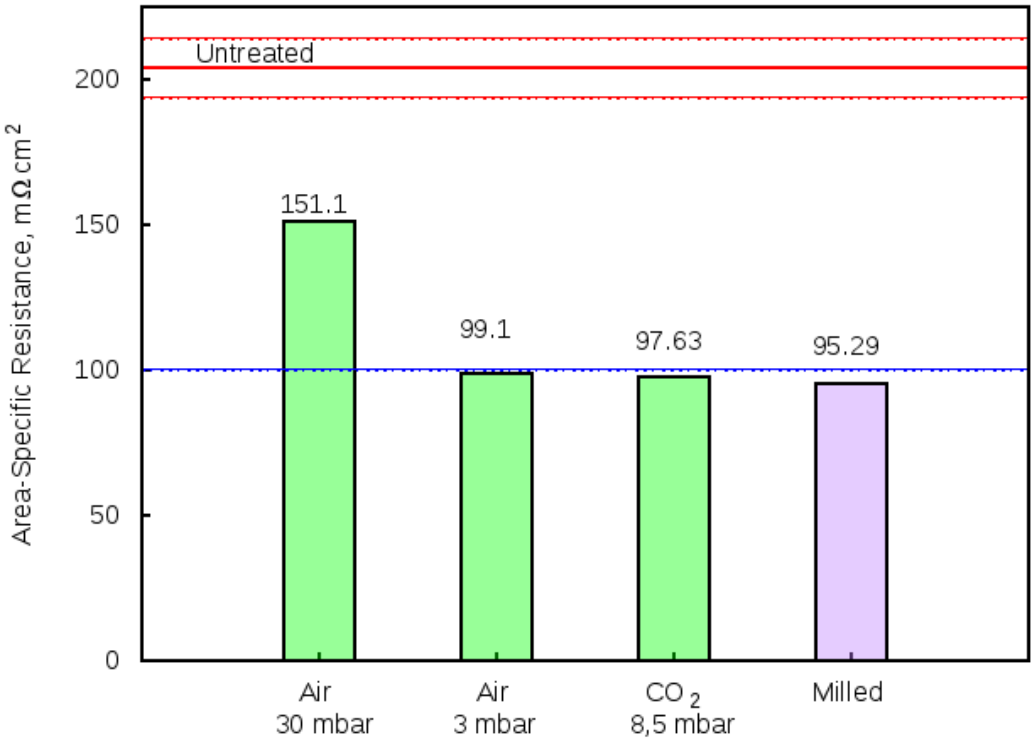

Figure 9.6: Comparison of ASR of untreated, plasma-treated in air and CO_2 and milled BPP.

Even though plasma treatment allows to reduce ASR significantly, the chemical composition of BPP should meet the requirements of minimal possible PP and minimal possible deviations of the composition to achieve the required electrical conductivity by plasma treatment.

Composition of a sample defines its electrical properties. The higher is PP content, the higher is the initial ASR value of the sample. Fig. 9.7 shows ASR of

foils with different PP content, untreated and treated by oxygen plasma (35 wt% and 33 wt% of PP) and by air plasma (31 wt% and 29 wt% of PP).

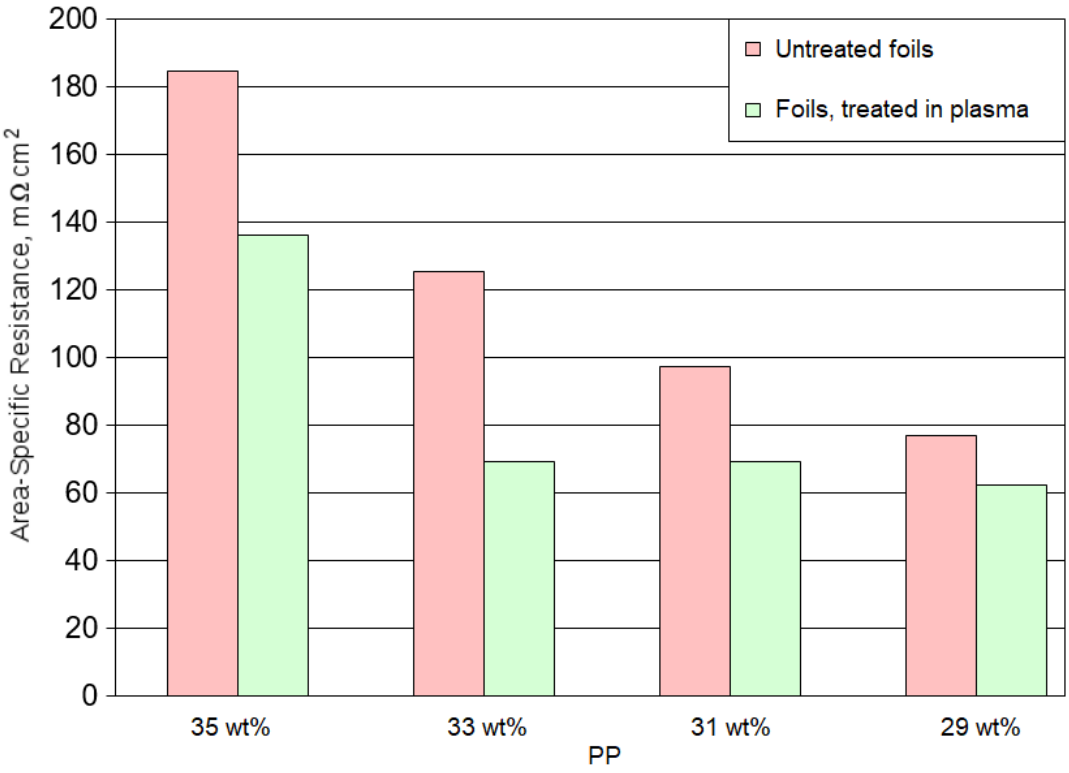

Figure 9.7: ASR of untreated and treated foils with different PP content.

Foils are especially suitable samples to investigate the optimal properties, because their composition can be changed advisedly for this purpose. Foils have no pattern on the surface and ASR was measured for each foil separately. ASR values of two foils (20 wt% PP and 18 wt% PP) before and after plasma treatment are shown in Fig. 9.8. The values of contact resistance significantly decrease in this case and bulk resistance does not change, considering the measurement error.

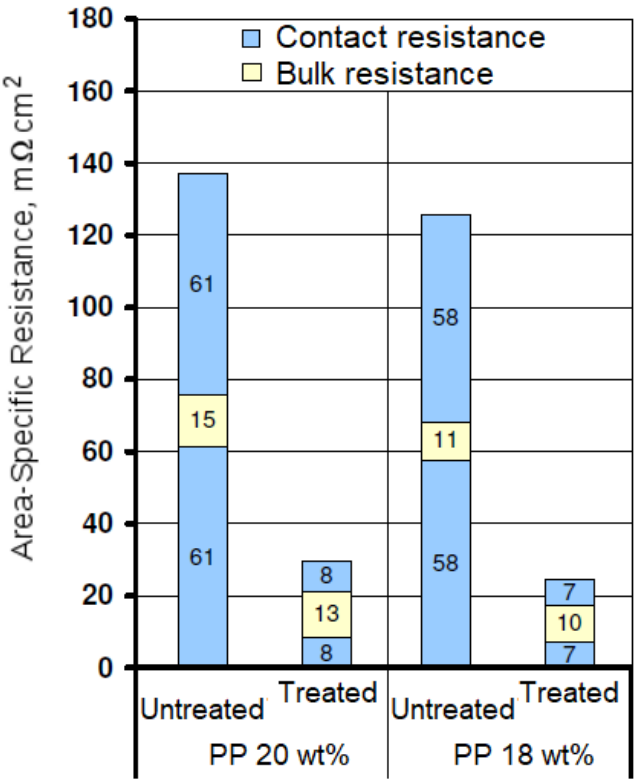

Figure 9.8: ASR of two different foils before and after plasma treatment.

Summarizing the information above, one can say that besides the composition of the sample the following parameters of plasma treatment influence the resulting ASR value: process pressure, treatment duration, distance from the sample surface to the plasma, gas flow and the gases used.

First of all, as experiments with foils of different composition show, the less PP a sample contains, the easier it is to reach the required value of ASR by plasma treatment. Therefore, the BPP should be produced with as small binding PP content as possible in their composition and the composition deviations of single BPP should be minimal. ZBT GmbH in Duisburg is currently working on this problem.

The increase of the treatment duration, as well as decrease of the distance be-

tween the sample and the plasma improves the electrical conductivity, but too long treatment and too small distance may lead to significant unwanted damages of the graphitic surface. Increase of the gas flow leads to decrease of ASR values.

Regarding the plasma chemistry, the best results are obtained using CO_2 as a working gas, because of higher content of oxygen than in air and presence of carbon in it. However, air is more interesting for industrial application of plasma treatment of BPP, therefore much effort was applied to investigate ASR of the samples treated by air plasma. Here the process pressure is especially important, because even a difference of several mbar influences the resulting ASR value. Generally, the ASR values decrease with the decrease of the process pressure, because low pressure provides longer mean free paths what results into higher energies of the active particles which interact with the surface. In case of air plasma treatment, the best ASR values were reached at the process pressure of 3 mbar and below. Considering the air plasma treatment at atmospheric pressure, which is especially interesting for industrial applications, it is possible to reach the required ASR values additionally optimizing the composition of the samples, increasing the treatment time and if necessary decreasing the distance between the sample and the plasma.

10 Conclusions

The importance of this research is dictated by the serious need of development of modern ecological energy sources, such as fuel cells, and solving the related problems of insufficient electrical conductivity of BPP, high cost of production and other, which still remain unsolved. This research work offers one of the possible solutions of these problems.

The aim of this work was to find out whether mechanical milling of BPP can be replaced by plasma treatment, so that plasma-treated BPP would have the same ASR values as milled BPP. Successful plasma treatment allows to achieve the required ASR values. It was shown that plasma treatment by oxygen-containing gases allow to reduce the ASR values as successfully as milling does, avoiding the drawbacks of mechanical milling, namely high cost, time consuming and serious mechanical damages of the surface. Even using atmospheric air as a working gas at ambient pressure allows to reach sufficient electrical conductivity and can replace costly and time-consuming mechanical milling. This discovery is especially important for industrial and large-scale application of plasma treatment of injection-molded BPP with a view to improve their electrical conductivity, because using ambient air without any additional technics for pressure stabilization would decrease the costs and the duration of the treatment process very significantly. Furthermore, plasma treatment, in contradistinction to mechanical milling, excludes the possibility of significant mechanical damages of the flow-field structure on the BPP surface, the damages, which make the BPP unusable.

Since it was necessary to find the suitable experimental parameters to provide successful plasma treatment, the IPLAS CYRANNUS® plasma source was chosen to maximize the possibility of variation of the experimental parameters. An additional variable parameter – the composition of the sample, should be

taken into account by choosing the treatment parameters (treatment duration, pressure, microwave power, gas flow, gas or gas composition and position of the sample, if IPLAS CYRANNUS® plasma source is used).

The starting point of this work was to remove PP from the surface of BPP by plasma etching, but molecular spectroscopy investigations (FTIR and Raman) allowed to find out that, except physical etching, plasma affects the chemical processes on the surface. FTIR spectroscopy corroborated the expected removal of the polymer matrix at the surface by plasma. Due to this important change the electrical properties of BPP are improved. But this is not the only change occurring due to the successful plasma treatment and contributing to the improvement of electrical conductivity of BPP. Raman spectra allow to estimate the efficiency of plasma treatment on the whole by evaluating the intensity ratio I(D)/I(G), the shift of the G peak and the shape of the peaks G, D and 2D. It was surprising to find out by the Raman spectroscopy that the amount of graphite nanoparticles was reduced after the plasma treatment, while other graphitic structures of larger size remained on the surface. Less interfaces between the crystals lead to less scattering of electrons and hence the conductivity of the plasma-treated samples is improved. The removal of polymer matrix from the surface and the change of the graphite structure after the plasma treatment allow to reduce the area-specific resistance, so that plasma treatment can successfully replace mechanical milling.

Another possibility to optimize the electrical properties of BPP is to adapt their composition to the following process of plasma treatment.

The measurements of water wettability done allow to understand the changes of the surface chemistry during the process of plasma treatment. Already in the first minutes of treatment by oxygen-containing plasma, the plasma starts to destroy the macromolecules of PP and chemical functionalization of the surface takes place, increases hydrophilicity. If the duration of the treatment is long enough, PP will be removed from the surface and the hydrophilicity of the surface will decrease again. The measurements of the mass of the samples after

plasma treatment allow to suppose that surface chemistry changes take place even after the treatment process. Chemistry of the surface was studied also by XPS, AES and EDX methods. SEM investigations gave a visual idea about the changes of the surface structure after the plasma treatment. Also roughness measurements and quantification of topography of the sample before and after plasma treatment was done for the completeness of the research. Investigation of morphology of the samples showed that plasma treatment by different gases removes PP and carbon black bound with PP from the graphitic surface of BPP and the duration of treatment influences on the result very much. Roughness and topography investigation showed the alignment of the height of the surface in millimeter-range. However, the treatment by carbon dioxide increases the roughness due to the high amount of oxygen and its high chemical activity. The roughness in nano-range increases after the plasma etching and higher amount of oxygen in plasma leads to higher roughness of the surface after the plasma treatment. No negative influence of the roughness, increased after the plasma treatment, on electrical conductivity of the samples was found.

A few experiments conducted using another plasma source TIGRES MEF7/56 (see Chapter 11), which operates using air at atmospheric pressure, showed the same efficiency as plasma treatment using IPLAS CYRANNUS® plasma source described in this work. This fact can give a direction for further investigation of plasma treatment of BPP on a more advanced level, using plasma equipment more suitable for this application. The duration of plasma treatment and other experimental parameters must be found experimentally for each type and content of BPP and for each plasma source.

11 Outlook

Further work supposes experimental application of atmospheric pressure air plasma sources for quick and effective treatment of BPP with a view of industrial application.

For large-scale application it makes sense to use the plasma sources, designed to work with air plasma at atmospheric pressure. The usage of TIGRES MEF7/56 plasma system, in which compressed air directs the plasma beam to the surface, has already allowed to achieve successful results of plasma treatment. The drafting of this device is presented in Appendix B.

Thanks to the research and results obtained by Ana Luiza F. Ferraz, it is possible to compare the Raman spectra of BPP, 20 minutes treated by air plasma using IPLAS CYRANNUS® and TIGRES MEF7/56 plasma sources. This comparison is shown in Fig. 11.1.

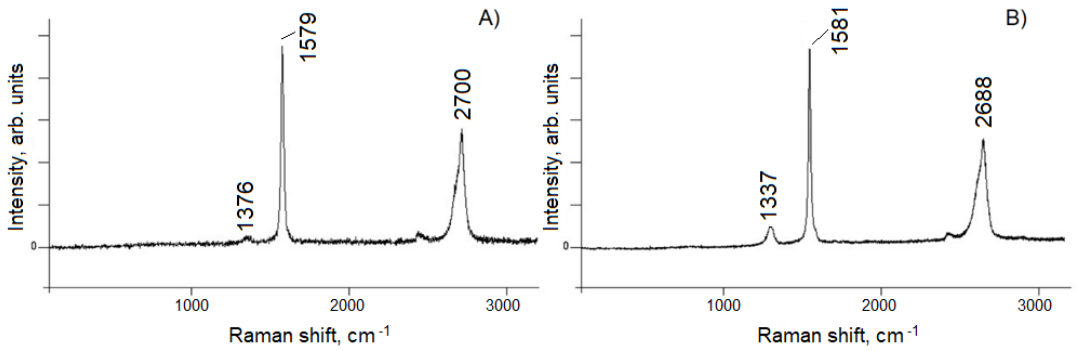

Figure 11.1: Raman spectra of BPP treated in air plasma for 20 min using: A) CYRANNUS® plasma source and B) MEF7/56 plasma source.

Comparing to the Raman spectrum of an untreated BPP in Fig. 7.17 (A), the

spectra in Fig. 11.1 obviously show the effect of plasma treatment, which does not seem to differ depending on the plasma source used. It is an example that the atmospheric pressure plasma devices may allow to treat the surfaces of BPP as successful as IPLAS CYRANNUS® device does, saving time and without the additional expenses. However, the detailed investigation of plasma treatment using other than IPLAS CYRANNUS® plasma sources is not in the scope of this work.

12 Appendix

12.1 Appendix A - Overview of the Roughness Parameters

The values of roughness parameters can be calculated from a line (profile roughness parameters R_a, R_q and etc.) and on a specific area (area roughness parameters S_a, S_q, etc.).

The basic parameters used to define the roughness are listed below [113–120].

- **y** – Profile deviation. The direct distance between a point of the profile and the baseline.
- **l** – Sampling length. The length of the baseline used to highlight the irregularities which characterize the surface roughness (Fig. 12.1).
- **m** – Mean line of the profile. A baseline, drawn so that within the sampling length the gauge standard deviation of the profile to this line is minimal (Fig. 12.1).

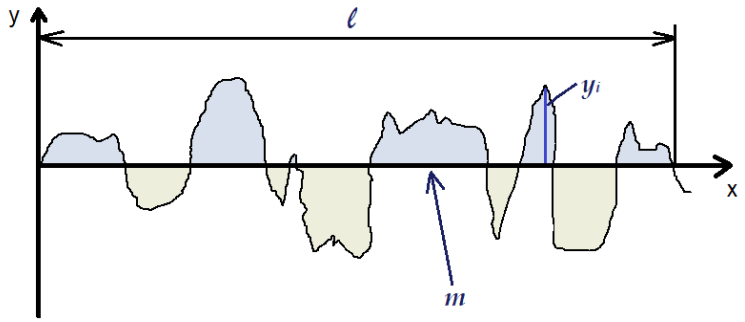

Figure 12.1: Profile deviation, sampling length and mean line of the profile.

- Central line of the profile. The sum of the areas enclosed between this line and the profile line is the same from both sides of the central line (Fig. 12.2).

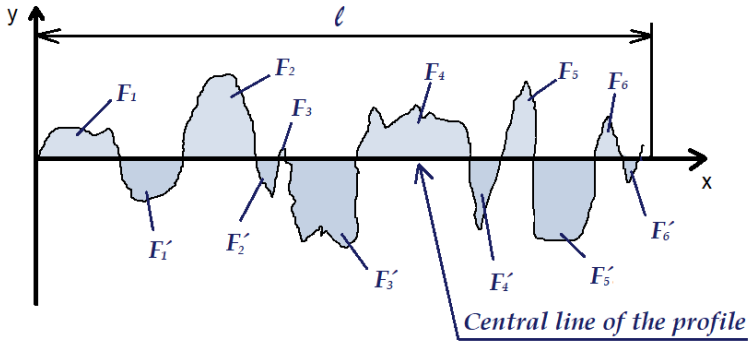

Figure 12.2: Central line of the profile.

- $\mathbf{y}_p$ – Profile peak height. The distance from the mean line of the profile to the highest peak point of the profile.

- $\mathbf{y}_v$ – Profile valley depth. The distance from the mean line of the profile to the lowest valley point of the profile.

- Profile irregularity height. The sum of the height of the profile and the depth of the conjugated valley of the profile.

Amplitude parameters (**R**) are defined by deviations of the roughness profile from the mean line.

- $\mathbf{R}_a$ – Arithmetical mean deviation of the roughness profile. Arithmetic average of the absolute values of deviation of the profile within the sampling length:

$$R_a = \frac{1}{l}\int_0^l |y(x)|dx$$

$$R_a = \frac{1}{n}\sum_{i=1}^{n} y_i$$

- **R_q (RMS)** – Root mean square average of the profile height deviations from the mean line, recorded within the sampling length [120]:

$$R_q = \sqrt{\frac{1}{l}\int_0^l y^2(x)dx}$$

- **R_v** – Maximum profile valley depth. The distance from the lowest point of the profile to the mean line within the sampling length (Fig. 12.3):

$$R_v = min_i(y_i)$$

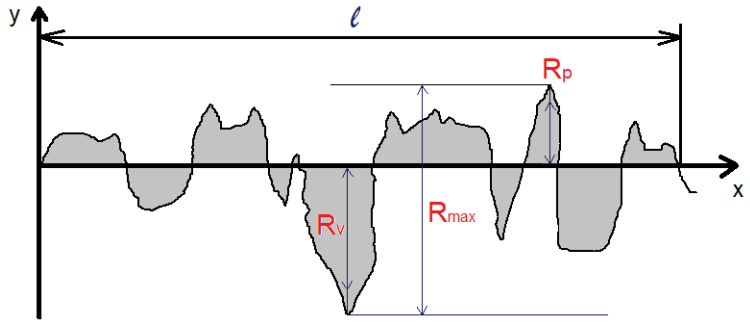

Figure 12.3: Maximal valley depth, maximal peak height and maximal height of the profile.

- **R_p** – Maximal peak height. The distance from the mean line to the highest point of the profile within the sampling length (Fig. 12.3):

$$R_v = max_i(y_i)$$

- **R_{max}** – Maximal height of the profile. The maximal distance between the line of the profile peaks and the line of the profile valleys within the sampling length
(Fig. 12.3).

- **R_t** – Total height of the roughness profile. The sum of the maximum value of the profile peak height and the maximum value of profile valley depth on the profile curve but in the entire evaluation length, not only the sampling

length:

$$R_t = max(R_p) + max(R_v)$$

- $\mathbf{R}_z$ – Ten-point height of irregularities. A sum of the average absolute values of the 5 highest and the 5 deepest valleys of the profile within the sampling length (Fig. 12.4):

$$R_z = \frac{\sum_{i=1}^{5} |y_{pi}| + \sum_{i=1}^{5} |y_{vi}|}{5}$$

where y_{pi} is the height of the i-th highest projection of the profile; y_{vi} is the depth of the i-th lowest valley of the profile.

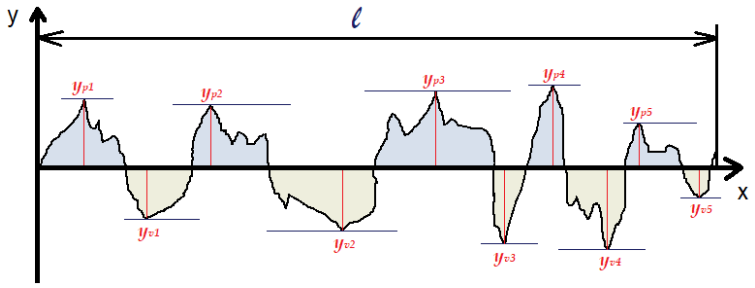

Figure 12.4: Ten-point height of irregularities.

- $\mathbf{R}_{z_{din}}$ (or $\mathbf{R}_{tm}$) – an average value of R_{max} of 5 sequential sites of measurement.

- $\mathbf{R}_c$ – Mean height of the roughness profile elements:

$$R_c = \frac{1}{m} \sum_{i=1}^{m} y_i$$

- $\mathbf{R}_{sk}$ – Skewness of the roughness profile – the degree of skew. The cubic mean of y_i in a sampling length rendered dimensionless as the cube of R_q. It expresses the symmetry of peaks and valleys using the average line as the center:

$$R_{sk} = \frac{1}{R_q^3} \left(\frac{1}{l} \int_0^l y^3(x) dx \right)$$

$R_{sk} = 0$: Symmetrical about the average line (normal distribution).
$R_{sk} > 0$: Skewed downward relative to the average line.
$R_{sk} < 0$: Skewed upward relative to the average line [112].

- $\mathbf{R}_{ku}$ – Kurtosis of the roughness profile – kurtosis which is a yardstick for the sharpness of a surface. This expresses the biquadratic mean of y_i in a sampling length rendered dimensionless as the biquadratic of R_q – the pointing (sharpness) of the height distribution:

$$R_{sk} = \frac{1}{R_q^4}\left(\frac{1}{l}\int_0^l y^4(x)dx\right)$$

$R_{ku} = 3$: Normal distribution.
$R_{ku} > 3$: The height distribution is sharp.
$R_{ku} < 3$: The height distribution is not sharp [112].
The probability density of a height y_i being obtained in the sampling length can be expressed by probability density function, obtained by differentiating the material ratio curve. Material ratio curve is also called Bearing curve or Abbott-Firestone curve [112].

- $\mathbf{R}_{mr}\mathbf{(c)}$ – Material ratio of the roughness profile (Fig. 12.5) is often used for evaluation of wear resistance. This expresses the ratio of the material length $Ml(c)$ of a profile curve element to the evaluation length at the sectioning level c.

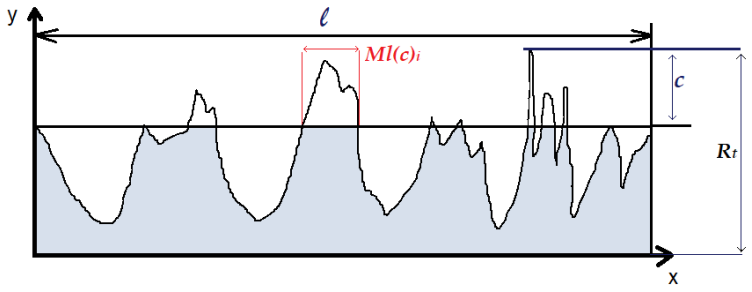

Figure 12.5: Material ratio of the roughness profile.

$$R_{mr}(c) = \frac{1}{l}\sum_{i=1}^{n} Ml(c)_i$$

- $\mathbf{R}_{dc}$(or $\mathbf{R}_{\sigma c}$) – Profile section height difference of the roughness profile (Fig. 12.6) is often used for evaluation of electrical contact resistance. This expresses the difference in sectioning level c in the height direction that matches the two material length ratios.

$$R_{\sigma}(c) = c(R_{m1}) - c(R_{m2})$$

if $R_{m1} < R_{m2}$

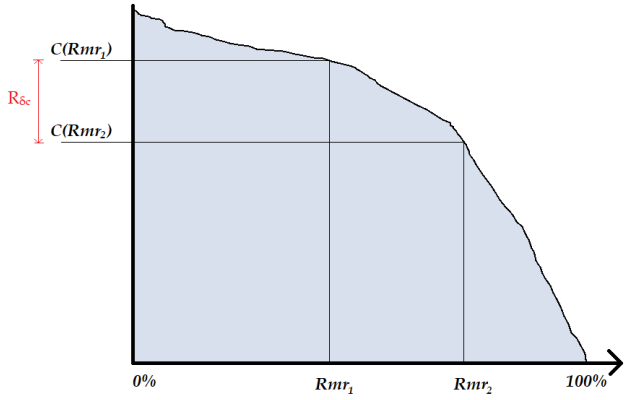

Figure 12.6: Profile section height difference of the roughness profile.

- $\mathbf{R}_{mr}$ – Relative material ratio of the roughness profile (Fig. 12.7). R_{mr} expresses the material length ratio that is determined from the reference sectioning level c_0 and the sectioning level difference $R_{\sigma c}$ of the profile curve [112]:

$$R_{mr} = R_{rm}(c_1)$$

$$c_1 = c_0 - R_{\sigma c}$$

where $c_0 = C(R_{mr0})$.

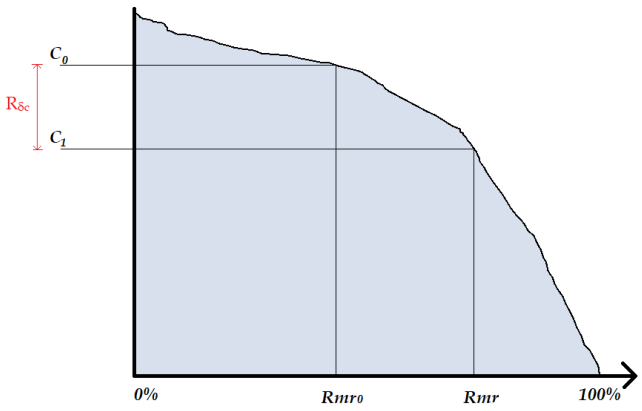

Figure 12.7: Relative material ratio of the roughness profile.

12.2 Appendix B - Drafting of TIGRES MEF7/56 Plasma Source

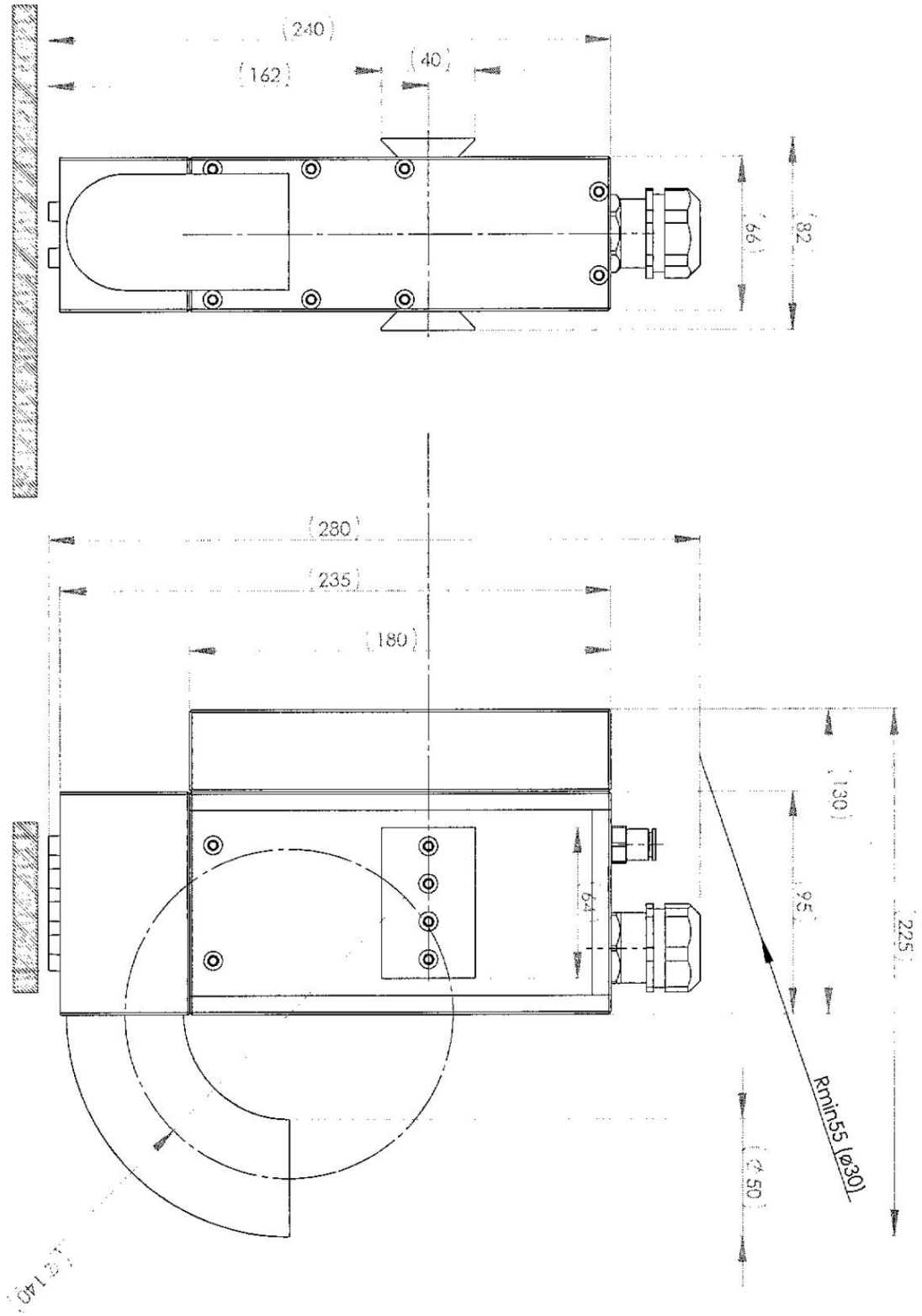

List of Abbreviations

AES ..... Auger electron spectroscopy
AFM ..... atomic force microscope/atomic force microscopy
arb. unit..... arbitrary unit
ASR ..... area specific resistance
BPHP ..... bipolar half-plates
BPP ..... bipolar plate
CCD ..... charge coupled device
DMM..... digital multimeter
EDX..... energy dispersive X-ray spectroscopy
FTIR..... Fourier transform infrared spectroscopy
GDL..... gas diffusion layer
IR ..... infrared
LED ..... light emitting diode
MEA ..... membrane electrode assembly
MW ..... microwave
OES ..... optical emission spectroscopy
PEM ..... proton-exchange membrane
PP ..... polypropylene
SEM..... scanning electron microscope/scanning electron microscopy
SPM..... scanning probe microscopy
UHV ..... ultra high vacuum
UV ..... ultraviolet
XPS ..... X-ray photoelectron spectroscopy
ZBT ..... Zentrum für BrennstoffzellenTechnik

List of Figures

List of Tables

13 Bibliography

[1] J. Garche et al. *Encyclopedia of Electrochemical Power Sources, Vol. 2, Proton-Exchange Membrane Fuel Cells: Bipolar Plates*. 3rd ed. Elsevier B. V., 2009.

[2] J. Wind, R. Späh, W. Kaiser, G. Böhm. In: *J. Power Sources* 105 (2002), p. 256.

[3] X.Z. Yuan, H. Wang, J. Zhang, D.P. Wilkinson. In: *J. New Mat. Electrochem. Systems* 8 (2005), pp. 257–267.

[4] A. Hermann, T. Chaudhuri, P. Spagnol. In: *Int. J. Hydrogen Energy* 30 (2005), pp. 1297–1302.

[5] H.S. Park, S.J. Kim, Y.Q. Wu, J.K. Lee. In: *IEEE T. Plasma Sci.* 31 (2003), pp. 703–710.

[6] Mar. 2018. URL: `https://www.conserve-energy-future.com/Advantages_Disadvantages_HydrogenEnergy.php`.

[7] Mar. 2018. URL: `http://www.fuelcell.su/index.php?Itemid=49&option=com_zoo&view=category&category_id=11`.

[8] T.N. Fedosenko, N. Wöhrl, V. Buck. *Influence of Various Plasma Treatments On Properties of Nanoparticle Containing Polymer Matrices*. Hakone XIV, 2014.

[9] M. Carmo, D.L. Fritz, J. Mergel, D. Stolten. In: *Int. J. Hydrogen Energy* 38 (2013), pp. 4901–4934.

[10] C. Kreuz. *Dissertation*. University of Duisburg-Essen, 2007.

[11] R.L. Borup, N.E. Vanderborgh. In: *Mater. Res. Soc. Symp. Proc.* 393 (1995), pp. 151–155.

[12] V. Mehta, J.S. Cooper. In: *J. Power Sources* 114 (2003), pp. 32–53.

[13] J.S. Cooper. In: *J. Power Sources* 129 (2004), pp. 152–169.

[14] A. Heinzel, F. Mahlendorf, O. Neimzig, C. Kreuz. In: *J. Power Sources* 131 (2004), pp. 35–40.

[15] AIF. "Kontinuierliches Fertigungskonzept zur Herstellung großfächiger Compound Bipolarplatten". In: *Final Report for the IGF Project 498 ZN of Research association Institut für Energie- und Umwelttechnik e. V. (IUTA)* (2016). (In German).

[16] J.-F. Zou, Zh.-Zh. Yu, Y.-X. Pan, X.-P. Fang, Y.-Ch. Ou. In: *J. Polym. Sci. Part B: Polym. Phys* 40 (2002), pp. 954–963.

[17] J.V. Lipin, A.V. Rogachev, S.S. Sidorsky, V.V. Haritonov. *Technology of Vacuum Metallization of Polymeric Materials.* (In Russian). Gomel Department of Belorussian engineering and technological academy, 1994.

[18] P.I. Zubov, L.A. Suhareva. *Structure and Properties of Polymer Coatings.* (In Russian). Himiya, Moscow, 1982.

[19] G.F. Ivanovsky, V.I. Petrov. *Ion-Plasma Treatment of Materials.* (In Russian). Radio i svyaz, Moscow, 1986.

[20] A. Meiners, M. Leck, B. Abel. In: *Plasma Sources Sci. Technol.* 18 (2009), p. 045015.

[21] N. Wöhrl. *Dissertation.* University of Duisburg-Essen, 2010.

[22] G. Franz, F. Schamberger, I. Krstev, S. Umrath. In: *Plasma Sci. Technol.* 15 (2013), pp. 43–51.

[23] A.N. Goyette et al. In: *Plasma Sources Sci. Technol.* 7 (1998), pp. 149–153.

[24] B.-D. Huang, X.-M. Zhu, K. Takashima, Y.-K. Pu. In: *J. Phys. D, Appl. Phys.* 46 (2013), p. 464011.

[25] M.V. Malyshev, V.M. Donnelly. In: *Phys. Rev. E* 60 (1999), pp. 6016–6029.

[26] C.O. Laux, T.G. Spence, C.H. Kruger, R.N. Zare. In: *Plasma Sources Sci. Technol.* 12 (2003), pp. 125–138.

[27] Z. Machala et al. In: *Mol. Spectrosc.* 243 (2007), pp. 194–201.

[28] F.S. Parker. *Applications of Infrared, Raman, and Resonance Raman Spectroscopy in Biochemistry*. Springer Science & Business Media, 1983, p. 568.

[29] K. Meyberg, P. Vachenauer. *Höhere Mathematik 2. Differentialgleichungen, Funktionentheorie, Fourier-Analysis, Variationsrechnung*. Vol. 4. (In German). Springer, 2001, p. 338.

[30] D.S. Sivia. *Elementary Scattering Theory for X-Ray And Neutron Users*. Oxford University Press, 2011.

[31] P.R. Griffiths, J.A. De Haseth. *Fourier Transform Infrared Spectrometry*. John Wiley & Sons, 2007.

[32] F.I. Grigorjev. *Ion-plasma Treatment of Polymeric Materials in Microelectronics Technology*. (In Russian). Moscow, 2008, p. 21.

[33] Polypropylene. June 2017. URL: `http://pslc.ws/macrog/pp.htm`.

[34] B.N. Tarasevich. *Fundamentals of Infrared Fourier Transform Spectroscopy. Sample preparation in IR spectroscopy*. Vol. 19. (In Russian). State University named after Lomonosov, 2012.

[35] D.V. Kuznetsov et al. *Investigation of the stability of polymer composites based on polypropylene after UV radiation*. Vol. 6. (In Russian). Modern Problems of Science and Education, 2012.

[36] Yu. Gorokhovatskii et al. *IR-spectroscopy of electrets on the basis of polythene and polypropylene*. (In Russian). News of A. I. Herzen Russian State Pedagogical University, 2004, pp. 69–75.

[37] B. Wunderlich. "The ATHAS Database on Heat Capacities of Polymers". In: *Pure Appl. Chem.* 67 (1995), pp. 1019–1026.

[38] V.L. Karpov. "Radiation Chemistry of Polymers". In: *M.: Nauka* (1966). (In Russian).

[39] A.N. Elliot. "Infrared Spectra and Structure of Organic Long Chain Polymers". In: *Acta Cryst.* B26 (1970), p. 1387.

[40] L.I. Kravets et al. *Research of the Surface and Electrochemical Properties of Polypropylene Track Membrane Modified by Non-Polymerizing Gas Plasma.* (In Russian). Electrochemistry, Dubna, 2012.

[41] A.S. Zolkin, E.S. Yurkovskaya. *Ion-Beam and Magnetron Deposition of Carbon Nanofilms on Glass and Silicon Substrates.* (In Russian). Novosibirsk State University, 2009.

[42] R.V. Bekarevich. Shizuoka University, 2013.

[43] J. Robertson. In: *Mater. Sci. Eng.* 37 (2002), pp. 129–281.

[44] M.S. Dresselhaus, A. Jorio, M. Hofmann, G. Dresselhaus, R. Saito. In: *Nano Lett.* 10 (2019), pp. 751–758.

[45] Film Analysis. Aug. 2017. URL: `http://www.chm.bris.ac.uk/pt/diamond/jamespthesis/chapter2.htm#_edn3`.

[46] R.J. Nemanich, J.T. Glass, G. Lucovsky, R.E. Shroder. In: *J. Vac. Sci. Technol. A.* 6 (1988), p. 1783.

[47] A.C. Ferrari, J. Robertson. In: *Phys. Rev. B* 61 (2000), p. 14095.

[48] A.C. Ferrari, J. Robertson. In: *Phil. Trans. R. Soc. Lond.* A 362 (2004), p. 2483.

[49] A.C. Ferrari. In: *Solid State Commun.* 143 (2007), pp. 47–57.

[50] A.C. Ferrari et al. In: *Phys. Rev. Lett.* 97 (2006), p. 187401.

[51] C.N. Banwell. *Fundamentals of Molecular Spectroscopy.* McGraw-Hill, 1983.

[52] N.B. Colthup, L.H. Daly, S.E. Wiberley. *Introduction to Infrared and Raman Spectroscopy.* Vol. 3. Academic Press, 1990, p. 387.

[53] D. Briggs, M.P. Seah. *Practical Surface Analysis. Volume 1 – Auger and X-ray Photoelectron Spectroscopy.* Vol. 2. John Wiley and Sons, 1990.

[54] T.A. Carlson. *Photoelectron and Auger Spectroscopy.* Vol. 2. Plenum Press, 1975.

[55] S. Hoffmann. *Auger- and X-Ray Photoelectron Spectroscopy in Materials Science.* Vol. 2. Springer, 2013.

[56] Photoelectron and Auger electron spectroscopy for surface research. (In Russian). Jan. 2018. URL: http://surface.spbu.ru/images/data/PESandAuger.pdf.

[57] V.N. Petrov. *Electronic Auger Spectroscopy with a Spin Resolution*. (In Russian). Publishing house of SPBSTU, 2011.

[58] J.F. Watts. *An Introduction to Surface Analysis by Electron Spectroscopy*. Oxford University Press, 1990.

[59] D. Chattarji. *The Theory of Auger Transitions*. Academic Press, 1976.

[60] F.F. Komarov, M.A. Kumahov, I.S. Tashlykov. *Non-Destructive Analysis of the Surfaces of Solids by Ion Beams*. (In Russian). Universitetskoye, 1987.

[61] ICAN: Rasteraugerelektronenmikroskopie. (In German). Jan. 2018. URL: https://www.uni-due.de/cenide/ican/sam/.

[62] I.G. Kozlov. *Modern Problems of Electron Spectroscopy (Electron Spectrometers and Their Application)*. (In Russian). Atomizdat, 1978.

[63] D.V. Fomin. *Experimental Methods of Solid State Physics*. (In Russian). Directmedia, 2014.

[64] L.E. Davis et al. *Handbook of Auger Electron Spectroscopy*. Vol. 2. Perkin-Elmer Corporation, Physical Electronics Division, 1976.

[65] L.C. Feldman, J. W. Mayer. *Fundamentals of Surface and Thin Film Analysis*. Elsevier, 1986.

[66] Physical Basis of Electron Auger Spectroscopy. (In Russian). Jan. 2018. URL: http://www.sibsauktf.ru/courses/surface/LAB/LAB4/aes_2.htm.

[67] G.A. Somorjai. *Chemistry in Two Dimensions: Surfaces*. Cornell University Press, 1981.

[68] Surface Physics: An Introduction, Philip Hofmann. Jan. 2018. URL: http://www.philiphofmann.net/downloads/hofmann_surfphys_small_preview.pdf.

[69] X. Zha, Ch. G.H. Walker, M. El-Gomati. In: *J. Phys. Conf. Ser.* 522 (2014), p. 012027.

[70] J.J. Lander. In: *Phys. Rev.* 991 (1953), p. 1382.

[71] L.A. Harris. In: *J. Appl. Phys.* 39 (1968), p. 1419.

[72] R. Celotta, J. Levine. *Methods of Experimental Physic.* Vol. 22. Academic Press, 1985.

[73] G. Endredi, Ch.-M. Liegener. In: *J. Mol. Struct.* 312 (1994), pp. 275–279.

[74] G. Schiewitz et al. In: *Phys. Rev. Lett.* 69 (1992), p. 628.

[75] D.R. Baer, D.J. Gaspar, P. Nachimuthu, S.D. Techane, D.G. Castner. In: *Anal. Bioanal. Chem.* 396 (2010), pp. 983–1002.

[76] C.J. Powell. "Growth and trends in Auger-electron spectroscopy and x-ray photoelectron spectroscopy for surface analysis". In: *J. Vac. Sci. Technol.* 21 (2003), pp. 42–53.

[77] F. Reniers, C. Tewell. In: *J. Electron. Spectrosc. Relat. Phenom.* 142 (2005), pp. 1–25.

[78] E. Jagst. Freie Universitaet Berlin, 2010.

[79] C. Malitesta, I. Losito, L. Sabbatini, P.G. Zambonin. In: *J. Electron. Spectrosc. Relat. Phenom.* 97 (1998), pp. 199–208.

[80] A. Hollaender, F. Pippig, M. Dubreuil, D. Vangeneugden. In: *Plasma Process. Polym.* 5 (2008), pp. 345–349.

[81] A. Chilkoti, B.D. Ratner. "Chemical Derivatization Methods for Enhancing the Analytical Capabilities of X-ray Photoelectron Spectroscopy and Static Secondary Ion Mass Spectrometry". In: *Surface Characterization of Advanced Polymers* (1993), pp. 221–256.

[82] G. Beamson, D. Briggs. *High Resolution XPS of Organic Polymer.* Vol. 70(1). The Scienta ESCA300 Database, 1993.

[83] G. Fedosenko. (In German). Bergische Universitaet Gesamthochschule Wuppertal, 2002.

[84] H.H. Perkampus. *Lexikon Spektroskopiey*. (In German). VCH, Weinheim, 1993.

[85] I.S. Osmushko, V.I. Vovna, V.V. Korochentsev. *X-ray Photoelectron Spectroscopy of Solids: Theory and Practice*. (In Russian). Publishing house of the Far Eastern Federal University, 2010.

[86] U.J. Hagemann. *Dissertation*. Universitaet Duisburg-Essen, 2014.

[87] XPS Interpretation of Carbon. Jan. 2018. URL: `https://xpssimplified.com/elements/carbon.php`.

[88] D.V. Sviridov, Physical Methods of Research in Chemistry. Methods of Surface Investigation in Schemes and Graphics. (In Russian). Jan. 2018. URL: `https://www.bsu.by/Cache/pdf/587393.pdf`.

[89] L. Reimer. *Scanning Electron Microscopy*. Springer, 11985.

[90] V. Buck, F. Deuerler. In: *Diamond Relat. Mater.* 7 (1998), pp. 1544–1552.

[91] S.J.B. Reed. *Electron Microprobe Analysis*. Vol. 2. Cambridge University Press, 1993.

[92] V.D. Scott, G. Love, S.J.B. Reed. *Quantitative Electron-Probe Microanalysis*. Vol. 2. Ellis Horwood, 1994.

[93] B.K. Agarwal. *X-ray Spectroscopy*. Vol. 2. Springer, 1991.

[94] J.C. Russ. *Fundamentals of Energy Dispersive X-ray Analysis*. Butterworth, 1984.

[95] M. Watanabe, D.B. Williams. In: *Ultramicroscopy* 78 (1999), p. 89.

[96] J.I. Goldstein, D.E. Newbury, J.R. Michael, N.W.M. Ritchie, J.H.J. Scott, D.C. Joy. *Scanning Electron Microscopy and X-Ray Microanalysis*. Vol. 4. Springer, 2018.

[97] Scanning Electron Microscopy. Apr. 2018. URL: `https://cmrf.research.uiowa.edu/scanning-electron-microscopy`.

[98] EM Technology Overview – Scanning Electron Microscopy. Mar. 2018. URL: `http://www.nanoimages.com/sem-technology-overview/`.

[99] Scanning Electron Microscopy with EDX. Mar. 2018. URL: http://gems-inclusions.com/inclusions-studies/analytical-methods/sem-eds-wds-analysis/.

[100] Electronics Tutorials. Jan. 2018. URL: https://www.electronics-tutorials.ws/resistor/resistivity.html.

[101] A.V. Pirogov, N.V. Malehonova, A.I. Bobrov, N.O. Krivulin, D.A. Pavlov. *Energy-dispersive X-ray Spectroscopy. Electronic teaching aid.* (In Russian). N. I. Lobachevsky State University of Nizhny Novgorod, 2014.

[102] Zh.R. Li. *Industrial Applications of Electron Microscopy.* Marcel Dekker, 2003.

[103] Zh. L. Wang, J. Bentley. In: *Microsc. Microanal. Microstruct.* 2 (1991), pp. 569–588.

[104] P. Zhang. University of Michigan, 2012.

[105] M.R. Gomez et al. In: *Appl. Phys. Lett.* 95 (2009), p. 072103.

[106] R. Holm. *Electric Contact.* Vol. 4. Springer, 1967.

[107] J.A. Greenwood. In: *Brit. J. Appl. Phys.* 17 (1966), p. 1621.

[108] S.P. Morgan. In: *J. Appl. Phys.* 20 (1949), pp. 352–362.

[109] Y.H. Jang, J.R. Barber. In: *J. Appl. Phys.* 94 (2003), pp. 7215–7221.

[110] T. Homola et al. In: *Polym. Degrad. Stab.* 97 (2012), pp. 2249–2254.

[111] M. Nosonovsky, B. Bhushan. In: *Microsyst. Technol.* 11 (2005), pp. 535–549.

[112] OLYMPUS. Roughness (2D) parameter. Feb. 2018. URL: https://www.olympus-ims.com/en/knowledge/metrology/roughness/2d_parameter/.

[113] State Standard of the Union of SSR. Surface roughness. Terms and definitions. (In Russian). Jan. 2018. URL: http://docs.cntd.ru/document/gost-25142-82.

[114] S. F. Sobolev, Electronic Textbook on Discipline: (In Russian). Feb. 2018. URL: http://de.ifmo.ru/bk_netra/page.php?dir=4&tutindex=38&index=8&layer=1.

[115] A.P. Husu, J.R. Vitenberg, V.A. Palmov. *Surface Roughness (Theoretical-Probabilistic Approach)*. (In Russian). Nauka, 1975.

[116] D.J. Whitehouse. *Handbook of Surface Metrology*. Vol. 2. CRC Pres, 2011.

[117] D.J. Whitehouse. In: *Meas. Sci. Technol.* 8 (1997), pp. 955–972.

[118] Surface Metrology Guide. Feb. 2018. URL: `http://www.digitalsurf.fr/en/guide.html`.

[119] J.P. Davim. *Surface Integrity in Machining*. Springer, 2010.

[120] R_a and RMS: Calculating Surface Roughness. Feb. 2018. URL: `http://www.harrisonep.com/electropolishing-ra.html`.

[121] Instruments for Measuring Roughness. Profilometers, Profilographs and Their Modifications. (In Russian). Feb. 2018. URL: `http://www.xn--80aggyh2a5bzb.xn--p1ai/info/articles/Pribori_sherohovatosti.htm`.

[122] How a Profilometer Works. Jan. 2018. URL: `https://www.nanoscience.com/technology/optical-profiler-technology/how-profilometer-works/`.

[123] A.R. Shulman, S.A. Fridrihov. *Secondary-emission methods for studying a solid*. (In Russian). Nauka, 1977.

[124] A.A. Maradudin. *Light Scattering and Nanoscale Surface Roughness*. Springer Science & Business Media, 2007.

[125] O. Noel, H. Awada, G. Castelein, M. Brogly, J. Schultz, Jacques. In: *J. Adhes.* 82 (2006), pp. 649–669.

[126] A.S. Duwez, C. Poulenis, P. Bertrand, B. Nysten. In: *Langmuir* 17 (2001), pp. 6351–6357.

[127] S.C. Clear, P.F. Nealy. In: *J. Colloid Interface Sci.* 213 (1999), pp. 238–250.

[128] A. Noy, D.V. Vezenov, C. Lieber. In: *Annu. Rev. Mater. Sci.* 27 (1997), pp. 381–421.

[129] F.L. Leite, P.S.P. Herrmann. In: *J. Adhes. Sci. Technol.* 19 (2005), pp. 365–405.

[130] A. Noy, S. Zepeda, C.S. Orme, Y. Yen, J.J. De Yoreo. In: *J. Am. Chem. Soc.* 125 (2003), pp. 1356–1362.

[131] H. Schonherr, Z. Hruska, G.I. Vancso. In: *MacromoleculesMacromolecules* 31 (11) (1998), pp. 3679–3685.

[132] J. Drelich, K.L. Mittal. *Atomic Force Microscopy in Adhesion Studies.* CRC Press, 2005.

[133] G. Haugstad. *Atomic Force Microscopy: Understanding Basic Modes and Advanced Applications.* John Wiley & Sons, 2012.

[134] R. Wiesendanger. *Scanning Probe Microscopy and Spectroscopy: Methods and Applications.* Cambridge University Press, 1994.

[135] Cappella, G. Dietler. In: *Surf. Sci. Rep.* 34 (1999), pp. 1–104.

[136] G. Binnig, C.F. Quate, Ch. Gerber. In: *Phys. Rev. Lett.* 56 (1986), pp. 930–933.

[137] B. Anyamesem-Mensah. State University, 2007.

[138] M. Marrese, V. Guarino, L. Ambrosio. In: *J. Funct. Biomater.* 8 (2017), p. 7.

[139] S. Morita, R. Wiesendanger, E. Meyer. *Noncontact Atomic Force Microscopy.* Springer, 2002.

[140] J.A. Conchello, J.W. Lichtman. In: *Nat. Methods* 2 (2005), pp. 920–931.

[141] J. Pawley. *Handbook of Biological Confocal Microscopy.* Springer Science & Business Media, 2006.

[142] NanoFocus: μsurf Technology. Feb. 2018. URL: `http://www.nanofocus.com/technology/measurement-principles/usurf-technology/`.

[143] I.D. Burlakov, I.A. Denisov, A. L.Sizov, A.A. Silina, N.A. Smirnova. *The Surface Roughness Investigation of CdZnTe Substrates by Different Measuring Methods of Nanometer Accuracy.* (In Russian). Prikladnaya Fizika (Applied Physics), 2014.

[144] R. O Hayre, S.-W. Cha, Wh. Colella, F.B. Prinz. *Fuel Cell Fundamentals.* John Wiley & Sons, 2016.

[145] J.G. Webster. *Electrical Measurement, Signal Processing, and Displays*. CRC Press, 2003.

[146] Electronics Tutorials. Jan. 2018. URL: `https://www.electronics-tutorials.ws/resistor/resistivity.html`.

[147] CYRANNUS® III Patent. *Device for the Production of Homogenous Microwave Plasma*. European Patent No. 0 992 058, USA Patent No. 6,543,380.

[148] CYRANNUS by IPLAS. Mar. 2018. URL: `http://www.iplas.de/applications.html`.

[149] R. Sharma et al. In: *Thin Solid Films* 519 (2011), pp. 7632–7637.

[150] S. Mohsenian, M.S. Esmaili, B. Shokri, M. Ghorbanalilu. In: *J. Electrostat.* 76 (2015), pp. 231–237.

[151] A.V. Krivonosenko, D.A. Krivonosenko, V.E. Prokop ev. "The emission characteristics of a pulsed discharge in a water jet in air". In: *Atmospheric and Oceanic Optics* 25 (2012). (In Russian), pp. 268–272.

[152] M.A. Elliott et al. In: *Diam. Relat. Mater.* 9 (2000), pp. 311–316.

[153] N. De Geyter et al. In: *Plasma Chem. Plasma Process.* 33 (2013), pp. 165–175.

[154] V.G. Samojlovich, V.I. Gibalov, K.V. Kozlov. In: *Physical Chemistry of Barrier Discharge* (1989). (In Russian), p. 176.

[155] I.P. Vinogradov, K. Wiesemann. In: *Plasma Sources Sci. Technol.* 6 (1997), pp. 307–316.

[156] J. Ristein, R.T. Stief, L. Ley, W. Beyer. In: *J. Appl. Phys.* 84 (1998), p. 3836.

[157] R.O.F. Verkuijlen, M.H.A. van Dongen, A.A.E. Stevens, J. van Geldrop, J.P.C. Bernards. In: *Appl. Surf. Sci.* 290 (2014), pp. 381–387.

[158] N.J. Harrick. *Internal Reflection Spectroscopy*. Interscience, New York, 1967.

[159] J. Dechant, R. Danz, W. Kimmer, R. Schmolke. *Ultrarotspectroscopische Untersuchungen an Polymeren*. (In German). Akademie Verlag, Berlin, 1972.

[160] D. Lin-Vien, N. Colthup, W. Fateley, J. Grasselli. *The Handbook of Infrared and Raman Characteristic Frequencies of Organic Molecules*. Academic Press, 1991.

[161] F. Higgins. *Determination of Percent Polyethylene in Polyethylene/Polypropylene Blends Using Cast Film FTIR Techniques*. Agilent Technologies, 2012.

[162] G. Herzberg. *Molecular Spectra and Molecular Structure*. Vol. 2. van Nostrand, 1945.

[163] C.N.R. Rao. *Chemical Applications of Infrared Spectroscopy*. Academic Press, 1963, p. 683.

[164] H.A. Szymanski. *Infrared Band Handbook*. Plenum Press, 1963, p. 484.

[165] L.J. Bellamy. *The Infra-Red Spectra of Complex Molecules*. Methuen & Co. Ltd, 1954, p. 323.

[166] S. Jarmelo, I. Reva, P.R. Carey, R. Fausto. In: *Vib. Spectrosc.* 43 (2007), pp. 395–404.

[167] J.V. Gulmine, P.R. Janissek, H.M. Heise, L. Akcelrud. In: *Polym. Test.* 21 (2002), pp. 557–563.

[168] A.D. Bykov, O.N. Ulenikov. *Vibrational-Rotational Spectroscopy of Water Vapor*. (In Russian). Nauka, Novosibirsk, 1989, p. 295.

[169] A.A. Skovoroda, A.V. Spitsyn, S.V. Yanchenkov, Ya.V. Zubavichus. "Carbon Structures and Hydrogen Fuel Recycling in Fusion Devices". In: *The Problems of Atomic Science and Technology* 3 (2008). (In Russian), pp. 15–34.

[170] M. Schade et al. In: *Surf. Coat. Technol.* 240 (2014), pp. 255–260.

[171] B. Wunderlich, H. Baur. *Heat Capacities of Linear High Polymers*. Vol. 7/2. Springer-Verlag, 1970, p. 219.

[172] J.H. Kaufman, S. Metin, D.D. Saperstein. In: *Phys. Rev. B* 39 (1989), p. 13053.

[173] J.H.S. Yang, K. Teii. In: *Diam. Relat. Mater.* 24 (2012), pp. 54–58.

[174] Mark Wainwright Analytical Centre. Dec. 2017. URL: http://www.analytical.unsw.edu.au/facilities/speclab/instruments/raman-spectrometer-532-nm.

[175] E.A. Smorgonskaya, V.I. Ivanov-Omsky. "Investigation of Carbon Structure of Composite Films $a-C:H<Cu>$ and $a-C:H<Co>$ by the Method of Raman Spectroscopy". In: *Physics and Technics of Semiconductors* 36 (2005). (In Russian), pp. 971–973.

[176] A.M. Danishevsky, E.A. Smorgonskaya, S.K. Gordeev, A.V. Grechinskaya. "Raman Scattering of Light in Nanoporous Carbon Obtained from Silicon Carbides and Titanium Carbides". In: *Solid-State Physics* 43 (2001). (In Russian), p. 132.

[177] I. Pocsik, M. Hundhausen, M. Koos. In: *L. Ley. Intern. Symp. of Carbon.;J. Non-Cryst. Sol.* 90;1083 (1998), pp. 652, 227–230.

[178] Carbon-Carbon Bonds: Hybridization. Dec. 2017. URL: http://www.physik.fu-berlin.de/einrichtungen/ag/ag-reich/lehre/Archiv/ss2011/docs/Gina_Peschel-Handout.pdf.

[179] Handbook of a chemist. (In Russian). Dec. 2017. URL: http://chem21.info/info/1127250/.

[180] VersaProbe II Spezifikation. (In German). Dec. 2017. URL: https://www.uni-due.de/cenide/ican/pes/spezifikation_pes.php.

[181] Chemical Bonds of Nitrogen. Jan. 2018. URL: http://orgchem.ru/chem5/n12.htm.

[182] E. Gonzalez, M. D. Barankin, P. C. Guschl, R. F. Hicks. In: *Langmuir* 24(21) (2008), pp. 12636–12643.

[183] R. McCann, S. Roy, P. Papakonstantinou, J.A. McLaughlin, S.C. Ray. In: *J. Appl. Phys.* 97 (2005), p. 073522.

[184] M. Schade. *Dissertation.* University of Duisburg-Essen, 2015.

[185] V.L. Berkovits, A.B. Gordeeva, T.V. L'vova, V.P. Ulin. In: *Physics and Techniques of Semiconductors* 46 (2012). (In Russian), pp. 1463–1467.

[186] Converting Atomic Percent to Weight Percent and Vice Versa. Jan. 2018. URL: `http://www.plasmaterials.com/august16-blog.php`.

[187] A.S. Chaus, T.N. Fedosenko, A.V. Rogachev, L. Čaplovič. In: *Diam. Relat. Mater* 42 (2014), pp. 64–70.

[188] R.J. White. *Porous Carbon Materials from Sustainable Precursors*. The Royal Society of Chemistry, 2015.

[189] D.H. Bangham, J. Stafford. In: *J. Chem. Soc., Trans.* 127 (1925), pp. 1085–1094.

[190] M. Inagaki, K. Feiyu. *Carbon Materials Science and Engineering: From Fundamentals to Applications*. singhua University Press, 2006.

[191] M. Vukčević et al. In: *Chem. Eng. J.* 235 (2014), pp. 284–292.

[192] Sh. Gupta, N.-H. Tai. In: *J. Mater. Chem. A* 4 (2016), pp. 1550–1565.

[193] M.V. Buj, A.V. Rogachev. *Relaxation-Diffusion Theory of Interphase Processes*. (In Russian). Belorussian State University of Transport, 1997.

[194] A.V. Rogachev, S.S. Sidorsky. *Restoration and Increase of Wear Resistance of Machine Parts, Educational Establishment*. (In Russian). Belorussian State University of Transport, 2005.

[195] V.A. Titov, V.V. Rybkin, S.A. Smirnov. "Physico-Chemical Processes in the System of Non-Equilibrium Plasma – Polymer". In: *Chemistry of High Energy – Plasmochemistry* 43 (2009). (In Russian), pp. 218–226.

[196] Chemical Handbook 21, Chemistry and Chemical Technology. (In Russian). Jan. 2018. URL: `http://chem21.info/page/12917708618202521.025303017518218721913114822900 5/`.

[197] E.V. Kuvaldina, D.A. Shutov, V.V. Rybkin, V.A. Titov, Impact of the Plasma of Nitrogen-Oxygen Mixture On the Surface of Polypropylene and Polyethyleneterephthalate. (In Russian). Jan. 2018. URL: `http://main.isuct.ru/files/konf/ISTAPC2005/proc/4-17.pdf`.

[198] A.W. Nicol. *Physicochemical Methods of Mineral Analysis*. Plenum Press, 1975.

[199] Introduction to Energy Dispersive X-ray Spectrometry (EDS). Jan. 2018. URL: https://cfamm.ucr.edu/documents/eds-intro.pdf.

[200] J.I. Paredes, A. Martínez-Alonso, J.M.D. Tascón. In: *Langmuir* 23 (2007), pp. 8932–8943.

[201] D. Ketenoğlu, B. Ünal. In: *PHYSICA A* 392 (2013), pp. 3008–3017.

[202] B.Ch. Bai, D.-W. Park, H.V. Vo, S. Dessouky, J.S. Im. In: *J Nanomater.* 4 (2015), p. 255.

[203] G.-Sh. Wang, X.-M. Meng, X.-J. Zhang, Y.-F. Pan, Ch. Lu. In: *J. Mater. Chem. A.* 2 (2014), pp. 18725–18730.

[204] O.A. Al-Hartomy et al. In: *J. Compos. Mater.* 3 (2015), p. 50.

[205] Q. Cheng et al. In: *Sci. Rep.* 7 (2017), p. 14782.

[206] M. Imran, A.R.A. Khan, S. Megeri, Sh. Sadik. In: *Resource-Efficient Technologies* 2 (2016), pp. 81–88.

[207] G. Öztürk. *Dissertation*. (In German). Technical University of Darmstadt, 2012.

[208] R. Ramasamy, K. Yang, M. Rafailovich. In: *RSC Adv.* 4 (2014), pp. 44888–44895.

[209] Ph. Brown, Bh. Bhushan. In: *Philos. Trans. A Math. Phys. Eng. Sci.* 374 (2016), p. 2073.

[210] B. Xu et al. In: *J. Thermoplast. Compos. Mater.* 29 (2014), pp. 48–57.

[211] Asbury Carbons. Vein Graphite. Jan. 2018. URL: https://asbury.com/technical-presentations-papers/materials-in-depth/vein-graphite/.

[212] Megantech. Natural Kish Graphite (Grade 200). Jan. 2018. URL: http://www.megantech.pl/en/top/graphene/graphite/kish-graphite-1/natural-kish-graphite-grade-200-1/.

[213] ACS Material. Pyrolytic Graphite Powder. Jan. 2018. URL: https://www.acsmaterial.com/pyrolytic-graphite-powder.html.

[214] ACS Material. Low-Defect Graphite Oxide. Jan. 2018. URL: https://www.acsmaterial.com/low-defect-graphite-oxide.html.

[215] Graphene Supermarket. Flake Graphite. Jan. 2018. URL: https://graphene-supermarket.com/Flake-Graphite-100-grams.html.

[216] A. Méndez-Vilas, M. Nuevo, M.L. González-Martín, L. Labajos-Broncano. In: *Mater. Sci. Forum.* 408 (2002), pp. 239–244.

[217] J.V. Escobar, C. Garza, R. Castillo. In: *Beilstein J. Nanotechnol.* 8 (2017), pp. 813–825.

[218] Dektak Stylus Capabilities: How to Choose the Correct Stylus for Any Application. Feb. 2018. URL: https://www.bruker.com/products/surface-and-dimensional-analysis/stylus-profilometers/dektak-xtl/learn-more.html.

Publications, Presentations and Poster

Publications:

- T.N. Fedosenko, N. Wöhrl, V. Buck, Influence of Various Plasma Treatments on Properties of Nanoparticle Containing Polymer Matrices, The 14th International Symposium on High Pressure Low Temperature Plasma Chemistry (HAKONE XIV), Zinnowitz (2014)

Presentations:

- 78. DPG-Frühjahrstagung, Dresden, 30.03 – 04.04 2014, T. N. Fedosenko, N. Wöhrl, V. Buck, Improvement of The Electrical Conductivity of Bipolar Plates for Fuel Cells by Plasma Etching in Carbon Dioxide Environment

- 79. DPG-Frühjahrstagung, Berlin, 15.03 – 20.03 2015, T. N. Fedosenko, N. Wöhrl, V. Buck, Reduction of the Contact Resistance of Bipolar Plates and Foils for Fuel Cells by Air-Plasma Treatment

- Präsentation bei dem 3. Treffen des AiF-Projektes "Kontinuierliches Fertigungskonzept zur Herstellung großflächiger Compound Bipolarplatten"(ZN 09570/12), 2013 – 2015, Duisburg (ZBT), 08.07.2015, M. Gillmann, T. Derieth, A. Heinzel, O. te Heesen, W. Philippi, N. Wöhrl, T. Fedosenko

- 80. DPG-Frühjahrstagung, Regensburg, 06.03 – 11.03 2016, T. N. Fedosenko-Becker, N. Wöhrl, V. Buck, M. Gillmann, Remote Plasma Treatment as a Method to Improve the Surface Conductivity of Bipolar Plates for Fuel Cells

Poster:

- HAKONE XIV – The 14th International Symposium on High Pressure Low Temperature Plasma Chemistry, Zinnowitz, 21.09 – 26.09 2014, T. N. Fedosenko, N. Wöhrl, V. Buck, Influence of Various Plasma Treatments on Properties of Nanoparticle Containing Polymer Matrices

- 7. Workshop AiF-Brennstoffzellen-Allianz (Abschluss des AiF-DFG-Clusters MT-PEM-Brennstoffzelle und aktuelle Ergebnisse der mittelstandsorientierten Forschung in Deutschland), Duisburg (ZBT), 07.05.2014, M. Gillmann, T. Derieth, A. Heinzel, O. te Heesen, W. Philippi, N. Wöhrl, T. Fedosenko, Kontinuierliches Fertigungskonzept zur Herstellung großflächiger Compound Bipolarplatten

- PT-17 – 17. Fachtagung für Plasmatechnologie, Kiel, 23.02 – 25.02 2015, T. N. Fedosenko, N. Wöhrl, V. Buck, Air Plasma Treatment of Bipolar Plates for Fuel Cells to Decrease the Contact Resistance

- 8. Workshop AiF-Brennstoffzellen-Allianz (Abschluss des AiF-DFG-Clusters MT-PEM-Brennstoffzelle und aktuelle Ergebnisse der mittelstandsorientierten Forschung in Deutschland), Duisburg (ZBT), 11.05.2015, M. Gillmann, T. Derieth, A. Heinzel, O. te Heesen, N. Wöhrl, T. Fedosenko, Kontinuierliches Fertigungskonzept zur Herstellung großflächiger Compound Bipolarplatten

- 9. Workshop AiF-Brennstoffzellen-Allianz (Mittelstandsforschung für die Energiewende), Duisburg (ZBT), 21.06.2016, M. Gillmann, A. Heinzel, O. te Heesen, M. Burgfeld, J. Siepmann, J. Wortberg, N. Wöhrl, T. Fedosenko-Becker, V. Buck, Kontinuierliches Fertigungskonzept zur Herstellung großflächiger Compound Bipolarplatten

- PSE 2016 – 15th International Conference on Plasma Surface Engineering, Garmisch-Partenkirchen, 11.08.2016, V. Buck, N. Wöhrl, T. Fedosenko-Becker, M. Gillmann, Improvement of Electrical Conductivity of Bipolar Plates for Fuel Cells by Surface Plasma Modification

- PT-18 – 18. Fachtagung für Plasmatechnologie, Göttingen, 20.02 – 22.02 2017, T. N. Fedosenko-Becker, N. Wöhrl, A. L. F. Ferraz, M. Gillmann, V. Buck, Improvement of Electrical Conductivity of Bipolar Plates for Fuel Cells by Surface Plasma Modification

Erklärung

Hiermit versichere ich, Tatiana N. Fedosenko-Becker, dass ich die Arbeit selbständig verfasst, Zitate kenntlich gemacht und keine anderen als die angegebenen Quellen und Hilfsmittel benutzt habe. Die Arbeit wurde bisher weder im Inland noch im Ausland in gleicher oder ähnlicher Form einer anderen Prüfungsbehörde vorgelegt.

Die Arbeit wurde unter wissenschaftlicher Betreuung durch Herrn Prof. Dr. rer. nat. Dr. h.c. Volker Buck an der Fakultät für Physik der Universität Duisburg-Essen angefertigt.

Duisburg, 17. Oktober 2018 Tatiana N. Fedosenko-Becker

Erklärung „Kommerzielle Promotionsberatung“ (§ 6 Abs. 2 Buchstabe f)

Ich gebe folgende Erklärung ab:

Die Gelegenheit zum vorliegenden Promotionsverfahren ist mir nicht kommerziell vermittelt worden. Insbesondere habe ich keine Organisation eingeschaltet, die gegen Entgelt Betreuerinnen und Betreuer für die Anfertigung von Dissertationen sucht oder die mir obliegenden Pflichten hinsichtlich der Prüfungsleistungen für mich ganz oder teilweise erledigt.
Hilfe Dritter wurde bis jetzt und wird auch künftig nur in wissenschaftlich vertretbarem und prüfungsrechtlich zulässigem Ausmaß in Anspruch genommen. Mir ist bekannt, dass Unwahrheiten hinsichtlich der vorstehenden Erklärung die Zulassung zur Promotion ausschließen bzw. später zum Verfahrensabbruch oder zur Rücknahme des Titels führen können.

Duisburg, 17. Oktober 2018 Tatiana N. Fedosenko-Becker

Der Lebenslauf ist in der Online-Version aus Gründen des Datenschutzes nicht enthalten.